D. Serikbayev East Kazakhstan Technical University

UDC 553.411:528.8 On the rights of the manuscript

YESKALIYEV YERTAY TALGATOVICH

Methodology for prospecting of gold-bearing deposits using modern satellite technologies, case study of the West Kalba gold belt

8D07201 – Geology and exploration of mineral deposits

Doctoral Dissertation

Research advisors:
Mizernaya M.A., Candidate of Geological and Mineralogical Sciences, associate professor, Leading Researcher of Center of Competence and Technology Transfer in the field of Geology and Mining, School of Earth Sciences, EKTU

Rakhymberdina M.Ye., PhD, associate professor, Dean of School of Earth Sciences, EKTU

External Research Advisor:
Roman Shults, DSc, PhD, Associate Professor, Research Scientist, Head of the Remote Sensing and Analysis Lab, Interdisciplinary Research Center for Aviation and Space Exploration, King Fahd University of Petroleum and Minerals, Dhahran, Kingdom of Saudi Arabia

Republic of Kazakhstan
Ust-Kamenogorsk, 2026

CONTENT

ABBREVIATIONS

ASTER - Advanced Spaceborne Thermal Emission and Reflection Radiometer
ATCOR - Atmospheric and Topographic Correction
BRDF - Bidirectional Reflectance Distribution Function
CAOB - Central Asian Orogenic Belt
DEM - Digital Elevation Model
DLR - German Aerospace Center (Deutsches Zentrum für Luft- und Raumfahrt)
EKTU - East Kazakhstan Technical University (D. Serikbayev EKTU)
EnMAP - Environmental Mapping and Analysis Program
FCC - False Color Composite
FLAASH - Fast Line-of-sight Atmospheric Analysis of Spectral Hypercubes
GDEM - Global Digital Elevation Model
GFZ - Helmholtz Centre Potsdam (GFZ German Research Centre for Geosciences)
JHU - Johns Hopkins University
L2 / L2A - Level-2 product / Level-2A surface reflectance product
LIDAR - Light Detection and Ranging
METI - Ministry of Economy, Trade and Industry (Japan)
MSS - Multispectral Scanner System
MSI - MultiSpectral Instrument (Sentinel-2)
NASA - National Aeronautics and Space Administration
NDVI - Normalized Difference Vegetation Index
NOAA - National Oceanographic and Atmospheric Administration
OLI - Operational Land Imager (Landsat 8/9)
PGE - Platinum Group Elements
PRISMA - PRecursore IperSpettrale della Missione Applicativa
REE - Rare Earth Elements
RMSE - Root Mean Square Error
SAR - Synthetic Aperture Radar
SFF - Spectral Feature Fitting
SNR - Signal-to-noise ratio
SWIR - Short-Wave Infrared
TIR - Thermal Infrared
TM -Thematic Mapper
USGS - United States Geological Survey
UTM - Universal Transverse Mercator
VNIR - Visible and Near-Infrared
VMS - Volcanogenic Massive Sulfide

INTRODUCTION

Relevance of the research. In recent decades, global demand for gold and the scale of gold mining have continued to grow, while discovery and development have become more difficult due to depletion of the richest deposits, declining ore grades, and increasing environmental constraints. East Kazakhstan contains numerous gold deposits of different genetic types, with a major concentration in the West Kalba gold belt, which has long been a key contributor to the country's mineral resource base. At the same time, the potential for discovering new large objects using only traditional exploration approaches is decreasing, creating a need for scalable and reproducible screening methods. Satellite remote sensing provides such capability by mapping surface alteration footprints and structural controls at regional scale, but its application in Kazakhstan remains limited and requires a consistent workflow and clear validation.

Aim of the research: To develop a consistent remote sensing methodology for gold exploration in the West Kalba gold belt (East Kazakhstan) that maps hydrothermal alteration footprints and supports delineation of prospective zones.

Research objectives:

1) Identify and justify a set of key indicators of hydrothermal alteration in the gold-ore systems of the West Kalba gold belt that reflect the staged nature of ore formation and are suitable for interpreting Earth remote sensing data; then assess their diagnostic value and limitations for prospective delineation of promising gold-ore sites.

2) Build a mineral targeting framework that maps alteration minerals and diagnostic absorbers using regional geological sources and reference laboratory spectra.

3) Develop a reproducible processing pipeline for ASTER multispectral data, including alignment, NDVI masking, band ratios, false color composite generation, and multi-scene mosaicking.

4) Validate alteration mapping results using independent object-based comparison and hyperspectral EnMAP spectra where coverage is available.

5) Produce regional selection of hydrothermal alteration composites and identify prospective zones for follow-up work.

Scientific novelty. The scientific novelty of this work lies in integrating a geology-driven mineral targeting framework for the West Kalba belt with a reproducible multi-scene ASTER processing pipeline that produces comparable merged products across the study area, combined with a two-level validation strategy that merges object-based spatial correspondence with deposits and exploration footprints together with hyperspectral EnMAP spectral confirmation in the area of coverage overlap, thereby strengthening minerals interpretation and uncertainty assessment. At the gold-ore sites, these works are being carried out in Kazakhstan for the first time, which will undoubtedly make a significant contribution to the development of the use of remote technologies for prospecting and exploration of deposits of various genetic types.

Practical significance. The practical significance consists in the creation of a methodology for using remote methods for the preliminary forecasting of promising areas

of possible gold-ore occurrences and deposits, which will significantly increase the efficiency of geological exploration works

The research outcomes have also been implemented in the production activities of LLP “GEOSAT” and are used in the educational process of NJSC «D. Serikbayev East Kazakhstan State University» under the educational program 7M07302 “Geodesy” for the discipline “Authomated systems for collecting and processing the results of remote sensing”.

Main defended statements:

1) For the first time for the West-Kalba gold belt, a geologically justified spectral data catalog has been developed, based on integrating regional geological data, mineralogical-petrographic characteristics of deposits, and hydrothermal alteration models with laboratory reference spectra (USGS library). It is demonstrated that using diagnostic spectral features of Al–OH, Mg/Fe–OH, carbonate, and Fe^{3+} oxide minerals, along with their electromagnetic absorption and reflection properties, establishes a reproducible relationship between satellite spectral responses and the zonality of hydrothermal alterations genetically linked to gold mineralization.

2) An integrated multi- and hyperspectral methodology for gold exploration with mineralogical verification has been developed, combining ASTER multispectral analysis with hyperspectral mineralogical verification using EnMAP data. It is shown that the combination of multispectral ratios targeting diagnostic absorption bands of Al–OH, Mg/Fe–OH, carbonates, and Fe^{3+} oxides, with high-resolution spectral matching, enables the transition from regional exploration mapping to local mineralogical identification and enhances the geological justification of remotely detected anomalies.

3) The high effectiveness of remote mapping of hydrothermal alterations for identifying prospective gold-bearing zones within the West Kalba belt has been demonstrated. Over an area of approximately 30,750 km², a stable spatial correlation has been established between alteration zones identified from ASTER data and more than 80 known gold deposits and occurrences. Based on comprehensive validation, the district-scale zonality of hydrothermal alterations has been reproduced, and three perspective zones (B1, B2, and A1) have been identified, confirming the possibility of detecting concealed and previously unidentified mineralization targets.

Methodology of research. Review and analysis of research on gold deposits of the West Kalba belt and global analogues; detailed analysis of deposit mineral composition and creation of a catalog compiled from laboratory spectral measurements of minerals from multi- and hyperspectral images; comprehensive analytical studies, including processing of satellite remote sensing data (ASTER multispectral and EnMAP hyperspectral data), spectral analysis, spectral index calculations, false color composite generation, spatial correlation analysis, and integration with geological and mineralogical data.

The factual material and authors personal input

The core research data consist of information, that is collected by author during educational and participation in following projects:

1. Project IRN BR24992854 “Development and implementation of competitive science-based technologies to ensure sustainable development of mining and metallurgy industry East Kazakhstan region”, funded by the Science Committee of the Ministry of Science and Higher Education of the Republic of Kazakhstan.

2. Project IRN AP25795761 “Development of a combined method for forecasting gold mineral deposits based on satellite technology, geoinformation science and deep learning AI”, funded by Science Committee of the Ministry of Science and Higher Education of the Republic of Kazakhstan.

Author has participated in two research internships to Technical University Berlin (Germany), where the learning program was fully aligned with methodology of our research.

The author analyzed monographic, reference, and scientific publications on gold deposits of the West Kalba belt, as well as relevant international analogues. The dissertation draws on regional geological materials and datasets compiled and interpreted by the author, together with the results of satellite remote sensing analysis and related thematic products. In addition, the study uses information from known deposits and exploration sites within the study area, including data provided through prior investigations and, where available, supplementary materials obtained in collaboration with colleagues who conducted field work on the examined objects.

Satellite-based data processing was as a part of the project AP25795761 “Development of a combined method for forecasting gold mineral deposits based on satellite technology, geoinformation science and deep learning AI”, which was completely done by author. Based on results of which, author has developed a combined methodology for prospecting gold-bearing mineral deposits, highlighting remote sensing as a powerful tool enabling to enhance the traditional geological exploration.

Approbation of the work and publications

The results of the work have been published in 7 articles, including 3 in publications recommended by the Committee for Quality Assurance in Science and Higher Education of the Republic of Kazakhstan (Proceedings of the University, Mining Journal of Kazakhstan), and 1 in a journal indexed in Scopus / Web of Science (Minerals).

The research results were reported in following contributions:

- The open source peer-reviewed journal, included in Scopus / Web of Science:

1. D'yachkov B.A., Mizernaya M.A., Khromykh S.V., Bissatova A.Y., Oitseva T.A., Miroshnikova A.P., Frolova O.V., Kuzmina O.N., Zimanovskaya N.A., Pyatkova A.P., Zikirova K.T., Ageyeva O.V., Yeskaliyev Y.T. Geological history of Great Altai: Implications of Mineral Exploration. Minerals 12 (6), 744, 2022. https://doi.org/10.3390/min12060744

Scientific journals, recommended by SHEQAC of MSHE of Republic of Kazakhstan:

1. Mizernaya M.A., Zikirova K.T., Yeskaliev Y.T., Aitkazyyev T., JoyaShish T. The Scientific Basis of the Investment Attractiveness of Geological Structures on the

Example of Rudny Altai. Universitet Enbekteri – University Proceedings. №1 (90), 2023, P. 144-150.

2. Mizernaya M.A., D'yachkov B.A., Miroshnikova A.P., Zikirova K.T., Yeskaliyev Y.T. Features of Geological Structure, Magmatism and Ore Formation of Bakyrchik ore Field Deposits. Universitet Enbekteri – University Proceedings. №3 (84), 2021. P. 94-99.

3. Mizernaya M.A. Agaliyeva B.B., Shayakhmetova Z.A., Yeskaliyev Y.T. Features of the microelement composition of ore of the Artemyevskoye deposit (Rudny Altai). Mining journal. № 1, 2026. P. 25-30.

Presentation in international conferences:

1. Methodology of scientific forecasting based on GIS of precious metal deposits in Eastern Kazakhstan. 20 International Conference Geoinformatics: Theoretical and Applied Aspects, 11- 14 May, 2021. Kiev, Ukraine.

2. Structural position, magmatism and mineralization of Bakyrchik ore field (Kazakhstan). 22nd International Multidisciplinary Scientific GeoConference SGEM 2022. 4-10 July, 2022, Albena, Bulgaria.

3. WeedsGalore: A Multispectral and Multitemporal UAV-Based Dataset for Crop and Weed Segmentation in Agricultural Maize Fields. IEEE/CVF Winter Conference on Applications of Computer Vision (WACV), Feb. 28 – Mar. 4, 2025, Tucson, Arizona, USA.

Thesis volume and structure. The content is represented by 161 pages, which include 6 chapters, conclusions and 94 of bibliography, 56 figures, 14 tables, 2 appendixes.

Acknowledgements. The author would like to deeply thank the main scientific advisor, candidate of geological and mineralogical sciences, Mizernaya M.A. (Republic of Kazakhstan) for enlightening with great knowledge of regional geology and endless help with writing and understanding the research. The author would also highlight that the endpoint of this research would not come to an end without help of scientific advisors, PhD Rakhymberdina M.Ye. (Republic of Kazakhstan) and PhD Shults Roman (Ukraine), their support had enhanced the dissertation by far. Additional appreciation goes to School of Earth Sciences of D. Serikbayev EKTU for brightening a daily research environment and continuous support. The last, but not least, the author thank a Ministry of Science and Higher Education of Republic of Kazakhstan for the support of project AP25795761.

1 CURRENT STATE OF RESEARCH AREA

1.1 Kazakhstan placement on Global gold mine producers

Gold serves as the primary currency equivalent in all countries worldwide and finds extensive application in jewelry (70–80% of production), electronics, and medicine. The unique properties of gold enable the formation of alloys with virtually all rare and base metals, allowing their use in rocket components, nuclear reactors, and supersonic aircraft. In recent times, gold has become actively used in the form of so-called gold loans for financing new mining projects. Furthermore, on the world market (Fig. 1.1), the use of gold as various forms of insurance has spread rapidly, allowing major gold mining companies to weather falling gold prices during crisis periods with virtually no losses.

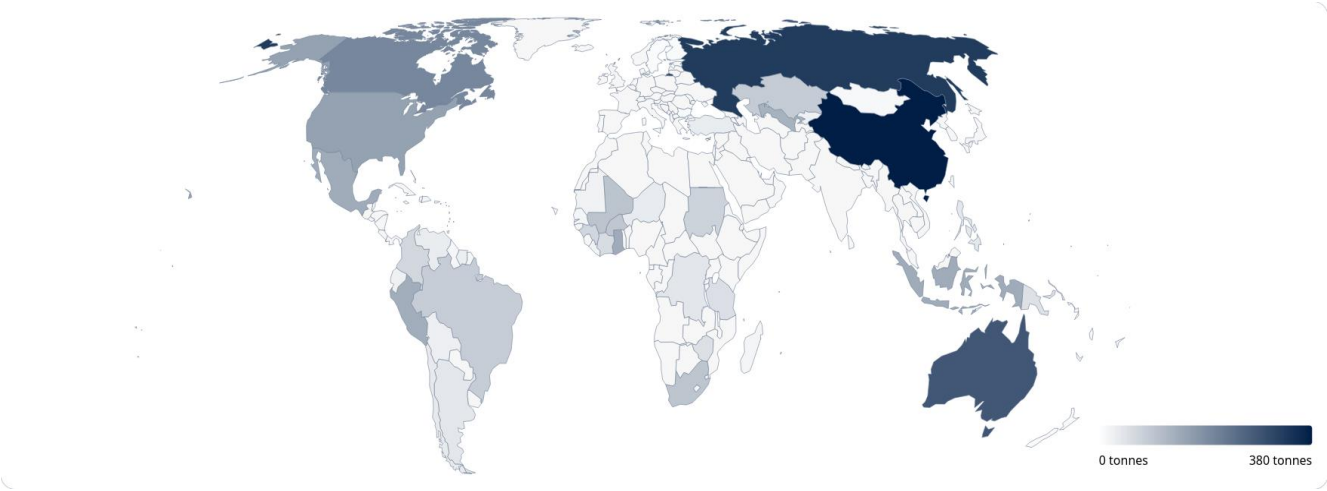

Figure 1.1. Global gold mining by World Gold Council

Note - compiled from [86]

Analysis of global indicators of gold mining and exploration development over the past 25 years shows active trends toward increasing production volumes, while simultaneously decreasing the production of precious metals overall. The multiple increases in market gold prices in the 1970s fundamentally influenced the activity of gold producers in most countries of the world community. It became profitable to process poor and refractory ores: to bring off-balance reserves into operation (previously considered unsuitable for mining due to technical-technological and economic reasons); to resume operation of previously abandoned and "mothballed" quarries, mines, and shafts; and to process technogenic waste dumps from mining and processing plants containing significant quantities of metals (as by-product components or incompletely extracted during primary processing). The decline in gold-production costs was driven by a rapid industry shift from underground mining to open-pit operations, over the last 15 years,

open-pit mining's global share rose from about 30% to 70% - together with the wider adoption of higher-capacity equipment for mining, haulage, and ore processing.

Major advances in extraction, such as heap leaching with cyanidation, column bioleaching, the carbon-in-pulp process, and upgrades in both pyro- and hydrometallurgical routes (including autoclave treatment of refractory ores), made it feasible to reprocess low-grade ore and residual tailings from gold plants, even when gold grades were as low as of 1.0–0.3 g/t and less economically viable. According to GlobalData, in 2022 Kazakhstan ranked 13th among the largest gold-producing countries, with gold ore reserves of 373.4 tons. Furthermore, Kazakhstan leads in gold reserves among Central Asian countries in the first quarter of 2022. Overall, Kazakhstan shows steady reserve growth (2017–2022) from 2,298.3 tons to 2,324.9 tons, while metal production fluctuates within 78.1–76.7 tons per year. Kazakhstan accounts for 2% of world production, with the largest producers being China, Australia, Russia, and Canada.

A clear trend of increasing gold production is observed in the Republic of Kazakhstan. According to the Bureau of National Statistics, in 2021, 33 million tons of ore and 66 tons of refined gold were mined; in 2022, 39.4 million tons were mined. Thus, production increased by 19% relative to 2021 (+6.4 million tons). The resource base of Kazakhstan's gold mining industry consists mainly of small deposits (reserves up to 25 tons) and medium deposits (25 to 100 tons), which currently account for approximately 70% of all produced gold. Total gold reserves across the republic are estimated at approximately 2,400 tons. The state balance of Kazakhstan accounts for 237 gold-bearing objects, including primary deposits (122), complex deposits with associated gold (81), and placer deposits (34).

According to some estimates, the largest producer in the republic is LLP "Kazzinc", which annually produces approximately 580,000 ounces of gold (18 tons). Second place is held by LLP "Corporation Kazakhmys", where gold is produced as a by-product of copper production, averaging approximately 108,000 ounces (3.4 tons) per year. Overall, gold production volumes in the country amounted to over 78.4 tons in 2024. The largest gold-bearing objects in Kazakhstan are the Vasilkovskoye deposit (operated by LLP "Kazzinc"), located near the city of Kokshetau, Central Kazakhstan, and the Bakyrchik deposit (developed with participation from Russian OJSC "Polymetal"), located in East Kazakhstan region. Leading gold producers in Kazakhstan are companies Glencore, Polymetal International, and KAZ Minerals. During 2020–2021, Glencore's production volume decreased by 7%, Polymetal International increased by 1%, and KAZ Minerals' production volume decreased by 15%. Gold deposits are distributed across all regions of the republic, with the largest number located in East Kazakhstan and Akmola regions (Fig. 1.2).

1.2 Mineral resources of East Kazakhstan

Relative to the total reserves of the Republic of Kazakhstan, East Kazakhstan (East Kazakhstan region and Abai region) concentrates significant shares of metals with balance reserves: copper -38.15%, lead -21.1%, zinc - 36.38%, gold - 32.6%, silver - 32.06%,

nickel - 9%, cobalt - 6%, titanium - 10.6%, zirconium - 29%, and coal - 3%. As of January 1, 2025, East Kazakhstan accounts for a total of 718 subsurface use objects. Reserve growth for main metals in East Kazakhstan over 30 years amounted to: gold - 450.40 tons, silver - 4.81 thousand tons, copper - 1,116.24 thousand tons, lead - 585.46 thousand tons, zinc - 2,417.26 thousand tons, manganese ores - 868.70 thousand tons, nickel - 2.40 thousand tons, and tin - 2,692.98 tons. In the East Kazakhstan region, gold is extracted both from gold deposits themselves and as a by-product, as a component of polymetallic raw materials during the production of non-ferrous metals.

According to available geological data, the potential extractable value of balance reserves for main types of mineral resources in East Kazakhstan amounts to approximately 461 billion USD, with forecast resources of 2.016 trillion USD. In total, based on balance reserves and forecast resources of solid minerals, the subsurface wealth of East Kazakhstan is estimated at approximately 2.5 trillion USD, including: lead - 90.0 billion USD; zinc - 109.66 billion USD; copper - 740.2 billion USD; gold - 275.5 billion USD; iron - 308 billion USD; lithium - 5.7 billion USD; platinum - 21.5 billion USD; niobium - 23.35 billion USD; tantalum - 10.5 billion USD; tin - 8.15 billion USD; titanium - 741.5 billion USD; nickel and cobalt - 43.94 billion USD; coal - 56.9 billion USD; oil - 29.8 billion USD; and gas - 0.4 billion USD. Prospects for identifying new deposits in the region exist. However, their identification and exploration will require investments in geological exploration work.

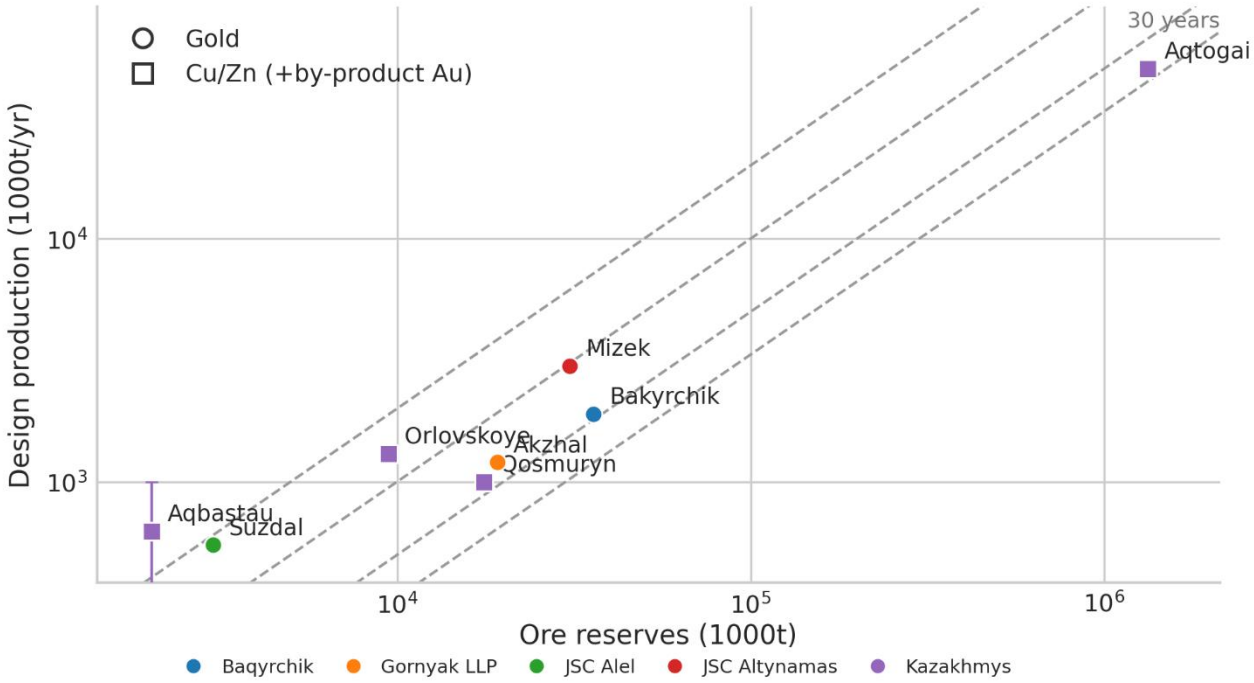

Figure 1.2. Main gold mining operators in East Kazakhstan

Two mining (gold) districts are distinguished in East Kazakhstan: Kalbinsky and Rudny Altai [84]. The leading geological-industrial types of deposits are mineralized

zones, complex gold-polymetallic deposits [40], and gold-bearing weathering crusts. As of January 1, 2025, the region's balance accounts for gold reserves at 126 deposits. Primary deposits account for 80, placer deposits for 37, technogenic deposits for 7, and waste dumps for 2. During the period of Independence of the Republic of Kazakhstan, reserves have been explored for 43 gold deposits: Kuludzhun, Kaskabulak, Balazhal, Zagadka, Sarbas, Zhila 31, Dalniy section, placer deposits of the Kozhabulak River, Northwestern flank of the Boko-Vasilyevskoye ore field, placer of the Shar River, placer deposits of the Agynykatty-Bylykydyk rivers, Miyaly, East Miyaly, Zhayma, Belaya Gorka, Rodnikovoye, Zhanan, Kedey, Mamontovskoye, Chang, placer of the Zhanama River, placer of the Daubay River, placer of the Sarybulak River, Mirazh, placer of the Kystav-Kurchum River, placer of the Tersayryk River, placer of the Bodyk River, Maralikha, placer of the Kurchum River, Boldykol, placer of the Karamyrza River, placer of the Chernaya Uba River, placer of the Levaya Latchikha River, placer of the Yeligen-Bulak River, placer of the Nizhniy Bylykydyk River, Ayaguzskoye, Pridorozhnoye, placer of the Bykuy River, Kokbory, Zhalpak Tobe, Aulnoye, Kara-Choko, Skak-Yuzhnyy, and Yuzhnyye Ashaly.

Gold reserves listed on the state balance for the East Kazakhstan region as of January 1, 2025, and accounted forecast resources amount to approximately 6.5 tons. In the gold mining industry of East Kazakhstan, 24 enterprises are engaged in mining, and 27 in exploration (excluding licenses for exploration of solid minerals). Although a significant share of mined gold comes from massive sulfide-polymetallic deposits, from which gold is extracted as a by-product component. State balance-accounted reserves of actual gold deposits account for 70%. More than half of them belong to refractory "stubborn" ores, and solving technological problems will not only increase production volumes at developed deposits but also bring new objects into operation. The most progressive mining method today is heap leaching, allowing the involvement of large and small deposits with low-grade ores. A biohydrometallurgical scheme for processing "stubborn" ores for deposits of the East region of Kazakhstan was previously introduced.

Analysis of the current state of the mineral resource base of East Kazakhstan deposits allows the following conclusions: practically all previously explored deposits of polymetallic, copper, and gold-bearing ores are in operation; the share of deposits in state reserve is extremely insignificant, ore reserves are minimal and characterized by low grades, making their operation unprofitable at present; by 2025–2040, practically all large polymetallic, copper, and gold deposits will be exhausted. Taken together, more than a century of large-scale geochemical, geological and geophysical mapping across gold and polymetallic targets in East Kazakhstan suggests that the scope for finding new medium-to large-size deposits by conventional prospecting approaches is now largely depleted [83]. To fulfill the tasks set in this dissertation work, two most characteristic ore fields or tracts for the West Kalba metallogenic zone were selected, the geological structure of which is sufficiently well studied, and they represent certain interest for further prospecting and evaluation work. Tract 1 - Bakyrchik ore field; Tract 2 - Akzhal-Bokon ore field.

1.3 Study Area

This section provides a general characterization of the two research areas selected for detailed remote sensing analysis within the West Kalba gold belt: the Bakyrchik and Akzhal-Vasilyevskoye ore fields. Both districts represent distinct gold deposit styles and provide contrasting endmember cases for testing ASTER-based alteration mapping methodologies.

Bakyrchik Ore Field

In administrative terms, the Bakyrchik ore field is located in the Zharminsky district of Abai region, near the border with East Kazakhstan region. The city of Semey is located approximately 120 km northwest, and the city of Ust-Kamenogorsk is located approximately 80 km northeast of the center of the study area (Fig.1.3). Geographic coordinates of the corner points defining the field boundaries are presented in Table 1.1.

Table 1.1. Geographic coordinates of corner points for Bakyrchik ore field

Point	Latitude	Longitude
1	49°45'46.2"N	81°27'05.9"E
2	49°46'43.7"N	81°41'59.2"E
3	49°41'13.4"N	81°42'03.0"E
4	49°40'29.6"N	81°26'49.6"E

From a geomorphological perspective, the area comprises a mix of landforms, including plains, gently undulating uplands, hilly low-mountain terrain, and ridged, strongly dissected mid-mountain relief [85]. Absolute elevations range from 295 m (in the interfluve between the Kyzylsu and Espe rivers) to 657 m (in the southeastern part of the area near the Akbiik winter camp). The total area of the ore field encompasses approximately 1,668 km^2.

The Climatically, the region has a strongly continental regime, with mean monthly air temperatures around −17∘C in winter (December–March) and about +18.1∘C in summer (June–August). Temperature extremes range from roughly +45∘C to −44∘C, while the mean annual temperature is close to +1.4∘C. Windy conditions prevail for most of the year; southeast and northeast winds are most common, typically blowing at about 4–10 m/s. frequently reaching 20–25 m/s. The hydrographic network of the region is represented by the Kyzylsu River, which flows through the entire area, along with its tributaries.

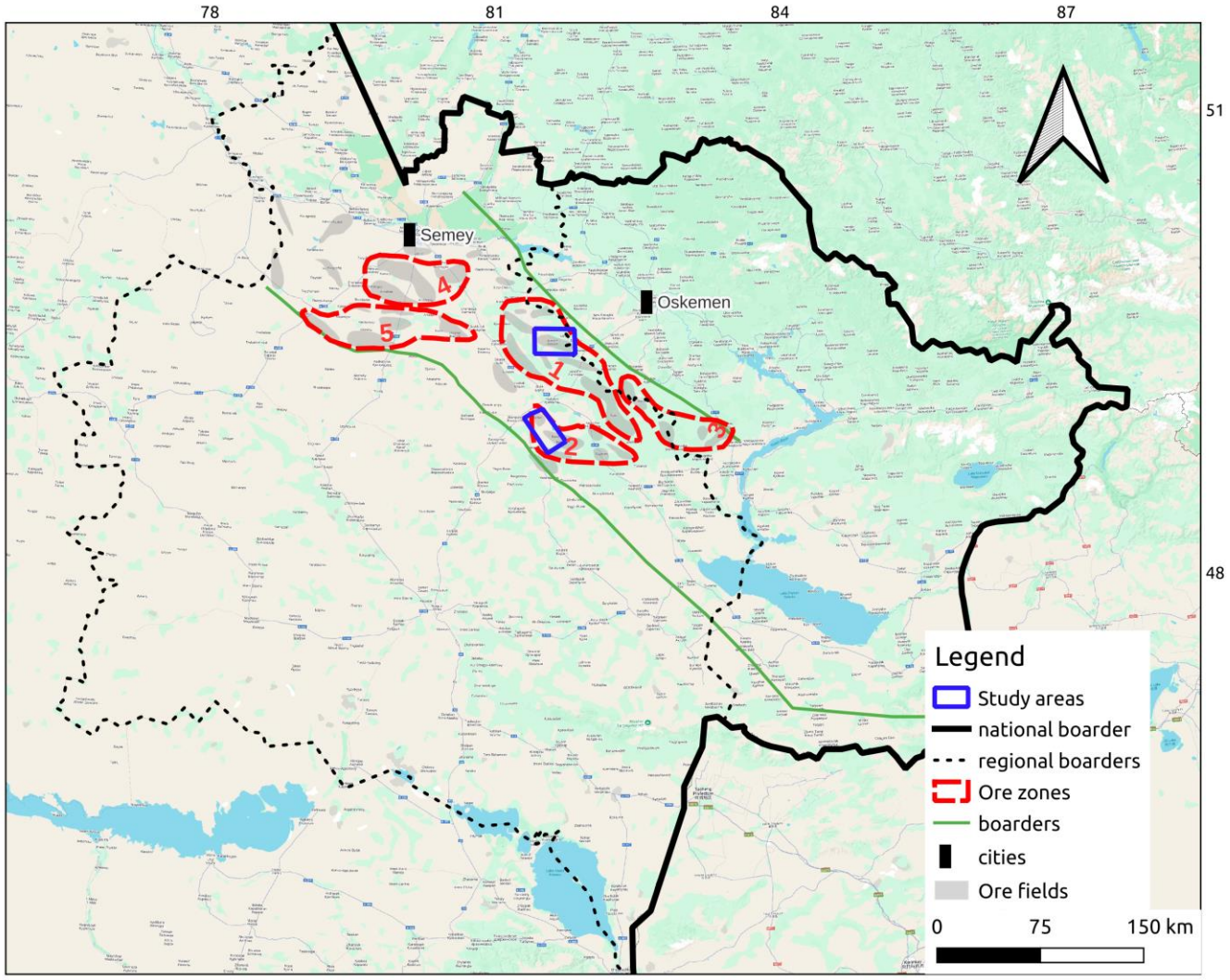

Figure 1.3. Scheme showing the location of the research areas

Akzhal-Vasilyevskoye Ore Field

The Akzhal-Vasilyevskoye ore field is located in the Zharminsky district of East Kazakhstan region of the Republic of Kazakhstan (Fig.1.3). Locationally, the closest settlements to the deposit are the mining towns of Boko (Yubileiny), about 0.5 km away, and Akzhal, about 10 km away. The geographic coordinates of the corner points defining the field boundaries are given in Table 1.2.

From Akzhal, the distance to the district center, Kalbatau village (formerly Georgievka), is roughly 30 km; to Semey, about 210 km [39]; and to the regional center of Ust-Kamenogorsk, about 170 km. Akzhal is linked to Kalbatau and to the nearest railway station at Zhangiz-Tobe (approximately 20 km away) by a gravel road about 8 km long, while an asphalt highway passing through Kalbatau provides access to Ust-Kamenogorsk, Semey, Zaisan, and Almaty.

Topographically, the district is dominated by plains and low mountains, where small groups of elevations alternate with broad, gently sloping flats. Absolute elevations range from 500 to 600–700 m, with relative elevations reaching 100-200 m.

Table 1.2. Geographic coordinates of corner points for Akzhal-Vasilyevskoye ore field

Point	Latitude	Longitude
1	49°11'58.1"N	81°18'23.3"E
2	49°16'54.0"N	81°29'41.6"E
3	49°00'11.4"N	81°50'19.2"E
4	48°55'20.0"N	81°42'05.2"E

The hydrographic network is represented by the Boko and Tandy rivers, which are left tributaries of the Char River. The rivers break up (unfreeze) in April and freeze in November, and they dry up during the summer months. There are a number of small lakes and artificial reservoirs in the area.

The climate of the district is sharply continental, with significant diurnal and annual temperature variations. In terms of precipitation, the mean annual total is about 290–300 mm. Summers are typically hot and dry, with maximum air temperatures reaching around 35–40°C. The lowest winter temperatures, about −35 to −40°C, usually occur in January-February. Snow cover reaching average maximum depths of roughly 50–90 cm on plains and in foothill areas, generally melts by the end of April. The depth of soil freezing depends on the thickness of the snow cover and reaches 1.5–2.0 m.

The district is notable for its absence of forests. Only in river valleys are there shrub thickets, individual birch and aspen trees. Vegetation is represented by mixed types of steppe and semi-desert zones-primarily grasses (feather grass, fescue, wormwood) and shrubs (caragana, rosehip, willow).

1.4 Recorded history of geological investigations

Broadly, this covers the geological framework of the West Kalba belt, including the investigation of geological and magmatic complexes, stratigraphy and age constraints for the identified units, and the spatial distribution of mineral resources across the area., have been addressed in works by Nekhoroshev V.P. (1934, 1946, 1956, 1958); Mikhaylov N.P. (1955); Moiseeva E.G. (1962); Lopatnikov V.V. (1964); Stuchevskiy N.I. (1969, 1974); Khisamutdinov M.G. (1972); Svechenkov G.G. (1980); D'yachkov B.A. (1985); Zhdanova L.Ya. (1991); and Kozlov M.S. (2000). Importantly, these studies made a substantial contribution to revising stratigraphic, magmatic, and tectonic schemes, as well as to refining the systematics and spatial distribution of mineral resources in Rudny Altai and Kalba.

More broadly, prognostic metallogenic work addressed the general patterns and controls governing the distribution of mineral resource. and assessment of ore potential of areas, structures, and sites were conducted by Moiseeva E.G. (1962); Ivankin P.F. (1962); Flerov A.E. (1963); Demidov T.Ya. (1962); Ermolenko A.E. (1977); Ermolov P.V. (1979, 1981); and Malygin A.A. (1983, 1984). Drawing on these investigations, metallogenic zoning of Rudny Altai and Kalba was completed using a structural–formational approach, resulting in the delineation and description of ore provinces, nodes, districts, and zones.

The work also clarified the principal regularities of mineral-resource distribution and their links to specific geological units and ore-forming assemblages, including questions of gold metallogeny, forecasting, and the assessment of gold potential for particular areas and structural elements., and sites in Central Kalba were addressed in works by Nechayev N.E. (1960); Poltorikhin P.I. (1963); Shibko V.S. (1969, 1970); Ovechkin Yu.A. (1969); Borodayevskiy N.I. (1970); Akhmetov K.S. (1971); Yesenbayev Z.E. (1972); Maslennikov V.V. (1975); Zubkov G.K. (1975); Fogelman N.A. (1977, 1985); Alektorov E.A. (1982); Zhuravlev E.M. (1987); and D'yachkov B.A. (1997). These works reflect the results of studying conditions of gold mineralization localization in Kalba and relationships between mineralization and geological and magmatic formations. Based on the obtained results, prognostic maps of various scales were compiled and prospective assessments of gold potential of areas, zones, and sites were given.

In addition, study of individual deposits of Kalba and experimental-methodological work were carried out by Borodayevskiy N.I. (1968); Shibko V.S. (1969); Kudryavtseva I.A. (1970); Kostin Yu.A. (1971); Starov M.M. (1972); and Ermolenko A.E. (1977).

The study area is located in the central part of the West Kalba gold-bearing belt, at the intersection with the Chara belt of ultrabasics. Among metallic mineral resources located in the territory of the sheet, gold occurrences sharply predominate. Several gold deposits are known (Bakyrchik, Espe, Miyaly, etc.) along with numerous gold occurrences. The Bakyrchik deposit is currently being developed by LLP "Bakyrchik Mining Enterprise" while other deposits are mothballed. Notably, strong exploration interest, especially in gold, has led to a relatively detailed but spatially uneven level of investigation across the area.

Geological study before 1932 was largely episodic, whereas systematic 1:50,000-scale geological mapping started in 1956. After the discovery of gold deposits Bakyrchik, Espe, and Miyaly (1945–1950), the intensity of gold and other mineral resource prospecting in this region increased significantly from the mid-1950s. The main direction of prospecting was the discovery of new gold objects and study and exploration of previously identified ones.

At the Bakyrchik gold deposit, prospecting, deep prospecting, prospecting-evaluation work, exploration, reserve calculation, and revision of gold reserves were conducted at different times by Katkovskiy G.I. (1944-1946), Shaveykin R.I. (1950, 1955), Nechayev N.K. (1954), Podsevatkin F.S. (1954), Kotov A.Ya. (1959–1962), Ovechkin Yu.A. (1963, 1964, 1970), Ganzha E.A. (1976), and Akhmetov K.S. (1979). Gold reserve

calculations were performed in 1960, 1976, 1979, and 1997. Development of the deposit began in 1958. Down to depths of 40–70 m, mining was carried out by open-pit method. Currently, the deposit is operated by LLP "Bakyrchik Mining Enterprise".

Similar work on the Espe and Miyaly gold deposits was conducted by Sheverin T.R. (1954), Semenov Yu.A. (1956), Kotov A.Ya. (1962), Ovechkin Yu.A. (1963, 1964, 1970), and others. In 2001–2003, Stepanov A.E. calculated gold reserves in oxidized ores at the Miyaly deposit. Currently, the Miyaly deposit is mothballed.

Gold potential of the Akzhal–Vasilyevskoye ore district has been known since the mid-19th century. Individual quartz veins were mined in even earlier times, as evidenced by numerous archaeological finds dating to the Bronze Age. Until the end of the 19th century, numerous small gold placers were mined. Hard-rock gold mining began in 1903 (Akyndygek vein). In the 20th century, mining activity peaked in 1909-1914, when a large number of the district's gold-bearing quartz veins were put into production (Magistralnaya, Colorado, Aleksandrovskaya, Aulnaya, and others). In the early 1940s, mining of quartz veins in the Vasilyevskoye deposit area was discontinued due to depletion of explored reserves.

From 1960, intensive geological exploration work was initiated in the Akzhal–Vasilyevskoye ore district. Work was performed by the South Kalba Geological Survey Party of EKTU under the leadership of Bocharov I.V. (1961–1967). Within the Vasilyevskoye deposit, more than 20,000 m of drilling was completed. Accordingly, the results were used to compile a 1:10,000-scale geological map of the Vasilyevskoye ore field and to carry out reserve calculations in the C2 category [38]. High gold concentrations were not encountered, except in the ore body No. 2 area, and considering these negative results, geological exploration work by EKTU was discontinued here.

The Akzhal mine, as a gold mining facility, existed until 1958; however, work on additional study of the territory continued. Results of work for the period from 1960 to 1968 were summarized in the work by Okunev E.V. and Kazakevich I.V. "Geological structure, gold potential and directions for further work within the Akzhal-Vasilyevskoye ore field". In 1965, Strizhov E.V. performed the work "Prospective assessment of the Akzhal gold deposit based on exploration and mining materials." Here, along with a thorough historical summary of deposit mining, a prospective resource assessment of its central part was first provided, amounting to: ore 2,500 thousand tons, gold 25-30 tons. In 1984-1985, prospecting-evaluation work was conducted within the Akzhal-Vasilyevskoye ore field. For the first time for the Akzhal deposit, gold potential of the oxidized part of ore zones was assessed. Gold contents were established at 1–2 g/t level, which were not industrial at that time.

The third stage of object development began in 1996. Until 2005, 17.37 thousand tons of ore and 61.37 kg of gold of categories C1 + C2 were mined and written off from the balance sheet. From 2005, geological exploration work on the deposit has focused on assessment of oxidized ores for heap leaching technologies. As a result, in 2008, oxidized ore reserves in the Dolinnaya, Ygrek I, Novaya, and No. 36 zones were registered in the State Balance.

Since 2008, the deposit has been investigated by the "Gornyak" party. In April 2010, as part of efforts to develop a processing route for oxidized ores, a heap-leaching facility with an annual capacity of about 0.3 million tonnes of ore was put into operation. The product of the heap leaching facility is gold-saturated sorbent, sent for further processing to obtain Dore alloy.

Within the Boko-Vasilyevskoye ore field, research from 1969 to 1994 was carried out by the thematic party of the "Altayzoloto" combine, later transformed into the Altay Geological Survey Expedition. Of great interest are the results of work in 1983–1987 on GDP-50, conducted with a complex of geophysical and geochemical methods in the Akzhal-Vasilyevskoye ore field area (Vorontsov S.N., 1987). During GDP-50 production, core drilling under 40–60 m thick Cenozoic cover identified an ore occurrence in well No. 2003.

In 1987, generalization of exploration and mining materials for the mine from 1970–1986 was carried out (Laptev Yu.V., Maslennikov V.V., Omarov B.A.). Based on the work results, geological maps of the ore field at 1:10,000 scale and the deposit at 1:2,000 scale were compiled, stratigraphy, lithology, and magmatism were refined. The absence of influence of plicative structures on ore localization was proven, and the confinement of the richest ore bodies to northeastern extension zones was established.

In 2003, OJSC "AlmatySnab" (Serdyukov A.N.) performed calculation of gold reserves in oxidized ores of the central part of the Vasilyevskoye deposit between exploration lines 3–10 down to the 50 m level from the surface, using archival materials from the Altayzoloto mining and processing plant and Semipalatinsk Geological Survey Expedition of PGO "Vostkazgeologiya." For the calculation, regional evaluation conditions approved by Protocol TKZ No. 201 of 04.12.92 (Ermolayev P.V.) were applied. Category C2 reserves were approved in the State Committee for Reserves of the Republic of Kazakhstan and registered in the state balance in amounts of: ore 578.0 thousand tons, gold 1,278.0 kg at average grade 2.2 g/t (Protocol No. 253-03-A of 04.09.2003). Operational economic assessment showed the possibility of processing oxidized ores of the deposit by heap leaching method. Resumption of exploration work for the purpose of reassessment of deposit reserves was recommended.

From 2007 to 2014, geological exploration work on the northwestern flank of the Boko-Vasilyevskoye ore field was conducted by LLP "Boke." The work results are reflected in the report "Preliminary geological-economic assessment with calculation of gold ore reserves of the northwestern flank of the Boko-Vasilyevskoye ore field as of 01.01.2014." By Protocol No. 1474-14-A of 24.10.2014, the following evaluation conditions for calculation of balance reserves of gold in the northwestern flank of the Boko-Vasilyevskoye ore field for open-pit mining conditions were approved:

- cut-off gold grade in samples included in reserve calculation when outlining ore bodies: oxidized ores – 0.5 g/t; primary ores – 1.0 g/t;
- minimum thickness of ore body included in reserve calculation contours (at lower thickness but high gold grade, use corresponding meter-gram) – 2.0 m;

- maximum allowable thickness of interlayers of barren rocks and non-commercial ores included in reserve calculation – 3.0 m;

- ore and gold reserves calculated outside the limits of projected pit contours are assigned to off-balance sheet.

As of 01.02.2014, preliminary evaluated (C2 category) gold reserves for the northwestern flank of the Boko-Vasilyevskoye ore field were also approved, based on open-pit mining conditions [38].

The Vasilyevskoye deposit was exploited by the Boko mine of the "Altayzoloto" combine in 1947–1994. Ore bodies No. 1 and No. 2 down to a depth of 315 m were accessed by shaft No. 4, which is currently abandoned and in emergency condition. The shaft had rectangular cross-section, area 6.8 m^2 in the clear, and ensured output of 40 thousand tons of ore per year. It was driven in the footwall of the ore zone. At each level, crosscuts and drifts were driven from it. The height of the mining level was 40 m. A total of 9 levels of mine workings were driven from shaft No. 4 – 25 m, 50 m, 73 m, 103 m, 143 m, 183 m, 223 m, 263 m, and 303 m.

In 1977, driving of the exploration-mining shaft RÉSh-1 with depth of 310 m and cross-section of 14.1 m^2 was completed at the deposit; its designed productivity was 100 thousand tons of ore per year. RÉSh was connected with shaft No. 4 by a crosscut and drift driven at the 223 m level. Currently, RÉSh is also abandoned and in emergency condition.

Mining of ore bodies of the deposit was carried out by the room-and-pillar system with roof caving. Mainly reserves of ore body No. 2 and adjacent ore lenses between the surface and 263 m level in the area of profiles 101A(-1A)-103A were mined. Also mined was part of ore body No. 1 between levels 143 m and 223 m in the area of profiles 5A-6A.

Maximum production (250-300 kg per year) was achieved in 1957-1972. According to available data for 1947-1985, 920.3 thousand tons of ore and 6,724.1 kg of gold were mined. Average annual ore losses were 3.5%. The majority of reserves (82.2% of ore and 86.5% of gold) were mined from ore body No. 2; ores of the mineralization zone were mined in small volume. For the period 1986–1994, data on mining volumes are not available in accessible archival materials.

In small volumes, ore mining was carried out by open-pit method from ore body No. 7 in pit No. 1 (area of profiles 34-38) and ore body No. 1 in pit No. 2 (area of profiles 4-10). Pit 1 was driven to a depth of 29 m from the surface, pit No. 2 – to the 7 m level. In the contours of pit No. 1, approximately 30 thousand tons of ore were mined; in the contours of pit No. 2 – 15 thousand tons.

According to archival data, a small volume of ore was mined by pit in the position of ore body No. 2 in the area of profile 1. Currently, this pit is reclaimed and covered by technogenic formations.

Mined ore was used mainly as flux raw material at non-ferrous metallurgy plants. Gold recovery during pyrometallurgical processing was 96%. Remaining reserves are

represented by mineralized zone-type ores, poorly suitable for use as fluxes due to low silica and high alumina content.

By a complex of geophysical and geochemical methods, the reporting area has been studied fairly well. In 1957, the entire territory of Western Kalba was covered by aeromagnetic survey at 1:200,000 scale (Kabanov O.M.), and in 1960 gravimetric survey of the same scale was conducted (Serikov A.V.). Work was performed by the Northwestern Geophysical Trust and Altay Geophysical Expedition. Based on the work results, a set of magnetic and gravimetric field maps of corresponding scale was compiled, on the basis of which contours of distribution of magnetic rocks were identified and tectonic elements of the region were distinguished.

Starting from the 1960s to the present, with some interruptions, systematic geophysical investigations at 1:50,000 scale have been conducted in the territory of both sheets using a complex of geophysical methods in support of geological mapping of the same scale. The method complex included gravimetric survey, ground magnetometric survey, lithochemical survey of loose and bedrock deposits, electrical prospecting in profile variant and on small areas of prospecting sites (methods VÉZ, VÉZ-VP). Geophysical investigations were conducted mainly by the forces of AGF EKTU. Gravimetric survey at 1:50,000 scale covered about 65% of the sheet area (Logunov Yu.N., 1967; Lyutyy A.G., 1966, 1967; Borodayev A.D., 1967; Averin O.K., 1967; Azovskiy Yu.G., 1968, 1969; Yurchenkov E.M., 1986; Lopatnikov V.V., 1989; Permitin A.B., 2000). Only the southern parts of the sheets remained uncovered (about 35%). Ground magnetometric investigations at 1:50,000-1:25,000 scale covered about 85% of the reporting territory (Bagisheva T.N., 1959-1962; Arminbayev K.B., 1962; Tarasenko V.I., 1962; Aleksandrov B.A., 1963-1965; Markushin Ya.V., 1963; Logunov Yu.N., 1964-1965; Kuznetsov V.A., 1965; Kudryavtsev D.Ya., 1968–1969; Lopatnikov V.V., 1989; Permitin L.B., 1991; Kudinov I.F., 1997, and others); the remaining area was covered by aeromagnetic survey at 1:50,000-1:25,000 scale (Pak V.P., 1963; Belousov N.P., 1974; Yakovenko A.F., 1986, 1989, and others). Lithochemical survey was conducted simultaneously with geological mapping and ground magnetometric investigations. It covered up to 85% of the reporting area.

As a result, the geophysical and geochemical surveys produced integrated base datasets in the form of map series showing gravity and magnetic anomalies, as well as secondary and primary geochemical dispersion halos, at scales of 1:200,000 to 1:50,000 to support geological mapping and prospecting. Gravity data made it possible to delineate major fold and fault structures, to map intrusive massifs both exposed at the surface and concealed at depth, to describe their shallow and deep morphology, and to identify and investigate deep structural elements of volcano-plutonic complexes. Magnetic surveying proved particularly effective for mapping intrusive bodies and effusive complexes, especially those of basic to ultrabasic composition and for recognizing and tracing mineralized tectonic zones. Lithochemical survey by secondary dispersion halos of elements showed high effectiveness in prospecting for ore objects under cover of loose deposits up to 5 m thick. Thanks to this method, numerous extended and smaller zones of

hydrothermal alteration of rocks with gold and sulfide-polymetallic mineralization were identified in the work area and adjacent territories, within which ore objects of various scales were discovered during subsequent detailed prospecting.

In recent years, both in Kazakhstan and abroad, new modern methods of prospecting and exploration are being increasingly successfully introduced into the practice of geological exploration work: analysis of geodynamic settings and terranes, high-precision geochemistry, deep-focus geophysical methods, and Earth remote sensing methods.

Conclusions. This chapter has established the economic and regional context for applying remote sensing to gold exploration in the West Kalba belt. Kazakhstan ranks 13th globally in gold production, with East Kazakhstan accounting for 32.6% of the country's gold reserves, but the potential for discovering new large and medium deposits using traditional exploration methods is increasingly limited. The mineral resource base of East Kazakhstan, while substantial, faces depletion of major deposits by 2025-2040, creating a clear need for scalable and reproducible screening methods. The West Kalba gold belt has been extensively studied through over a century of geological investigations, providing a well-documented foundation for remote sensing validation, but systematic application of satellite remote sensing methods has not been implemented. Two characteristic ore fields - Bakyrchik and Akzhal - Vasilyevskoye -have been selected for detailed focus, representing contrasting gold deposit styles within the belt and providing test cases for the remote sensing methodology developed in subsequent chapters.

2 GEOLOGICAL STRUCTURE OF THE WEST KALBA GOLD BEARING ZONE (CHAR)

2.1 Position of the West Kalba Zone in the Structures of the Irtysh-Zaisan Fold System

The Ob-Zaisan (or Irtysh-Zaisan) fold system represents the geological structure that developed during Late Paleozoic interactions between the Siberian and Kazakhstan continental blocks. Northward from Semipalatinsk, the system extends beneath the West Siberian Plate cover, with geophysical and drilling evidence indicating its continuation through the Ob basin to the latitude of Norilsk [66]. Southeastward, the system extends into Chinese territory, where it connects with the Hercynides of Dzungaria, and the South Mongolian system joins as a gently concave arc that borders the Caledonides of Mongolia to the south.

In East Kazakhstan, the Irtysh and Zaisan Lake basins expose the most complete structural-material complexes of the Ob-Zaisan system, which display a pronounced northwest strike and are bounded by faults that separate them from the Chingiz-Tarbagatai zone to the southwest and the Rudny Altai zone to the northeast. This junction region is collectively referred to as the Great Altai [2].

Within the Ob-Zaisan fold system, the West Kalba (Char) zone occupies an axial position. Current understanding indicates that the Char zone's foundation consists of oceanic lithosphere fragments from the Ob-Zaisan basin, with surface exposures preserved in the Char ophiolite belt [4]. The belt contains three types of serpentinite mélange [3], incorporating blocks of volcanic and sedimentary rocks derived from oceanic floor, oceanic islands, and intra-oceanic island arcs. Stratigraphically, sedimentary deposits in the Char zone range from Ordovician to Carboniferous in age, with the oldest units represented by the Berkutin Formation (O2–D2gv) and the Karaoitas Formation (O2–D3).

These successions are dominated by aphyric to microporphyritic basaltic lava flows, plagioclase porphyrites, spilites, and variolites, with interbeds of sealing-wax red or light-gray cherts, phthanites, and siliceous–clayey siltstones. The volcanic component is chiefly tholeiitic, while alkaline basalts occur in subordinate amounts. [67]. Serpukhovian deposits occupy more than 50% of the Char zone area and exhibit tectonic contacts with older rocks (Fig. 2.1). The youngest Paleozoic sedimentary deposits in the Char zone are Middle Carboniferous in age and assigned to the Bukonskaya Formation C2, which fills separate depressions and synclines and lies unconformably on Serpukhovian-age rocks. The Bukonskaya Formation comprises gray polymictic sandstones, gravelites, conglomerates, sedimentary breccias, and clayey and carbonaceous-clayey siltstones, with a thickness of 1.5 -2 km.

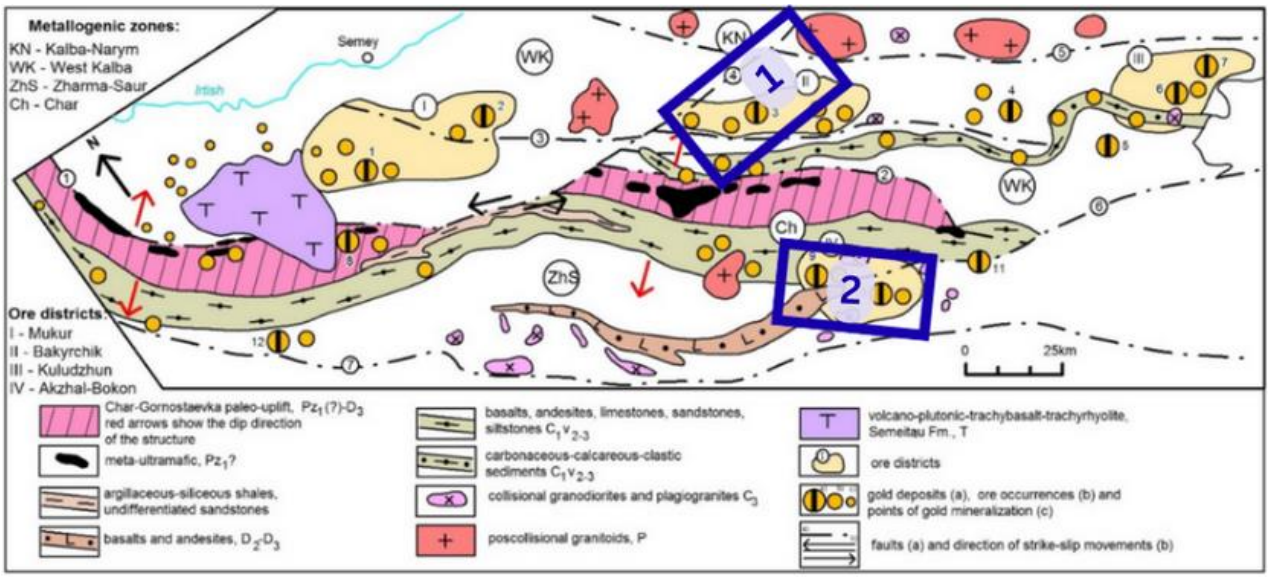

Figure 2.1. Gold deposits in West Kalba and Zharma Saur belts with metallogenic zones. The descriptions and labels can be found at [81]. Our study areas are marked blue

Note - Modified after [81]

East Kazakhstan's primary gold-bearing structure is the West Kalba metallogenic zone, which hosts more than 450 known gold deposits and occurrences, including large and superlarge deposits. These principal gold deposits developed during [1] the collisional stage of the Zaisan suture zone evolution and are grouped into ore districts (Fig. 2.2).

Suzdal-Mukur Ore District. This district occupies the northwestern portion of the West Kalba zone, covering an area of 75×47 km^2 and lying geographically east of the Semeytau Mountains. Regionally, this important industrial district includes the Semeytau and Kedey ore nodes, which host numerous gold occurrences and deposits spread over a broad area. The most significant deposits include Zherek, Eastern Semeytau, Central Mukur, Tas-Kuduk, and Eastern Mukur, which primarily belong to quartz-vein gold, gold-arsenic-carbonaceous, and quartz-beresite ore formations. Several known deposits are currently being developed using heap leaching methods (Central Mukur, etc.) [40].

Bakyrchik Ore District. Situated southeast of the Mukur ore district on sheet M-44-XXII, this district's northwestern boundary lies in the exocontact zone of the Del'begetei granitoid massif. The district extends for 100 km, with width varying from 45 km in the northwestern portion to 15–20 km in the southeast [40]. The district contains 123 known gold occurrences, including East Kazakhstan's largest gold-arsenic-carbonaceous formation deposits (Bakyrchik, Bolshevik, Gluboky Log, etc.). Additionally, the district hosts quartz-vein gold occurrences, many of which have undergone mining and prospector development.

The spatially isolated Miyalinskoye ore field, situated in the northern portion, is of particular interest. Stretching northwest for about 10 km and roughly 4 km in width, this

field contains two small deposits - Miyaly and East Miyaly - of the gold–arsenic–carbonaceous ore formation that warrant further investigation [40].

The Sentash–Kuludzhun Ore District lies southeast of the Bakyrchik ore district, in the central part of sheet M-44-G. Across an area of approximately 3000 km^2, more than 80 gold deposits and occurrences, primarily of quartz-vein type [40], are registered within deposits of the graywacke formation (Aganaktinskaya suite, C1s). The district contains four ore nodes: Sentash, Khamitovsk, Dzhumbinsk, and Kuludzhun, which collectively include most of the previously exploited gold-quartz-vein and placer deposits of the West Kalba zone. The largest deposits are the Kuludzhun and Dzhumba vein fields, while Sentash, Terekty, Kucheko, and Laily are less significant. Currently, private companies are resuming development of several deposits (Kuludzhun, Dzhumba).

Baladzhalsk Ore District. The district's structural-geological position is defined by the junction section of the northern branch of the Akzhal regional fault and the Char-Zimunaisk deep fault. Across an area of approximately 400 km^2, eight gold-quartz-vein and gold-sulfide beresite occurrences are concentrated, with the largest being the Baladzhal deposit, which is associated with a gold-bearing placer. Certain veins and their associated fracture zones contain gold-pyrite-arsenopyrite dissemination (Ashmet), representing a distinctive morphological mineralization type known as mineralized sulfide zones. The Baladzhal deposit is currently under development.

Akzhal-Daubay-Ashalinsk Ore District extends for more than 100 km with a width of approximately 25 km, representing the southeastern flank of the West Kalba zone that developed in the continent-to-ocean transition zone within a marginal volcano-plutonic complex. This tectonic position results in distinctive geological features: increased crustal thickness, melanocratic character, and a combination of ophiolitic, island-arc volcanic-terrigenous, and molasse section types. From northwest to southeast, the ore district encompasses the Akzhal, Boko-Vasilievsk, and Daubay-Ashalinsk ore fields.

The Akzhal-Boko-Ashalinsk ore zone contains numerous small and medium gold deposits that have been worked since 1909 and are currently being reactivated. Gold occurrences in this zone exhibit ore-formational characteristics fundamentally similar to other West Kalba deposits. Mineralization occurs as veins of the gold-low-sulfide-quartz formation and mineralized zones of the gold-sulfide formation (Akzhal, Vasilyevskoye, Vasilievsk, Tokum, etc.), accompanied by near-ore alteration processes including sericitization, chloritization, silicification, carbonatization, and albitization. Host rocks include both intrusive types (Daubay, Baladzhal) and terrigenous-volcanic rocks (Southern Ashaly, Anomalny, Teninsk) [81].

Below is a description of the features of the geological structure, magmatism, and tectonics of the Bakyrchik and Akzhal-Vasilyevskoye ore field districts.

2.2 The Geological Structure of the Bakyrchik Ore District within West Kalba Metallogenic Zone

2.2.1 The Bakyrchik Ore District Deposits Stratigraphy

Geological structure of the district incorporates stratified subdivisions of Devonian and Carboniferous age [38]. Cenozoic deposits are widely distributed along river valleys, streams, and intermontane depressions (Fig. 2.2). The stratigraphic scheme and district division established during GDP-200 (Klepikov, 2008) serve as the foundation, along with materials from the Legend of the Zaisan series sheets. Subdivision descriptions utilize materials from GDP-200 (Klepikov, 2008).

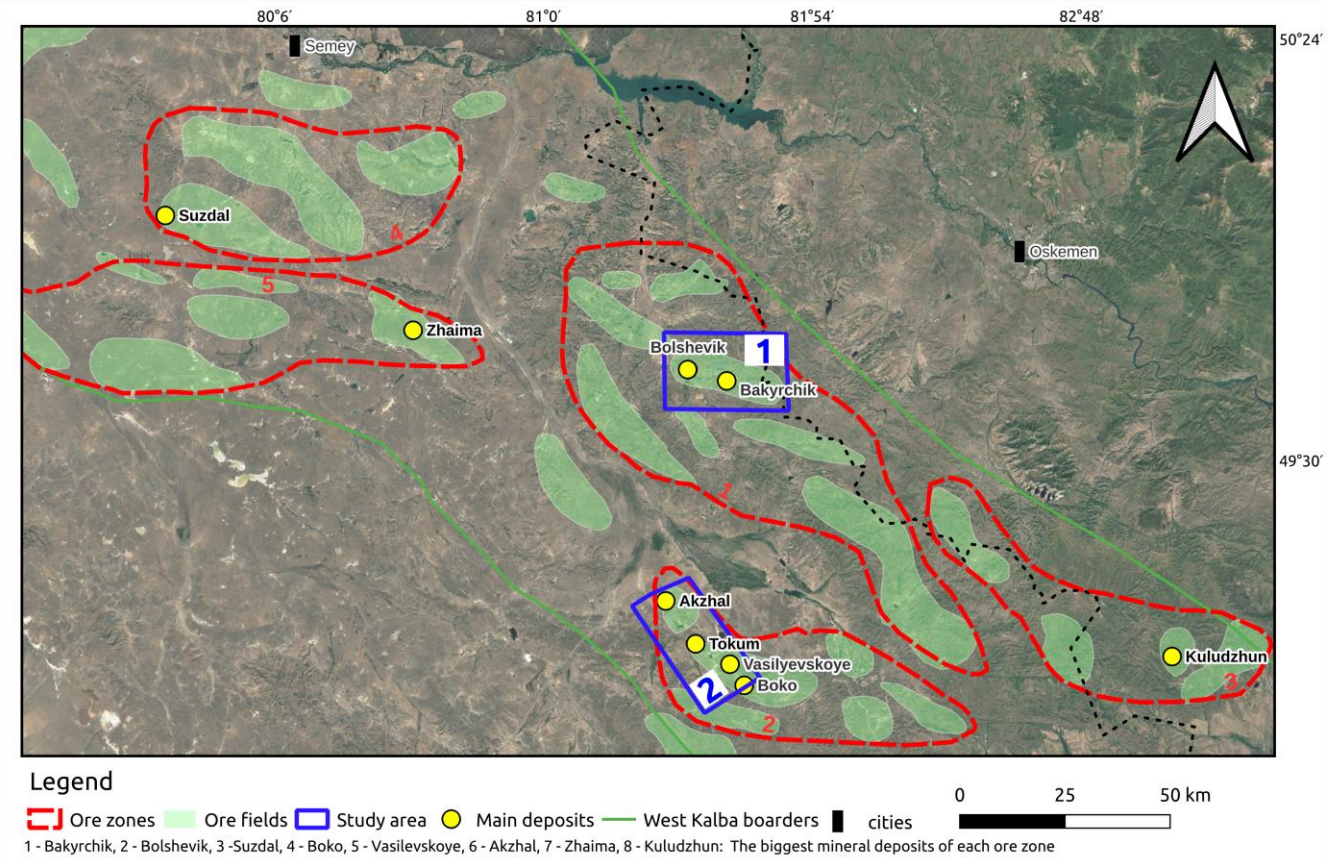

Figure 2.2. Scheme of the West Kalba gold belt with ore districts and our study areas

Devonian System. The Devonian system includes Famennian deposits, consisting of volcanics of the Karabaiskaya Formation and jasperoids of the Urumbevskaya Formation. These deposits occur in the southwestern portion of the work area, with distribution limited by the Igorev fault, and in the southeastern portion between the Igorev and West Kalba faults.

Karabaiskaya Formation (D3 kr). The Karabaiskaya Formation consists of volcanic rocks, with chloritized basic-composition rocks predominating and frequently

alternating with porphyritic varieties. Amygdaloidal varieties are present. Fine-clastic tuff horizons, along with interbeds of siltstones and volcanomic sandstones, occur rarely.

Urumbevskaya Formation (D3 ur). The Urumbevskaya Formation comprises olistoplaks of jasperoids with small sizes and limited distribution, whose blocks are frequently appressed against blocks of Karabaiskaya Formation volcanics. The formation's jasperoids exhibit pelitic to micropelitic structure and consist of extremely fine silica grains.

Carboniferous System. Upper Visean deposits (C1v2) are characterized by allochthonous occurrence as remnants of tectonic nappes (xenoforms), klippes, olistoplaks, and olistoliths of variously marbleized reef limestones. Geological mapping at 1:50000 scale, based on fauna studies in limestones, distinguished the Arkalykskaya Formation of Upper Visean age, which includes, in addition to limestones, terrigenous rocks as inter-reef facies, intermediate and basic composition volcanics, and siliceous formations.

Reef limestones typically form massive, variously marbleized rocks [85], with bedding and color variations discernible only in isolated locations. Upper Visean limestones are readily identifiable on satellite imagery of all scales due to their light tone.

Dalankarninskaya Formation (C1dk). The Dalankarninskaya Formation deposits are extensively distributed along the northeastern margin of the work area on the right bank of the Kyzylsu River and in the southeastern portion.

During 1:50,000 scale geological survey work by Yurchenkov E.M. (1986), these deposits, together with part of the Taubinskaya Formation, were dated as Serpukhovian stage of Lower Carboniferous to the base of Middle Carboniferous. Lithologically, the formation is distinguished by a clear dominance of bluish-gray to dark-gray graywacke sandstones, commonly massive in texture, which are interbedded with smaller volumes of greenish-gray to dark-gray polymictic sandstones, black sandy siltstones, and carbonaceous–clayey siltstones.

Taubinskaya Formation deposits unconformably overlie the Dalankarninskaya Formation, with a hidden angular unconformity. The following section provides petrographic characterization of formation rocks.

Taubinskaya Formation C2tb. The Taubinskaya Formation deposits are extensively developed throughout the work area, forming synclinal structures that overlie Dalankarninskaya Formation deposits, often with brachyform appearance.

Taubinskaya Formation rocks rest on different horizons of the Dalankarninskaya Formation without visible angular unconformity. In the northwestern portion, they are unconformably overlain by terrigenous rocks of the Bukonskaya Formation (C2bk), with conglomerates at the base.

The Taubinskaya Formation deposits comprise polymictic, oligomictic, volcanogenic, and graywacke sand–siltstones of variable grain size (most commonly fine to medium), together with clayey and carbonaceous–clayey siltstones (locally schistose), which occur as alternating individual horizons or packs and frequently form complex intercalations.

Compared to the Dalankarninskaya Formation, the Taubinskaya Formation deposits exhibit increased silica content, reaching up to 60.4% in sandstones and 60.2% in siltstones.

Bukonskaya Formation C2bk. On the studied territory, the Bukonskaya Formation deposits exhibit local distribution. They form an extensively developed (up to 80 km) synclinal structure (Del'begeteisk syncline), truncated in the northeast by the West Kalba fault and in the northwest by the Del'begetei intrusion.

The formation rests unconformably on Taubinskaya Formation deposits. The Bukonskaya Formation's lower boundary is defined by the first sustained conglomerate horizon.

The formation is composed of variably grained polymictic sandstones (gray to dark-gray and greenish-gray), together with gravelites, conglomerates, clayey and carbonaceous siltstones, and sand–pelitolites. The conglomerates contain pebbles derived from clayey-cherty siltstones, cherty pelitolites, sandstones, limestones, and porphyrites [39; 58].

Bakyrchik Thickness C3br. A.K. Kagarmanov first distinguished the Bakyrchik thickness in 1964 within the Kyzylovsky fault zone, based on Upper Carboniferous flora discoveries in the Bakyrchik deposit quarry. In 1982, while studying the Bakyrchik ore field structure, N.A. Fogelman concluded that coal-bearing continental deposits should be distinguished as an independent thickness, based on their distinctive lithological composition, lower rock lithification, and Upper Carboniferous flora finds. These deposits were noted to occupy a complex tectonic position within a graben structure beneath the thrust surface.

The deposits consist of black, highly carbonaceous argillites and siltstones, with rare lenses of poorly sorted coarse gravel sandstones, gravelites, and fine-pebble conglomerates. Terrigenous rocks, primarily sandstones, comprise the clastic material.

Within the Kyzylovsky fault zone, Bakyrchik thickness section fragments are observable in the "Bolshevik" quarries, No. 4, 2, and "Sarbas". These deposits are invariably highly dislocated and typically emerge as tectonic wedges with unclear relationships to terrigenous rocks of the northern hanging block. In many cases, they are difficult to distinguish due to similar lithological and facies compositions among the thicknesses.

The Bakyrchik thickness deposits display several characteristic lithological features: coarse rocks exhibit lithic composition with predominance of graywacke sandstone fragments. Sedimentologically, coarse sandstone beds commonly display cross-bedding, with poor sorting and weak rounding of grains. The deposits are notably carbon-rich, and coal seams occur as lenses and thin layers, typically about 1–10 cm thick. Sandstones and argillites of the thickness commonly contain leaf and stem flora detritus, often with large, well-preserved imprints. The coal-bearing section contains siderite concretions and phosphatic nodules.

Within the Kyzylovsky fault zone the Bakyrchik Formation is exposed as brown to cherry-brown and yellowish-brown sandstones and siltstones, commonly silicified,

containing fragments of brownish-gray quartz within a band up to about 200 m wide. A deluvial-proluvial depression, 100 m wide, lies to the south, and further south, Taubinskaya Formation deposits are exposed, dipping northeastward beneath the Kyzylovsky zone at an angle of 40°.

Mesozoic weathering crusts are extensively developed on sedimentary and magmatic rocks, forming deposits of limited thickness.

Cenozoic deposits (Neogene and Quaternary) are also widely distributed within the district. They fill river valleys, intermontane depressions, and peneplainized areas, covering 20–30% of the territory with an uneven cover.

Neogene deposits result from weathering crust erosion and sediment redeposition under lacustrine-lagoon conditions. They occur primarily in river valleys and are divided into two formations: Aral and Pavlodar. Neogene deposit thickness ranges from 30–90 m.

Cenozoic Era. Cenozoic-age deposits occur throughout the work area. These deposits fill gorges, ravines, and intermontane depressions; form thin covers on gentle mountain and hill slopes; and display the most extensive areal accumulations along the sides and valleys of the Kyzylsu, Alaygyr, and Kuyeli rivers [85].

2.2.2 Intrusive Formations of the Bakyrchik Ore District

Intrusively, the work area contains only limited exposures of small igneous bodies, including the Bizhansk gabbro–diorite complex, the Kunush plagiogranite–granodiorite complexes, Kalba granodiorites and granites, isolated leucogranite outcrops of the Monastyr complex, and minor gabbro bodies of the Semipalatinsk complex [81].

Bizhansk gabbro–diorite–diorite–dolerite complex (nδC2–3b) [81]. On the considered territory, the Bizhansk complex is represented by the Bizhan massif, situated near Mount Keregetas. The massif displays an approximately isometric shape, somewhat elongated meridionally, with an area of 0.55 km^2. Massif contacts are irregular, bay-like, and steeply dipping. The massif consists of unevenly grained, less commonly porphyritic gabbro, gabbro-essexites, and monzodiorites. Transitions between lithological varieties are gradual. Northwestern and meridional dikes, probably belonging to the Semipalatinsk complex, cut the intrusion. According to Yurchenkov E.M., the Bizhan massif itself is assigned to the Lower Triassic intrusive complex (Yurchenkov, 1986).

The massif is mapped by a variably gradient alternating magnetic field with intensity ranging from –500 nT to +700 nT. Detailed interpretive profile data indicate that the massif produces a relatively positive anomaly with intensity up to 1.5 mGal, and it was determined to have a stock form with a visor in the southwestern portion and general northeastward dip (Yurchenkov, 1986).

Kunushsk Granodiorite-plagiogranite Complex (γδ, γπ, ργC3–P1ku). The Kunushsk complex comprises hypabyssal intrusions of acid composition, adjacent to the West Kalba fault. Intrusions form small stock-like bodies, along with dike and vein-like formations. Intrusive body emplacement is controlled by northwestern and northeastern faults, as well as their intersection nodes. Many dikes are confined to interlayer detachment zones in folded structures. The Saratov massif, located in the northeastern

corner of the area, consists of granodiorites transitioning into plagiogranites and displays active contacts with Taubinskaya Formation (C2tb) host rocks, producing hornfels zones from a few metres to several tens of metres thick. The principal dike suite is made up of plagiogranite-, granodiorite-, and granite-porphyries. Individual dikes are generally straight, slab-like bodies, several metres thick (locally up to 20–50 m) and extending for roughly 0.5–4 km. Dike dips are commonly steep, ranging from 70–90°.

Kunushsk complex intrusive bodies cut Middle Carboniferous Taubinskaya Formation deposits; in Kyzylovsky zone quarries, crosscutting relationships between complex dikes and Upper Carboniferous Bakyrchik Formation deposits are documented. The complex's upper boundary is not geologically defined. Potassium-argon absolute age determinations for six samples yield values in the range of 254–282 ± 14 Ma (Yurchenkov, 1986). Considering previously obtained results by the authors (Stasenko, 2005), the complex age is accepted as Late Carboniferous–Permian.

Granodiorite-granite Complex of Kalba Type γ, γπP1. These complex formations have limited distribution and occur as stocks of isometric or elongated shape with sinuous contacts and apophyses extending into host rocks, transitioning into vein bodies.

Southeast of Mount Boka, subparallel to the West Kalba fault, unnamed stockworks of Mount Uitas and Mount Kyzyltas extend in the southwestern wing, accompanied by dikes. Their cross-sectional sizes do not exceed 1–2 km.

Intrusions of the Kalba type complex consist of granodiorites, biotite-amphibole and biotite granites, leucogranites, and frequently granite-porphyries [85].

Potassium feldspar constitutes 10%. Biotite packets (5%) are present, and plagioclase crystals are intensely sericitized and partly saussuritized. Hornblende is moderately chloritized and carbonatized. Biotite is chloritized and often decomposed with release of ore minerals.

The above-mentioned massifs' granites and granodiorites are weakly magnetic, with magnetic susceptibility ranging from 2–7 to 10–5 SI units. Due to their small sizes, the complex's intrusive bodies are not reflected in the gravitational field.

Del'begeteisk Granosyenite-granite Complex (γξP1db). The Del'begetei massif, located in the northwestern portion of the area, contains only a small stock-like body of fine-grained leucocratic granites of the Monastyr complex.

According to research data from different years, granite absolute ages vary in the range of 226.5–261.3 Ma, indicating a Late Permian–Triassic age for the massif.

Semipalatinsk Complex of Gabbros (δπJs). The Jurassic-age Semipalatinsk gabbro complex was studied in detail by the authors on sheets M-44-XIV, XV as a northwestern-striking belt extending northwestward from the Del'begetei massif (Stasenko, 2005). The complex consists of dike bodies characterized by high magnetization and increased alkalinity. On the considered territory, these formations continue southeastward from the Del'begetei massif. Overall, these dikes have limited distribution here. During GDP-50, E.M. Yurchenkov included gabbro dikes in the Late Triassic-age gabbro-monzonite-granite complex and assigned them to the first intrusion phase (Yurchenkov, 1986).

Dike thicknesses vary from several meters to 7–10 m, with extents ranging from hundreds of meters to 2–3 km. Their position in section is discordant, forming lens-like and slab-like bodies. Most dikes display steep dips or are inclined up to 70° toward the southwest or northeast. Dikes consist mainly of diabase porphyrites. Diorite porphyrite dikes are subordinate. Among diabases, chemical, petrographic, and physical properties distinguish amphibole weakly magnetic diabases of normal alkalinity and pyroxene magnetic subalkaline diabases.

Amphibole diabases occur on the northeastern side of the Kyzylsu River valley from the Kyzylovsky fault northwestward to the Kuyeli River mouth.

Subalkaline pyroxene porphyrites form numerous and extended dikes. Due to low weathering resistance, these dikes rarely outcrop at the surface but are well mapped in the magnetic field as narrow linear positive anomalies with intensity up to 1000 nT.

Diorite porphyrite dikes occur together with amphibole diabase dikes but significantly less frequently.

2.2.3 Structural Position of the Kyzylovsky Shear Zone

The studied district lies in the central portion of the Zaisan Hercynian eugeosyncline, at the junction between the Char inner anticline and the northeastern part of the intra-geosynclinal central depression (South Kalba synclinorium).

The Northeastern brachyform anticline measures 20×15 km. Its core portion is complicated by a series of higher-order folds, among which the Kuelinsk syncline is distinguished. The Northwestern fault bounds the Northeastern brachyanticline from the southwest, while the Karauz rupture group bounds it from the north.Structurally, the area is disrupted by numerous disjunctive faults of northwest and near-east–west strike, which partition the rocks into narrow, linear blocks where they are compressed into elongate, keel-like folds with limb extents on the order of 100–150 m. Wing dips range from 75–80°.

The Northwestern fault lies northwest of the West Kalba fault and displays a similar strike (310°). In the junction zone with the Kyzylovsky structure, it makes a smooth turn to the east-southeast (strike azimuth 105°). The fault dips northeastward at an angle of 50°. Between the Kyzylovsky and Kuelinsky faults, the Northwestern fault exhibits gentle dip. Kinematically, horizontal and vertical offset magnitudes generally do not exceed about 1–1.5 km. The fault is expressed almost everywhere as a single zone, but near its junction with the Kyzylovsky shear zone it splits into a set of closely spaced, subparallel disjunctive faults.

Regionally, the near-east–west–trending Kyzylovsky zone occupies the central part of the district, extending for about 17.5 km and varying from roughly 25 to 250 m in width. It is bounded on the west by the West Kalba fault and meets the Northwestern fault to the east at an acute angle. The zone dips north at about 35–40°, flattening at depth to approximately 25–30°. Bends occur locally along the zone’s strike and dip. The shear zone’s footwall boundaries are defined by the fault, often healed by dikes, while the

hanging wall boundary consists of a tectonic zone represented by broken and boudinaged rocks and friction clay.

The Kyzylovsky zone structure incorporates sand-silt-argillite rocks of the Kalbinsk and Bukonsk formations with northern dip. Blocks consist of sandstones, gravelites, and carbonaceous siltstones that are intensely altered, dynamometamorphosed, silicified, graphitized, and accompanied by pyrite-arsenopyrite mineralization with gold. A system of close, en echelon, and subparallel higher-order faults of sublatitudinal, northeastern, and northwestern strike breaks these rocks into smaller blocks. All these disjunctives dip northeastward at angles of 30–45°.

Along the Kyzylovsky shear zone, the Bakyrchik and Bolshevik deposits are situated within a set of segments that, from west to east, include Western Bolshevik, Bolshevik, Chalobay, Cold Spring, Bakyrchik, Intermediate, Deep Log, and, in the far eastern part, the area beyond the junction of the KZS with the Northwestern fault - the Carmen section and the Sarbas deposit.

Morphologically, the Kyzylovsky shear zone represents a left strike-slip-thrust. Horizontal strike-slip displacement amplitude is 1.5–2 km, while vertical displacement does not exceed 1 km. The magnitude of tangential movement of the northern block over the southern block does not is limited to a few kilometres. Seismic data show that the zone can be followed to depths of about 3.0–3.5 km, dipping northward at roughly 30–45°.

Additionally, other near-east–west shear zones are conjugate with the principal northwest-trending faults (the West Kalba and Northwestern faults) - Parallel, Kuelinsk, Kostobinsk, and Karauz.

The Parallel zone, located approximately one kilometer north of the KZS, extends for 1.5 km and also dips to the north. The Parallel zone hosts the Dalny 1 gold ore section, and after its junction with the Northwestern fault - sections Dalny, Dalny 2, and Dalny 3.

2.2.4 Mineral Resources of the Bakyrchik Ore District

The West Kalba zone displays predominantly gold ore metallogenic specialization, while the Gornostaev-Char subzone within its composition also contains non-ferrous metal deposits and occurrences, iron and manganese mineralization points, as well as jasperoids, chalcedony, and magnesites.

Black Metals. Black metals have limited distribution and occur mainly within the Gornostaev-Char metallogenic subzone southwest of the work area. Iron hydroxides are extensively distributed in weathering crusts, especially nontronite type developed on ultrabasics, but they are not of practical interest.

Disseminated magnetite or hematite is occasionally noted in various rocks, but these are also not of practical interest due to limited distribution and low contents. The Troitsk mineralization point represents a typical example of this mineralization type.

Elevated manganese contents are frequently encountered in the northwestern portion of the Gornostaev-Char subzone. Solyanik V.P. studied this mineralization (Solyanik, 2001), delineating several manganese occurrences expressed as thin veins (about 2–5 cm), where manganese grades generally remain below 1–2%, but sometimes

reaching 8-21%. Their formation apparently occurred during weathering crust development through removal of this element from ultrabasic rocks and subsequent redistribution [82].

Chromites. The Char zone contains numerous known chromite occurrences. These most commonly occur as lens-like or stock-like bodies of massive chromite with small sizes ranging from 0.5×0.5 m to 4×5 m, with Cr_2O_3 content from 23.49% to 50.9% (Charsk-Kibat, Suukbulak, Kyzylsu, etc.). Areas with chromite dissemination in serpentinites over small areas (15×0.4 m) are also encountered. Due to their limited sizes, they are not of practical interest.

Non-Ferrous Metals. Silicate cobalt-nickel ores occur in the Char zone, where they are confined to nontronite-type weathering crust developed on serpentinites. Similar small occurrences of this type are also known on the Surov section, where they are also confined to oxidation zones on serpentinites and other ultrabasics. The Belogorsk deposit represents the largest cobalt-nickel ore object. In addition to Belogorsk, several cobalt-nickel mineralization occurrences of similar type exist in the area, with the largest being Bukorsk and Severny.

Mercury mineralization in the Char zone has been known since 1956, when heavy mineral sampling covered a significant portion of the area and identified several heavy mineral halos of cinnabar, confined to areas of serpentinite, listvenite, and porphyrite development.

Subsequently, several mercury occurrences were identified that lack industrial significance. These are most commonly confined to small faults and fractures that have undergone carbonatization and silicification.

Mercury mineralization occurrences directly in the area (Kyzyl-Char Severny, Ties, Zhilandy), also confined to fracture zones in serpentinites and listvenites, have limited sizes, low concentrations, and are not of practical interest.

Gold. Gold constitutes the primary mineral resource of the West Kalba metallogenic zone. Within the zone, gold ore objects are distributed unevenly. Virtually all deposits and large occurrences are concentrated in the Kyzylsu-Alaygyr ore zone, which extends through the central portion of the West Kalba metallogenic zone in a northwestern direction across nearly the entire sheet M-44-XXII for a distance of up to 70 km with a width of 7–12 km. The West Kalba fault bounds it from the southwest, and the Northwestern fault bounds it from the northeast.

Within tract 1, metallic mineral resources are represented solely by gold-bearing targets, comprising 11 deposits, 43 occurrences, and 32 gold mineralization, along with isolated points of arsenic mineralization.

Centrally, the area includes the near-east–west Kyzylovsky gold-ore shear zone, traceable for about 17.5 km and varying in width from roughly 100–200 m to as much as 500 m. The zone is confined between faults on its northern and southern margins. The northern boundary fault dips north at around 35–40° and becomes gentler with depth, flattening to approximately 25–30°. The southern fault also dips to the north somewhat steeper – up to 50°. In general, the Kyzylovsky zone is understood by many researchers

as a thrust structure with elements of left strike-slip. Stratified rocks within the zone lie discordantly relative to rocks of the hanging and foot walls. The zone is complicated by transverse faults mainly of submeridional and northwestern direction.

Gold mineralization host rocks divide into three lithofacies complexes. The lower complex consists of volcanomic sandstones with thin interbeds of carbonaceous-cherty siltstones and sand-siltstones. This complex is assigned to the Dalankarninskaya Formation (C1dk). The rocks host only weakly gold-bearing quartz veins, and no gold–sulfide ore bodies have been identified. Middle Carboniferous Taubinskaya Formation deposits unconformably overlie this complex, represented by a shallow-water sand-siltstone complex with conglomerates and gravelites at the base. Here, veinlet-disseminated gold-sulfide and shungite mineralization occurs.

The Bakyrchik Formation crowns the stratigraphic section, with its lower part consisting of gravelites, sandstones, and breccias cemented by carbonaceous–clayey material, with interbeds of siltstones of similar composition. In the upper part of the formation, siltstones and argillites rich in carbonaceous matter are common and contain lenses and layers of shungite up to 10 cm thick. Most gold-sulfide ore bodies of the Bakyrchik and Bolshevik deposits are confined to the formation's upper portion. Intrusive rocks consist of porphyry dikes, plagiogranite-porphyries of the Kunushsk complex, and gabbro-diabases and porphyrites of basic and intermediate composition of the Bizhansk complex.

The Kyzylovsky ore zone contains the largest industrial gold ore objects, which are conditionally subdivided into three sections from west to east: Western section - Bolshevik deposit, Western Bolshevik occurrence, Shalobay, Cold Spring, Riddle; Central part-Bakyrchik deposit, Central, Intermediate, Deep Log sections; Eastern part-Sarbas deposit, Carmen, Bizele occurrences.

Bakyrchik Deposit lies on the northern outskirts of the Auezov settlement and is confined to the central portion of the Kyzylovsky zone.

Currently, the Bakyrchik deposit encompasses a strip of the Kyzylovsky zone up to 4 km long, which includes, in addition to the Bakyrchik section itself, the Intermediate and Deep Log sections.

The deposit's primary ores belong mainly to the low-sulfide carbonaceous formation. These ores form numerous ore bodies. Based on size and reserves, four types of ore bodies are distinguished at the deposit (Maslennikov, 1997).

The first type includes the most widespread (40.6% of all ore bodies) balance and off-balance ores in the Intermediate and Deep Log sections, along with some apophyses of large ore bodies [85]. Their plan dimensions are 40–290×10–120 m, with thickness not exceeding 4 m. They characteristically dip along azimuth 3–21°.

The second type ore bodies are also extensively distributed at the deposit and comprise 34.5% of all ore bodies. Their plan dimensions are 130–850×60–150 m with thickness ranging from 2.59 to 10.7 m (averaging 6.5 m). These contain 14.3% of explored ore reserves.

The third type ore bodies comprise 21.8% of all deposit ore bodies but contain 44% of all deposit reserves. Their dimensions vary in the range of 400–1020×130–330 m, with average thickness of 6.24 m. They characteristically display ribbon-like form and clearly expressed northwestern dip (320–330°). Apophyses are typically absent.

The fourth type consists of the largest ore body No. 1, with dimensions of 1200×600 m and thickness up to 9 m. The body dips northward at an angle of 35° and has northwestern (320°) dip. It is not closed along dip. This body contains 39% of all explored deposit reserves (more than 10,000 thousand tons of ore). It characteristically contains apophyses confined to northwestern ruptures in the ore body's footwall.

Gold distribution in ores is uneven. Most gold (95–97%) associates with sulfides-pyrite and arsenopyrite. Sulfide amounts vary from 1 to 8%, indicating that ores belong to the low-sulfide type.

The deposit also contains finely dispersed gold in hydrocarbon formations (Marchenko, 2007; Antonov, 2008).

Carbonaceous matter (CM) consists of a group of kerite-anthraxolite-shungite. Its amount increases proportionally with the degree of hydrothermal rock reworking. Gold association with carbonaceous matter appears to be sorptive. Oxidized ores extended to depths of 30-40 m and are now completely worked out. Ores consist of quartz-sericite and quartz-chlorite-sericite composition rocks with significant admixtures of kaolin and oxidized ore minerals - hydrogoethite, limonite, jarosite, psilomelane, scorodite, and valentinite [85].

Gold occurred in native state and was distributed relatively evenly. Most gold existed in microscopic and submicroscopic state as inclusions in the limonite-hydrogoethite-scorodite main mass. Gold content in these ranges from 7.8–10.4 g/t.

Primary ores are traced along dip for distances exceeding 1200 m. As noted, most gold associates with sulfides - pyrite and arsenopyrite. Based on seven technological sample studies (Maslennikov, 1997), the mineral composition of these ores is as follows: quartz 52.65%, micas 3.47%, carbonates 3.45%, sericite material 23.03%, carbonaceous matter 14.04%, pyrite 2.25%, arsenopyrite 1.81%, and barite, chalcopyrite, sphalerite, tetrahedrite, stibnite, pyrrhotite, galena 0.11% [39].

Gold is the primary valuable component of ores, with by-products including silver, sulfide sulfurs, arsenic and shungite [39].

A 2–8 m near-surface leached zone is recognized at the deposit and is characterized by very low gold grades, whereas gold contents increase markedly downward.

According to most researchers who have examined these deposits (Narseev, 1970, Kotov, 1966; Maslennikov, 1989 and 1997; Antonov et al.) currently accept a hydrothermal hypothesis of deposit formation involving gold introduction from depth. This hypothesis is supported by the clearly expressed crosscutting position of ore bodies relative to host deposit bedding, the confinement of the Bakyrchik deposit (along with several others such as Bolshevik and Sarbas) to the major tectonic structure of the Kyzylovsky zone with ore bodies controlled by rupture faults, the superposition of gold on Kunushsk complex (C2–3P1ku) intrusive bodies, and the presence of a "blind"

intrusion several kilometers north of the zone, toward which the Kyzylovsky tectonic zone plunges. This intrusion apparently functioned as an energy source during deposit formation (Bortsov, Antonov, Ermolenko, 1977).

The deposit contains the majority of gold reserves not only in the Kyzylovsky zone but in the entire West Kalba metallogenic zone. Balance reserves were calculated to a depth of 500 m. Individual drill holes have established ore intervals at depths of 1200 m without decrease in ore quality. Geophysical data suggest that mineralization may extend to depths of 2–2.5 km and beyond.

The deposit is currently actively exploited by LLP "Bakyrchik Mining Enterprise," a subsidiary of the Russian company "Polymetal".

Bolshevik Deposit lies 6 km west of the Auezov settlement and is confined to the western flank of the Kyzylovsky zone.

The deposit's sedimentary and intrusive rocks are similar to those at the Bakyrchik deposit. Primary ores belong to the low-sulfide carbonaceous formation and partly to the quartz-sulfide formation. Ore bodies consist of intensely crumpled brecciated carbonaceous rocks and are accompanied by silicification, as well as beresitization of Kunushsk complex plagiogranite-porphyries. Ore bodies form ore columns, within which series of short lenses are traced in zones of veinlet-stockwork silicification. Column forms are ribbon-like and lens-like with east-northeastern and west-northwestern strike, predominantly dipping to the north. Body dimensions along strike range from 120–460 m, along dip from 200-700 m, with thickness from 0.1–38 m. Six ore columns are explored in total. Ore body contours are determined only by sampling. The largest ore bodies are accompanied by series of en echelon smaller bodies and lenses, which collectively form an ore column. Gold mineralization is mainly confined to areas of rock decompaction in the system of shear fractures. Studied ore body thicknesses range from 0.4 to 38 m, with gold content by workings ranging from 1–1.2 g/t to 58.2 g/t and exceptionally reaching 177.7 g/t.

The main exploration objects were: 1. Western Bolshevik section (3–4 ore bodies); 2. Bolshevik (5–6 ore bodies); 3. Chalobay (7–10 ore bodies); 4. Cold Spring (11–12 ore bodies).

Native gold is confined to cataclasis fractures in arsenopyrite and pyrite, to interstices between sulfide, quartz, carbonate, and sericite grains, as well as in the form of intergrowths with carbonaceous matter. Gold sizes range from 0.001 to 0.005 mm, with individual grains up to 0.3–0.5 mm. Gold fineness is 915. Ore and gold reserves at the deposit have been repeatedly calculated and approved by various authorities.

The deposit has been worked since 1960. Over the entire exploitation period, 4477.2 kg of gold was mined at an average content of 5.9 g/t. Remaining balance gold reserves as of 01.01.1999 amounted to category C1: 13585 kg at an average content of 7.02 g/t, category C2: 18260 kg with content of 6.08 g/t. Off-balance gold reserves at an average content of 2.87 g/t amount to 109 kg.

In 1999–2000, an assessment of poor oxidized ores was carried out in the eastern part of the Bolshevik section and western part of the Chalobay section, covering 700 m

length and 26,000 m^2 area. Reserve calculation was performed for 13 ore bodies, with length along surface ranging from 40 to 700 m and thickness from 1 to 40 m. Reserve increment for poor oxidized ores amounted to category C1: 167.2 kg with average content of 1.2 g/t, and category C2: 239.1 kg with average content of 0.9 g/t.

Deposit weathering crusts consist mainly of areal covers with thicknesses of 5–25 m. In zones of increased permeability, linear weathering crusts develop with thicknesses of 50–60 m.

Hypergene ores are represented by brown, clay-like rocks of kaolinite–hydromica composition, enriched with detrital fragments of sedimentary and intrusive rocks as well as quartz. Gold is free and of high fineness. By size, it is divided into dust-like (<0.05 mm), very fine (0.05–0.1 mm), and fine (0.1–0.3 mm). The deposit was worked by quarry. Currently, it belongs to LLP "Bakyrchik Mining Enterprise" and further development is planned.

Kostobe Deposit lies 16 km southwest of the Auezov settlement within the Kyzylsu-Alaygyr ore zone.

Host deposits consist of Taubinskaya Formation sandstones and siltstones, crumpled into small folds and cut by dikes and small bodies of plagiogranite-porphyries, diorite porphyrites [40], and diabase porphyrites. Dike sizes range from 100 m to 1.5 km along strike, with thicknesses of 1–20 m. At the deposit section, a series of sublatitudinal zones of increased fracturing with widths of 50–300 m are developed. The largest zones - Latitudinal, Central, Northern - are bounded on the west by the West Kalba fault and on the east by the Northwestern fault.

Several sections are distinguished at the deposit. The Kostobe Severny section is confined to the Northern fracture zone. A band of mineralized rocks is confined to one of the small faults. Here, one ore body, 250 m long and 1-6 m thick, dipping southwestward at an angle of 40-60°, is distinguished. Average gold content is 7.6 g/t. The ore body consists of silicified, sericitized rocks with quartz veins.

The Kostobe Yuzhny section is confined to the Central zone of fracturing and hydrothermal metasomatism. Three ore bodies up to 180 m long and 1–25 m thick are distinguished. The zone contains dike bodies of beresitized porphyries. Mineralization consists of dissemination of pyrite, arsenopyrite, limonite, and scorodite. Average gold content is 4.6 g/t. Kostobe - Central zone - is confined to the zone’s southeastern branch, saturated with listvenitized microdiorites and beresitized dikes of plagiogranite-porphyries.

In the intrusive stock’s supra-intrusive portion, two "blind" ore bodies up to 2.1 m thick with gold content of 7.8–8 g/t were intersected; ores are veinlet disseminated.

Further southeastward up to 2 km, a zone of mineralized rocks with poor gold content is traced along several identified intervals up to 5 m thick with gold content of 2.4–4.4 g/t. The deposit at the Kostobe Severny section was partly worked by quarry. Currently, it is mothballed.

Kara-Shoka Deposit lies 15–20 km southeast of the Bakyrchik deposit. Situated within a deeply eroded Alaygyr–Uitas tectonic block, the deposit is hosted by

Carboniferous massive polymictic sandstones and carbonaceous cherty siltstones. At the surface, it is accompanied by stock-like exposures of Kunush complex granitic intrusions with plan dimensions up to about 400 × 100 m. Faults and fracture systems strike predominantly northwest, northeast, and near-east–west. The deposit is interpreted as representing the rear, deepest segment of the Bakyrchik district ore–magmatic column. The terrigenous host rocks are tightly folded into small isoclinal structures and are strongly hornfelsed, cataclasized, and sericitized, while the granites (apical parts of the intrusive body) are silicified, beresitized, and sulfidized. Within the sandstones and siltstones, gold-bearing zones of fracturing, schistosity, and sulfidation extend for up to 2–3 km and are typically 5–50 m thick, corresponding to a veinlet-disseminated sulfide style of mineralization [73].

Gold associated with pyrite and arsenopyrite commonly occurs at first g/t levels and only rarely reaches the first tens of g/t. In granite stocks, in association with plagiophyre dikes, quartz veins, beresite alteration, and silicification zones extending roughly 30–400 m and several metres thick, “non-traditional” Au–Mo mineralization is recorded (Au up to about 4–5 g/t; Mo 0.1–1.0%) [73].

in the granites is described as occurring in three generations: 1 - linked to an early rare-metal stage with molybdenite; hosted by middle-stage metasomatic pyrite in quartz–sericite rocks; and 3 - present as free gold in late quartz veins. Two monomineralic molybdenite samples contain 1.67 and 2.97 g/t Au. From surface, ore zones are expressed by a complex geochemical anomaly (Au 0.01–0.1 g/t; Mo 10–100 g/t; As 0.01–0.1% [73]; Cu 0.01–0.06%; Ag up to 1.0 g/t; Bi up to 40 g/t; Zn 0.01–0.4%). The Kara-Shoka deposit is therefore considered a transitional type between rare-metal vein/vein-stockwork mineralization in granitic massifs and disseminated gold mineralization in black-shale sequences of the supra-intrusive zone.

Riddle Occurrence lies between the Bolshevik and Bakyrchik deposits and is confined to the Kyzylovsky shear zone.

From surface, the occurrence was unevenly studied by trenches, shafts, and mapping drill holes on a network of 400–50×50–10 m. To depths of 100–200 m, the section was intersected by exploration drill holes on a network of 400–100×100 m, additionally, individual drill holes reached depths of up to 400 m [85], and an operating open pit was developed in the western part of the site. Within this section, the ore zone is restricted to the footwall of a diorite-porphyrite dike.

On the eastern flank of the section, five ore bodies with thicknesses from 1 to 4 m and lengths of 10-25 m were identified. Gold content reaches up to 8.4 g/t. At depths of 10-20 m, they pinch out and have no industrial significance. On the section’s western flank, similar small ore bodies were identified, but here mineralization is traced without pinching out to depths of 250 m. The section’s deep horizons are prospective for identifying blind mineralization.

Located about 10 km southeast of the Bakyrchik deposit, the Bizhan occurrence is associated with the exocontact of the eponymous massif composed of gabbro, gabbro-diorite, diorite, and plagiogranite. A mineralized zone 2–40 m thick was exposed from the

surface by trenching over roughly 1 km and was followed to depths of up to about 250 m by drilling on a 200 × 200 m grid.

Based on sampling from underground workings and drill holes, gold grades in individual intervals range from trace amounts to 6.2 g/t., which do not correlate with each other into ore bodies. The occurrence was given a negative assessment.

Dalny I, II and III Occurrences are confined to the Parallel tectonic zone in the area of its junction with the Northwestern deep fault. From surface, the occurrences were intersected by trenches and shafts in profiles every 100 m, and to depth by individual exploration-structural drill holes. A zone of sulfide mineralization in Taubinskaya Formation silicified sand-schist rocks is confined to contacts of acid and intermediate composition dikes or located at their pinch-out along strike. Typically, the zones extend for about 1.4–2.0 km, while their thickness varies both along strike and down dip and generally remains below 20 m.

Gold grades in sulfidized rocks are most commonly around 2–3 g/t, but locally increase to roughly 6–9 g/t. Individual small ore bodies were worked by open pit.

Miyaly Deposit lies outside the work area, 24 km north of the Auezov settlement. In Taubinskaya Formation siltstone-sandstone deposits, more than 20 mineralized zones are developed, represented from surface by rubble-clay weathering crust with kaolin and limonite cement. Zones are traced for distances from 200 m to 3000 m with thicknesses from several meters to 100 m. Predominant zone strike is sublatitudinal and northwestern. Oxidized ores consist of limonite, scorodite, goethite, and psilomelane. Ore bodies with industrial content have relatively small sizes of 40–80×1–17 m with average content of 4.2–5.8 g/t. Currently, the richest oxidized ores are worked out. Primary sulfide ores were practically not studied. The deposit is temporatily suspended.

2.3 Geological Structure of the Akzhal-Vasilyevskoye Ore District of the West Kalba Metallogenic Zone

2.3.1 Stratigraphy of Deposits of the Akzhal-Vasilyevskoye Ore District

Positioned in the axial part of the West Kalba structural–formational zone, the Akzhal–Vasilyevskoye ore district reflects the interaction of two major structural domains: the Zharminsk synclinorium to the southwest and the Char-Gornostaev anticlinorium to the northeast [38], which are separated by the Sardzhalsk deep fault zone of transform character. Gold mineralization is spatially linked to Middle–Upper Carboniferous subvolcanic bodies and dikes of moderately acidic to intermediate composition and is interpreted as pre-folding. Ore bodies are controlled by palaeo-extensional settings within the Sardzhalsk transform fault system.

The Char-Gornostaev anticlinorium represents an ophiolitic structure that plunges northeastward. According to Ermolov P.V. [75], the Char-Gornostaev ophiolites correspond by all parameters to a suture zone (a boundary structure separating two tectonic plates). With maximum width in a bulge of 8–10 km, the structure’s extent within Kazakhstan alone exceeds 320 km.

Within the Zharminsk synclinorium, facially similar deposits are assigned to the Karabaisk thickness (D3fm–C1t) of Upper Devonian–Lower Carboniferous. The deposit composition here is dominated by basalt covers and andesite-basalts, with less developed basic-composition tuffs, packs of variegated jaspers, jasper-quartzites, and microquartzites. Pelites, medium-grained tuffaceous sandstones and thin-bedded limestones are present. Above the Karabaisk deposits, Lower Carboniferous volcano-sedimentary rocks of the Tersairyk Formation (C1t) occur and include lavas and lava breccias, andesite and andesite–basalt tuffs, tuff-conglomerates and tuff-gravelites, calcareous and polymictic sandstones, siliceous and clayey–siliceous siltstones, and clayey limestones [38].

Across the Char–Gornostaev anticlinorium and the Zharminsk synclinorium, these volcano-sedimentary units are overlain by Middle–Upper Visean [38] (C1v2–3ar) deposits of the Arkalykskaya Formation. This formation comprises two main packages. The lower package is dominated by volcanic-clastic sandstones, gravelites, polymictic and siliceous sandstones, and siliceous–clayey siltstones, with rare flows of andesite lavas and tuffs (locally andesite-basalts) [39]; near its base, interbeds and lenses of organogenic limestones containing crinoid, bryozoan, and brachiopod fauna are observed. The upper package is calcareous–terrigenous: its basal part includes coarse-clastic conglomerates and tuff-conglomerates, grading upward into gravelites and sandstones, then into siliceous–clayey siltstones with subordinate sandstone lenses, and finally into carbonaceous and carbonaceous–clayey siltstones that contain nodules and small lenses of pelitomorphic, bituminous limestones at the top of the section.

Aganaktinskaya Formation of Serpukhovian stage of Lower Carboniferous (C1s ag) lies conformably on Arkalyk deposits and consists of essentially sandy flyschoid terrigenous formations. Lithologically, the formation clearly divides into two subformations: lower coarse-layered, essentially sandy, and upper flyschoid, essentially siltstone. The formation is characterized by scarcity of fossil organic remains, confined mainly to individual horizons in the section’s upper part. The fauna is marine, represented by brachiopods, bryozoans, goniatites, gastropods, and pelecypods.

Middle Carboniferous formations assigned to the Kokpektinskaya (C2kp) and Bukonskaya formations (C2bk) lie with angular unconformity on Aganaktinskaya Formation deposits.

Kokpektinskaya Formation consists of marine the terrigenous-sedimentary succession comprises variably grained polymictic sandstones, boulder- and gravel-pebble polymictic conglomerates, and carbonaceous-clayey to clayey siltstones, with thin lenses of limestone and calcareous sandstone. The Kokpektinsk fault forms the formation’s southwestern distribution boundary [39].

The Bukonskaya Formation (C2bk) section base contains variably grained polymictic sandstones, boulder-pebble and gravel-pebble polymictic conglomerates with interbeds of carbonaceous-clayey and clayey siltstones, and thin lenses of limestones and calcareous sandstones [39]. Throughout the section, plant detritus remains, stem and bark fragments are noted. Crinoid, brachiopod, and bryozoan remains occur less commonly.

Higher in the formation section, a pack of coarse terrigenous sandy deposits is distinguished, consisting of light gray and greenish-gray subarkose and polymictic sandstones, less commonly gravelites with interbeds of gray and dark gray clayey and carbonaceous-clayey siltstones. The formation section is completed by a pack of calcareous sandstones and siltstones with high carbonaceous matter saturation [73]. Formation deposits developed under continental conditions in limnic basins. The West Vasilyevskoye fault forms the southwestern boundary of Bukonskaya Formation deposit distribution. Total Bukonskaya Formation thickness is estimated at 3500-4000 m.

Daubaiskaya Formation (C2–3db) The Daubaiskaya Formation volcanic-sedimentary deposits are confined to tectonic depressions (grabens). They lie with sharply expressed angular unconformity on underlying Lower and Middle Carboniferous deposits. Fossil fauna remains were not found in sedimentary members of the Daubaiskaya Formation section. The formation consists of two subformations lower, volcanic-sedimentary, and upper, volcanic. The lower subformation consists of clastically coarse tuff-conglomerates are accompanied by lavas and lava breccias of andesite, andesite–basalt, and basalt composition, together with variably clastic intermediate to basic tuffs [38]. Dacites and rhyodacites occur in subordinate amounts. Interbeds of siltstones, sandstones, and gravelites are noted. The upper subformation formations consist of poorly sorted variegated conglomerate-gravelite-sandstone deposits.

Maitubinskaya (gray-colored) Formation (C3mt) lies with erosion on various Daubaiskaya Formation horizons. The lower part is essentially gravelite-sandy, while the upper part is more coarse-clastic with two basalt lava horizons. Younger Paleozoic and Mesozoic system deposits were not established in the district.

Mesozoic weathering crusts develop on Paleozoic sedimentary and magmatic rocks, lie beneath Neogene-Quaternary deposit covers, and in places emerge at the surface on hilltops and steep slopes. Based on occurrence conditions and structure, weathering crusts subdivide into areal and linear-fracture morphological types.

Cenozoic deposits (Neogene and Quaternary) are also widely distributed within the district. They fill river valleys, intermontane depressions, and peneplainized areas, covering 20–30% of the territory with an uneven cover. Neogene deposits result from weathering crust erosion and sediment redeposition under lacustrine-lagoon conditions. They occur mainly in river valleys and divide into two formations: Aral and Pavlodar. Neogene deposit thickness ranges from 30–90 m. Quaternary sediments - clays, sandy loams, loams, sands, and pebble deposits - occupy most topographic depressions and form river-terrace sequences and alluvial fans, reaching total thicknesses of roughly 40–70 m.

2.3.2 Intrusive Formations of the Akzhal-Vasilyevskoye Ore District

Magmatically, intrusive rocks are only sparsely developed within the district. The largest intrusive bodies belong to the Char-Gornostaev ophiolitic complex, located in the northeast outside the Contract area. These are represented by protrusions of serpentinized ultramafics and lens-like gabbro bodies. On the studied territory, small listvenitized

serpentinite bodies are confined exclusively to the Vasilyevskoye fault zone and its en echelon fractures.

Argimbaisk Hypabyssal Intrusive Complex (C3). The complex intrusive rocks form large massifs and dike belts; on the Contract territory, they have limited distribution. Complex formation occurred in two phases. Petrologically, the first phase is dominated by pyroxene gabbros, gabbro-diorites, diorites, and diorite porphyrites, with rarer pyroxenites [38], monzonites, monzodiorites, and quartz diorites. The second phase is represented mainly by dikes and small sills of diorite and diorite porphyrite, together with gabbro, gabbro-diorite, and diabase.

Saldyminsk Subintrusive Complex (C3–P1). The complex formations form both very large massifs and small stocks and dike bodies. Complex formation involved two phases. The first phase consists of granodiorite, granodiorite-porphyry massifs, less commonly diorite porphyrites, quartz diorites, and granites [54]. The second phase includes small dikes and sills of granodiorite-porphyries and granite-porphyries.

Most complex formations belong to the granodiorite group; granite group intrusions are significantly less common. The porphyritic appearance of intrusions indicates shallow emplacement depth (0.5–1.5 km). Carbonate-quartz veins, beresitization zones, and listvenitization zones are spatially and genetically related to complex intrusions.

2.3.3 Tectonics of the Akzhal-Vasilyevskoye Ore Field

The territory's structural-tectonic plan developed during the Hercynian tectono-magmatic epoch. At this time, most folded and fault structures formed, which were further complicated during the Meso-Cenozoic.

The district's largest folded structures are the Sardzhalsk and Karasuisk volcanic-tectonic structures of graben-synclinal type, separated by the Akdyngesk anticline. Graben-synclines consist of Daubaiskaya Formation volcanics. The Sardzhalsk structure extends northwestward for 27 km, with width up to 6 km. The Vasilyevskoye fault, which has thrust character, bounds it from the southwest. The Karasuisk syncline also extends northwestward for more than 25 km and frequently undulates. Wing span is 10 km. Their dip is probably gentle. The Akdyngesk anticline has near-latitudinal strike, with its axis practically coinciding with the Akdyngesk fault zone.

The district's largest fault disturbances are the Sardzhalsk and Vasilyevskoye faults. The Sardzhalsk fault is oriented northwestward along azimuth 340°. The fault plane dips southwestward at an angle of 70°. It forms the boundary between the Zharminsk synclinorium and the Char-Gornostaev anticlinorium. Along the fault, the southwestern block is downthrown by 1000 m. The Vasilyevskoye fault is confidently traced as a single zone until its junction with the Sardzhalsk fault. Along the fault, Bukonskaya Formation deposits are thrust over Daubai volcanics of the Sardzhalsk graben-syncline. The fault plane dips southwestward at angles of 50–60°. The fault consists of a system of close ruptures, accompanied by schistosity, fracturing, and rock crumpling. It hosts protrusions of Char complex ultrabasics, a belt of small Saldyminsk and Argimbaisk complex intrusions, beresite and listvenite zones, quartz veins, and arsenopyrite-pyrite

mineralization zones. Practically all industrially important gold deposits and occurrences of the district (Vasilievsk, Colorado, Football zone, Akzhal, Tokum, etc.) are confined to the Vasilyevskoye fault. The fault was the most mobile and permeable structure of the district, both during the Hercynian cycle and in the subplatform Alpine period.

2.3.4 Mineral Resources of the District

Gold constitutes the district's primary mineral resource. The number of gold deposits and occurrences here reaches 75. The main role among them is played by deposits and occurrences of mineralized zones in black shale formations and vein low-sulfide gold-quartz types. Most gold ore objects are concentrated in the Vasilyevskoye regional fault zone [39], forming the Akzhal-Vasilyevskoye ore district. Within it, two ore fields are distinguished: Boko-Vasilievsk, including the largest mineralized zone type deposits, and Akzhalsk, whose main reserves are concentrated in vein and stockwork zones of gold-quartz type.

Deposits of mineralized zones in black shale formations include Vasilievsk, Tokum, Yuzhny, Koitas, No. 15 (Zhenishke), Igrek zone, Football, and others. The medium-sized Akzhal deposit represents a typical gold-quartz type example. Structurally, gold mineralization at the deposit is controlled by mineralized schistosity and fracture zones that are cut by a quartz stockwork and contain short quartz veins. Ore bodies in these zones have flattened lens forms and are most gold-bearing. Most gold-containing quartz veins are localized in a granodiorite intrusion.

Copper occurrences associated with Argimbaisk and Saldyminsk complex intrusions are confined to fracturing zones (Chudsk, Argimbai, Tiepkai, etc.). Mineralized zone scales are small 100 - 200 m in length with thickness up to 15 m. These zones contain poor malachite mineralization, less commonly chalcopyrite-azurite-malachite mineralization. Gold contents do not exceed 0.1-0.5 g/t, sometimes reaching 3.2 g/t. Objects are small and do not represent industrial interest.

The district contains two small, completely worked-out gully and valley gold placers. Ancient buried marine placers, represented by ilmenite sandstones, are known in Arkalykskaya Formation deposits. They outcrop in the near-contact portion of the Argimbaisk diorite massif, where they form the small Sokratovsk deposit. The ore pack contains 3 horizons of titanomagnetite sandstones, with total thickness of 2–3 m, traced along strike for 800 m. Contents include Fe_2O_3 10–58%, FeO up to 41%, TiO_2 8–19%, V_2O_5 0.1%, and Ga_2O_3 0.01–0.02%.

Akzhal Deposit.

The deposit structure incorporates two large lithological-stratigraphic Paleozoic complexes, with the boundary between them quite confidently established visually and serving as one of the object's marker surfaces.

The lower complex consists of roughly intercalated siliceous formations with interbeds and lenses of jaspers and jasperoids. Correlation-wise, it corresponds to units identified in Southwest Kalba within the Arkalykskaya Formation, which is assigned to the Middle–Upper Visean substages of the Lower Carboniferous (C1v2–3ar) [38].

The upper complex consists of fairly uniform thicknesses of effusive, pyroclastic, terrigenous–pyroclastic, and terrigenous rocks. Volcanic members include dacites and andesite porphyrites, dacitic tuffs, tuffaceous sandstones and tuffites, and liparite porphyries, whereas the terrigenous component is dominated by widespread gray polymictic sandstones.

The upper complex belongs to Serpukhovian stage formations of the Lower Carboniferous Aganaktinskaya Formation (C1sag).

Neogene deposits are significantly developed in the deposit's northern and western portions, represented by the Upper Miocene–Lower Pliocene (N_1^3–N_2^1pv) Pavlodarskaya Formation cover. The formation consists of uniform plastic red-brown clays, sometimes sandy. When clays are sandy, quicksand can form, seriously complicating drill hole drilling. The Pavlodarskaya Formation cover thickness averages 20–60 m, reaching values of 100 m and more in the deposit area's western portion.

Tectonics. In the summary work of Okunev E.V., the deposit's western and northwestern flanks are characterized by a near-east–west-trending anticline developed in sedimentary rocks and showing an asymmetric geometry: the southern limb is steeper (about 70–80°) than the northern limb (about 50–60°).

The anticlinal structure's axial part is traced for approximately 3 km from east to west and controls the deposit's central portion. This fold structure is designated as the Akzhalsk anticline.

The most widespread disjunctives at the deposit are of west-northwestern (Az. 290–310°) and northwestern (Az. 330–340°) directions. West-northwestern direction structures are main, with northwestern-strike ruptures relative to them being en echelon. Main structure examples include zones Vertical, Diagonal, Kitaiskaya I, Sergey I, and Izmaylovsk, while en echelon structures include zones Igrek I, No. 36, Krasno-Musinsk, Staro- and Novo-Mikhailovsk, Border, Funrovaya II, and a number of unnamed ruptures.

Ruptures of northeastern direction, oriented orthogonally to northwestern disturbances, play a very noticeable role in the deposit's structural appearance. The largest of these is the Dolinny fault, which crosses the entire deposit area and continues beyond its limits.

In addition to the Dolinny fault, three more northeastern-strike disturbances are known to the east, with spacing between them from 200 to 300 m. Along these, normal and left strike-slip displacements are also manifested, complicating the structure of zones Diagonal and Kitaiskaya I.

Northeastern ruptures are clearly later than northwestern ones; they intersect and displace the latter by left strike-slip and normal fault types; similarly, they complicate fold dislocation occurrence, shifting the anticlinal fold's axial line in plan.

Magmatism. The deposit's magmatic rocks consist of two small stocks composed of quartz diorites and diorites. Stock plan dimensions are approximately 400×250 and 400×100 m; they are confined to the anticlinal fold's axial portion and northern wing, at the position of inflection of its axial line. The Dolinny fault "cuts off" stocks from the northwest; from the south, diorite distribution is limited by the west-northwestern fault of

zone Vertical. The remaining stock contacts are normal magmatic contacts with thin (not more than 3–5 m) rims of hornfelsed rocks, manifested mainly in the intrusions' southeastern portion.

In addition to diorite intrusions, in the fold's northern wing, closer to its axial portion, rare small gabbro-diorite composition intrusions are noted, elongated along the axial line strike and having plan sizes not exceeding 15-20×60-80 m.

The deposit's vein magmatic rocks, at least in the portion studied by us, consist of diorite aplites, gravitating toward diorite stock boundaries and confined mostly to northeastern fault zones. Rocks have leucocratic appearance, fine-grained structure, and belong to the subintrusive magmatism facies.

According to existing concepts, small intrusions and vein magmatic rocks are derivatives of the diorite intrusion.

Overall, the known ore bodies - at least within the central part of the object - are essentially mineralized fault-zone tectonites that have been metasomatically altered, representing structures of different orders and orientations [38]. Ore tectonites consist mainly of fracturing and cataclasis zones of host rocks with varying degrees of quartz metasomatism processes, expressed in extensive development of veinlet silicification and silicification of rocks in mass. Sulfide mineralization (pyrite, to a lesser extent arsenopyrite) is invariably present as dissemination, as well as thin veinlet and nest-like aggregates.

The majority of the deposit's leading ore bodies are confined to west-northwestern or northwestern-strike fault disturbance zones, which are the most widespread ore-localizing structures. Ore bodies are localized in tectonites of northeastern disturbance zones. These include, first of all, mineralized lenses in tectonites of the Dolinny fault, one of which (zone Dolinnaya) was previously explored and is currently being exploited. Additionally, during exploration of zones Diagonal and Kitaiskaya I, ore bodies (ore bodies No. 11) and lenses (D-1 and D-2) were also identified, localized in northeastern-direction fracturing zones. Mineralization in these zones is not sustained along strike, represented by bead-like arranged ore accumulations as lenses and nests in tectonites. To date, the degree of study of these ore-bearing structures does not allow reliable assessment of their possible potential; further study of their ore content is certainly a promising direction for exploration and assessment work on the object.

In addition to fault tectonics, fold structures also play a very important role in ore localization. In particular, one can quite definitely speak about the position of inflection in plan of the Akzhalsk anticlinal fold's axial line, as one of the main factors controlling the most ore-saturated block of the deposit's central portion. Higher-order fold forms, complicating the Akzhalsk anticline wings, also play a noticeable role in ore localization.

The considered oxidized ore deposits compose the upper, hypergenesis-affected portions of linear ore-bearing structures, which generally predetermine their morphology and occurrence features.

In plan, these are extensive (first hundreds of meters) ore bodies elongated in west-northwestern direction, less commonly lenses with lengths in first tens of meters. Explored

ore zones are represented either by single ore bodies (zone Vertical, southeastern flanks of zones Kitaiskaya I and Diagonal), or by groups of close ore bodies, such as groups No. 7 and 8 in subzone Sergey I or the group of ore bodies No. 9 along the northwestern flank of zone Kitaiskaya I.

Ore body thickness in plan varies mainly within 4 to 10 m, with sharp breaks and pinches being rare. Body pinching out along strike is mostly natural; in individual cases, particularly along the southeastern flank of zone Diagonal, ore bodies are cut off by transverse ruptures.

In section, ore bodies have relatively simple morphology; sharp power changes along dip are rather rare and observed only along zone Diagonal, where with depth the ore body thickness noticeably decreases, taking values up to 2-4 m at depths of 20-30 m, while on the surface its thickness is sustained at 6–8 m, reaching values of 20 m and more along exploration lines 0–2.

Overall, ore body morphology can be attributed to the linear type, characterized by variable morphological parameters along strike and dip with a small degree of occurrence disturbance.

Overall, gold distribution in ores of all explored zones can be attributed to uneven or extremely uneven. Ore bodies are localized in most cases within tectonic zones of fracturing and cataclasis. Only in rare cases do body contours extend beyond tectonites due to adjacent mineralized rock blocks located mainly from the hanging wall of ruptures. Thus, ore body occurrence is completely subordinate to ore-localizing structure occurrence. Practically all ore bodies and lenses dip north-northeastward at angles of 55–70°.

Currently, the Akzhal deposit is in the process of development; ores are processed by heap leaching method.

Material Composition of Ore Bodies. the Akzhal deposit hosts a gold–sulfide–quartz type in which ore is concentrated in fracture-controlled zones, with sulfides and gold distributed unevenly. Ore bodies are expressed both as gold-bearing quartz veins containing free gold (commonly up to about 1–1.5 m thick) and as broader mineralized zones that may reach roughly 100 m in thickness. Disseminated mineralization is developed mainly in terrigenous carbonaceous–cherty rocks, whereas vein and breccia sulfide–quartz mineralization occurs in a wide range of host and magmatic lithologies [39].

Mineralogically, the ore assemblage is relatively simple. Pyrite and arsenopyrite are dominant, with galena, sphalerite, and chalcopyrite also present. The principal gangue minerals include several generations of quartz, calcite, plagioclase, chlorite, and muscovite. Less common and accessory ore phases comprise native gold, tetrahedrite, pearceite, stephanite, shakhovkite, and benleonardite. The most typical associations are a gold–pyrite–arsenopyrite assemblage and a gold–polymetallic assemblage [39]. Gold occurs in native form (in quartz veins) and as isomorphous admixtures in pyrite and arsenopyrite [73].

Vasilievsk Deposit

The Vasilievsk deposit lies in the central portion of the Boko-Vasilievsk ore field and covers a section 2.6 km long and 100-300 m wide [6] along the Vasilyevskoye fault seam

[40]. The deposit's geological structure incorporates Middle Carboniferous Bukonskaya Formation deposits, thrust along the Vasilyevskoye fault over Middle-Upper Carboniferous volcanics of the Daubaiskaya Formation of the Sardzhalsk graben-synclinal structure. Small bodies and dikes of the Upper Paleozoic Daubai subvolcanic complex cut sedimentary and volcanic rocks, and northeastern faults break them into a series of tectonic blocks.

Host rocks consist of sedimentary deposits of the Bukonskaya Formation's upper pack, represented by flyschoid intercalation of carbon-containing calcareous siltstones and sandstones.

Carbonaceous matter occurs as finest inclusions, forming bedded and lens-like segregations in clayey and carbonate cement, as well as macro and microscopic interlayers. Carbon is structureless and opaque.

Daubaiskaya Formation volcanics lie in the deposit's footwall. These consist of cherry and greenish-gray varieties of andesite-basalt composition. Subalkaline rocks (trachyandesite-basalts) with high alumina content and unsustained potassium-to-sodium ratio predominate. Silica content in cherry varieties ranges from 53-55%, in green varieties from 47-52%.

Intrusive rocks have relatively limited distribution. These consist of bodies and dikes of the Middle-Upper Carboniferous Daubai subvolcanic complex.

Subvolcanic intrusions are localized in the Vasilyevskoye fault zone. They form dikes, dike-like and lens-like bodies. Their extent usually does not exceed 150 m along strike and 150–250 m along dip, with thickness up to 40 m. Low-thickness dikes are usually boudinaged, often fragmented and broken into separate fragments. Fragments along the thrust zone are pulled apart from each other and usually well rounded. The most widespread are dacite, andesite-dacite, and andesite porphyrite dikes; less commonly, diorite porphyrites, diabases, and gabbro-diabases are noted.

Daubaiskaya Formation volcanics in the thrust footwall have general northeastward dip at angles of 50–60°. Bukonskaya Formation deposits compose the northeastern wing of a synclinal fold in the Hercynian structural stage and have monoclinal occurrence with rocks dipping southwestward at angles of 40–70°. On the deposit's northwestern flank, folds are disharmonic, sometimes asymmetric with varying wing span magnitudes (from 200–240 m to 500–550 m) and axis plunge directions (from 230-240° to 205-215°). Folding intensity increases in the southeastern direction.

The main fault disturbances are faults of northwestern and northeastern strike. The Vasilyevskoye thrust represents a low-thickness tectonic seam. The seam's usual filling consists of fractured, crumpled rocks, in places polished, clayized, significantly altered under the influence of dynamometamorphism and hydrothermal metasomatism processes.

A host zone adjoins the thrust seam from the hanging wall side, extending over 3 km with non-constant thickness (on the southeastern flank in the Zhanominsk fault area - 80–110 m, on the northwest – 15-45 m). The zone's characteristic feature is its intense tectonic reworking, increased carbonaceous material content, and high degree of silicification. The zone's lower boundary is clear, drawn along the thrust seam. The

hanging wall's upper boundary is also expressed quite clearly, marked along a tectonic fault seam, separating weakly dislocated siltstones and sandstones from carbonaceous tectonites.

Northeastern faults intersect and displace the Vasilyevskoye thrust zone, causing block structure. Drilling and mine work confirm only the Zhanominsk fault, along which displacement of structures and gold ore mineralization zones by 330 m is established. The remaining northeastern-direction faults are assumed and are not unambiguously confirmed by drilling work.

Structure of the Host Zone of the Deposit. The deposit's host zone differs from surrounding rocks by the degree of tectonic reworking, amount of carbonaceous material, and intensity of quartz-vein and sulfide mineralization. The zone rocks' original composition consists of flyschoid intercalation of sandstones, sand-siltstones, siltstones, and sand-pelites of the Bukonskaya Formation. Zone contacts are controlled by dike belts of the hanging and foot walls. Footwall dikes throughout the deposit gravitate toward the thrust seam and contact with Daubaiskaya Formation volcanics, located at distances of 3–10 m from it, and only in the area of profiles No. 10–20 does the distance increase to 60–250 m. Hanging wall dikes are arranged en echelon, sometimes with breaks along strike up to 50–150 m. Their thickness usually does not exceed 10 m.

The host structure is studied in detail to a depth of 400 m along approximately 3500 m. Its general strike is northwestern along azimuth 300–310°, dipping southwestward at angles of 40–50°. Zone thickness varies from 10 m in pinches to 100–120 m in bulges.

In tectonic breccias, clastic material consists of rounded fragments of gold-bearing mono-quartzites, less commonly rounded fragments of sandstones, siltstones, porphyrite dikes, and listvenites. Breccia cement consists of carbonaceous mylonites. Gold-bearing quartz veins and veinlets essentially represent metasomatic mono-quartzites, developing along tension fractures [39]. Low-thickness veins and veinlets typically display fragmentation into separate rounded fragments, intense boudinage, and wide development of crenulated textures.

Within the host zone, especially on the southeastern flank, quartz-carbonate metasomatites-listvenites are manifested. Large listvenite bodies have lens-like, spindle-like forms and lengths along strike up to 200 m with thickness up to 30 m. Body contacts are clear and contrasting. Along strike, they are accompanied by a train of fragments of the same composition. As a rule, listvenites are confined to dike margins or localized in the zone of upper pinch-out of the latter, forming sheath-like structures. In addition to quartz (10–15%) and carbonate (85–90%), listvenites contain finely dispersed malachite dissemination, giving the rock a greenish color.

The Vasilievsk deposit's ore bodies are confined to the Vasilyevskoye thrust zone, composed of carbonaceous tectonites. These represent quartz-sulfide mineralized zones and are distinguished only by sampling data. Contacts with host rocks are gradual but sufficiently contrasting. Gold mineralization is characterized by persistence along strike and dip, with identical material composition. When contouring ore bodies by the

recommended cut-off grade variant (0.3 g/t), five ore bodies (No. 1, 2, 3, 4, and 7) and a number of accompanying small ore lenses (No. 1-1, 1-5, 7-1) are distinguished.

At Vasilievsk, two principal natural ore types are distinguished: oxidized ore and primary ore. Complete oxidation extends to depths of roughly 20–30 m, underlain by a transitional interval of partially oxidized material that grades downward into the primary mineralization zone.

Oxidized ores comprise thoroughly weathered rocks from the host zone, including schistose and fractured carbonaceous siltstones, sand–siltstones, sandstones, and tectonic breccias, all strongly permeated by a dense stockwork of quartz veinlets [40].

The ore mineral assemblage includes hydrogoethite, limonite, jarosite, psilomelane, chalcocite, covellite, scorodite, chrysocolla, cerussite, valentinite, malachite, and gold. Iron hydroxides are most abundant (about 60–70%) and commonly form colloform segregations [40].

Gold occurs as native metal; the dominant proportion is fine and microscopic (approximately 25–200 μm), mainly as inclusions in quartz and in limonite–goethite–scorodite material (83.59%) [81]. Free gold accounts for 7.61%, while 8.57% occurs in intergrowths with sulfides. Arsenic contents range from 0.08–0.17%, free carbon from 0.02–0.25%, copper from 0.01–0.04%, zinc up to 0.03%, lead up to 0.01%, iron 4.17%, and silver 1.0–4.6 g/t. Oxidized ores are characterized by hypergene replacement structures. Texturally, mesh-like, relict, and fragmented structures are most common and reflect the replacement of pyrite and arsenopyrite by hydrogoethite, limonite, jarosite, and scorodite.

Primary ores are dominated by carbonaceous tectonites. Quartz occurs as lens-shaped bodies, dense veinlet stockworks, and thin, bedded veins and veinlets, with overall quartz contents ranging from about 10–30% to nearly 100%. Stockwork silicification is strongest in ore-body swellings and in intervals where the enriched portion of the ore column is concentrated. Sulfide mineralization is represented mainly by fine, uneven dissemination of pyrite, marcasite, melnikovite-pyrite, arsenopyrite, with chalcopyrite, sphalerite, galena, and tetrahedrite present only in trace amounts. Total sulfides are typically 2–3% and only rarely rise to ~10%; pyrite dominates and is about 2.5–3 times more abundant than arsenopyrite.

Economically, gold is the only valuable component. Nearly half of it (49.1%) occurs as free gold, while the remainder is associated with pyrite and arsenopyrite. In quartz, gold is observed as wire-like, scaly, platy, foliated, and lumpy segregations and, in some cases, dendritic aggregates. Fineness is high (approximately 845–872) and generally tends to increase with depth. Grain sizes range from fractions of a millimetre up to about 1.5–2 mm. In sulfides, gold commonly forms inclusions and may also occur in grain interstices, where particle sizes are very fine (about 1–10 μm). Gold contents in pyrite range from 9.0 to 170.3 g/t, whereas arsenopyrite contains substantially higher concentrations (about 114–483 g/t); gold in galena does not exceed ~10 g/t.

Tokum Occurrence lies 2 km from the northwestern boundary of the Vasilievsk deposit mining allotment and is localized in an almost analogous geological-structural position - in the Vasilyevskoye thrust zone, in its hanging wall.

Located within the Vasilyevskoye fault (thrust) zone, the Tokum occurrence is hosted by rocks of the Bukonskaya and Daubaiskaya formations and is overlain by modern sediments of the Boko River valley.

Stratigraphically, the Bukonskaya Formation (C2bk) here corresponds to the lower part of the upper subformation and is represented by a sand–siltstone–argillite sequence. The siltstones are thinly banded and commonly contain graphite flakes aligned with bedding or schistosity; the graphitized component typically ranges from about 1–7%. The rock matrix is dominated by weakly rounded quartz and feldspar grains with subordinate lithic fragments. The argillites are dark gray to black and thinly banded, but the original layering is often overprinted by later schistosity; they are widely transformed into clayey and carbonaceous–clayey schists, with carbonaceous matter varying from near-zero up to ~10%. Graphite flakes emphasize micro-crenulation and the schistosity fabric, and the rocks are metamorphosed throughout.

To the northeast, on the eastern flank of the section beyond the Vasilyevskoye fault, the Daubaiskaya Formation (C2–3db) is exposed and is composed of cover andesite–basalts. Internally, it shows a coarse rhythmic layering, with rhythm thicknesses from fractions of a metre up to ~30 m. The base of each rhythm contains greenish-gray volcanic rocks with few amygdules, grading upward into cherry-colored varieties with abundant amygdules. The total (incomplete) thickness of the Daubaiskaya deposits studied at the occurrence exceeds 350 m.

Intrusively, despite the broader ore field containing diverse intrusive rocks, the Tokum occurrence itself is characterized mainly by plagiophyres (μC3). They form stock-like and dike-like bodies that become more numerous toward the northwest; plan dimensions range from roughly 5 × 80 m to 100 × 300 m, and most bodies are traced down to ~400 m without obvious pinch-out.

Structurally, the key feature of Tokum is its position within the Vasilyevskoye fault zone, a branch of the Boko–Kokpektinsk deep fault. Along this structure, Bukonskaya rocks are thrust over Daubaiskaya effusives, and the contact zone is disrupted into separate blocks by younger crosscutting breaks. Higher-order submeridional and northeast-striking faults further partition the occurrence into blocks and are expressed as relatively thin (about 3–5 m) fracture and silicification zones [73]; they offset the Vasilyevskoye fault zone with horizontal displacements on the order of 25–30 m.

Of particular interest, northwest-striking ruptures host all known ore bodies. These faults are en echelon relative to the Vasilyevskoye fault and postdate the northeast and submeridional breaks. Within the occurrence they appear as closely spaced tectonic seams, variably filled with silicified and metasomatically altered Bukonskaya terrigenous rocks; in the central and northwestern parts, many seams are sealed by subvolcanic plagiophyre intrusions, while small dikes are noted in the southeast. In the central area, the rupture traces bend toward a near-east–west trend, mirroring the plagiophyre contact.

The faults dip to the southwest and south at about 45–60°, flattening with depth to roughly 20–30°.

Alteration-wise, two main hydrothermal–metasomatic styles are reported: propylitization and beresitization–listvenitization. Propylites are widespread throughout the Daubaiskaya andesite–basalt sequence, and subvolcanic/hypabyssal plagiophyre bodies are propylitized unevenly; in places, propylitic zones are obscured by later metasomatic overprinting to that at the Vasilievsk deposit and has zonal structure. The host zone thickness is 120–150 m.

The Tokum occurrence's gold mineralization consists of zones and veinlet-disseminated mineralization. Ore bodies are located in the most reworked portions of inner beresite-listvenite zones. In total, 32 ore bodies are distinguished at the occurrence.

All ore bodies are located within a zone of quartz-carbonate veinlets, confined to the Bukonskaya Formation sand-schist thickness along the exocontact of a rather large plagiophyre stock. Additionally, beyond the principal ore bodies, several smaller bodies are recognized, mostly in the upper part of the occurrence. These thin ore bodies contain estimated reserves of about 0.7–9.4 kg of gold, with grades in the range of 0.45–3.25 g/t, and together account for roughly 0.88% of the reserves calculated for the section.

Main ore bodies have irregular lens forms, elongated along dip.

Zhenishke Occurrence lies 3.5 km northwest of the Tokum occurrence and is situated in the Vasilyevskoye fault zone. On the occurrence area, Kokpektinsk and Bukonskaya formation rocks are developed, composing the southern wing of an anticlinal fold with northeastern strike.

In the northern part of the occurrence, Kokpektinskaya Formation rocks are present and are represented mainly by polymictic sandstones of variable grain size with interbeds of conglomerate. Bukonskaya Formation deposits begin with medium-pebble conglomerates that include sandstone and siltstone interlayers at the base; down-dip these pass laterally into sand–siltstones. Conglomerate thickness reaches approximately 60–70 m, and upward in the section the conglomerates give way to weakly carbonaceous and carbonaceous siltstones, with lens-like interbeds of fine-grained sandstones with thickness up to 5–10 m. Siltstones in places are transformed into schists, which is explained by tectonic movements and intrusion of albitized granodiorites. Rocks have northeastern strike with southeastward dip at angles of 60–70° [40].

Intrusive bodies consist of granodiorites and granite-porphyries, forming two dike-like bodies with sublatitudinal strike in the area's eastern portion [39]. In the western portion, their strike changes to northeastern. Intrusive body lengths reach up to 700–800 m, width up to 100 m. Granodiorites are intensely albitized, in places completely transformed into albitophyres and beresitized varieties.

The occurrence area is broken by sublatitudinal and northeastern-strike fault disturbances, which are accompanied by fracturing and schistosity zones with thicknesses from several meters to 30–40 m. Gold ore mineralization is associated with these fault zones. Several zones of schistose, fractured, and insignificantly sulfide-mineralized rocks were identified, with thicknesses from several meters to 30–40 m. In the occurrence's

central portion, 2 zones were identified, localized in the northern and southern contacts of a granodiorite dike-like body. The indicated zones' strike changes from northeastern in the area's western portion to sublatitudinal in the central portion.

Zones prospective for gold mineralization are traced along strike for 600 m and have southeastward dip at angles of 50–60°. Zone thicknesses vary from several meters to 15–20 m. These represent sections of intense veinlet silicification with rare sulfide dissemination. Ore mineral content in individual zone sections reaches 3–4%. These consist mainly of pyrite, less commonly arsenopyrite and chalcopyrite. Ore minerals form rare dissemination in quartz veinlets and in host rocks. Rocks hosting ore mineralization are intensely silicified and have a greenish tint, probably caused by beresitization processes.

Based on earlier investigations, 13 ore bodies were delineated within zones that show low gold grades at the surface, using a cut-off grade of 0.3 g/t for contouring. Average gold content varies from 0.73 to 2.33 g/t, with thicknesses from 2 to 4.5 m.

Yuzhnoe Occurrence lies 2.7 km southwest of the Vasilievsk deposit. Gold mineralization is confined to the Daubaysk syncline's southern limb, to the contact between the Kokpektinsk and Bukonsk formations, complicated by a small Late Carboniferous-age subvolcanic intrusion of intermediate-acid composition and sublatitudinal fault tectonics.

Abnormal gold concentrations (more than 0.1 g/t) here are confined to crosscutting zones of fracturing, vein silicification, and quartz-albite metasomatism in subvolcanic intrusion rocks. The zones have northern dip with sublatitudinal strike. Sulfide amounts (oxidized pyrite) in ores are extremely insignificant and do not exceed 0.5%.

At the section, with a minimum cutoff gold content of 0.3 g/t, 45 ore bodies are distinguished. Average ore body strike azimuth is approximately 100°, with body dip angles varying from 15 to 42°. Body extents along strike range from 25 m to 139 m, along dip from 10 m to 50 m. Thicknesses range from 1 to 9 m. The mineralization is not closed at depth.

To summarize, the West Kalba metallogenic zone constitutes East Kazakhstan's principal gold-bearing structure, containing more than 450 gold deposits and occurrences, including large and superlarge deposits. The zone occupies an axial position within the Ob-Zaisan (Irtysh-Zaisan) fold system, which developed during Late Paleozoic collision between the Siberian and Kazakhstan continental blocks. The zone's structural foundation consists of the Char ophiolite belt, which preserves fragments of oceanic lithosphere from the Ob-Zaisan basin.

The zone's geological structure features northwest-striking structural-material complexes bounded by regional deep faults. Sedimentary deposits span from Ordovician to Carboniferous age, with Middle Carboniferous Serpukhovian and Bukonskaya Formation deposits covering more than 50% of the zone area. The West Kalba zone divides into several ore districts, each displaying distinct metallogenic characteristics: Suzdalsko-Mukur, Bakyrchik, Sentash-Kuludzhun, Baladzhalsk, and Akzhal-Daubay-Ashalinsk districts.

The Bakyrchik ore district hosts 123 gold occurrences, including East Kazakhstan's largest deposits of the gold-arsenic-carbonaceous formation. A 17.5 km-long sublatitudinal structure with left strike-slip-thrust kinematics, the Kyzylovsky shear zone, functions as the primary ore-controlling structure for the Bakyrchik and Bolshevik deposits. Gold mineralization principally associates with low-sulfide carbonaceous formation ores, where 95–97% of gold occurs bound to pyrite and arsenopyrite. Deposit formation is interpreted as hydrothermal, involving gold introduction from depth, controlled by major tectonic structures and linked to Late Carboniferous–Permian intrusive complexes [40].

Situated in the axial portion of the West Kalba zone, the Akzhal-Vasilyevskoye ore district contains 75 gold deposits and occurrences. The district's structure is controlled by the junction between the Zharminsk synclinorium and Char-Gornostaev anticlinorium, separated by the Sardzhalsk transform-type deep fault. The Vasilyevskoye fault zone functions as the primary ore-localizing structure for virtually all industrially significant deposits, including Vasilievsk, Akzhal, and Tokum. Gold mineralization occurs as mineralized zones in black shale formations and vein low-sulfide gold-quartz types, spatially and genetically linked to Middle–Upper Carboniferous subvolcanic intrusions of moderately acid to intermediate composition.

West Kalba zone gold deposits developed during the collisional stage of Zaisan suture zone evolution and display fundamental similarities in ore-formational characteristics, regardless of district location. Mineralization associates with hydrothermal alteration processes (sericitization, chloritization, silicification, carbonatization, albitization) and is controlled by regional and local fault systems. The interplay of tectonic, magmatic, and stratigraphic factors governs ore body localization and morphology, with bodies typically exhibiting linear, lens-like, or columnar forms that follow the geometry of controlling structures [73].

3 REMOTE SENSING METHODOLOGY FOR GEOLOGICAL APPLICATIONS

This chapter presents the theoretical foundations and methodological framework for remote sensing applications in geological studies, with particular emphasis on hydrothermal alteration mapping and mineral exploration. When we refer to satellite technologies in this thesis, this term is used in the exact meaning of the global term remote sensing; therefore, throughout this PhD thesis we refer to satellite technologies as remote sensing. the methodology is organized as a stepwise sequence that starts with the physical basis of electromagnetic radiation, then covers the spectral behavior of geological materials and remote-sensing instruments, followed by preprocessing, spectral transformations, and, finally, validation approaches. The chapter concludes with spectral signature validation using hyperspectral data, establishing the foundation for the application of these methods to gold deposits in Eastern Kalba, Kazakhstan.

3.1 Electromagnetic Radiation Fundamentals

Electromagnetic Spectrum

Electromagnetic radiation encompasses a continuous spectrum of energy (Fig. 3.1) that propagates through space as oscillating electric and magnetic fields perpendicular to each other and to the direction of propagation [29]. The electromagnetic spectrum spans from gamma rays with wavelengths on the order of 10^{-12} meters to radio waves with wavelengths exceeding 10^{3} meters. For geological remote sensing applications, the relevant spectral regions include the visible (0.4–0.7μm), near-infrared (0.7–1.3μm), shortwave infrared (1.3–3.0μm), and thermal infrared (3.0–15μm) portions of the spectrum [42; 18].

The relationship between wavelength (λ), frequency (ν), and the speed of light ($c = 3 \times 10^{8}$ m/s) is given by:

$$c = \lambda\nu. \tag{3.1}$$

The energy (E) of a photon is related to its frequency through Planck's constant ($h = 6.626 \times 10^{-34}$ J·s):

$$E = h\nu = \frac{hc}{\lambda}. \tag{3.2}$$

This relationship demonstrates that shorter wavelengths correspond to higher energy photons, which is critical for understanding the interaction of electromagnetic radiation with matter at different spectral regions. The spectral regions used in geological remote sensing are defined based on both atmospheric transmission windows and the spectral properties of geological materials. Atmospheric windows, regions where the

atmosphere is relatively transparent, determine which spectral regions are accessible from spaceborne platforms [26].

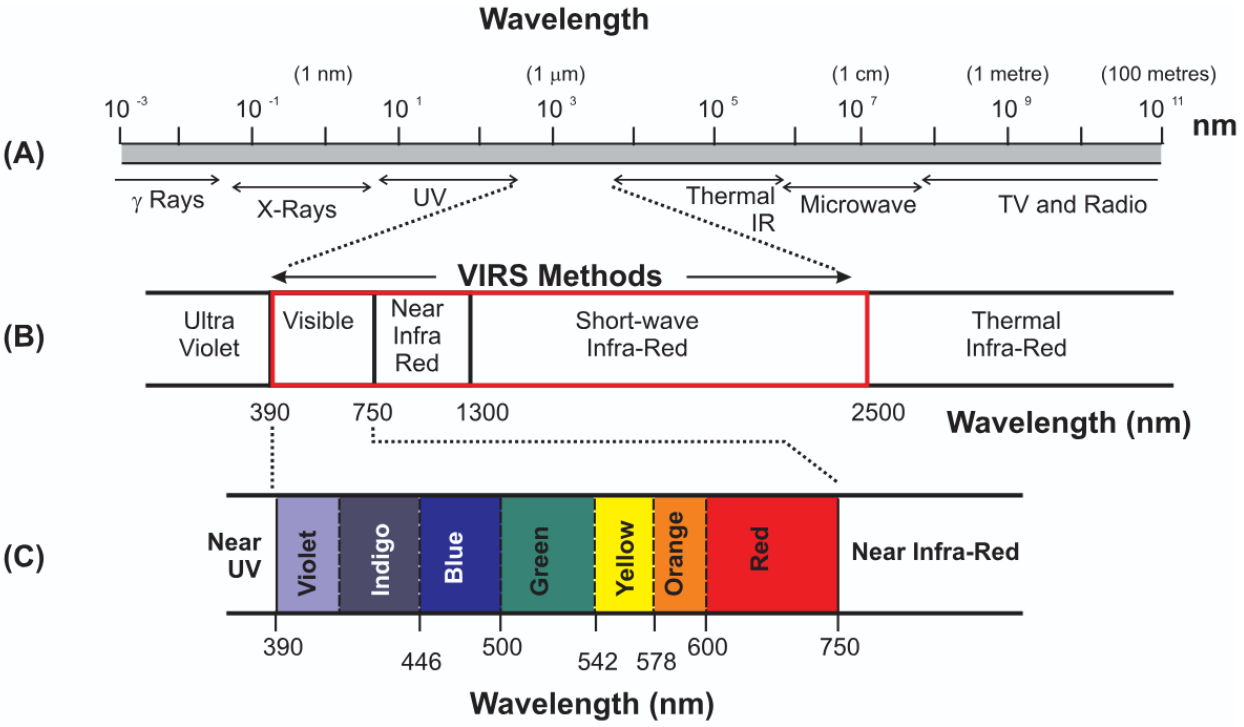

Figure 3.1. Electromagnetic spectrum with visible, VNIR and SWIR regions

Note – compiled from [93]

The visible region (0.4–0.7μm) corresponds to the peak of solar radiation and enables detection of colored minerals and ferrous iron-bearing silicates. The near-infrared region (0.7–1.3μm) includes the first overtone of O-H stretching and enables vegetation discrimination and detection of Fe^{2+} crystal-field transitions in ferrous silicates. The shortwave infrared region (1.3–3.0μm) contains fundamental vibrational absorption features for hydroxyl-bearing and carbonate minerals, making it critical for alteration mapping [23]. The thermal infrared region (3.0–15μm) captures thermal emission from Earth's surface and enables lithological discrimination based on emissivity differences [17]. Electromagnetic radiation exhibits both wave-like and particle-like properties, a fundamental concept established by the photoelectric effect and quantum theory [14]. The wave nature governs propagation, interference, and atmospheric scattering; the photon nature governs discrete absorption and emission in minerals. Diagnostic spectral signatures arise where photons are absorbed by electronic transitions (dominant in the visible–NIR) or vibrational/phonon processes (dominant in the SWIR–TIR), producing reflectance/emissivity minima that encode mineralogy.

Electromagnetic Radiation interaction with Matter

When electromagnetic energy reaches a material, it may be absorbed, reflected, transmitted through the medium, or scattered [23]. Which of these pathways dominates is

controlled by the radiation wavelength, the material's composition and internal structure, and the incidence angle [32; 21]. Understanding these interactions is fundamental to interpreting remote sensing data and extracting information about surface composition.

Absorption occurs when photons transfer their energy to atoms or molecules, exciting electrons to higher energy states or causing molecular vibrations [23]. The absorbed energy may be re-emitted at different wavelengths (fluorescence) or converted to thermal energy. In minerals, absorption features arise from electronic transitions in transition metal ions (e.g., Fe^{2+}, Fe^{3+}) and vibrational processes in molecular groups (e.g., OH^{-}, CO_3^{2-}, H_2O) [11]. The Beer-Lambert law describes the relationship between absorption and material properties:

$$A = \epsilon c l, \tag{3.3}$$

where A is absorbance, ϵ is the molar absorptivity, c is concentration, and l is path length. This relationship explains why absorption features become deeper with increasing mineral abundance and why particle size affects absorption depth [21].

Reflection can be specular or diffuse, scattered in all directions). The reflectance of a material varies with wavelength, creating its characteristic spectral signature [32]. Surface roughness, particle size, and viewing geometry all influence the reflectance properties. The bidirectional reflectance distribution function (BRDF) describes how reflectance varies with illumination and viewing angles, which is important for correcting for topographic effects and comparing spectra acquired under different conditions.

Transmission occurs when radiation passes through a material without significant interaction. In remote sensing, transmission is relevant for atmospheric correction, where radiation must pass through the atmosphere to reach the sensor [26]. The transmittance of the atmosphere varies with wavelength, creating atmospheric windows where transmission is high and absorption bands where transmission is low due to atmospheric gases such as water vapor, carbon dioxide, and ozone.

Scattering involves the redirection of radiation without absorption. Rayleigh scattering affects shorter wavelengths (blue light) more than longer wavelengths, following a λ^{-4} dependence, and is caused by particles much smaller than the wavelength [36]. Mie scattering occurs when particles are similar in size to the wavelength and affects all wavelengths more uniformly [30]. Atmospheric scattering is a major consideration in remote sensing data correction, as it adds path radiance that must be removed to recover surface reflectance [26]. Non-selective scattering occurs when particles are much larger than the wavelength and affects all wavelengths equally, as in the case of clouds and fog.

Passive and Active Sources of Radiation

Remote sensing systems can be classified based on their radiation source [42;76]. Passive systems detect naturally occurring radiation, primarily solar radiation reflected from Earth's surface and thermal radiation emitted by materials (Fig. 3.2). The Sun acts as a blackbody radiator with a temperature of approximately 5800 K, emitting maximum radiation in the visible region according to Wien's displacement law [49]. Solar radiation

provides the primary illumination for visible and near-infrared remote sensing during daytime, with the solar irradiance spectrum following Planck's law modified by atmospheric absorption.

The solar constant, approximately 1366 W/m² at the top of the atmosphere, represents the total solar irradiance integrated across all wavelengths. The spectral distribution of solar radiation peaks near 0.5μm (green light) and decreases toward longer and shorter wavelengths. Atmospheric absorption by gases such as ozone, water vapor, and carbon dioxide creates absorption bands in the solar spectrum, particularly in the ultraviolet and infrared regions [26].

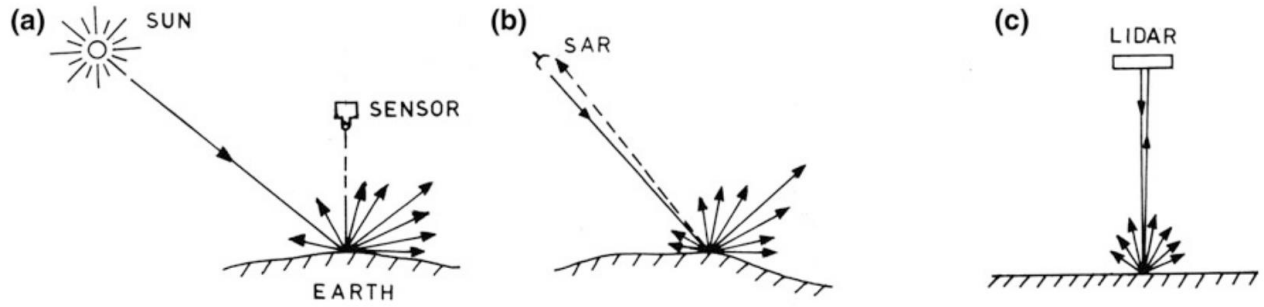

Figure 3.2. Geometric configurations in reflection sensing. A - Solar reflection sensing, b - SAR sensing, c - LIDAR sensing

Note – compiled from [94]

Thermal emission occurs according to Planck's law, where all objects above absolute zero emit radiation proportional to their temperature [35]:

$$B_\lambda(T) = \frac{2hc^2}{\lambda^5} \frac{1}{e^{hc/(\lambda k_B T)} - 1}, \tag{3.4}$$

where $B_\lambda(T)$ is spectral radiance, h is Planck's constant, c is speed of light, λ is wavelength, k_B is Boltzmann's constant, and T is temperature. The peak wavelength of thermal emission shifts to longer wavelengths as temperature decreases according to Wien's displacement law: $\lambda_{\max} = 2898/T$ (in micrometers). For Earth's surface materials (approximately 300 K), peak emission occurs in the thermal infrared region around 10 m [17]. The Stefan-Boltzmann law describes the total power radiated per unit area: $P = \sigma \epsilon T^4$, where σ is the Stefan-Boltzmann constant and ϵ is emissivity [45; 9].

Active systems provide their own source of radiation, such as radar for radio detection and ranging, lidar for light detection and ranging. These systems offer advantages including independence from solar illumination and the ability to control signal characteristics [48], though they are not the primary focus of this methodology chapter. Synthetic Aperture Radar (SAR) systems operate in the microwave region and are sensitive to surface roughness and dielectric properties, making them useful for

structural mapping and soil moisture estimation [47]. Lidar systems use laser pulses to measure distances and create high-resolution digital elevation models.

3.2 Spectral Properties of Geological Materials

Fundamentally, diagnostic spectral signatures used in geological remote sensing are produced by two key physical mechanisms: electronic transitions [42], which dominate in the visible and near-infrared regions, and vibrational/phonon processes, which dominate in the shortwave and thermal infrared regions. These processes create absorption features at specific wavelengths that encode mineral composition, crystal structure, and chemical bonding, forming the physical basis for all spectral analysis methods described in this chapter.

Electronic Absorption Processes in Minerals

Electronic absorption processes dominate in the ultraviolet (UV), visible (VIS), and near-infrared (NIR) regions and are responsible for many of the diagnostic spectral features observed in minerals [93]. They occur when incident photons promote electrons between discrete electronic energy levels that are controlled by the electronic structure of atoms and ions in the crystal lattice.

Charge-Transfer Transitions

Charge-transfer transitions involve the movement of an electron between neighbouring ions or between a central ion and its surrounding ligands. In these processes the electron does not enter a conduction band, but is transferred between localized states, typically at energies corresponding to the UV–VIS region. In Fe–O complexes, for example, oxygen-to-iron charge-transfer absorption produces strong attenuation of blue light, which leads to characteristic spectral features in ferrous iron-bearing silicates and sulfides. These intense, broad bands can dominate the visible spectra of Fe^{2+} bearing minerals including biotite, chlorite, and amphibole.

Band-Gap Absorption

In semiconducting and some metallic minerals, photons with energies equal to or greater than the band-gap energy can excite electrons from the valence band into the conduction band. This produces a sharp change in reflectance or transmittance at the wavelength corresponding to the band gap. The position of this spectral edge is controlled by the electronic structure and composition of the mineral and can therefore be used as a diagnostic feature in spectral measurements of sulfides and other semiconducting phases.

Metal Electronic Transitions and Crystal-Field Effects

Transition metal ions such as Fe, Mn, Ni, and Cu possess partially filled d-orbitals. When these ions are incorporated into mineral structures, the surrounding ligands create an electrostatic (crystal) field that splits the otherwise degenerate d-orbital energy levels. Electronic transitions between these split levels give rise to relatively narrow absorption bands in the VIS–NIR region. The energies (wavelengths) and intensities of these crystal-field transitions depend on the oxidation state of the ion (e.g. Fe^{2+} vs Fe^{3+}), its coordination geometry (octahedral vs. tetrahedral), and the nature of the ligands (Table

3.1). As a result, the positions and shapes of Fe-related absorption bands provide powerful constraints on both mineral identity and iron valence state in remote sensing spectra.

Table 3.1. Electronic transition types and their spectral characteristics for common geological materials

Transition Type	Wavelength Range (μm)	Intensity	Example Minerals
Crystal Field Fe^{3+}	0.9, 1.1	Medium	Olivine, pyroxene, biotite
Crystal Field Fe^{2+} in silica	0.9, 1.1	Medium	Biotite, chlorite, amphibole
Charge Transition from Fe^{2+} to Fe^{3+}	0.4–0.7	High	Magnetite, Fe-sulfides
Charge Transition from O^{2} to Fe^{2+}	0.4–0.6	High	Ferrous silicates
Conduction Band	0.4–2.5	Variable	Graphite, pyrite, galena

Vibrational Absorption Processes in Minerals

Vibrational absorption processes dominate in the shortwave infrared (SWIR) and thermal infrared (TIR) regions and arise from the normal modes of vibration of atoms within molecules and crystal lattices. Unlike electronic transitions, which involve changes in electronic energy levels, vibrational transitions correspond to changes in the vibrational energy of chemical bonds and structural groups (Table 3.2).

Fundamental, Overtone, and Combination Vibrations

A molecule containing *N* atoms has 3N-6 normal vibrational modes (for non-linear molecules), each associated with specific stretching or bending motions of bonds. Fundamental vibrations occur when a single mode is excited and typically produce strong absorptions in the mid- and thermal infrared. Higher-energy overtones, meaning multiples of a fundamental frequency, and combination bands, which is simultaneous excitation of two or more modes, appear at shorter wavelengths, especially in the near- and shortwave infrared. For example, hydroxyl (OH) groups show strong fundamental absorptions near 2.7–2.8μm, with weaker overtone bands near 1.4μm. These overtones and combinations extend the diagnostic influence of vibrational processes into the spectral region used by many imaging spectrometers.

Hydroxyl and Water Absorption Features

Hydroxyl ions and molecular water in mineral structures produce prominent vibrational absorption features due to their strong dipole moments. OH stretching vibrations generate distinctive SWIR absorptions, while combinations of OH stretching and bending modes give rise to additional bands at slightly different wavelengths. Molecular water commonly exhibits absorption features near 1.4μm and 1.9μm, which

are widely used in remote sensing to detect hydration and the presence of bound or adsorbed water in minerals, soils, and alteration zones.

Table 3.2. Key vibrational absorption features for geological remote sensing applications

Molecular Group	Wavelength (μ m)	Type	Target Minerals
O-H stretch	2.7–3.0	Fundamental	All hydroxyl-bearing minerals
O-H stretch	1.4	First overtone	Water, hydroxyl groups
Al-OH	2.2	Combination	Kaolinite, muscovite, illite
Mg-OH	2.3	Combination	Chlorite, talc, serpentine
CO_3	2.3–2.5	Asymmetric stretch	Calcite, dolomite
Si-O	9–10	Stretch	Quartz, feldspars, silicates

Silicate and Other Ionic Group Vibrations

In the TIR region (wavelengths 3 μm), fundamental vibrations of larger structural units, such as Si–O bonds in silicate tetrahedra, produce complex absorption features. These so-called Reststrahlen bands arise from coupled stretching and bending motions of Si–O groups and are critical for discriminating among silicate minerals in emissivity spectra. Other anionic groups, including carbonate, sulfate and phosphate, also display characteristic vibrational absorptions that reflect their molecular geometry and bonding environment. The positions and shapes of these features provide key constraints on mineral composition in the SWIR and TIR regions.

Mineral Absorption Features

Different mineral groups exhibit characteristic absorption features that enable their identification through remote sensing [23; 11]. The USGS Spectral Library provides reference spectra for hundreds of minerals acquired under controlled conditions and is widely used as a baseline for mineral identification [68]. Ferrous silicates such as biotite, chlorite, and amphibole show pronounced Fe^{2+} crystal-field absorption features in the near-infrared region (0.8–1.1μm) and Mg-OH/Al-OH combination bands in the SWIR (2.3–2.4μm). Biotite shows Fe^{2+} absorption near 0.9μm and 1.1μm, with Al-OH features near 2.20μm. Chlorite exhibits Mg-OH absorption near 2.32μm and Fe^{2+} features in the visible-NIR region. Amphibole shows similar Fe^{2+} absorption features with variations depending on composition. These minerals are particularly relevant for gold exploration because gold-bearing sulfides such as pyrite and arsenopyrite often develop via sulfidation of ferromagnesian silicates, as hydrothermal fluids replace biotite, chlorite, and amphibole with iron sulfides that can incorporate gold in a refractory form. [77; 78]. The ferrous

silicates ratio (B05/B04) serves as an indirect indicator of zones where sulfidation processes have occurred, complementing direct alteration mineral indices that form halos around sulfide-bearing zones [77; 78] (Table 3.3).

Table 3.3. Characteristic absorption features for key alteration minerals used in remote sensing

Mineral	Absorption Wavelength (μm)	Feature Type	Alteration Zone
Biotite	0.9, 1.1, 2.20	$K(Mg,Fe)_3AlSi_3O_{10}(OH)_2$	Sulfidation zones
Chlorite	0.9, 2.32	$(Mg,Fe)_3(Si,Al)_4\ O_{10}(OH)_2$	Sulfidation zones, propylitic
Amphibole	0.9, 1.1	$Ca_2(Mg,Fe)_5Si_8O_{22}(OH)_2$	Sulfidation zones
Kaolinite	2.17, 2.21	Al-OH doublet	Argillic
Alunite	2.17, 2.21	Al-OH, SO_4	Advanced argillic
Muscovite	2.20	Al-OH	Phyllic
Illite	2.20	Al-OH	Phyllic
Chlorite	2.32	Mg-OH	Propylitic
Epidote	2.33	Fe^{2+}, Al-OH	Propylitic
Calcite	2.33	CO_3	Propylitic
Dolomite	2.32	CO_3	Propylitic

Clay minerals (kaolinite, montmorillonite, illite, muscovite) exhibit Al-OH absorption features near 2.2μm, with variations depending on the specific clay species [11]. Kaolinite shows a doublet absorption near 2.17 and 2.21μm due to the presence of both inner and outer hydroxyl groups, which is a diagnostic feature enabling its discrimination from other clays. Muscovite and illite show single absorption features near 2.20μm, with muscovite typically showing a sharper, deeper feature than illite. Montmorillonite shows a broader, shallower absorption feature near 2.21μm, reflecting its expandable structure and variable interlayer water content. These features are critical for mapping argillic and phyllic alteration zones. The depth and shape of the Al-OH absorption feature can be quantified using band ratios, enabling discrimination of different clay species even with multispectral data [72].

Carbonate minerals (calcite, dolomite) display CO_3 absorption features [71] near 2.33μm (calcite) and 2.32μm (dolomite), with additional features in the thermal infrared. The slight difference in absorption position enables discrimination between calcite and dolomite using hyperspectral data, though multispectral systems like ASTER can detect the presence of carbonates but not always distinguish between species [37]. Carbonates also show absorption features near 2.5μm and in the thermal infrared region (11–12μm), providing additional diagnostic information [43]. Carbonates are important in propylitic

alteration zones and as reactive host rocks for gold mineralization, where they can serve as precipitation sites for gold deposition.

Sulfate minerals exhibit SO_4 absorption features, with alunite showing features near 2.17μm and 2.21μm. The 2.17μm feature is diagnostic for alunite and enables its discrimination from other Al-OH bearing minerals [72]. Jarosite $KFe_3(SO4)_2(OH)_6$ shows similar features but with additional Fe^{3+} absorption in the visible region, producing yellow colors. Gypsum also can show strong water absorption features near 1.4 and 1.9μm, enabling its identification even when mixed with other minerals [68].

3.3 Laboratory-based Reflectance Spectra

Laboratory reflectance spectroscopy provides the physical link between the processes described in the previous section and the spectral signatures observed by remote sensing systems. High-quality laboratory spectra, measured under controlled illumination, viewing geometry, and grain-size conditions, reveal the diagnostic absorption features of minerals and rocks without atmospheric or sensor effects. These spectra form the basis for defining spectral endmembers, interpreting satellite-derived spectra, and building spectral libraries used in spectral matching and classification.

Laboratory Reflectance Spectra of Rock and Mineral Groups

Laboratory spectra of whole rocks illustrate how mineralogical composition, grain size, and texture combine to produce bulk spectral signatures. The reflectance spectra for igneous, sedimentary, and metamorphic rocks, highlighting characteristic trends such as the higher albedo and stronger silica-related features of felsic rocks compared to mafic rocks, and the distinctive carbonate features of limestone and dolomite.

At the mineral scale, spectra are often grouped by mineral class, because each class is characterized by a distinct set of dominant electronic and vibrational absorption processes:

Carbonates

Calcite, dolomite, siderite, etc, as carbonate minerals, exhibit diagnosticCO_3 absorption features near 2.3–2.5μm (Fig. 3.3), with subtle shifts in band position and shape distinguishing individual species. In the thermal infrared, carbonates show characteristic Reststrahlen bands near 11–12μm and lower overall emissivity compared to silicates. Laboratory spectra of carbonates provide reference signatures used to interpret SWIR and TIR satellite data in propylitic alteration zones and carbonate host rocks.

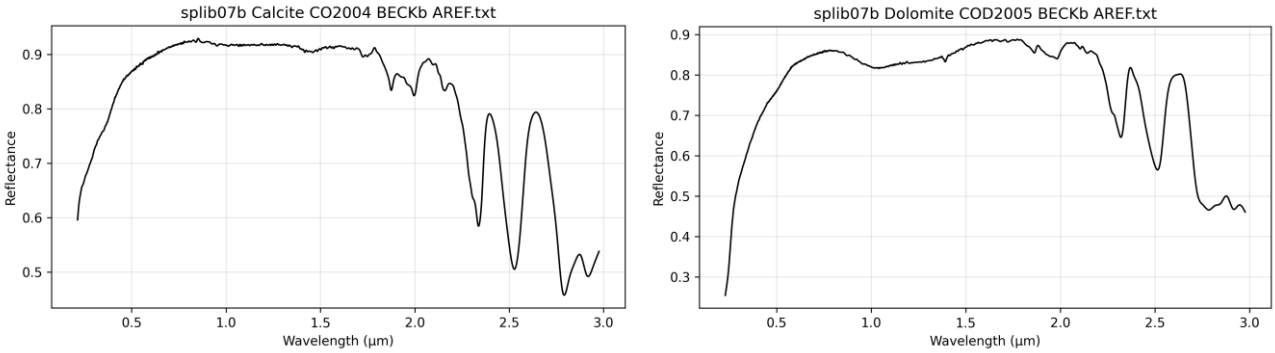

Figure 3.3. USGS spectras of carbonate minerals: left – calcite, right - dolomite

Clays and Phyllosilicates

Clay minerals (kaolinite, illite, montmorillonite) and phyllosilicates (muscovite, chlorite, biotite) show prominent Al-OH and Mg-OH absorption features between 2.1 and 2.4μm, with diagnostic differences in band position, shape, and doublet structure. Laboratory spectra (Fig. 3.4) allow precise discrimination between kaolinite (2.17/2.21μm doublet), muscovite/illite (single 2.20μm feature), and Mg-rich chlorite (2.32μm), providing the foundation for clay-mapping indices and hyperspectral mineral mapping.

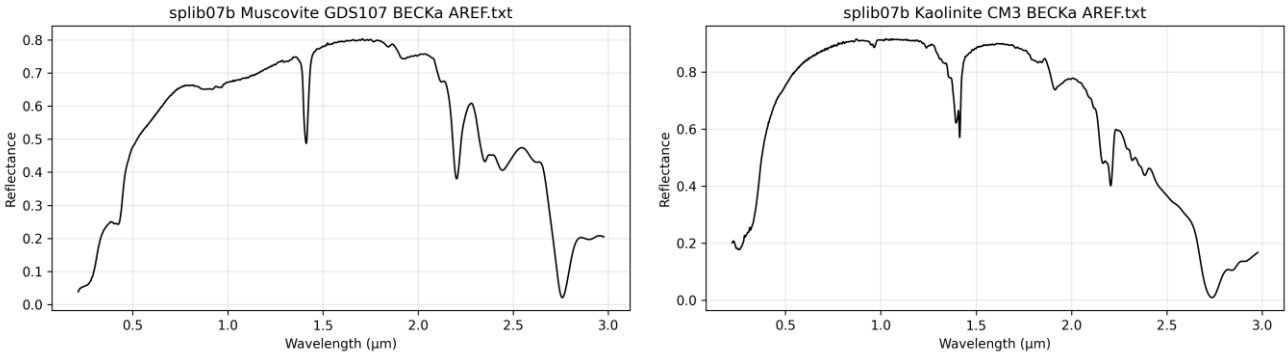

Figure 3.4. USGS spectras of clay-group minerals: left – muscovite, right – kaolinite

Ferrous Silicates and Sulfidation Zones

Ferrous silicates (biotite, chlorite, amphibole) exhibit Fe^{2+} absorption features in the SWIR region, detectable using laboratory reflectance spectroscopy. These minerals show characteristic Fe^{2+} crystal-field transitions near 0.9–1.1μm and Mg-OH/Al-OH combination bands near 2.3–2.4μm, enabling their identification in remote sensing data. Laboratory spectra reveal how variations in Fe^{2+} content, crystal chemistry, and particle size affect absorption depth and continuum shape, providing the foundation for mapping ferrous silicate zones in alteration systems [11].

In gold exploration contexts, in particular, ferrous silicates are important because gold-bearing sulfides (pyrite, arsenopyrite, chalcopyrite) commonly develop during sulfidation of ferromagnesian silicates: hydrothermal fluids replace or overprint biotite, chlorite, and amphibole (Fig. 3.5) with iron sulfides that can host gold in a refractory form [77; 78]. The sulfidation process involves replacement of Fe^{2} bearing silicates by Fe-sulfides, creating zones where ferrous silicate signatures may be preserved in wall-rock halos or replaced by sulfide-bearing assemblages. The ferrous silicates ratio (B05/B04) serves as an indirect indicator of zones where sulfidation processes have occurred, complementing direct alteration mineral indices (sericite, silica, carbonates) that form halos around sulfide-bearing zones [77; 78].

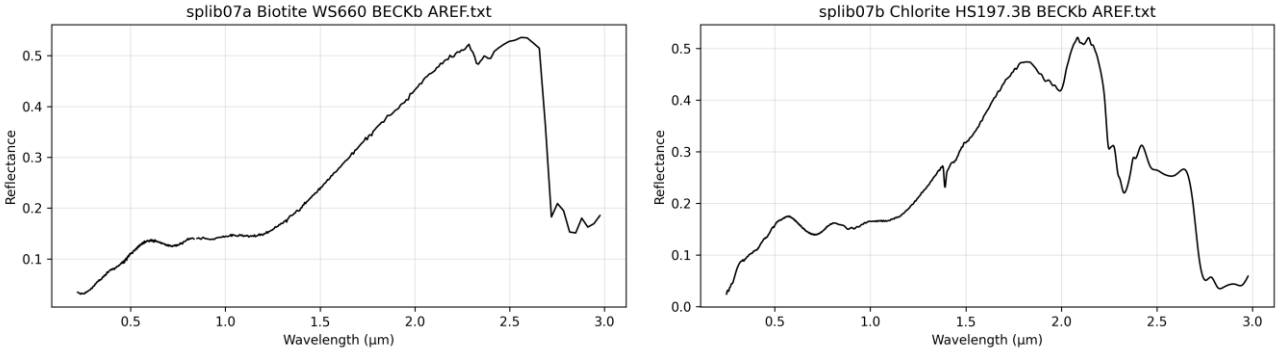

Figure 3.5. USGS spectras of silica minerals: left -biotite, right -chlorite

Ferrous Sulfides

Ferrous sulfides (pyrite FeS_2, arsenopyrite FeAsS, chalcopyrite $CuFeS_2$) are the primary gold-hosting minerals in refractory gold deposits, forming through sulfidation of ferrous silicates (biotite, chlorite, amphibole) where hydrothermal fluids replace Fe^{2+} bearing silicates with Fe-sulfides [77; 78]. Like ferrous silicates, these sulfides contain Fe^{2+}, but in sulfide form rather than silicate form (Fig. 3.6). These sulfides show relatively featureless, metallic-like spectra in the VNIR-SWIR regions, making them spectrally undetectable at ASTER wavelengths 11. Gold-bearing sulfides (pyrite, arsenopyrite) host gold in refractory form as fine inclusions within the sulfide lattice, but their featureless spectra mean that sulfide zones must be inferred from spatial associations with alteration minerals (sericite, silica, carbonates, ferrous silicates) that form halos around ore zones [77; 78]. Laboratory spectra of ferrous sulfides are shown here to illustrate their spectral characteristics and to demonstrate why they cannot be directly detected using ASTER SWIR bands, necessitating indirect detection through associated alteration minerals. Some sulfides show distinct emissivity signatures in the TIR region, though this is not the primary detection method for gold exploration in this study.

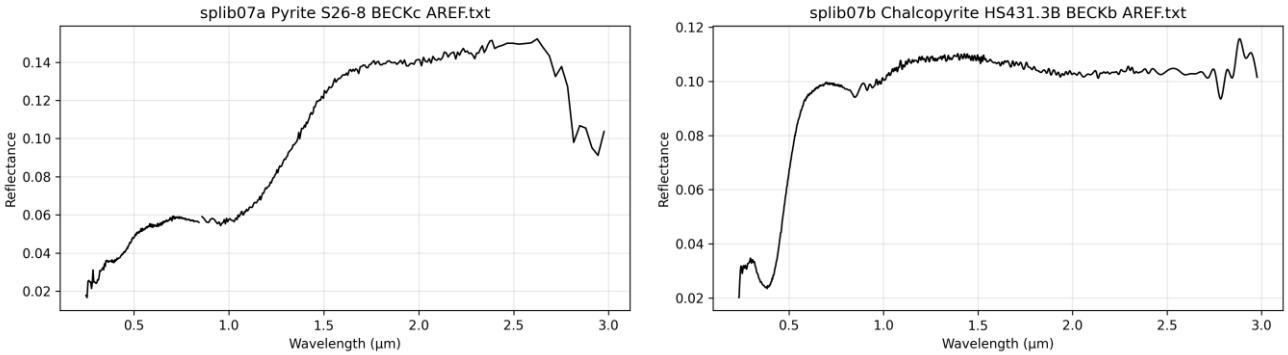

Figure 3.6. USGS spectras of sulfides: left – pyrite, right – chalcopyrite

These spectra illustrate the featureless, metallic-like character of ferrous sulfides in the VNIR-SWIR region, explaining why they are spectrally undetectable at ASTER wavelengths and must be inferred through associated alteration minerals. Ferrous sulfide mineral spectral signatures: Pyrite and Chalcopyrite. These spectra illustrate the featureless, metallic-like character of ferrous sulfides in the VNIR-SWIR region, explaining why they are spectrally undetectable at ASTER wavelengths and must be inferred through associated alteration minerals.

Framework Silicates

Framework silicates (quartz, feldspars) show weak features in the VNIR-SWIR but strong, diagnostic Si-O phonon bands near 8–12μm in the thermal infrared region. Quartz is particularly important in gold deposits as it forms veins and silicification zones that host mineralization, while feldspars are common in host rocks and intrusions. Laboratory spectra (Fig. 3.7) of these groups underpin lithological discrimination in the TIR and enable mapping of silicification zones that are associated with gold mineralization.

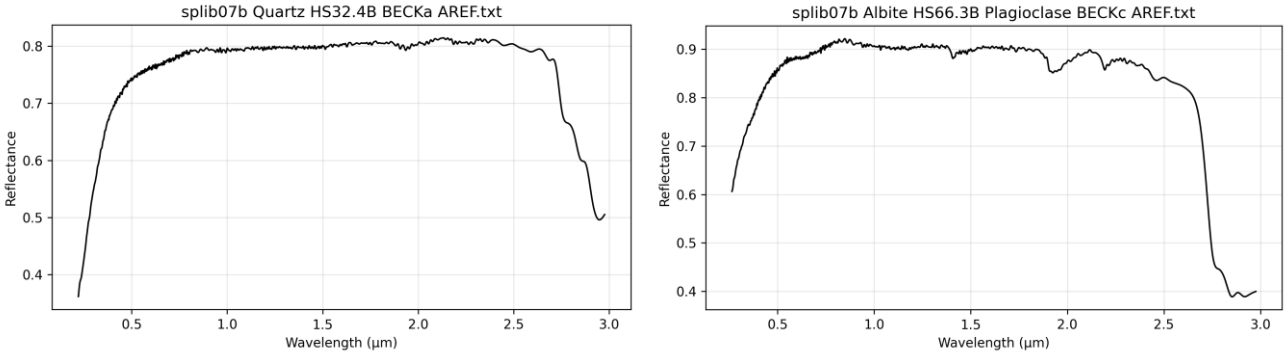

Figure 3.7. USGS spectras of target silicates: left – quartz, right - albite (plagioclase)

Factors Affecting Spectral Signatures

Several factors can modify the spectral signature of a material, complicating mineral identification [11; 21]. Understanding these factors is essential for accurate

interpretation of remote sensing data and for developing robust preprocessing and analysis methods.

Particle size affects the depth and shape of absorption features. Finer particles typically show deeper absorption features due to increased surface area and multiple scattering, which increases the effective path length for absorption. Coarse particles may show reduced absorption depth and shifted absorption positions due to volume scattering effects. The relationship between particle size and absorption depth follows a power law, with absorption depth increasing approximately as the square root of particle size for small particles and saturating for large particles (Fig. 3.8) [21]. This effect is particularly important for clay minerals, where particle size can vary significantly in natural samples, affecting the detectability of Al-OH absorption features [68].

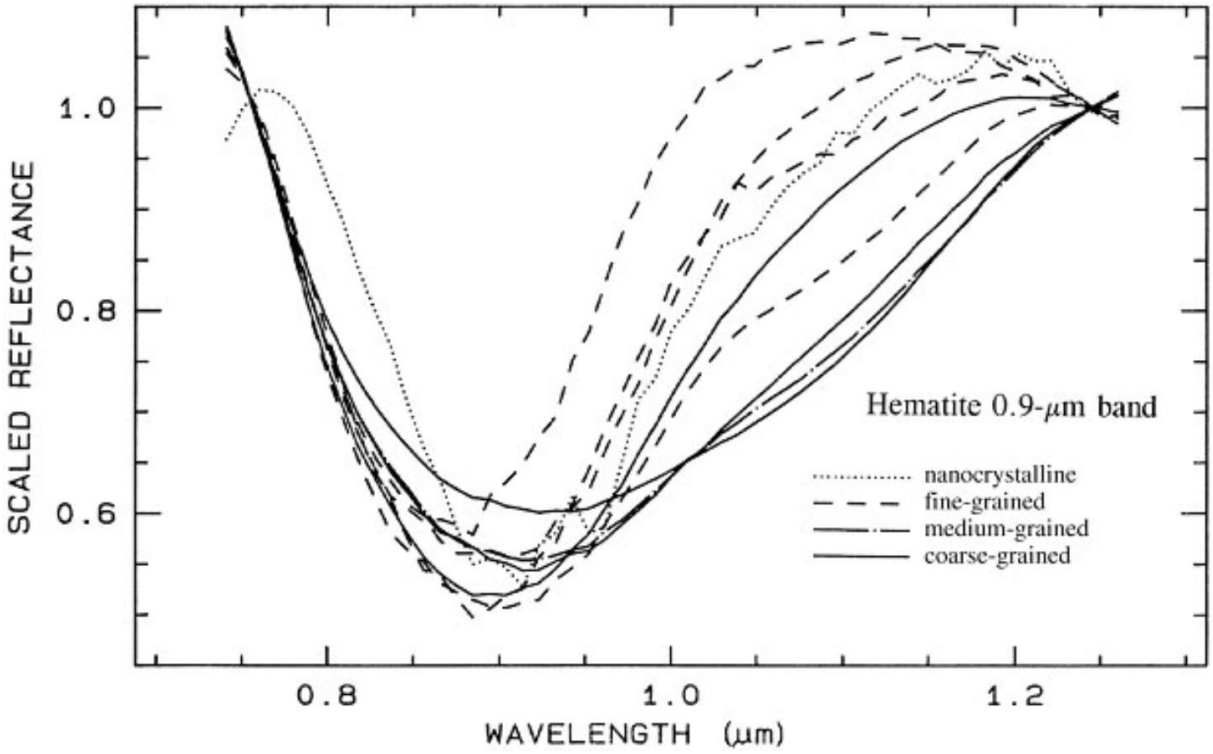

Figure 3.8. Mineral spectra variation based on grain-size

Note – compiled from [80]

Surface roughness influences the angular distribution of reflected radiation [32]. Rough surfaces produce more diffuse reflectance, scattering radiation in all directions, while smooth surfaces produce more specular reflectance, reflecting radiation in a mirror-like fashion. This affects the apparent brightness and spectral shape, particularly when comparing spectra acquired under different illumination and viewing geometries (Fig. 3.9). The bidirectional reflectance distribution function (BRDF) describes how reflectance varies

with these angles, and topographic normalization corrects for these effects in rugged terrain [12].

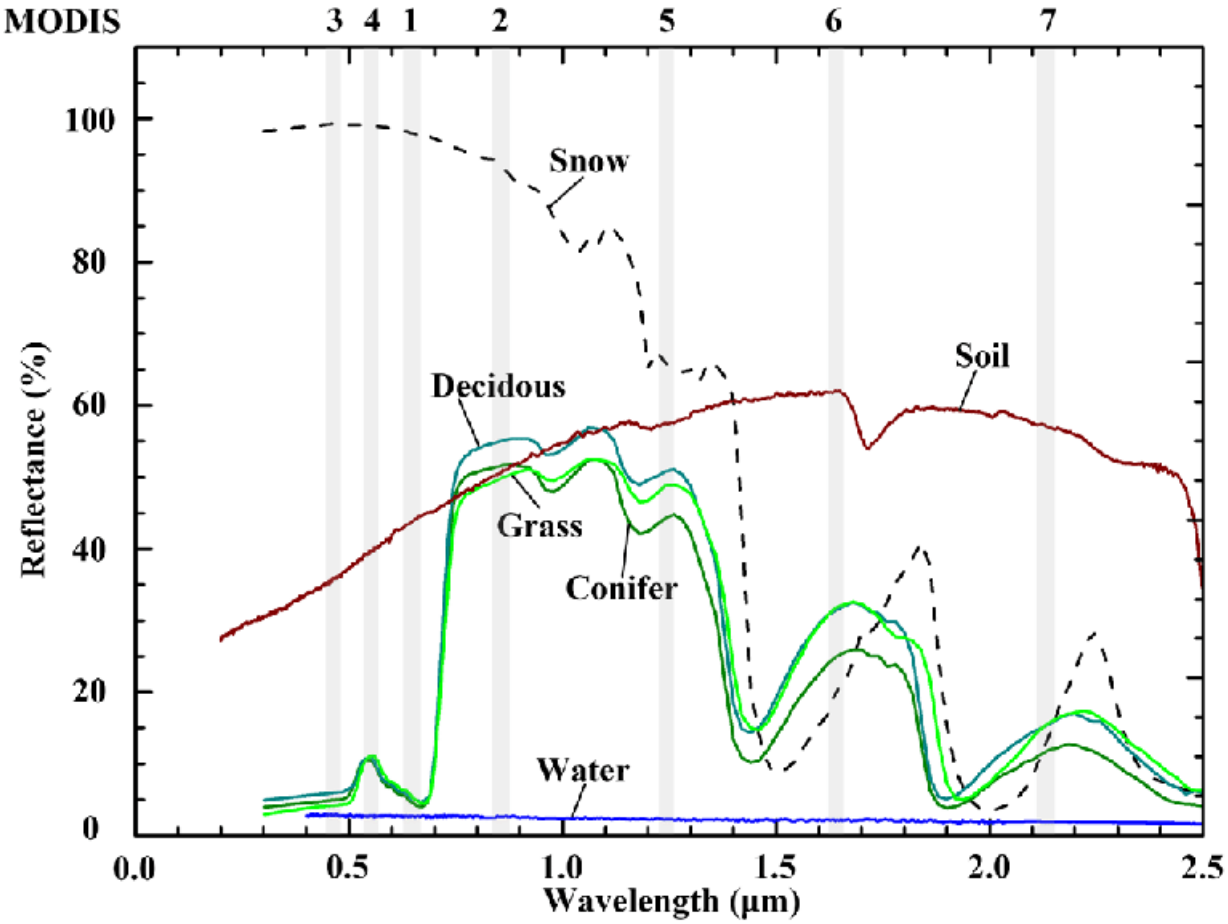

Figure 3.9. Spectral reflectance of snow, soil, vegetation (deciduous, conifer and grass) and water

Note – compiled from [69]

Moisture content significantly affects spectral signatures, particularly in the shortwave infrared region [16]. Water and hydroxyl groups produce strong absorption features near 1.4μm (first overtone of O-H stretching) and 1.9μm (combination of O-H stretching and bending) that can mask or modify mineral absorption features. Soil moisture increases the overall reflectance in the visible region while decreasing reflectance in the SWIR region due to water absorption. Atmospheric water vapor must be considered in spectral analysis, as it creates absorption bands that must be corrected during atmospheric processing [31]. The presence of adsorbed water on mineral surfaces can also modify absorption features, particularly for clay minerals where interlayer water affects the Al-OH absorption feature position and depth [69].

Vegetation cover presents a major challenge for geological remote sensing, as vegetation exhibits strong absorption features (chlorophyll near 0.68μm, water near 1.4

and 1.9μm) that can completely obscure underlying mineral signatures [16]. The red edge, a sharp increase in reflectance between 0.68 and 0.75μm, is a diagnostic feature of vegetation that can be used for masking [27]. Vegetation masking is essential for accurate mineral mapping, typically accomplished using NDVI thresholds or more sophisticated methods that account for sparse vegetation [22; 44]. In areas with partial vegetation cover, spectral unmixing techniques can separate the contributions of vegetation and mineral components [12].

Additional factors include mineral mixtures, where the spectral signature represents a weighted average of component minerals [12]. Linear mixing models assume that the reflectance of a pixel is a linear combination of endmember spectra, weighted by their fractional abundances. Non-linear mixing occurs when minerals are intimately mixed at scales smaller than the pixel size, requiring more complex models [26]. Weathering and alteration can modify mineral spectra over time, with fresh surfaces showing different signatures than weathered surfaces. Atmospheric effects must be corrected to recover surface reflectance.

3.4 Spectral Library Databases

Spectral libraries contain reference spectra of minerals and rocks measured under controlled conditions, providing the foundation for spectral matching, endmember selection, and mineral identification in remote sensing applications. These libraries are essential for validating satellite-derived spectra and for developing region-specific spectral signatures that account for local mineralogical variations. Table 3.4 summarizes widely used libraries.

Table 3.4. Various spectral libraries represented by spectroscopes in laboratory, field-spectroscope, air-, and space-borne instruments

Library	Spectral Range (μm)	Resource	Reference
USGS	0.2–15	Laboratory	USGS [68]
JHU	0.4–14	Laboratory	JHU [88]
DLR/GFZ	0.4–2.5; 8–12	Laboratory	DLR/GFZ lab [89]
ASD/HySpex	0.35–2.5; 0.4–2.5	Field/airborne	HySpex [90]
ECOSTRESS/JPL	0.4–14	Space	ECOSTRESS/JPL [91]

USGS Spectral Library

The USGS Spectral Library is one of the most widely used and comprehensive collections of mineral, rock, vegetation, and man-made material spectra [68]. The library contains spectra of hundreds of minerals measured under controlled laboratory conditions, covering the visible through thermal infrared regions (0.2–15μm). Spectra are measured at high spectral resolution with detailed metadata on sample composition, grain size, and

measurement conditions. The library provides reference spectra for most alteration minerals discussed in this chapter, including kaolinite, alunite, muscovite, chlorite, biotite, amphibole, calcite, dolomite, and many others. The USGS Spectral Library serves as the primary reference for spectral matching algorithms such as Spectral Angle Mapper (SAM) and Spectral Feature Fitting (SFF), and is widely used in both research and operational mineral mapping applications.

Johns Hopkins (JHU) Spectral Library

A classic laboratory collection spanning VNIR–SWIR–TIR for well-characterized minerals and rocks. Frequently used to cross-check USGS endmembers and to assess spectral variability among different sample sets and grain sizes. JHU spectra are often employed where multiple lab sources are compared for consistency of diagnostic absorption positions and shapes.

DLR and GFZ Laboratory Spectra

European institutions, including the German Aerospace Center (DLR) and the Helmholtz Centre Potsdam GFZ German Research Centre for Geosciences (GFZ), maintain state-of-the-art laboratory facilities for measuring high-quality reflectance and emissivity spectra relevant to EnMAP and other European hyperspectral missions. These laboratories provide:

- Mineral and rock spectra measured with instrumentation and spectral sampling similar to EnMAP and other hyperspectral sensors, ensuring compatibility between laboratory reference spectra and satellite data;
- Emissivity spectra in the thermal infrared region for lithological discrimination and thermophysical studies;
- Calibration and validation datasets used to verify sensor performance and atmospheric correction algorithms.

For planar measurements in the laboratory, in the field, or by aircraft, DLR and GFZ utilize hyperspectral line scan cameras from HySpex, including the VNIR-1600 and SWIR-320m-e systems. The HySpex VNIR-1600 provides high-resolution visible and near-infrared spectral imaging (typically 160 bands covering 0.4–1.0μm), while the SWIR-320m-e covers the shortwave infrared region (typically 256 bands covering 1.0–2.5μm). These systems enable detailed spectral characterization of mineral samples and outcrops under controlled illumination conditions. For thermal infrared measurements, the Telops HyperCam longwave provides high-resolution thermal imaging spectroscopy, enabling emissivity measurements in the 8–12μm region critical for lithological discrimination and silica content estimation.

Although not always distributed as formal public libraries on the same scale as the USGS Spectral Library, DLR and GFZ spectral datasets are used extensively in EnMAP calibration/validation activities and in algorithm development for European hyperspectral missions. Together with the USGS library, they provide the laboratory foundation for the spectral analyses and cross-sensor validation described later in this chapter.

Field and Aircraft Spectral Measurements

Field spectra collected using portable spectrometers provide ground truth data for validation, though they may be affected by environmental conditions including variable illumination, atmospheric effects, and surface moisture. Portable field spectrometers, such as the ASD FieldSpec series, provide full-range spectral coverage (0.35–2.5μm) with high spectral resolution, enabling collection of reference spectra directly at field sites. Aircraft-mounted hyperspectral systems, including the HySpex cameras mentioned above, provide intermediate-scale spectral data that bridge the gap between field measurements and satellite observations, enabling validation of satellite-derived spectral signatures at scales relevant to geological mapping (Fig. 3.10).

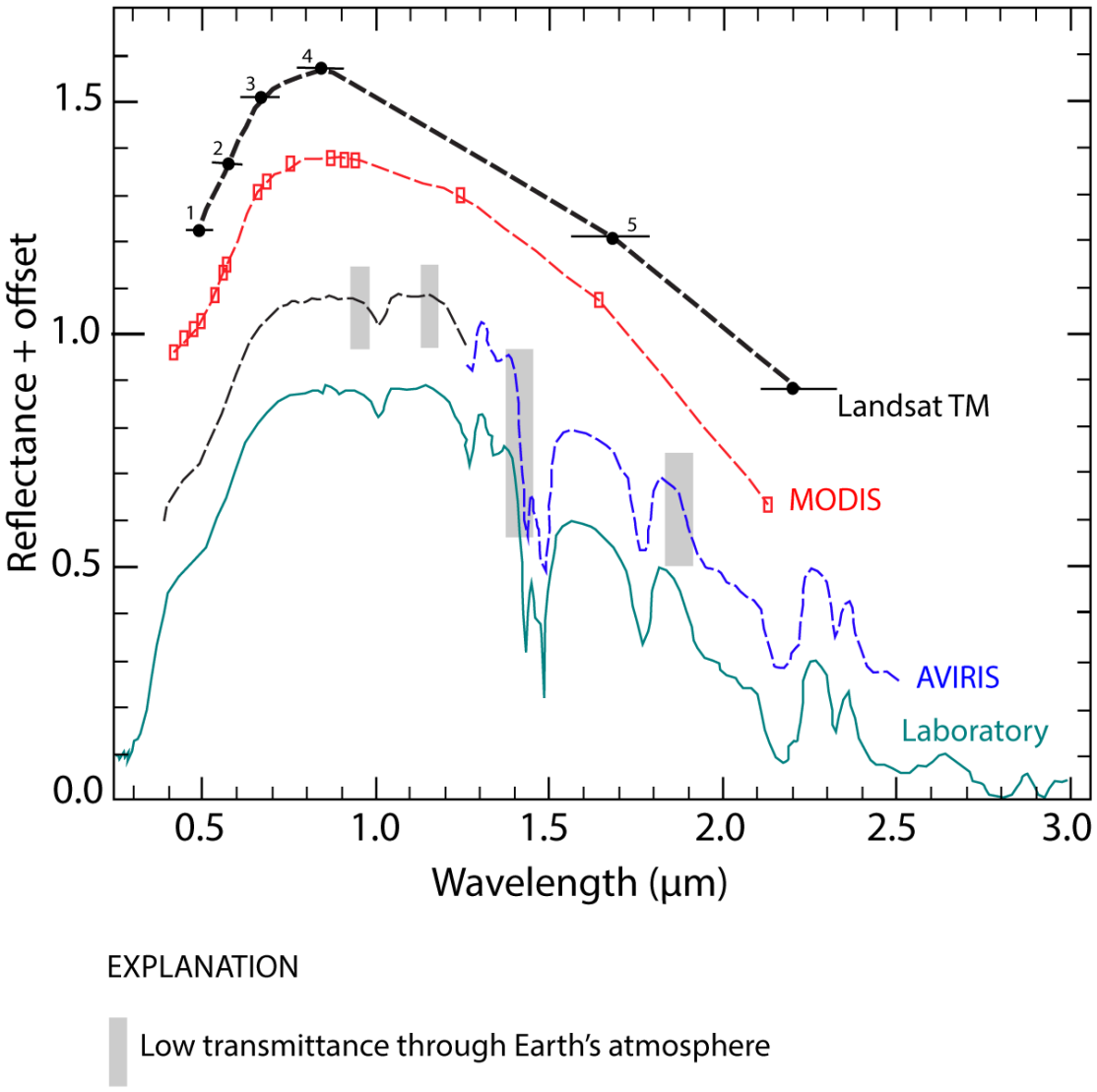

Figure 3.10. Showcase of the atmosphere effect on reflectance amplitude

Note – compiled from [80; 68]

ECOSTRESS/JPL Spectral Library

A sensor-ready spectral library (continuing the ASTER spectral library lineage) with consistent formatting and metadata, enabling direct use in spaceborne workflows. It bridges pure lab spectra and satellite data by providing resampled, quality-controlled spectra suitable for satellite bandpasses (VNIR–SWIR–TIR), easing cross-sensor comparisons and atmospheric correction testing.

3.5 Remote Sensing Spectroscopy missions

The evolution of spaceborne remote sensing for geological applications has progressed from early multispectral systems to current hyperspectral missions (Fig. 3.11), each offering different capabilities for mineral identification and mapping [37; 23]. The Landsat series [41], beginning with Landsat 1 in 1972, provided the first systematic multispectral coverage with four bands in the visible and near-infrared regions [55]. Landsat 4 (1982) introduced the Thematic Mapper with seven bands, including shortwave infrared and thermal infrared capabilities that enabled basic mineral discrimination. The addition of SWIR and TIR bands marked a fundamental advance, enabling detection of hydroxyl-bearing minerals and lithological discrimination [74].

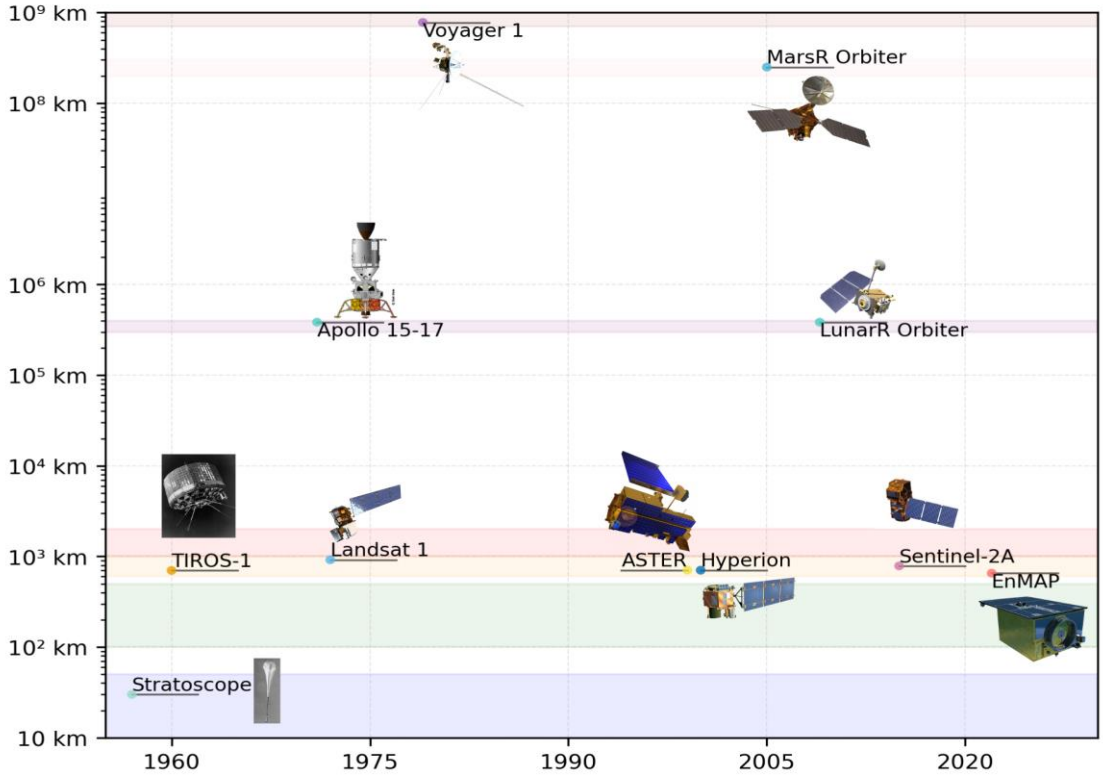

Figure 3.11. Evolution of spectroscopic satellite missions

The Advanced Spaceborne Thermal Emission and Reflection Radiometer (ASTER) represents a significant advancement specifically designed for geological applications

[10]. Recent multispectral systems including Landsat 8/9 (2013, 2021) and Sentinel-2 (2015) offer improved radiometric calibration, higher signal-to-noise ratios, and free data access, though with fewer spectral bands optimized for mineralogy compared to ASTER [46]. Landsat 8's Operational Land Imager (OLI) provides improved calibration and additional bands including a coastal/aerosol band and a cirrus band, while Sentinel-2's MultiSpectral Instrument (MSI) offers high temporal resolution (5-day revisit) and 13 spectral bands at 10–60 m resolution [18]. However, these systems lack the dedicated SWIR bands optimized for mineral identification that make ASTER effective for geological applications.

Hyperspectral missions such as Hyperion (2000) [34], PRISMA (2019), and EnMAP (2022) provide continuous spectral coverage with hundreds of narrow bands, enabling detailed mineral identification but with limited spatial coverage and higher data complexity. Hyperion, launched on NASA's Earth Observing-1 satellite, provided 242 spectral bands across 0.4-2.5μm at 30 m resolution, demonstrating the potential of hyperspectral data for mineral identification [36]. However, Hyperion's limited swath width (7.5 km) and higher noise levels restricted its operational use. PRISMA, launched by the Italian Space Agency, provides 240 spectral bands with improved signal-to-noise ratios and a 30 km swath [33]. EnMAP, launched in 2022, represents the current state-of-the-art with 224 spectral bands, high signal-to-noise ratios, and improved calibration [24].

For hydrothermal alteration mapping and mineral exploration, ASTER remains the most widely used system due to its optimal balance of spectral coverage, spatial resolution, global coverage, and data availability [11]. The following sections provide detailed descriptions of ASTER and EnMAP, the latter serving as a validation tool for spectral signatures derived from ASTER data.

Advanced Spaceborne Thermal Emission and Reflection Radiometer

ASTER is a joint mission of NASA and Japan's Ministry of Economy, Trade and Industry (METI), flown aboard NASA's Terra satellite since its launch in December 1999 [10], shown in Figure 3.12. The instrument is composed of three separate subsystems that operate in different spectral region, each optimized for specific applications (Table 3.5, 3.6) [11]. The Visible and Near-Infrared (VNIR) subsystem operates in three spectral bands with 15-meter spatial resolution and includes a backward-looking band for stereo imaging. The Shortwave Infrared (SWIR) subsystem operates in six spectral bands with 30-meter spatial resolution, specifically designed to detect hydroxyl-bearing minerals and carbonates [42]. The Thermal Infrared (TIR) subsystem operates in five spectral bands with 90-meter spatial resolution, enabling lithological discrimination and silica content estimation [33].

The VNIR subsystem uses silicon charge-coupled device (CCD) detectors and provides bands at 0.52–0.60μm (Band 1), 0.63–0.69μm (Band 2), and 0.76–0.86μm (Band 3N) [11]. Band 3B, viewing backward along the satellite track, enables along-track stereo imaging for digital elevation model generation with a base-to-height ratio of 0.6, providing vertical accuracy of approximately 15–30 meters [20]. The VNIR bands are used for detection of Fe^{2+} crystal-field transitions in ferrous silicates, vegetation mapping, and as reference bands for atmospheric correction 11. The VNIR subsystem has a signal-

to-noise ratio (SNR) exceeding 100 for typical Earth surface conditions, ensuring high-quality data for mineral mapping applications [11].

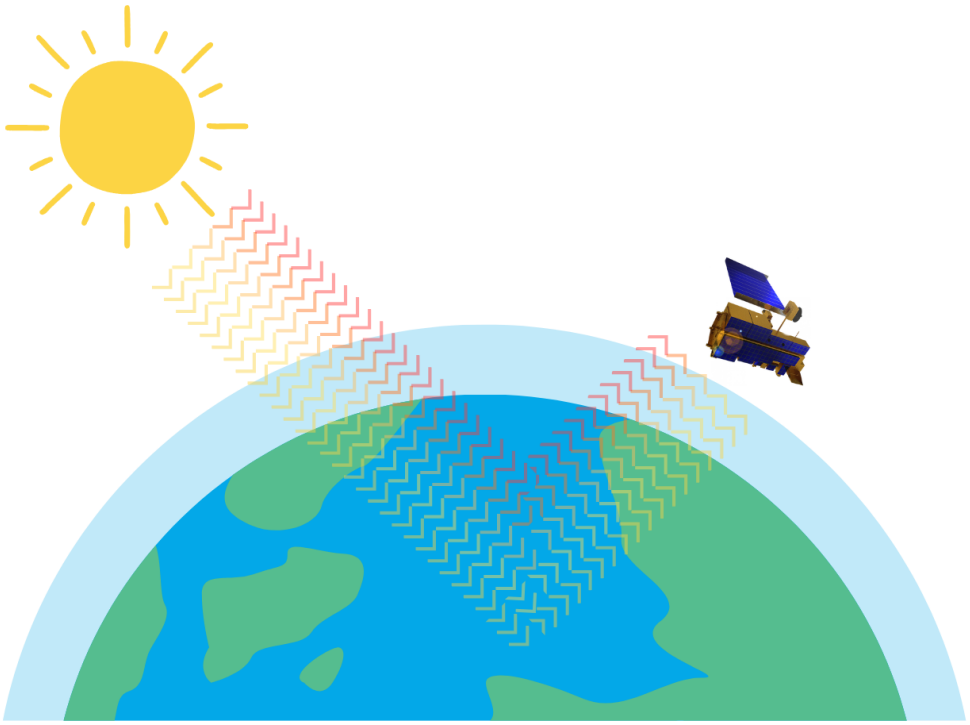

Figure 3.12. Solar radiation passive transfer to ASTER receiver

The SWIR subsystem uses platinum silicide (PtSi) detectors and provides six bands covering 1.600–2.430µm [11]. The band positions are: Band 4 (1.600–1.700µm), Band 5 (2.145–2.185µm), Band 6 (2.185–2.225µm), Band 7 (2.235–2.285µm), Band 8 (2.295–2.365µm), and Band 9 (2.360–2.430µm). These bands are strategically positioned to detect Al-OH absorption features (Band 6 at 2.20µm), Mg-OH absorption features (Band 8 at 2.32µm), and carbonate absorption features (Band 8 at 2.33µm) [42]. The SWIR subsystem experienced crosstalk issues in early data, where radiation from one detector affected adjacent detectors, producing striping artifacts [24]. These issues have been addressed through correction algorithms in Level-1B processing, and the crosstalk correction is now standard in ASTER data products [24].

The TIR subsystem uses mercury cadmium telluride (MCT) detectors and provides five bands covering 8.125–11.65µm: Band 10 (8.125–8.475µm), Band 11 (8.475–8.825µm), Band 12 (8.925–9.275µm), Band 13 (10.25–10.95µm), and Band 14 (10.95–11.65µm) [11]. These bands enable emissivity-based lithological discrimination, with Band 12 positioned near the quartz reststrahlen feature at 9µm, enabling silica content estimation [33]. The TIR subsystem has a noise equivalent temperature difference of less than 0.3 K, ensuring high-quality thermal data for lithological mapping [11]. The Temperature-Emissivity Separation algorithm, developed specifically for ASTER TIR

data, enables separation of temperature and emissivity, providing quantitative lithological information [17].

Table 3.5. ASTER mission and instrument specifications (selected). Values summarized based on Abrams (2015)

Parameter	Value	Notes
Platform	Terra (NASA)	Sun-synchronous, 10:30 LT descending
Launch	Dec 1999	NASA/METI cooperation
Orbit altitude	705 km	Inclination 98.2°
Revisit	16 days (nominal)	On-demand tasking
Swath width	60 km	VNIR/SWIR/TIR
Pointing	pm8.55° (cross-track)	Targeted acquisitions
VNIR spatial resolution	15 m	3 bands + stereo (3B)
SWIR spatial resolution	30 m	6 bands
TIR spatial resolution	90 m	5 bands
VNIR SNR	>100	Reference radiance, 30% albedo
SWIR SNR	>50	Reference radiance, 30% albedo
TIR NEDeltaT	<0.3 K	At 300 K target temperature
Data products	L1A, L1B, L2 (AST_07/08)	Radiance, reflectance, emissivity

Spectral Band Configuration for Geological Applications

The spectral band configuration of ASTER is specifically optimized for geological applications, particularly hydrothermal alteration mapping. The VNIR bands enable detection of Fe^{2+} crystal-field transitions in ferrous silicates through band ratios such as the Band 5/Band 4 ratio emphasizes biotite, chlorite, and amphibole. These ferromagnesian silicates are important in gold exploration because sulfidation commonly converts them into iron sulfides (notably pyrite and arsenopyrite), with hydrothermal fluids replacing or overprinting the original minerals and producing sulfide hosts capable of containing gold in refractory form. [77; 78]. The ferrous silicates ratio serves as an indirect indicator of zones where sulfidation processes have occurred, complementing direct alteration mineral indices (sericite, silica, carbonates) that form halos around sulfide-bearing zones.

Table 3.6. ASTER spectral band characteristics showing wavelength ranges, spatial resolution, and subsystem classification [5]

Subsystem	Band	Spectral Range (μm)	Spatial Resolution (m)
VNIR	1	0.52–0.60	15
	2	0.63–0.69	
	3N	0.76–0.86 (nadir)	
	3B	0.76–0.86 (backward)	
SWIR	5	2.145–2.185	30
	6	2.185–2.225	
	7	2.235–2.285	
	8	2.295–2.365	
	9	2.360–2.430	
TIR	11	8.475–8.825	90
	12	8.925–9.275	
	13	10.25–10.95	
	14	10.95–11.65	

The SWIR bands are positioned to capture key mineral absorption features. Band 6 (2.185–2.225μm) is centered on the Al-OH absorption feature at 2.20μm, enabling detection of clay minerals including kaolinite, alunite, and muscovite. Band 8 (2.295–2.365μm) captures Mg-OH absorption at 2.32μm (chlorite, epidote) and carbonate absorption at 2.33 micrometers (calcite, dolomite). The combination of Bands 5, 6, and 7 enables discrimination of different clay species based on the shape and position of the Al-OH absorption feature.

The TIR bands enable lithological discrimination based on emissivity contrasts. Felsic rocks (high silica content) show lower emissivity in Band 12 due to the quartz reststrahlen feature, while mafic rocks show higher emissivity. The ratio of Band 13 to Band 12 provides a silica index, with higher values indicating higher silica content. Carbonate rocks can be distinguished from silicate rocks using TIR band ratios.

Data Products and Availability

ASTER data are distributed in several processing levels (Fig. 3.13) [11]. Level-1A contains raw, unprocessed instrument data with radiometric and geometric coefficients. Level-1B contains radiometrically calibrated and geometrically corrected data, with radiance values. Level-2 products include surface reflectance (for VNIR and SWIR) and surface emissivity and kinetic temperature (for TIR), derived using atmospheric correction algorithms [11].

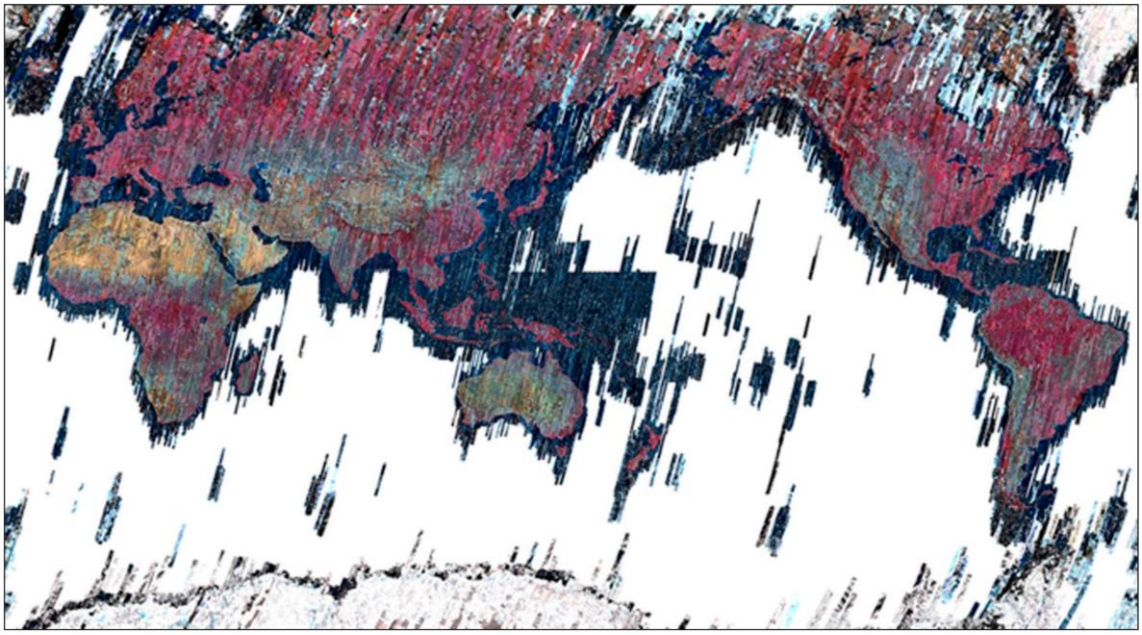

Figure 3.13. ASTER near-global coverage from life-time data acquisition

Note – compiled from [6]

ASTER data are freely available through NASA's Earthdata portal and Japan's ASTER GDS portal [11]. The global archive contains over 3.5 million scenes acquired since 2000, providing comprehensive coverage of Earth's land surface. Data acquisition is on-demand rather than systematic, meaning scenes are acquired based on user requests and cloud cover conditions. This acquisition strategy ensures that data are available for areas of interest while optimizing storage and transmission resources. The ASTER mission has been extended multiple times, with operations continuing through at least 2025, ensuring long-term data availability for geological applications [11].

The ASTER Global Digital Elevation Model (GDEM) provides 30-meter resolution elevation data derived from stereo VNIR pairs, covering land surfaces between 83°N and 83°S [20]. The GDEM has been updated multiple times (GDEM v1, v2, v3), with each version incorporating improvements in accuracy and coverage. The vertical accuracy of GDEM is approximately 20 meters at 95% confidence level, making it suitable for topographic normalization and structural analysis [20]. ASTER Geoscience products include global mineral maps derived from SWIR and TIR data, providing pre-processed alteration indices and lithological classifications [11]. These products enable rapid assessment of alteration zones and lithological units without requiring extensive preprocessing, though custom processing may be needed for specific applications.

Applications to Hydrothermal Alteration Mapping

ASTER's spectral band configuration makes it particularly well-suited for hydrothermal alteration mapping (Fig. 3.14).

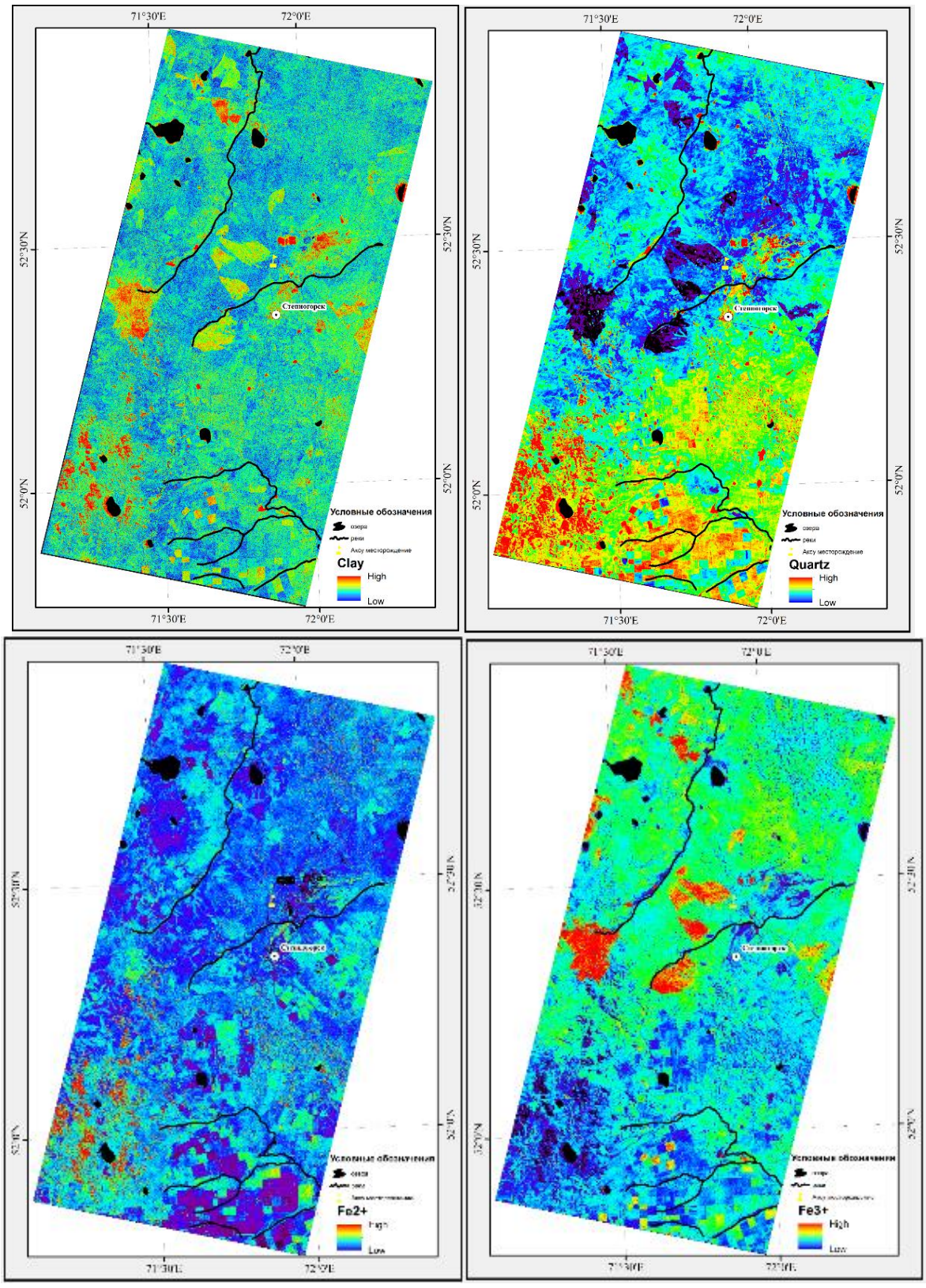

Figure 3.14. Hydrothermal alteration mapping using ASTER: Clay, Quartz, Fe^{2+}, Fe^{3+}

The SWIR bands enable systematic identification of alteration zones associated with porphyry and epithermal deposits:

- Phyllic alteration, characterized by muscovite/sericite, produces strong Al-OH absorption features detectable in Band 6. The muscovite index, calculated as Band 5/Band 6, highlights phyllic alteration zones.

- Argillic alteration, characterized by kaolinite and alunite, also shows Al-OH absorption but with different spectral shapes. Kaolinite exhibits a doublet absorption feature, while alunite shows absorption near 2.17μm. The argillic index, using Bands 5, 6, and 7, enables discrimination of these minerals.

- Propylitic alteration, characterized by chlorite, epidote, and calcite, shows Mg-OH absorption (Band 8) and carbonate absorption (Band 8). The propylitic index combines these features to map propylitic zones.

- Advanced argillic alteration, characterized by alunite and kaolinite, can be identified through specific band ratios targeting the 2.17μm alunite feature.

The combination of these alteration indices, integrated with structural analysis and geological context, enables comprehensive mapping of hydrothermal systems and identification of prospective areas for gold and base metal exploration.

EnMAP: Environmental Mapping and Analysis Program

The Environmental Mapping and Analysis Program (EnMAP) is a German hyperspectral Earth observation mission designed to provide high-quality, regional-scale hyperspectral data needed to address major environmental challenges related to human activities and climate change (Fig. 3.15) [24]. Launched in April 2022 from Florida, USA, aboard a SpaceX Falcon 9 rocket, EnMAP represents the current state-of-the-art in spaceborne hyperspectral imaging for geological and environmental applications. The mission is led by the German Aerospace Center (DLR) and represents a significant advancement in hyperspectral remote sensing capabilities, with improved signal-to-noise ratios, spectral resolution, and calibration compared to earlier hyperspectral missions [24; 19].

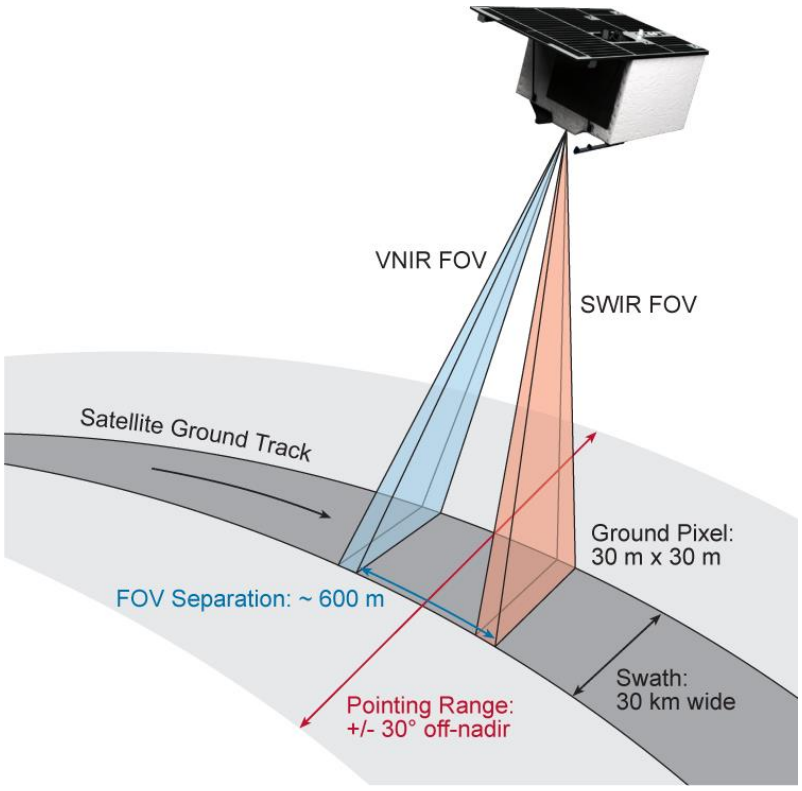

Figure 3.15. EnMAP spacecraft observing principle

Note – compiled from [19]

Instrument Design and Characteristics

EnMAP employs a pushbroom imaging spectrometer design with two separate spectrometers covering the visible-near-infrared (VNIR) and shortwave-infrared (SWIR) spectral regions. The instrument provides 224 spectral bands covering the 0.42–2.45μm spectral range, with a spectral sampling distance of 6.5 nm in the VNIR region (420–1000 nm) and 10 nm in the SWIR region (900–2450 nm) (Table 3.7). The spectral accuracy is 0.5 nm for VNIR and 1.0 nm for SWIR, with spectral stability of 0.5 nm for both regions, ensuring precise and stable spectral measurements critical for mineral identification.

The geometric resolution is 30 m × 30 m with a swath width of 30 km. The instantaneous field of view (IFOV) is 9.5 arcseconds with an integration time of 4.4 ms, and the field of view (FOV) is 2.63 degrees. The instrument can collect data up to 5000 km in length per day, with 512 Gbit on-board mass memory capacity. The modulation transfer function (MTF) specifications ensure high image quality: 0.25 at 60 m across track and 0.16 at 60 m along track, and 0.64 at 240 m across track and 0.62 at 240 m along track [24].

The radiometric resolution is ≥ 14 bits, providing high dynamic range for accurate reflectance measurements. The signal-to-noise ratio (SNR) exceeds 500 at 495 nm in the VNIR region and exceeds 150 at 2200 nm in the SWIR region, referenced to a radiance level representing 30% surface albedo, 30° Sun zenith angle, ground at sea level, and 40

km visibility with rural atmosphere. The radiometric accuracy is 5% with a stability of 2.5% between two consecutive calibrations. Polarization sensitivity is less than 5%, and smile and keystone distortions are maintained below 0.2 pixels, ensuring high geometric and radiometric quality [19].

Table 3.7. Selected EnMAP mission and instrument specifications. Values summarized from Guanter et al., 2015 [19]

Parameter	Value	Notes
Platform	EnMAP (DLR)	Sun-synchronous, 11:00 LT descending node
Launch	Apr 2022	Falcon 9, Florida
Orbit altitude	653 km	Inclination 97.96°
Repeat cycle	27 days (398 rev.)	4-day revisit at pm30° off-nadir
Swath width	30 km	Along-track pushbroom
Pointing	pm30° tilt	Targeted acquisitions
Ground sampling	30 m times 30 m	VNIR/SWIR
Spectral range	0.42–2.45~μ m	224 bands
Spectral sampling	6.5 nm (VNIR), 10 nm (SWIR)	
VNIR SNR	>500 @ 495 nm	Reference radiance
SWIR SNR	>150 @ 2200 nm	Reference radiance
Radiometric resolution	geq14 bit	
MTF	>0.25 (60 m, across-track)	Image quality
Data volume	up to 5000 km/day	512 Gbit on-board memory

The telescope design uses a three-mirror anastigmat configuration with a focal length of 522.4 mm and an aperture of 174 mm in diameter, providing an f-number of 3.0. On-board calibration capabilities include a full aperture diffuser, an integrated sphere with various calibration lamps, and a shutter for dark measurements, ensuring accurate and consistent radiometric calibration throughout the mission lifetime.

Orbit and Platform Specifications

EnMAP operates in a sun-synchronous polar orbit at an altitude of 653 km (semi-major axis of 7021.8 km) with an inclination angle of 97.96°. The orbital period is 5856 seconds, and the orbit repeat cycle is 398 revolutions in 27 days. The local time of the descending node is 11:00 h $\pm$ 18 minutes, providing consistent illumination conditions for data acquisition. The revisit time is 4 days for $\pm$30° off-nadir tilt and 21 days for $\pm$5° off-nadir tilt, providing flexibility for targeted acquisitions while maintaining regular global coverage.

The satellite platform has dimensions of 3.1 m $\times$ 2.0 m $\times$ 1.7 m with a launch mass of 980 kg (including 55 kg hydrazine for orbit control). The power system provides

nominal 32 V with 6.1 m² solar panels delivering 970 W at end of life (EOL), and Li-Ion battery cells with 2 modules providing 87 Ah capacity at EOL. The operational lifetime is designed to exceed 5 years.

The attitude control system is three-axis stabilized using star sensors, sun presence sensors, magnetometer, and gyroscope for attitude determination, with GPS for navigation. Actuators include reaction wheels and magnetic torquers, with 2 thrusters providing 1 N each for orbit control. The pointing system provides accuracy better than 500 m with knowledge better than 100 m, stability better than 1.5 m in 4 ms, and agility of 30° in 5 minutes with pointing stabilization.

Communication capabilities include S-band uplink at 4 kbit/s, S-band downlink at 32 kbit/s, and X-band downlink at 320 Mbit/s, enabling efficient data transmission for the large hyperspectral datasets.

Spectral Resolution and Capabilities

EnMAP's high spectral resolution enables identification of specific mineral species rather than mineral groups, representing a significant advancement over multispectral systems. The VNIR spectrometer provides 96 bands from 0.42 to 1.0μm, while the SWIR spectrometer provides 148 bands from 1.0 to 2.45μm, providing continuous spectral coverage across the entire range.

The high spectral resolution enables discrimination of spectrally similar minerals that cannot be resolved with multispectral systems like ASTER. For example, while ASTER can detect the presence of clay minerals through Al-OH absorption, EnMAP can distinguish between kaolinite, montmorillonite, illite, and muscovite based on subtle differences in their absorption feature positions and shapes. Similarly, EnMAP can discriminate between different carbonate species (calcite vs. dolomite) and ferrous silicate species (biotite vs. chlorite vs. amphibole) with higher confidence than multispectral systems.

The continuous spectral coverage eliminates the need for band ratio indices, allowing direct spectral matching against reference libraries. Spectral feature fitting and spectral angle mapper techniques can be applied to identify specific minerals and estimate their abundances. The high spectral resolution also enables detection of rare earth element (REE) signatures and other subtle spectral features that are not accessible with multispectral data.

The geometric co-registration accuracy is better than 0.2 pixels at Level 1C, ensuring precise alignment between VNIR and SWIR data for accurate spectral analysis across the full wavelength range.

EnMAP's hyperspectral capabilities enable diverse scientific applications across geology, soil science, vegetation monitoring, and cryosphere studies. Fig. 3.16 illustrates exemplary reflectance spectra for different applications, including soils with organic matter and clay minerals, alteration minerals (kaolinite, alunite, white mica), vegetation in various states (healthy, senescent, sparse, forest), and snow, ice, and water. The high spectral resolution enables identification of characteristic absorption features for each

material type, demonstrating the instrument's versatility for environmental and geological applications [25].

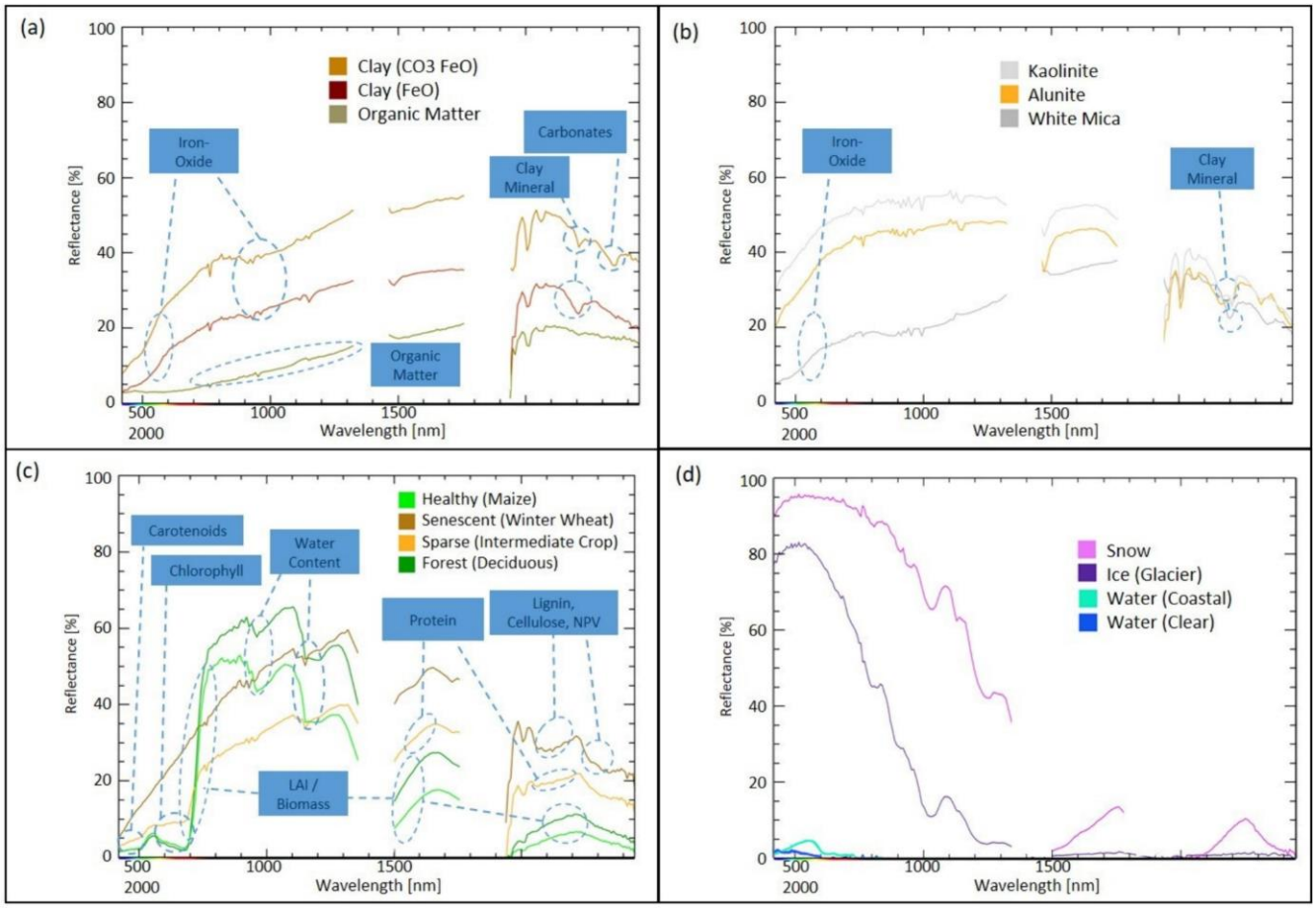

Figure 3.16. Various exemplary reflectance spectra representing different scientific applications: a) Soils, b) Minerals, c) Vegetation, and d) snow, ice and water. Important characteristic features of interest are highlighted with circles. The spectra were extracted directly from original EnMAP L2A products

Note – compiled from [25]

Spectral Band Specifications

The EnMAP instrument provides 224 spectral bands distributed across two spectrometers. The VNIR spectrometer covers bands 1–91 (418–993 nm), while the SWIR spectrometer covers bands 1–133 (902–2445 nm) in the SWIR numbering system.

The VNIR bands show FWHM values ranging from 5.80 nm (minimum at bands 15–16) to 10.75 nm (maximum at bands 88–89), with a general trend of increasing bandwidth toward longer wavelengths. The SWIR bands show FWHM values ranging from 7.16 nm (band 133) to 11.43 nm (bands 31–35), with peak bandwidths in the 1200–1300 nm region and decreasing bandwidths toward longer wavelengths. Notable spectral

gaps occur in the SWIR region at 1390–1461 nm (between bands 44-45) and 1759-1939 nm (between bands 72–73) due to strong atmospheric water vapor absorption, which prevents useful surface reflectance measurements in these regions.

The EnMAP spectral response functions (SRF) provided here correspond to band averages over illuminated pixels and are representative of Level-1B datatakes from March 2023. Small central wavelength differences are expected for other time periods due to instrument calibration variations and smile effects. For a specific EnMAP product, users should always refer to the product metadata, where the average SRFs and smile information are stored. This ensures accurate spectral matching and mineral identification, as small wavelength shifts can affect the position of absorption features relative to band centers.

Use for Spectral Signature Validation

EnMAP data serve as a validation tool for spectral signatures derived from ASTER data in this study. The methodology involves a systematic cross-sensor validation approach:

First, ASTER-derived alteration indices and mineral maps are generated for the study area using band ratio techniques. These maps identify zones of phyllic, argillic, and propylitic alteration based on ASTER's multispectral capabilities, providing initial alteration zone classifications.

Second, EnMAP hyperspectral data are acquired for the same area, providing continuous spectral coverage with 224 bands. Spectral libraries are developed from EnMAP data by extracting spectra from pixels identified as alteration zones in the ASTER maps, ensuring spatial correspondence between the two datasets.

Third, the EnMAP spectra are compared against reference spectral libraries (e.g., USGS Spectral Library) to identify specific mineral species present in each alteration zone. The high spectral resolution of EnMAP enables precise mineral identification, confirming whether the ASTER-derived alteration classifications correspond to the expected mineral assemblages. For example, phyllic alteration zones identified from ASTER should contain muscovite or sericite, which can be confirmed through EnMAP's ability to distinguish these specific minerals.

Fourth, the spatial distribution of minerals identified from EnMAP data is compared with the ASTER-derived alteration maps to assess accuracy and identify any misclassifications or areas where ASTER's limited spectral resolution prevents accurate mineral identification. This comparison quantifies the accuracy of ASTER classifications and identifies limitations where hyperspectral data provide additional information.

This cross-sensor validation approach ensures that ASTER-derived spectral signatures are geologically meaningful and that the alteration mapping methodology produces reliable results for mineral exploration targeting. The validation process also helps identify areas where ASTER's multispectral capabilities are sufficient for alteration mapping versus areas where hyperspectral data provide significant advantages for detailed mineral identification.

3.6 Image Preprocessing

Atmospheric Correction. Atmospheric correction is essential for converting at-sensor radiance to surface reflectance, removing the effects of atmospheric scattering and absorption. The at-sensor radiance (L_{sensor}) can be expressed as:

$$L_{\text{sensor}} = L_{\text{path}} + \frac{\rho}{1-\rho S}\frac{E_0 \cos(\theta_s) T}{\pi}, \tag{3.5}$$

where L_{path} is path radiance, ρ is surface reflectance, S is spherical albedo, E_0 is solar irradiance, θ_s is solar zenith angle, and T is atmospheric transmittance. Atmospheric correction inverts this relationship to recover surface reflectance from at-sensor radiance.

The Fast Line-of-sight Atmospheric Analysis of Spectral Hypercubes (FLAASH) algorithm is commonly used for ASTER data [21]. FLAASH uses the MODTRAN radiative transfer model to estimate atmospheric properties including water vapor, aerosols, and visibility, then applies corrections to derive surface reflectance [Berk et al., 2006]. The algorithm estimates water vapor content from the 1.13μm and 1.38μm absorption features, aerosol optical depth from dark pixels, and visibility from the scene itself [21]. FLAASH has been validated extensively and produces surface reflectance with accuracy better than 5% for typical Earth surface conditions [21].

The Atmospheric and Topographic Correction (ATCOR) algorithm provides an alternative approach, incorporating topographic correction simultaneously with atmospheric correction. ATCOR uses a digital elevation model to account for slope and aspect effects, which is particularly important in rugged terrain where topographic effects can significantly bias spectral indices [17]. The algorithm models the bidirectional reflectance distribution function (BRDF) to account for viewing geometry effects, improving accuracy in areas with complex topography.

For ASTER SWIR data, atmospheric water vapor absorption bands near 1.4 and 1.9 μm must be carefully handled, as these wavelengths are strongly affected by atmospheric conditions [21]. The correction process estimates water vapor content from the depth of absorption features and removes its effects to recover surface reflectance. However, these wavelengths are often unusable due to strong atmospheric absorption, particularly in humid conditions. The ASTER SWIR bands are positioned to avoid the strongest water vapor absorption features, enabling reliable surface reflectance retrieval [11].

Additional atmospheric correction methods include the 6S (Second Simulation of the Satellite Signal in the Solar Spectrum) algorithm, which provides a simplified radiative transfer model suitable for multispectral data [53]. Dark object subtraction methods estimate path radiance from dark pixels (typically water or shadow) and subtract it from all pixels, providing a simple correction method though less accurate than radiative transfer models [15].

Topographic Normalization

Topographic normalization corrects for illumination variations caused by slope and aspect, which can bias spectral indices in rugged terrain [17; 51]. In areas with significant relief, pixels on sun-facing slopes receive more illumination than pixels on shadowed slopes, creating brightness variations that are unrelated to surface composition. These variations can mask or create false spectral signatures, complicating mineral identification [17].

The C-factor correction method calculates a correction factor based on the cosine of the solar incidence angle, which varies with slope and aspect [17]. The solar incidence angle (i) is calculated as:

$$\cos(i) = \cos(\theta_s)\cos(\theta_n) + \sin(\theta_s)\sin(\theta_n)\cos(\phi_s - \phi_n), \tag{3.6}$$

where θ_s is solar zenith angle, θ_n is slope angle, ϕ_s is solar azimuth, and ϕ_n is aspect angle [17]. This correction ensures that similar materials show similar spectral signatures regardless of their topographic position.

Digital elevation models derived from ASTER stereo pairs or SRTM data are used to calculate slope and aspect [20]. The solar azimuth and elevation angles are obtained from the image metadata. The normalized reflectance (ρ_{norm}) is calculated as:

$$\rho_{\text{norm}} = \rho_{\text{obs}} \frac{\cos(i)}{\cos(e)}, \tag{3.7}$$

where ρ_{obs} is the observed reflectance, i is the solar incidence angle, and e is the solar elevation angle [17]. This simple correction assumes Lambertian reflectance, which may not hold for all surfaces but provides reasonable results for most geological applications [17].

More sophisticated topographic normalization methods account for non-Lambertian reflectance using the Minnaert correction, which includes a parameter (k) that describes the degree of non-Lambertian behavior [31]. The Minnaert correction is expressed as:

$$\rho_{\text{norm}} = \rho_{\text{obs}} \left(\frac{\cos(e)}{\cos(i)}\right)^k, \tag{3.8}$$

where $k = 1$ corresponds to Lambertian reflectance and $k < 1$ indicates increasing non-Lambertian behavior [17]. The Minnaert parameter can be estimated from the data itself or set based on surface type, with typical values ranging from 0.5 to 1.0 for geological surfaces [17].

Radiometric Calibration

Radiometric calibration converts digital numbers to physical units of radiance or reflectance. The calibration coefficients are embedded in the data headers and applied during Level-1B processing.

For TIR data, calibration converts radiance to brightness temperature using Planck's law, then to emissivity using the Temperature-Emissivity Separation (TES) algorithm. The TES algorithm exploits the relationship between minimum emissivity and the range of emissivity values to separate temperature and emissivity.

Geometric Correction

Geometric correction ensures accurate georeferencing and alignment with other spatial datasets. ASTER Level-1B data are provided in a standard map projection (typically UTM) with geometric correction applied using ground control points and the satellite's ephemeris data. The geometric accuracy is typically better than 50 meters, which is sufficient for regional-scale geological mapping.

For integration with other datasets, additional geometric correction may be required to improve alignment. Image-to-image registration can be performed using tie points between ASTER and reference datasets such as Landsat or high-resolution imagery.

3.7 Spectral Transformations and Indices

Normalized Difference Vegetation Index (NDVI)

The Normalized Difference Vegetation Index (NDVI) is calculated as:

$$\mathrm{NDVI} = \frac{\rho_{\mathrm{NIR}} - \rho_{\mathrm{Red}}}{\rho_{\mathrm{NIR}} + \rho_{\mathrm{Red}}}, \tag{3.9}$$

where ρ_{NIR} is the near-infrared reflectance and ρ_{Red} is the red reflectance. For ASTER, NDVI uses Band 3 (NIR) and Band 2 (red). NDVI values range from -1 to +1, with values greater than 0.3 typically indicating vegetation.

NDVI is used for vegetation masking in geological applications, as vegetation can completely obscure underlying mineral signatures. Pixels with NDVI values above a threshold (typically 0.2–0.3) are masked out before mineral mapping. NDVI also provides information about vegetation health and density, which can be useful for environmental monitoring.

Band Ratios for Geological Applications

Band ratios are fundamental tools for geological remote sensing, enabling detection of mineral absorption features and discrimination of different mineral groups [42; 87]. Ratios highlight absorption features by dividing bands on either side of an absorption feature (Table 3.8), creating indices that are relatively insensitive to illumination variations and surface roughness [70; 42].

Ferrous Silicates and Sulfidation Zone Indices

Ferrous silicate indices detect Fe^{2+} bearing silicates (biotite, chlorite, amphibole) through band ratios that highlight crystal-field absorption features [87. The ferrous silicates index uses Band 5/Band 4 (B05/B04), highlighting Fe^{2+} absorption in the SWIR region (0.9–1.1μm) [87]. Higher values indicate stronger Fe^{2+} absorption, characteristic of biotite, chlorite, and amphibole. These minerals are particularly relevant for gold

exploration because gold-bearing sulfides (pyrite, arsenopyrite, chalcopyrite) commonly form through sulfidation of ferromagnesian silicates, where hydrothermal fluids replace or overprint biotite, chlorite, and amphibole with Fe-sulfides that host gold in refractory form [77; 78]. The ferrous silicates ratio therefore serves as an indirect indicator of zones where sulfidation processes have occurred, complementing direct alteration mineral indices (sericite, silica, carbonates) that form halos around sulfide-bearing zones [77; 78]. The combination of ferrous silicate indices with alteration mineral indices enables comprehensive mapping of sulfidation zones and identification of prospective areas for gold exploration targeting.

Clay Mineral Indices

Clay mineral indices target Al-OH and Mg-OH absorption features in the SWIR region [42]. The Al-OH index, calculated as (Band 5 + Band 7) / Band 6, highlights minerals with Al-OH absorption near 2.20μm, including kaolinite, alunite, and muscovite [42]. The index uses bands on either side of the absorption feature (Bands 5 and 7) divided by the band at the absorption position (Band 6), creating high values where Al-OH absorption is present. The Mg-OH index, calculated as Band 8 / Band 6, highlights minerals with Mg-OH absorption near 2.32μm, including chlorite and epidote [42]. The combination of Al-OH and Mg-OH indices enables discrimination of different clay species and mapping of alteration zones. Kaolinite can be distinguished from muscovite using the kaolinite index, which uses Bands 4, 6, and 7 to detect the doublet absorption feature characteristic of kaolinite [72].

Carbonate Indices

The carbonate index targets CO_3 absorption near 2.33μm using Band 8 / Band 7 [42]. This index highlights calcite and dolomite, which are important in propylitic alteration zones and as reactive host rocks. Higher values indicate stronger carbonate absorption, enabling mapping of carbonate-rich lithologies and alteration zones. Carbonate rocks can also be distinguished in the TIR region using emissivity differences, with carbonates showing lower emissivity near 11–12μm compared to silicates [43]. The combination of SWIR and TIR carbonate indices provides robust identification of carbonate minerals.

Silica Indices

Silica indices use TIR bands to estimate silica content [33]. The quartz index uses Band 13 / Band 12, exploiting the quartz reststrahlen feature near 9μm [33]. Higher values indicate higher silica content, enabling discrimination of felsic from mafic rocks. The silica index can be calibrated against known rock compositions to provide quantitative estimates of SiO_2 content [33]. The index has been validated against laboratory measurements and geological maps, showing good correlation with actual silica content [33]. The combination of silica index with other TIR indices enables comprehensive lithological mapping based on rock composition.

Table 3.8. Standardized band ratio for ASTER remote sensing [87; 38]

Target	Formula	Target Feature	Application
Ferrous Silicates	B5/B4	Fe^{2+} in silicates	Biotite, chlorite, amphibole (sulfidation zones)
Ferrous Iron	B3/B2	Fe^{2+} absorption	Magnetite, ferrous silicates
Al-OH	(B5+B7)/B6	Al-OH at 2.20μm	Clay minerals, phyllic alteration
Mg-OH	B8/B6	Mg-OH at 2.32μm	Chlorite, epidote, propylitic
Carbonate	B8/B7	CO_3 at 2.33μm	Calcite, dolomite
Quartz	B13/B12	Quartz reststrahlen	Silica content, felsic rocks
Muscovite	B5/B6	Al-OH in muscovite	Phyllic alteration
Kaolinite	(B4+B6)/B7	Al-OH doublet	Argillic alteration

3.8 Hydrothermal Alteration Indices

Hydrothermal alteration zones are characterized by distinct mineral assemblages that reflect the temperature, pressure, and fluid composition conditions during alteration [79; 49]. The spatial distribution of alteration zones follows predictable patterns in porphyry (Fig 3.17), epithermal and magmatic systems (Fig. 3.18), with phyllic alteration typically surrounding the core, argillic alteration in intermediate zones, and propylitic alteration forming the outer halo. Remote sensing enables systematic mapping of these alteration zones using spectral indices that target characteristic mineral absorption features [42].

Phyllic Alteration

Phyllic alteration is characterized by muscovite/sericite, which shows strong Al-OH absorption near 2.20μm [42]. The muscovite index is calculated as Band 5 / Band 6, with high values indicating phyllic alteration [42]. Phyllic zones typically surround the core of porphyry systems and are important indicators of hydrothermal activity. The muscovite index has been validated against field observations and petrographic analysis, showing good correlation with phyllic alteration zones in porphyry copper deposits [88; 44]. The index can be combined with other indices to create composite alteration maps that show the spatial distribution of phyllic zones relative to other alteration types.

Argillic Alteration

Argillic alteration includes kaolinite and alunite, which also show Al-OH absorption but with different spectral characteristics [42]. The argillic index uses (Band 5 + Band 7) / Band 6, with modifications to distinguish kaolinite (doublet absorption near

2.17 and 2.21μm) from alunite (single absorption near 2.17μm) [72]. Kaolinite can be distinguished using the kaolinite index, which targets the doublet feature characteristic of kaolinite [72]. Alunite shows absorption near 2.17μm due to SO_4 groups, enabling its identification using specific band ratios [72]. Argillic alteration is common in epithermal and porphyry systems, where it forms intermediate alteration zones between phyllic and propylitic zones. Advanced argillic alteration, characterized by alunite and kaolinite, is particularly important as it is associated with high-sulfidation epithermal deposits and porphyry systems with advanced argillic caps [49].

Propylitic Alteration

Propylitic alteration includes chlorite, epidote, and calcite, showing Mg-OH and CO_3 absorption features [42]. The propylitic index combines Band 8 / Band 6 (Mg-OH) and Band 8 / Band 7 (carbonate) to map propylitic zones [42]. Chlorite shows Mg-OH absorption near 2.32μm, while epidote shows similar features with additional Fe^{2+} absorption in the visible region [42]. Calcite and dolomite show CO_3 absorption near 2.33μm, enabling their detection using carbonate indices [42]. Propylitic alteration typically forms the outer halo of hydrothermal systems, representing the lowest temperature alteration zone. The propylitic index has been validated against field observations, showing good correlation with propylitic alteration zones in porphyry and epithermal systems [72].

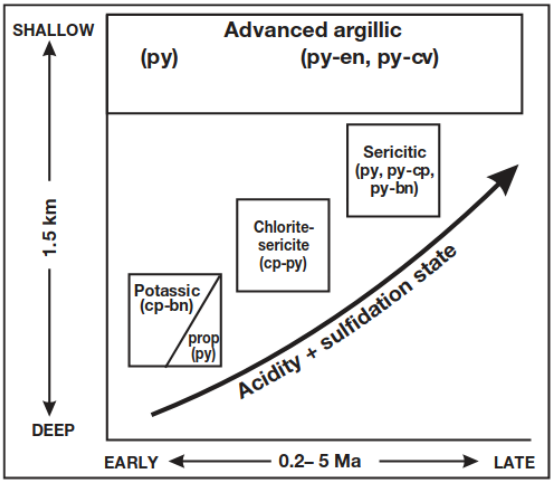

Figure 3.17. Schematic representation of generalized alteration-mineralization sequence in porphyry Cu systems in relation to paleodepth and system life span

Note – compiled from [44]

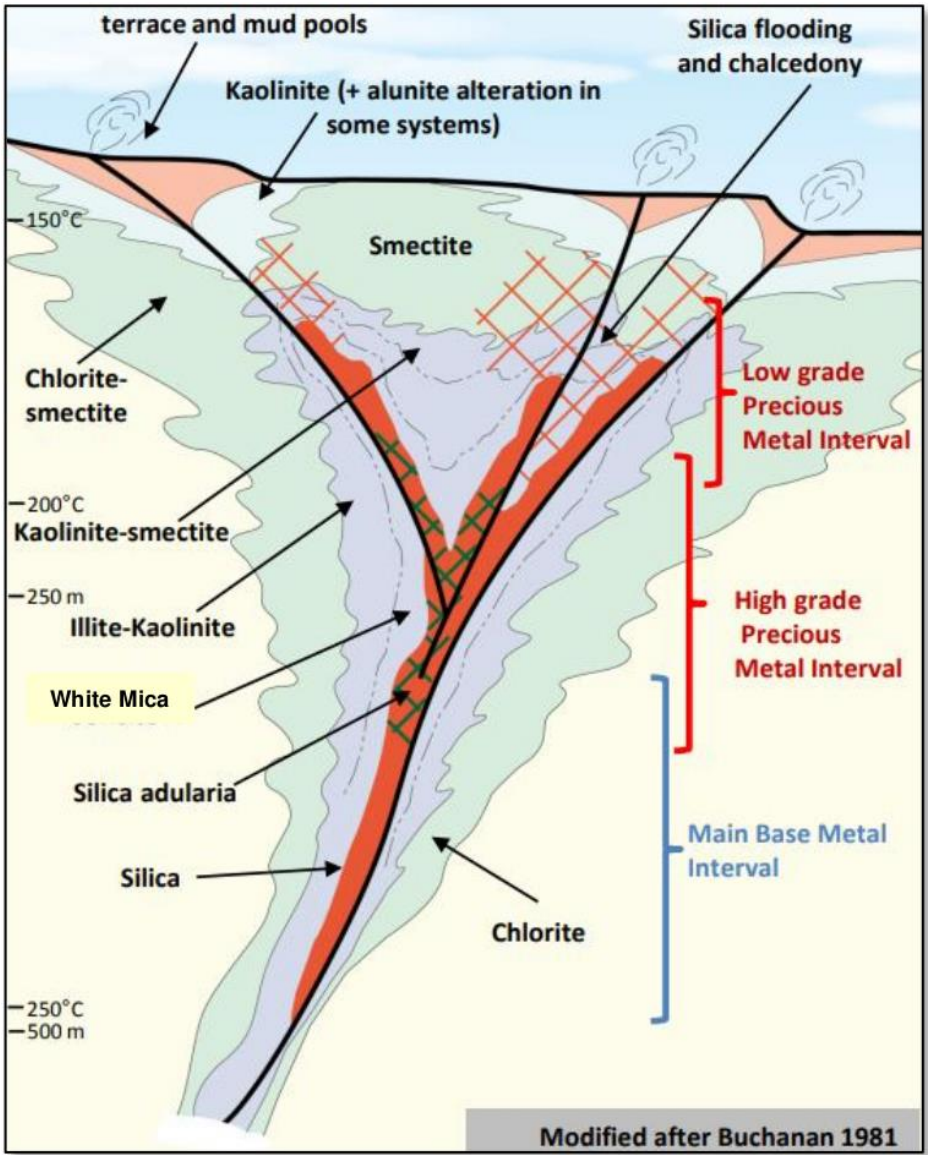

Figure 3.18. Low-sulfadation gold-silver vein system

Note – compiled from [92]

Composite Alteration Mapping

Composite alteration maps combine multiple indices to create comprehensive alteration zone classifications [42; 44]. A common approach uses the argillic, phyllic, and propylitic indices as input to a classification algorithm, producing maps that show the spatial distribution of different alteration types [44]. The indices can be combined using logical operators (AND, OR) to create binary maps showing areas with specific alteration types, or using classification algorithms such as maximum likelihood or support vector machines to create multi-class alteration maps [44].

The combination of alteration indices enables identification of alteration zonation patterns that are characteristic of porphyry and epithermal systems. The spatial

distribution of alteration zones, combined with structural data and geological maps, provides a powerful tool for identifying prospective areas for mineral exploration. Composite alteration maps can be integrated with other geospatial data layers, including geophysical data, geochemical data, and structural lineaments, to create prospectivity models that rank areas based on multiple evidence types.

Validation of composite alteration maps typically involves comparison with field observations, geological maps, and drilling results [44]. Reported accuracies for ASTER-based alteration mapping range from 70–85% when proper preprocessing and validation are applied [88; 44]. The accuracy depends on factors including preprocessing quality, vegetation cover, and the complexity of the alteration mineralogy. Areas with simple, well-exposed alteration zones show higher accuracy than areas with complex, mixed alteration or significant vegetation cover [44].

3.9 Spectral Library Development

Spectral libraries contain reference spectra of minerals and rocks measured under controlled conditions. The USGS Spectral Library is a widely used resource, containing spectra of hundreds of minerals measured in the laboratory. Field spectra collected using portable spectrometers provide ground truth data for validation, though they may be affected by environmental conditions.

For this study, the spectral signatures spectral libraries are developed from EnMAP hyperspectral data by extracting spectra from known mineral occurrences and alteration zones. These libraries serve as reference for validating ASTER-derived spectral signatures and for identifying specific mineral species present in the study area.

3.10 Validation methodology

Field validation is the principal verification approach in geological remote sensing, because it links image-based mineral/alteration interpretations to direct mineralogical and geochemical evidence (ground truth) [47; 75; 44]. In practice, remote sensing is used to prioritize targets at regional scale, while field observations and laboratory analyses provide the definitive confirmation needed to reduce uncertainty and improve interpretability of alteration maps [47; 44].

Field Validation. Field validation involves collecting ground truth data through field mapping, targeted sample collection, and petrographic/mineralogical assessment. Rock and soil samples are analyzed to identify mineral assemblages and alteration types, then compared with remote-sensing-derived classes and indices to confirm that mapped spectral responses correspond to expected alteration mineralogy and to identify potential misclassifications caused by mixed pixels, surface cover, or illumination effects [44].

Cross-Sensor Validation. Cross-sensor validation compares results from different remote sensing systems to strengthen mineral-level interpretation and reduce ambiguity inherent to multispectral indices. In this study, ASTER-derived alteration maps are cross-

checked using EnMAP hyperspectral data, whose higher spectral resolution enables more explicit identification of diagnostic absorption features and discrimination of specific mineral groups, supporting confirmation of whether ASTER multispectral classifications correspond to the expected mineral assemblages [24]. The validation workflow involves extracting EnMAP spectra from pixels mapped as alteration zones in ASTER products, comparing these spectra with established reference libraries (e.g., USGS) using spectral matching approaches such as Spectral Feature Fitting and correlation-based similarity metrics, assessing agreement between the minerals indicated by hyperspectral signatures and the alteration type inferred from ASTER indices, and summarizing agreement quantitatively using standard accuracy metrics where appropriate (e.g., confusion matrices, overall accuracy) [32].

3.11 Data Integration into Complex approach

Remote sensing provides spatially continuous information on surface properties, but its full value is realized when these data are integrated with other geological and geospatial layers. In this thesis, ASTER- and EnMAP-derived products (alteration maps, spectral indices, lithological proxies) are combined with digital elevation models (DEMs), existing geological maps, geophysical surveys, and geochemical datasets to build a multi-evidence framework for mineral prospectivity analysis. The goal of this integration is to exploit complementary information: spectral data highlight mineralogy and alteration; DEMs capture structure and geomorphology; geological maps provide lithological and structural context; geophysical and geochemical data reveal subsurface and compositional signals. Together, these layers enable more robust interpretation of hydrothermal systems and more reliable targeting of prospective zones than any single dataset alone.

Integration with Digital Elevation Models

Digital elevation models (DEMs) provide topographic context for remote sensing analysis [20]. DEMs derived from ASTER (Fig. 3.19) stereo pairs or SRTM data are used for topographic normalization, structural analysis, and lineament extraction [20]. The ASTER GDEM provides 30-meter resolution elevation data with vertical accuracy of approximately 20 meters, suitable for topographic normalization and structural analysis [20]. SRTM data provide similar resolution and accuracy, with global coverage between 60°N and 56°S.

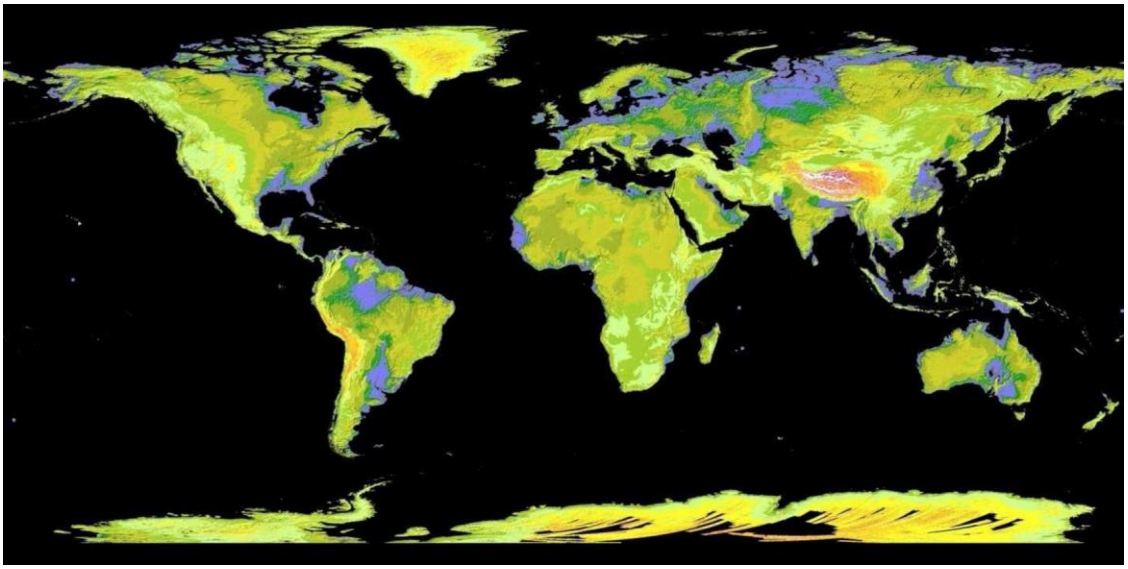

Figure 3.19. 30m resolution GDEM derived from ASTER life-time data acquisition

Note – compiled from [11]

Lineaments, representing faults, fractures, and other linear features, are extracted from DEMs using edge detection and directional filtering algorithms [30]. Common methods include directional filtering using Sobel or Prewitt operators, which highlight linear features in specific directions [30]. Lineament density maps show the concentration of linear features, with high density often correlating with areas of increased permeability and mineralization potential. Structural analysis using DEMs enables identification of fault-controlled alteration and mineralization, providing important context for interpreting remote sensing results [30].

Topographic analysis using DEMs includes calculation of slope, aspect, curvature, and other terrain attributes that can be integrated with spectral data for improved classification [30]. Slope and aspect are used for topographic normalization, while curvature can indicate areas of structural control or alteration-related topography. The integration of topographic and spectral data enables more robust classification and identification of alteration zones that may be obscured by topographic effects [30].

Integration with Geological Maps

Geological maps provide essential context for interpreting remote sensing results. Lithological boundaries, structural features, and known mineral occurrences from geological maps are used to validate and refine remote sensing classifications [44]. The integration process involves overlaying remote sensing alteration maps on geological maps to identify correlations between alteration zones and specific lithological units or structural features.

The integration enables identification of lithological controls on alteration, where certain rock types are more susceptible to alteration than others. For example, carbonate rocks are reactive hosts for gold mineralization, while felsic intrusions are common hosts

for porphyry systems. Structural features from geological maps, including faults, fractures, and fold axes, help identify structural controls on alteration and mineralization. Known mineral occurrences provide ground truth for validating remote sensing classifications and identifying areas with similar spectral signatures that may represent undiscovered mineralization [44].

Geological maps also provide information about regional geological context (Fig. 3.20), including tectonic setting, metamorphic grade, and geological history, which helps interpret remote sensing results. The integration of geological maps with remote sensing data enables development of geological models that explain the spatial distribution of alteration zones and their relationship to mineralization.

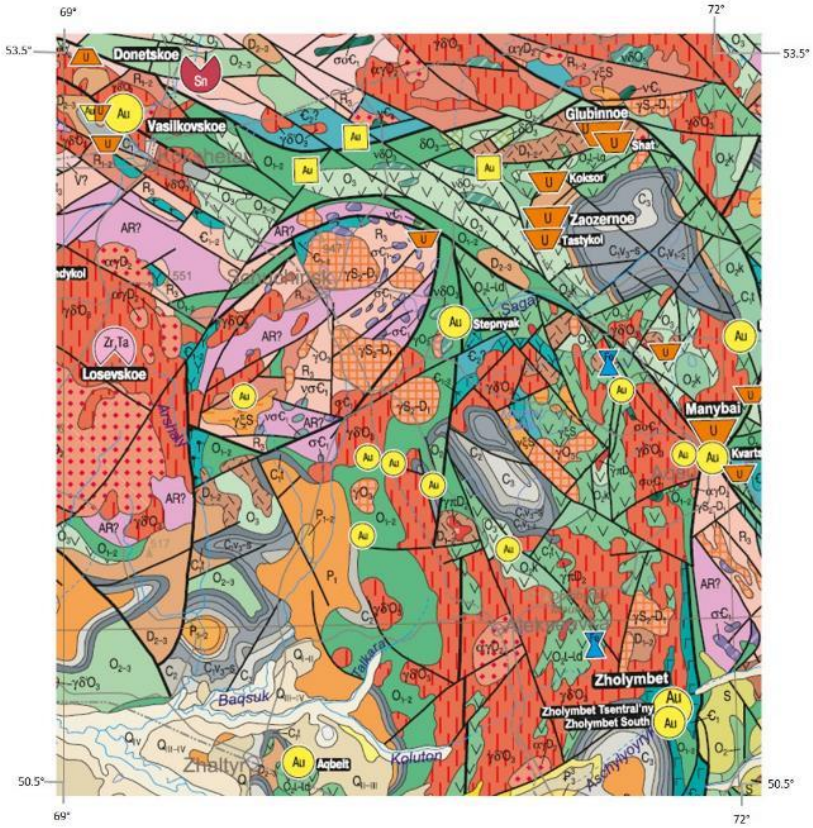

Figure 3.20. Geological map of Kazakhstan and Central Asia in scale 1:1,500,000

Integration with Geophysical and Geochemical Data

Geophysical data, including magnetic, gravity, and electromagnetic surveys, provide complementary information about subsurface geology and mineralization. Magnetic data can identify magnetic minerals such as magnetite, which is often associated with alteration zones in porphyry systems. Gravity data can identify density contrasts associated with intrusions or alteration zones, while electromagnetic data can identify conductive zones associated with sulfide mineralization.

The integration of geophysical and remote sensing data enables development of multi-evidence prospectivity models that combine spectral, magnetic, gravity, and other

evidence types. Weighted overlay methods assign weights to different evidence types based on their importance for mineralization, creating prospectivity maps that rank areas based on multiple criteria. Machine learning methods, including random forests and support vector machines, can learn relationships between multiple evidence types and known mineralization, enabling prediction of prospective areas.

Geochemical data provide ground truth for validating remote sensing classifications and identifying geochemical anomalies associated with mineralization [44]. The integration of geochemical data with remote sensing enables identification of areas with both spectral and geochemical signatures of mineralization, providing stronger evidence for prospectivity. Geochemical data can also help interpret spectral signatures, where certain geochemical associations correspond to specific alteration types or mineral assemblages [44].

Multi-Scale Analysis

Multi-scale analysis combines regional-scale mapping with detailed local analysis [44]. Regional-scale ASTER mapping identifies broad alteration zones and structural trends, while detailed analysis focuses on specific areas of interest identified from regional mapping [44]. This hierarchical approach enables efficient exploration targeting, focusing detailed work on the most prospective areas.

Regional-scale mapping typically uses ASTER data at 30-meter resolution, enabling coverage of large areas (hundreds to thousands of square kilometers) with reasonable processing time [44]. The mapping identifies broad alteration zones and structural trends that provide context for local-scale analysis. Detailed analysis uses higher resolution data, including ASTER VNIR bands at 15-meter resolution or hyperspectral data at 30-meter resolution, enabling identification of specific alteration minerals and detailed structural analysis [44].

The multi-scale approach enables efficient exploration targeting by identifying areas of interest at regional scale before committing resources to detailed analysis. The hierarchical approach also enables validation of regional-scale classifications using detailed local analysis, ensuring that regional classifications are geologically meaningful [44]. The combination of regional and local analysis provides comprehensive understanding of alteration systems and their relationship to mineralization.

The methodology presented in this chapter provides a comprehensive framework for applying remote sensing to geological studies, with particular emphasis on hydrothermal alteration mapping for gold exploration. The progression from fundamental physical principles through spectral properties, sensor characteristics, preprocessing, analysis, and validation ensures that the methods are grounded in theory and validated through practice [47; 42].

The theoretical foundations established in this chapter, including electromagnetic radiation fundamentals, spectral properties of geological materials, and the physical basis for mineral identification, provide the scientific basis for remote sensing applications [28; 16]. The detailed description of ASTER and EnMAP systems, including their spectral band configurations and capabilities, enables informed selection of appropriate sensors

and processing methods for specific applications [11; 24]. The preprocessing methods, including atmospheric correction, topographic normalization, and radiometric calibration, ensure that spectral signatures accurately represent surface composition [17].

The spectral transformation methods, including band ratios and alteration indices, provide practical tools for mapping alteration zones and identifying prospective areas for mineralization [42; 87]. The validation methods, including field validation, cross-sensor validation, and accuracy assessment, ensure that remote sensing classifications are geologically meaningful and reliable [44]. The integration methods, including integration with DEMs, geological maps, and geophysical data, enable comprehensive analysis that combines multiple evidence types for improved prospectivity assessment.

The following chapters apply this methodology to the specific case of gold deposits in Eastern Kalba, Kazakhstan, demonstrating the practical application of these methods and validating their effectiveness for gold exploration in similar geological settings. The methodology provides a replicable framework that can be applied to other geological settings and exploration targets, contributing to the broader application of remote sensing in mineral exploration.

In conclusion, this chapter has presented the theoretical and methodological framework for applying remote sensing to geological studies, with particular emphasis on hydrothermal alteration mapping for gold exploration. The progression from fundamental physical principles through spectral properties, sensor characteristics, preprocessing, analysis, and validation ensures that the methods are grounded in theory and validated through practice. The theoretical foundations, including electromagnetic radiation fundamentals, spectral properties of geological materials, and the physical basis for mineral identification, provide the scientific basis for remote sensing applications. ASTER's spectral band configuration, specifically optimized for geological applications, enables systematic mapping of hydrothermal alteration zones through band ratios targeting Al–OH, Mg/Fe–OH, CO_3, and Fe^{3+} absorption features. The preprocessing methods, including atmospheric correction, topographic normalization, and radiometric calibration, ensure that spectral signatures accurately represent surface composition. The spectral transformation methods, including band ratios and alteration indices, provide practical tools for mapping alteration zones and identifying prospective areas for mineralization. The validation methods, including object-based spatial correspondence and hyperspectral spectral confirmation, ensure that remote sensing classifications are geologically meaningful and reliable. The following chapter applies this methodology to the specific case of gold deposits in the West Kalba belt, demonstrating the practical application of these methods and validating their effectiveness for gold exploration in similar geological settings.

4 APPLICATION OF EARTH REMOTE SENSING DATA FOR PROSPECTING GOLD-SULFIDE AND GOLD-QUARTZ DEPOSITS

The West Kalba gold belt is considered as one of the key elements of the metallogenic architecture of East Kazakhstan, where gold ore objects are associated with deep faults, development of small intrusions/dike bodies and zonal "ore column", and the main types of mineralization include gold-quartz veins, gold-sulfide-quartz stockworks, gold-listvenite objects and gold-sulfide bodies in carbonaceous-carbonate-terrigenous thicknesses.

Gold ore systems of West Kalba formed under conditions of active fault tectonics, multiple reactivation of structures and long-term circulation of hydrothermal fluids, which caused the development of a wide spectrum of metasomatic alterations of host rocks. Analysis of the nature, spatial zoning and combinations of these alterations allows reconstruction of the architecture of ore systems and serves as the basis for prospecting gold ore objects, including using Earth remote sensing data. For West Kalba, the confinement of ore fields to nodes of fault intersections and to zones of increased fracturing is typical (example - Bakyrchik ore field (Kyzylovsky shear zone), confined to a NE-striking tectonic belt).

Known works by [47; 42; 43] demonstrate the use of RS data for recognition of lithology and zones of hydrothermal alteration (including phyllic/sericitic, argillic) on examples of fields in California and Australia, which became the basis for RS-interpretation methodology of hydrothermal systems.

Remote sensing does not allow direct detection of gold ore objects, however, it effectively identifies mineralogical and structural indicators, spatially and genetically associated with Au-mineralization. Application of Earth remote sensing data for prospecting gold deposits is based on identification of metasomatic halos and secondary minerals formed as a result of hydrothermal processes accompanying ore formation.

For gold ore systems, the zones of greatest importance are:

1. silicification;
2. sericitization and argillization;
3. chloritization and propylitization;
4. carbonatization;
5. sulfidation and subsequent oxidation;
6. beresitization and listvenitization, as characteristic manifestations of gold-bearing hydrothermal systems.

According to data [60; 44], ASTER and Sentinel-2 [50] satellite data are especially informative, providing registration of spectral characteristics of minerals in VNIR and SWIR ranges, sensitive to Fe3+-oxide and OH-containing phases. The laboratory spectral signatures of key alteration minerals, organized by mineral groups relevant to West Kalba gold systems, are presented in Fig. 4.1, providing the spectral foundation for ASTER band ratio selection and mineral identification.

Below is considered the significance of the main types of hydrothermal alterations characteristic of gold ore systems of West Kalba, with emphasis on their genetic role and prospecting significance and possibilities for remote sensing.

4.1 Silicification

Silicification is one of the most widely developed and structurally controlled processes in gold-bearing hydrothermal systems of West Kalba. It reflects silica saturation of hydrothermal fluids and manifests in the form of quartz veins, veinlets and stockworks, forming predominantly in zones of increased fracturing and along deep and en echelon faults.

This process plays a key role as an indicator of channels of ore-bearing fluid migration and marker of ore-controlling structures. Although quartz rarely is a direct carrier of gold, it is precisely in quartz veins and veinlet-stockwork zones that favorable physicochemical conditions for Au precipitation are created, related to decrease in temperature and pressure, change in pH-Eh environment and fluid mixing [62; 63; 65].

It is noted that formation of gold-quartz veins is widely manifested in fracture structures (including in gray-colored terrigenous complexes of Carboniferous age), which corresponds to the classical model of "vein" gold of West Kalba.

Zones of silicification serve several key prospecting functions. First, maximum silicification almost always marks zones of stress localization, including nodes of fault intersections, en echelon fracture systems, and fracturing zones, thereby mapping main ore-controlling structures. Second, silicification indicates places of sharp change in physicochemical conditions (decrease in temperature, drop in pressure, fluid mixing), where Au precipitation is possible, often together with sulfides. Third, the distribution and intensity of silicification can indicate the degree of erosional truncation; in a number of fields, intensive silicification may be confined to certain levels of the "ore column", which is important for depth prognosis.

Quartz itself usually manifests in RS worse than OH minerals or Fe oxides, therefore in West Kalba, silicification is often identified indirectly by linear morphostructures, by associated zones of sericitization/carbonatization/oxidation of sulfides and by clustering of anomalies coinciding with veinlet zones.

4.2 Sericitization and Argillization

Sericitization and argillization are among the most informative types of hydrothermal alterations for gold ore systems of West Kalba, especially in vein-stockwork and gold-sulfide-quartz objects. Sericitization (sericite/illite) reflects development of potassic metasomatism under the influence of moderately acid hydrothermal fluids and is accompanied by formation of sericite and illite. These alterations are characteristic of near-vein and central parts of gold ore systems and often spatially coincide with zones of sulfidation and increased concentrations of gold pathfinder elements (As, Sb, less

commonly Bi) [60; 49; 59]. Within West Kalba, sericitization is considered as a reliable indicator of zones of active hydrothermal reworking and potential ore-bearing capacity.

Argillization, represented by kaolinite ± alunite, reflects the influence of more acid fluids and often marks the most permeable sections of fault zones and channels of hydrothermal discharge. In a number of objects of West Kalba, argillization enhances the contrast between ore-bearing and host rocks, which substantially increases the effectiveness of its identification by RS data.

The role of these processes in formation of West Kalba gold ore systems is very significant. These alterations can be critical for West Kalba. This is related to the fact that many gold ore objects, especially vein stockwork and sulfide/quartz demonstrate central and near vein halos with development of OH-containing minerals, well-detectable in SWIR.

Zones of sericitization (sericite/illite) indicate the presence of potassic metasomatism and stable near vein conditions, and often spatially coincide with zones of pyritization/sulfidation, characterized by increased contents of pathfinder elements (As, Sb, sometimes Bi), which is characteristic of gold ore systems of the region. Argillization (kaolinite ± alunite) reflects the influence of more acid fluids and often marks discharge channels, i.e., the most permeable sections of fault zones. In West Kalba, argillization is especially important as a sign increasing the contrast of RS-mapping of the core of the hydrothermal system compared to the periphery.

Sericite/illite and kaolinite are the minerals for Sentinel-2/ASTER approaches in the region, because they form stable SWIR features, including in the composition of complex beresite-listvenite halos.

4.3 Propylitization and Chloritization

Propylitization and chloritization is a complex type of regional hydrothermal alteration of rocks, characterized by wide development of chlorite–epidote–carbonates ± albite association, forming under the influence of low-temperature, predominantly neutral hydrothermal fluids and reflecting peripheral conditions of functioning of ore-hydrothermal systems. These processes form wide halos, covering significant areas. They often develop around intrusive bodies, dike fields and fault zones and in gold ore systems occupy the outermost position in the zonal structure.

These hydrothermal alterations are rarely directly related to industrial gold concentrations; however, their significance lies in the possibility of reconstructing the spatial zoning of the hydrothermal system. Chlorite-epidote-carbonate associations form wide halos, framing more productive sericite/quartz and beresite zones, and allow estimation of the scale of the ore system [13].

For West Kalba, chloritization/propylitization most often fulfill the function of a system profile, rather than a direct indicator of maximum Au concentrations. This is especially important in the belt, where ore fields form as cluster manifestations along faults or are confined to fracture networks at their intersections, as well as local centers,

including with participation of small intrusions and dikes. For West Kalba, chloritization and propylitization are especially important as regional prospecting features, allowing determination of the direction to the ore-bearing center and justification for placement of detailed prospecting-assessment works.

This type of hydrothermal alterations allows identification of the peripheral zone of the hydrothermal field, enabling estimation of its size; provides a vector to the center, from chlorite-epidote-carbonate associations to more productive sericite-quartz and beresite zones; and reveals association with magmatic factors, when propylitization frames sections related to dikes/small intrusions, which in West Kalba are considered as important elements of ore-magmatic systems.

In complex remote sensing models, propylitization functions as a mask for isolating more productive zones, provides a baseline in multifactor analysis, and supports the "periphery → center" logic when prospecting ore bodies. For gold ore systems, propylitization is seldom a direct target; instead, it supplies essential context. Without this context, remote sensing data interpretation lacks spatial and genetic justification.

4.4 Carbonatization

Carbonatization is one of the key processes of gold ore metasomatism in West Kalba, which is related both to the composition of host thicknesses and to active fault tectonics, which ensured circulation of CO_2 saturated fluids.

Formation of calcite, ankerite and dolomite promotes buffering of pH environment and destabilization of gold-bearing complex compounds, which creates favorable conditions for Au precipitation. Carbonatization often spatially and genetically is related to sericitization and silicification, forming characteristic beresite halos [67].

In prospecting terms, carbonatization serves as an important indicator of zones of fluid discharge and increased permeability, and in combination with sulfidation and subsequent oxidation as a reliable sign of gold ore sections.

The role of carbonatization in West Kalba gold ore systems is fundamental, due to localization of practically the majority of objects in terrigenous and carbonate-terrigenous thicknesses, as well as under conditions of active fault tectonics, where CO_2 fluids and the reaction are widely realized.

Carbonatization contributes to gold ore formation by buffering pH and shifting redox conditions, which destabilizes Au-complexes and promotes gold precipitation. It also forms stable associations with sericite and quartz, characteristic of beresite zones. In many deposits, carbonatization serves as an important field and remote sensing marker of ore discharge zones, particularly when combined with sulfidation and subsequent oxidation.

In prospecting terms, carbonatization serves as an important indicator of zones of fluid discharge and increased permeability, and in combination with sulfidation and subsequent oxidation as a reliable sign of gold ore sections.

4.5 Sulfidation and Subsequent Oxidation of Sulfides

Sulfidation is a key stage of gold concentration in gold ore systems of West Kalba. It is precisely in pyrite and arsenopyrite that finely dispersed gold is often concentrated, associated with inclusions, isomorphous substitution or surface sorption. Zones of sulfidation, as a rule, are confined to fault structures, vein systems and sections of intensive sericitization and beresitization.

Subsequent oxidation of sulfides under near-surface conditions leads to formation of gossans and iron oxide caps (hematite, goethite, limonite) [52], which are the most contrast objects for remote sensing [64; 58; 57].

For West Kalba, this has special practical significance, since many objects are characterized by well-developed weathering zones, which allows effective use of spectral remote sensing for primary identification of prospective gold ore sections.

Gold ore mineralization within West Kalba is concentrated in the form of free gold and microscopic inclusions in sulfides such as pyrite and arsenopyrite, and zones of sulfidation usually are related to fault control and vein-veinlet structures. Subsequent oxidation of sulfides forms gossans and iron oxide caps (hematite-goethite-limonite), which produce maximally contrast VNIR features and serve as convenient surface indicators of hidden ore bodies.

For West Kalba, this is especially important, because for a number of objects, weathering zones and oxidized gold-sulfide ores are targets for detection using RS and are used in planning prospecting works, including by zones of beresitization/listvenitization and silicification.

Sulfidation has key significance for remote sensing as a source of the most contrast and reliable secondary features of gold ore systems [51]. Primary sulfides (pyrite, arsenopyrite) themselves are weakly distinguishable by remote sensing, however, their subsequent oxidation leads to formation of iron oxide gossans (hematite, goethite, limonite), possessing brightly expressed VNIR-spectral characteristics. Hematite (Fe_2O_3) exhibits strong Fe^{3+} crystal-field absorptions near 0.65μm, while goethite (FeOOH) shows characteristic absorptions near 0.90μm; limonite, as a mixture of goethite and other iron hydroxides, produces variable but typically strong VNIR absorption features. These Fe^{3+} oxides form stable remotely identifiable anomalies detectable through ASTER band ratios B2/B1 (ferric iron index, threshold > 1.0), B4/B2 (gossan index, threshold > 1.05), and B4/B3 (iron oxide index, threshold > 1.0), which serve as direct surface indicators of hidden gold-sulfide mineralization and are widely used for primary identification of prospective sections by ASTER, Sentinel-2 and Landsat data. The contrast provided by these iron oxide caps makes them among the most effective remote sensing targets for gold exploration in oxidized terrains.

4.6 Beresitization and Listvenitization

Beresitization, represented by quartz + sericite ± carbonates association with pyritization, is widely developed in vein-stockwork gold ore objects of West Kalba and often directly coincides with zones of mineralization. These alterations reflect stable conditions of fluid to rock interaction and a circulation of gold-bearing solutions.

Listvenitization, characterized by quartz-sericite-kaolinite associations ± alunite, is related to more acid fluids and, as a rule, is confined to deep faults and zones of high permeability. Within West Kalba, listvenitization is especially valuable as a prospecting feature, since it combines features of sericitization, argillization, carbonatization and sulfidation.

These types of alterations can be considered as integral signs of gold-bearing hydrothermal systems in West Kalba gold ore systems, because they combine silicification + sericitization/argillization + carbonatization + sulfidation and often, subsequent oxidation) (Fig. 4.1). This is why in the regional practice of West Kalba, beresitization and listvenitization are regularly used as criteria for concentration of works and identification of priority targets [56; 61].

Beresitization (quartz + sericite ± carbonates, often with pyritization) is typical for vein stockwork gold ore objects of West Kalba, including models of gold/quartz vein + beresite alteration, which are directly discussed as characteristic for the belt, and well-correlates with zones of increased fracturing, dike bodies and local centers of hydrothermalism. Listvenitization (quartz + sericite + kaolinite ± alunite; often in association with silicate/carbonate" transformations of ultrabasics/metaophiolites and along mélange zones) within the belt is related to zones of deep faults and sections where high permeability and long-term fluid circulation are possible, since it combines Fe oxides (VNIR) and OH minerals/kaolinite (SWIR), producing high contrast on satellite images.

The spatial distribution and mineralogical composition of alteration types vary between different ore field types within West Kalba. Table 4.1 summarizes the target minerals and absorption components characteristic of the Bakyrchik ore field, a black-shale-hosted Au–sulfide system with zonal structure from outer carbonatization and chloritization to inner listvenitization and beresitization. Table 4.2 presents the mineral assemblages for the Akzhal–Vasilyevskoye ore field, representing vein/beresite gold systems where alteration zones are more structurally controlled and spatially constrained along fault corridors. These zone-specific mineralogical frameworks provide the foundation for ASTER-based alteration mapping discussed in subsequent sections.

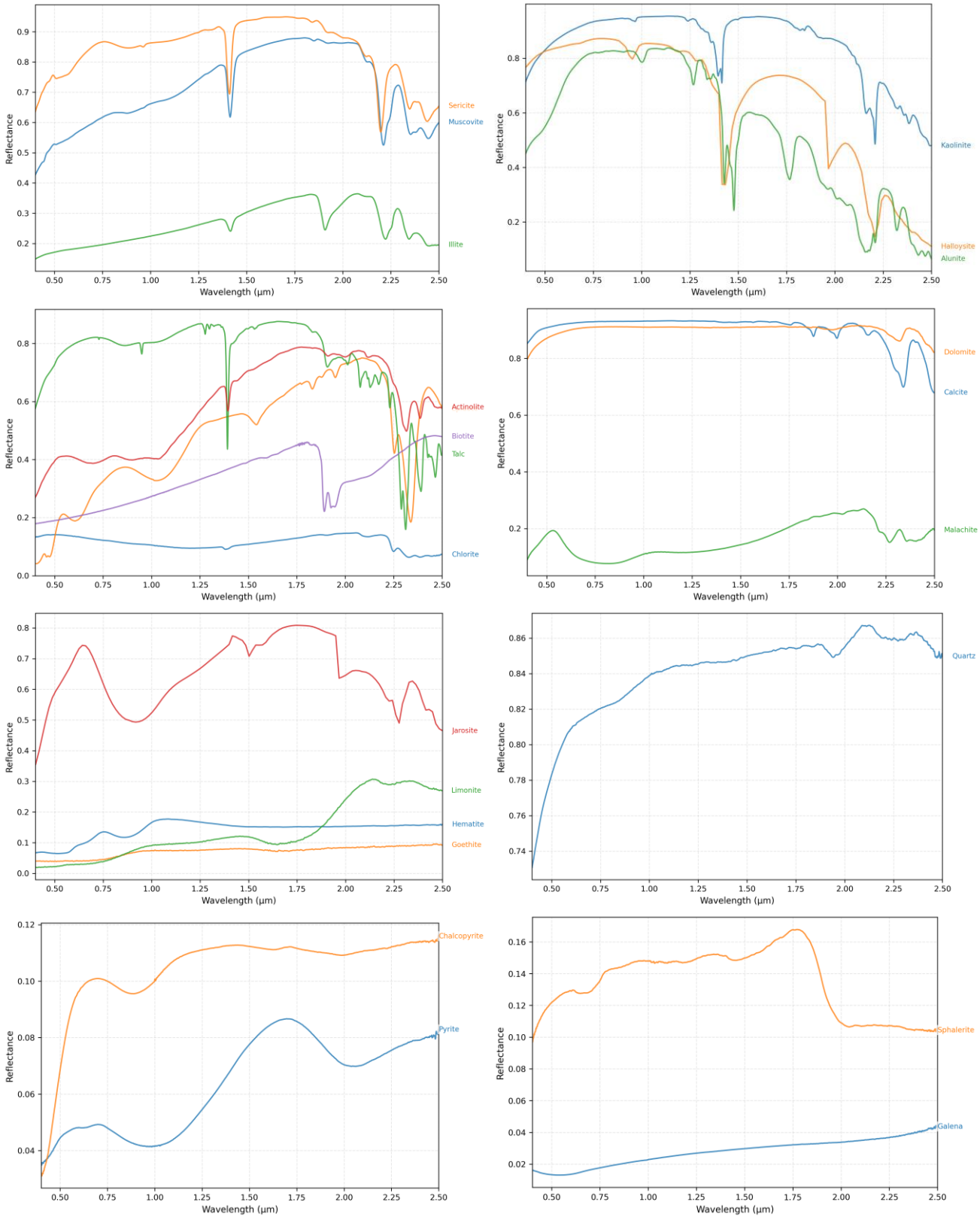

Figure 4.1. USGS laboratory spectra selection focused on West Kalba mineralogy

Table 4.1. Target minerals and absorption components in Bakyrchik ore field

Alteration zone	Mineral	Ore context	Absorbing components
Outer zoning: carbonatization	Calcite, dolomite, ankerite, siderite; locally breinerite	Common halo around ore zones; part of quartz–carbonate stages	CO_3^{2-} in carbonate minerals
Outer zoning: chloritization	Chlorite(±epidote)	Distal to inner metasomatites; halo around structures	OH in phyllosilicates; Fe^{2+}/Fe^{3+} in Fe-bearing silicates
Inner zoning: listvenitization	Quartz + carbonates (±ankerite/dolomite) + Fe-carbonates; locally sericite	Inner metasomatic domain along shear zones and ore bodies	CO_3^{2-} and OH
Inner zoning: beresitization	Sericite, quartz; carbonates	Typical alteration in and near ore zones; accompanies Au–sulfide stages	Al–OH in sericite/illite; OH in phyllosilicates
Inner zoning: albitization	Albite (± K-feldspar relicts)	Inner metasomatic domain; may occur with beresite/listvenite patterns	Structural water/OH is minimal; visibility mainly through association with mica/carbonate halos rather than albite itself
Sulfide-rich ore zones (endogenic)	Pyrite, arsenopyrite; minor pyrrhotite, marcasite, melnikovite-pyrite; late stibnite/antimonite, tetrahedrite; base-metal sulfides (chalcopyrite, galena, sphalerite)	Assemblages from early Fe-sulfides to Au–pyrite–arsenopyrite; late Sb stage; polymetallic stages; form through sulfidation of ferrous silicates (biotite, chlorite, amphibole)	Broad absorption dominated by opaque minerals; Fe and As-bearing sulfides reduce reflectance; Sb-bearing's similarly dark; spectrally featureless in VNIR–SWIR, detected indirectly through associated alteration halos
Quartz vein/stockwork domains	Quartz; quartz–carbonate veins; locally scheelite with chalcopyrite	Gold–quartz–carbonate–chalcopyrite with scheelite; redeposited stages	Quartz has weak intrinsic absorbers; visibility mainly from associated carbonates CO_3^{2-}, micas Al–OH, and ferrous silicates Mg–OH, Fe^{2+}
Oxidation zone: iron oxide gossans	Hematite, goethite, limonite (mixture); locally jarosite, hydrogoethite	Near-surface oxidation of pyrite/arsenopyrite; weathering zones extend to 30–50~m depth; well-developed at Bolshevik	Fe^{3+} crystal-field absorptions (hematite: ~0.65~μm; goethite: ~0.90~μm); strong VNIR features at B2/B1, B4/B2
Tungsten-bearing late stage	Scheelite (± wolframite) with quartz–carbonate–chalcopyrite; trace REE in concentrates	Late Au–Mo–W overprint; W increases with depth in Bakyrchik field	Oxyanion/polyhedral vibrations in tungstates (W–O); overall brightness/contrast often modified by associated sulfides and carbonates

Table 4.2. Target minerals and absorption components in Akzhal-Vasilyevskoye ore field

Alteration zone	Mineral	Ore context	Absorbing components
Beresitization	Sericite/muscovite/illite, quartz; carbonates; locally fuchsite, albite	In/near ore zones; on volcanogenic-terrigenous rocks; accompanies Au–sulfide stages	Al–OH CO_3^{2-}
Listvenitization	Quartz + carbonates locally sericite, talc	Inner metasomatic domain along shear zones; common in Boko-Vasilievskoye	CO_3^{2-} Mg–OH (talc)
Propylitization	Chlorite, epidote calcite; locally albite	Distal halo around structures; widespread at Tokum	OH Fe^{2+}
Albitization	Albite (± K-feldspar)	Inner metasomatic domain; may occur with beresite/listvenite	Minimal OH
Quartz vein/stockwork	Quartz (multiple generations); quartz–carbonate veins; locally scheelite, barite	Gold–quartz veins and crush zones; main ore host at Akzhal/Vasilyevskoye	CO_3^{2-} Al–OH
Sulfide-rich ore zones	Pyrite, arsenopyrite; minor chalcopyrite, galena, sphalerite, tetrahedrite; native gold/silver; scheelite, cassiterite	Gold–pyrite–arsenopyrite assemblages; early/late stages; form through sulfidation of ferrous silicates	Opaque minerals spectrally featureless, detected via alteration halos
Graphite/carbonaceous zones	Graphite, carbonaceous matter; associated with pyrite–arsenopyrite	In carbonaceous shales/aleurolites	Carbon (graphite) absorbs across visible–SWIR; reduces reflectance
Argillic alteration	Kaolinite, halloysite; locally sericite/chlorite	Argillic alteration zones; may occur in Mesozoic profiles	Al–OH doublet; OH
Oxidation zone: iron oxide gossans	Hematite, goethite, limonite; locally jarosite, scorodite, psilomelane	Near-surface oxidation of sulfides; oxidation zones extend to 15–40~m depth; well-developed weathering crusts	Fe^{3+} absorptions detected via B2/B1, B4/B2, B4/B3
Accessory minerals	Rutile, tourmaline, barite, fuchsite, talc; magnetite, ilmenite, chromite	Altered rocks/metasomatites; common in beresites/listvenites	Ti–O, B–OH, SO_4^{2-}, Fe^{2+}/Fe^{3+}

Table 4.3. Complete mineral profile for study areas

Mineral	Formula	Target	Spectral Features
1	2	3	4
Pyrite	FeS_2	Au (95–97% in B)	Sericite/illite (Al–OH); carbonates (CO_3); ferrous silicates (Fe^{2+}, Mg–OH)
Arsenopyrite	FeAsS	Au (95–97% in B)	Sericite/illite (Al–OH); carbonates (CO_3); ferrous silicates (Fe^{2+}, Mg–OH)
Chalcopyrite	$CuFeS_2$	Au, Cu (minor)	Carbonates (CO_3); ferrous silicates (Fe^{2+})
Galena	PbS	Au, Pb (minor)	Carbonates (CO_3); ferrous silicates (Fe^{2+})
Sphalerite	ZnS	Au, Zn (minor)	Carbonates (CO_3); ferrous silicates (Fe^{2+})
Stibnite	Sb_2S_3	Au (remobilized)	Carbonates (CO_3); ferrous silicates (Fe^{2+})
Bornite	Cu_5FeS_4	Au, Cu (minor)	Carbonates (CO_3); ferrous silicates (Fe^{2+})
Graphite	C	Au (sorption)	Broad VIS–SWIR darkening
Sericite	Fine muscovite	Au–sulfide systems	Al–OH 2.20µm
Muscovite	$KAl_2(AlSi_3O_{10})(OH)_2$	Au–sulfide systems	Al–OH 2.20µm
Chlorite	$(Mg,Fe)_3(Si,Al)_4O_{10}(OH)_2$	Distal Au halos; sulfidation zones	Mg–OH 2.32µm; Fe^{2+} 0.9–1.1µm
Calcite	CO_3	Au–carbonate stages	CO_3 2.33µm
Biotite	$K(Mg,Fe)_3AlSi_3O_{10}(OH)_2$	Sulfidation zones	Al–OH 2.20µm; Fe^{2+} 0.9–1.1µm
Amphibole	$Ca_2(Mg,Fe)_5Si_8O_{22}(OH)_2$	Sulfidation zones	Mg–OH 2.32µm; Fe^{2+} 0.9–1.1µm
Kaolinite	$Al_2Si_2O_5(OH)_4$	Argillic alteration	Al–OH 2.17/2.21µm
Quartz	SiO_2	Au–quartz veins	Featureless
Dolomite	$CaMg(CO_3)_2$	Au–carbonate	CO_3 2.32µm
Ankerite	$Ca\ (Fe,Mg)(CO_3)_2$	Au–carbonate stages	CO_3 2.33µm
Siderite	$FeCO_3$	Au–carbonate stages	CO_3 2.35µm

Continuation of table 4.3

1	2	3	4
Epidote	$Ca_2(Al,Fe)_3(SiO_4)_3(OH)$	Distal Au halos	Fe^{3+}, OH
Jarosite	$KFe_3(SO_4)_2(OH)_6$	Advanced argillic alteration	SO_4 2.30μm; Al–OH 2.20μm
Scorodite	$FeAsO_4 \cdot 2H_2O$	As-bearing assemblages	SO_4/As–O
Illite	$(K,H_3O)(Al,Mg,Fe)_2(Si,Al)_4O_{10}$	Au–sulfide systems	Al–OH 2.20μm
Halloysite	$Al_2Si_2O_5(OH)_4$	Argillic alteration	Al–OH 2.17/2.21μm
Talc	$Mg_3Si_4O_{10}(OH)_2$	Metasomatism (A)	Mg–OH 2.32μm
Malachite	$Cu_2CO_3(OH)_2$	Cu-bearing assemblages	CO_3 2.33μm
Cerussite	$PbCO_3$	Pb-bearing assemblages	CO_3 2.33μm
Hematite	Fe_2O_3	Oxidation zones	Fe^{3+} ~0.65μm; VNIR strong
Goethite	FeOOH	Oxidation zones	Fe^{3+} ~0.90μm; VNIR strong
Limonite	$FeOOH \cdot nH_2O$	Oxidation zones	Fe^{3+} variable (0.65–0.90μm); VNIR strong
Magnetite	Fe_3O_4	Accessory/magnetic context	Fe^{2+}/Fe^{3+}; magnetic properties; weak spectral
midrule Albite	$NaAlSi_3O_8$	Host rock / context	Weak
Orthoclase	$KAlSi_3O_8$	Host rock / context	Weak
Tourmaline	Complex	Accessory indicator	B–OH weak
Actinolite	$Ca_2(Mg,Fe)_5Si_8O_{22}(OH)_2$	Host rock / context	Mg–OH weak
Barite	Batextit{SO}_4	Vein accessory	SO_4 weak
Cassiterite	$BaSO_4$	Accessory context	Weak

Conclusions. The hydrothermal alteration assemblages characteristic of gold ore systems in the West Kalba belt demonstrate systematic relationships between alteration zones, mineralogical compositions, and spectral absorption features detectable by multispectral sensors. The six primary alteration types - silicification,

sericitization/argillization, chloritization/propylitization, carbonatization, sulfidation/oxidation, and beresitization/listvenitization - form diagnostic spectral signatures that serve as indirect indicators of gold mineralization. While primary ore minerals (pyrite, arsenopyrite, native gold) are spectrally featureless in the VNIR–SWIR range, their detection is enabled through associated alteration halos dominated by OH-bearing phyllosilicates (Al–OH at 2.20μm), carbonates (CO_3 at 2.32–2.35μm), and Fe-oxide oxidation products (Fe^{3+} in VNIR). The laboratory-measured spectral signatures of these key mineral groups, based on local mineralogy from the West Kalba belt, are illustrated in Fig. 4.1, demonstrating the characteristic absorption features that enable ASTER-based mineral identification. The zonal distribution of these alteration types, from peripheral propylitic halos through inner beresite/listvenite zones to core sulfide-bearing domains, provides a predictive framework for remote sensing-based mineral targeting. Tables 4.1 and 4.2 document the field-specific manifestations of these alteration zones for the Bakyrchik and Akzhal–Vasilyevskoye ore fields, respectively, highlighting differences in spatial distribution and mineralogical composition between black-shale-hosted systems (Bakyrchik) and vein/beresite systems (Akzhal–Vasilyevskoye). The complete inventory of target minerals and their spectral characteristics, organized by alteration type and ore context, is presented in Table 4.3, providing the mineralogical foundation for spectral library development and ASTER band ratio selection described in subsequent methodological sections.

5 REMOTE SENSING RESULTS: HYDROTHERMAL ALTERATION MAPPING AND VALIDATION IN THE WEST KALBA GOLD BELT

This chapter presents the application of remote sensing methodology to map hydrothermal alteration zones and validate their spatial correlation with known gold deposits in the West Kalba gold belt of Eastern Kazakhstan. The analysis integrates three foundational components established in previous chapters: the geological and metallogenic framework of the West Kalba zone, the theoretical and methodological principles for multispectral alteration mapping, and the mineralogical and spectral characteristics of alteration assemblages specific to gold ore systems in the region.

The West Kalba metallogenic zone, as summarized in Chapter 2, represents the main gold-bearing structure of East Kazakhstan, hosting more than 450 documented gold deposits and occurrences formed during the Late Paleozoic collisional stage of the Zaisan suture zone development. The zone is characterized by northwest-striking structural-material complexes bounded by regional deep faults, with gold mineralization associated with hydrothermal alteration processes (sericitization, chloritization, silicification, carbonatization, albitization) and controlled by regional and local fault systems. The Bakyrchik ore district, containing 123 gold occurrences with gold-arsenic-carbonaceous formation ores where 95–97% of gold is bound to pyrite and arsenopyrite, and the Akzhal–Vasilyevskoye ore district, containing 75 gold deposits and occurrences with vein low-sulfide gold-quartz types, provide representative endmembers for testing remote sensing approaches across different deposit styles within the belt.

The methodological framework established in Chapter 3 provides the theoretical foundation for applying ASTER multispectral data to hydrothermal alteration mapping. The progression from electromagnetic radiation fundamentals through spectral properties, sensor characteristics, preprocessing, and analysis methods ensures that the applied techniques are grounded in physical principles and validated through practice. ASTER's spectral band configuration, optimized for geological applications, enables systematic mapping of alteration zones through band ratios targeting Al–OH (2.20μm), Mg/Fe–OH (2.32μm), CO_3 (2.32–2.35μm), and Fe^{3+} (VNIR) absorption features. The preprocessing methods, including atmospheric correction and radiometric calibration, ensure that spectral signatures accurately represent surface mineralogical composition, while spectral transformation methods (band ratios and alteration indices) provide practical tools for mapping alteration zones and identifying prospective areas for mineralization.

Chapter 4 established the mineralogical and spectral framework specific to West Kalba gold systems, demonstrating that six primary alteration types - silicification, sericitization/argillization, chloritization/propylitization, carbonatization, sulfidation/oxidation, and beresitization/listvenitization - form diagnostic spectral signatures that serve as indirect indicators of gold mineralization. While primary ore minerals (pyrite, arsenopyrite, native gold) are spectrally featureless in the VNIR–SWIR range, their detection is enabled through associated alteration halos dominated by OH-bearing phyllosilicates, carbonates, and Fe-oxide oxidation products. The laboratory-

measured spectral signatures of key mineral groups, based on local mineralogy from the West Kalba belt (Fig. 4.1 in Chapter 4), demonstrate the characteristic absorption features that enable ASTER-based mineral identification. The zonal distribution of alteration types, from peripheral propylitic halos through inner beresite/listvenite zones to core sulfide-bearing domains, provides a predictive framework for remote sensing-based mineral targeting, with field-specific manifestations documented for the Bakyrchik and Akzhal–Vasilyevskoye ore fields.

This chapter applies the integrated methodology to ASTER multispectral data covering the Bakyrchik and Akzhal-Vasilyevskoye focus districts, implementing band ratio calculations, false color composite generation, and spatial correlation analysis with documented mineral deposits and exploration footprints. The validation approach quantifies both spectral precision and spatial precision of alteration pixel, providing a quantitative basis for assessing the reliability of the remote sensing workflow in capturing the mineralogical and spatial expression of targeted hydrothermal systems. The results demonstrate that ASTER-derived alteration mapping successfully recovers expected alteration zonation patterns at district scale, with strong spatial correlation between mapped anomalies and known deposits, supporting the use of multispectral remote sensing for rapid screening and mineral targeting in similar geological settings.

5.1 Datasets

This study uses ASTER multispectral surface reflectance (regional hydrothermal alteration mapping). Hyperspectral datasets are discussed as potential validation material, but they are not used for the district-scale analysis presented in this chapter.

The ASTER dataset was selected to provide comprehensive coverage of the West Kalba gold belt focus districts, encompassing Bakyrchik and Akzhal–Vasilyevskoye and their surrounding geological context (Fig. 5.1). Five ASTER Level-2 surface reflectance scenes (AST_07XT) were acquired, covering a total area of approximately 30,750 km^2 (Table 5.1) The spatial extent spans from northwest corner coordinates 50.12°N, 80.64°E to southeast corner coordinates 48.44°N, 82.90°E, ensuring complete coverage of the target districts and adjacent structures.

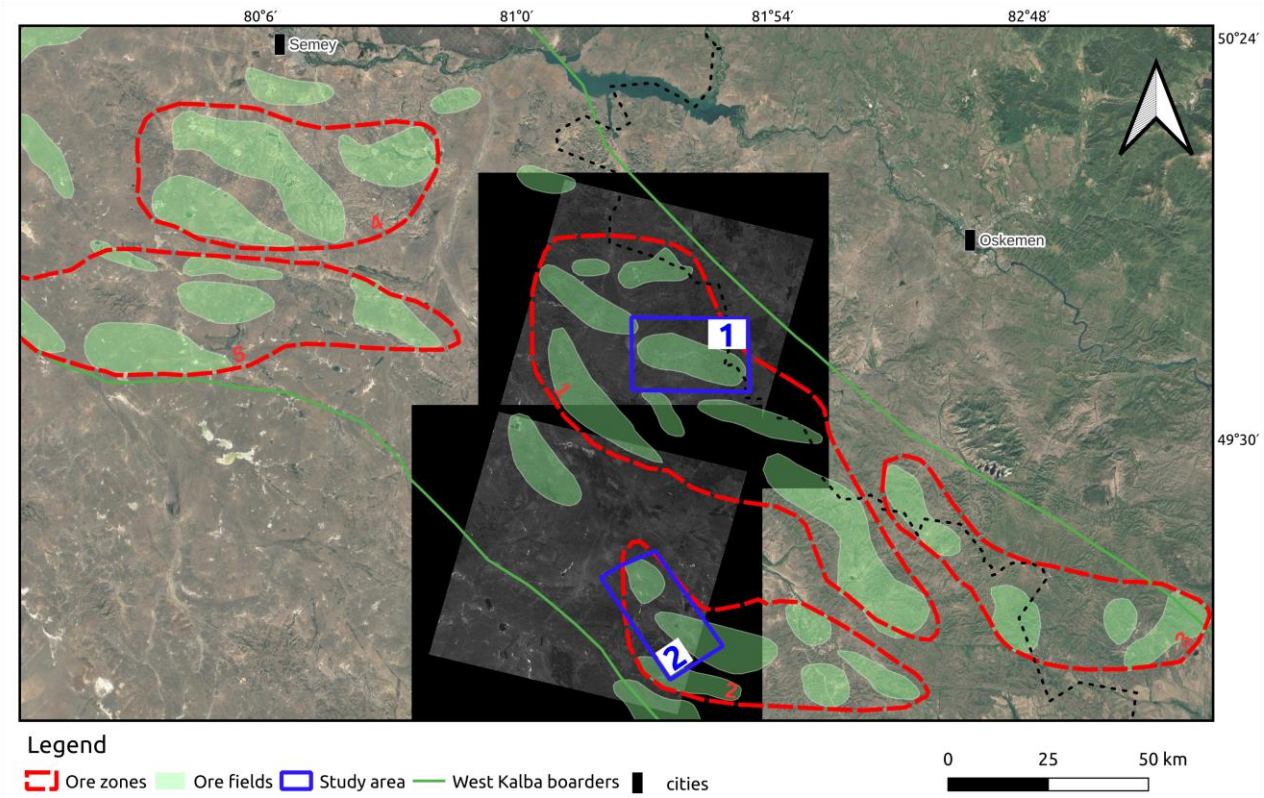

Figure 5.1. ASTER data spatial coverage by raw multispectral images

Table 5.1. ASTER data acquisition summary

Scene ID	Acquisition	Spatial extent	Technical specifications
AST_07XT_004	UTC	Latitude, Longitude	
05152003054915	2003–05–15 05:49:15	48.89°–50.12°N, 80.64°–82.09°E	VNIR + SWIR
05152003054924	2003–05–15 05:49:24	48.89°–50.12°N, 80.64°–82.09°E	VNIR + SWIR
06112004054247	2004–06–11 04:25:47	48.96°–49.66°N, 82.48°–83.52°E	VNIR + SWIR
06112004054256	2004–06–11 04:25:56	48.42°–49.15°N, 81.51°–82.50°E	VNIR + SWIR
06132007053652	2004–06–13 07:05:36	48.64°–49.33°N, 82.20°–83.15°E	VNIR + SWIR

Scene selection criteria prioritized data quality and temporal consistency. All scenes were filtered for cloud coverage less than 2%, ensuring minimal atmospheric contamination and reliable spectral signatures for alteration mapping. Additionally, scenes were restricted to acquisitions prior to 2008 to minimize temporal variations in

surface conditions and to align with the period of active exploration when geological mapping and deposit characterization were most comprehensive.

Acquisition timing is also important for spectral analysis in semi-arid to arid climates: optimal conditions occur during the dry season (mid-July to mid-October in Eastern Kazakhstan), when vegetation cover is minimal, soil moisture is low, and surface exposure of alteration minerals is maximized. The selected ASTER scenes were acquired in May–June (2003–2004), representing late spring to early summer conditions with moderate vegetation cover; while not ideal dry-season acquisitions, these scenes provide acceptable spectral quality given the constraints of pre-2008 temporal filtering and cloud-free coverage requirements. This temporal constraint also reduces potential complications from recent land-use changes, vegetation growth, or anthropogenic modifications that could obscure alteration signatures. The selected scenes provide optimal balance between spatial coverage, spectral quality, and geological relevance for hydrothermal alteration detection.

The EnMAP hyperspectral dataset provides high spectral resolution but its spatial coverage does not include the two focus districts analyzed here (Fig. 5.2); therefore, it is not used in the mail analysis pipeline. Also due to temporal and spatial limitations from clouds, a big part of EnMAP and ASTER2 are useless. Only small part can be and will be used as a validation deposits, where we test spectral signature of EnMAP based results on absorption features.

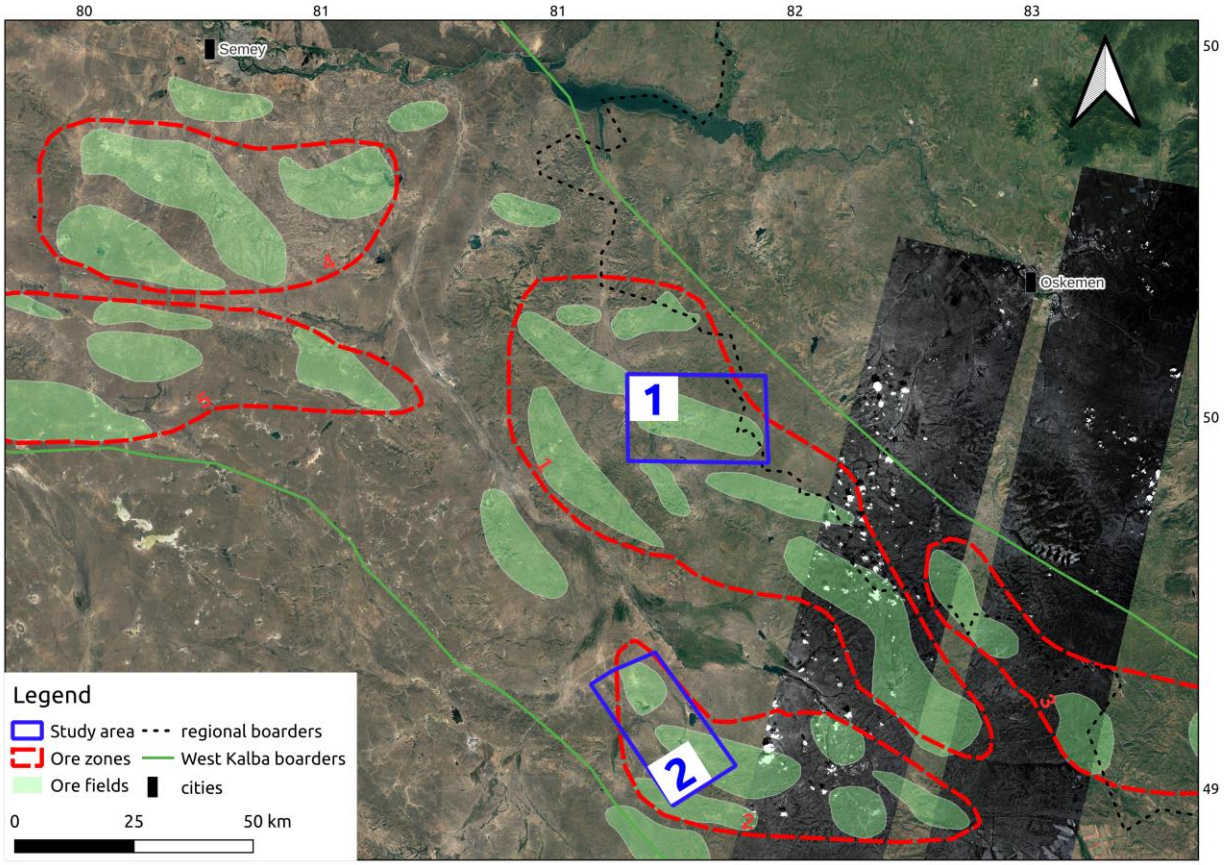

Figure 5.2. EnMAP scene coverage map

The EnMAP datatake was acquired on August 28, 2025, falling within the optimal dry season window (mid-July to mid-October) for Eastern Kazakhstan, ensuring minimal vegetation interference and maximum surface exposure of alteration minerals. This acquisition timing is particularly advantageous for hyperspectral mineral identification, as dry conditions enhance spectral contrast and reduce atmospheric scattering effects. From the available EnMAP datatakes, only one sub-dataset (Folder 4, comprising 50% of the originally downloaded tiles) was utilized for this study. Folder 1 (DT0000144372) was excluded due to extensive cloud cover that obscured critical alteration zones, while Folder 2 was fully cloud-covered and Folder 3 showed spatial offset from the target study areas.

Regarding our study areas, our multispectral and hyperspectral images meet only at two potential deposits in your ore fields. Moreover, due to partial cloud coverage in both of datasets of the territory, we are limited to use it as full potential. Therefore, in this study EnMAP will play a role as a validation part via high-resolution pixel-based spectral signatures. Pixels will be chosen from well-studied and investigated areas/deposits and will be examined carefully on any absorption feat

5.2 Finalizing a Processing Pipeline

This section applies the remote sensing methodology described in Chapter 3 to ASTER data for the West Kalba belt. ASTER Level-2 Surface Reflectance (AST_07XT) products were used directly, eliminating the need for additional atmospheric or geometric correction. The processing workflow focuses on band ratio calculations and spatial mapping of alteration zones across the focus districts of Bakyrchik and Akzhal-Vasilyevskoye (Fig. 5.3). Geological and mineralogical data from published references and the institute mineral museum were integrated to validate spectral signatures and guide interpretation of alteration zones. Manual quality control, including identification and removal of outliers in both raster and vector maps, was performed throughout the processing pipeline to ensure that final products represent genuine mineralogical responses rather than artifacts from vegetation, water bodies, cloud shadows, or other non-geological features. This manual checking and outlier removal is a standard procedure in remote sensing workflows and was applied at multiple stages to maintain data quality. The following subsections detail the specific processing steps applied to this dataset.

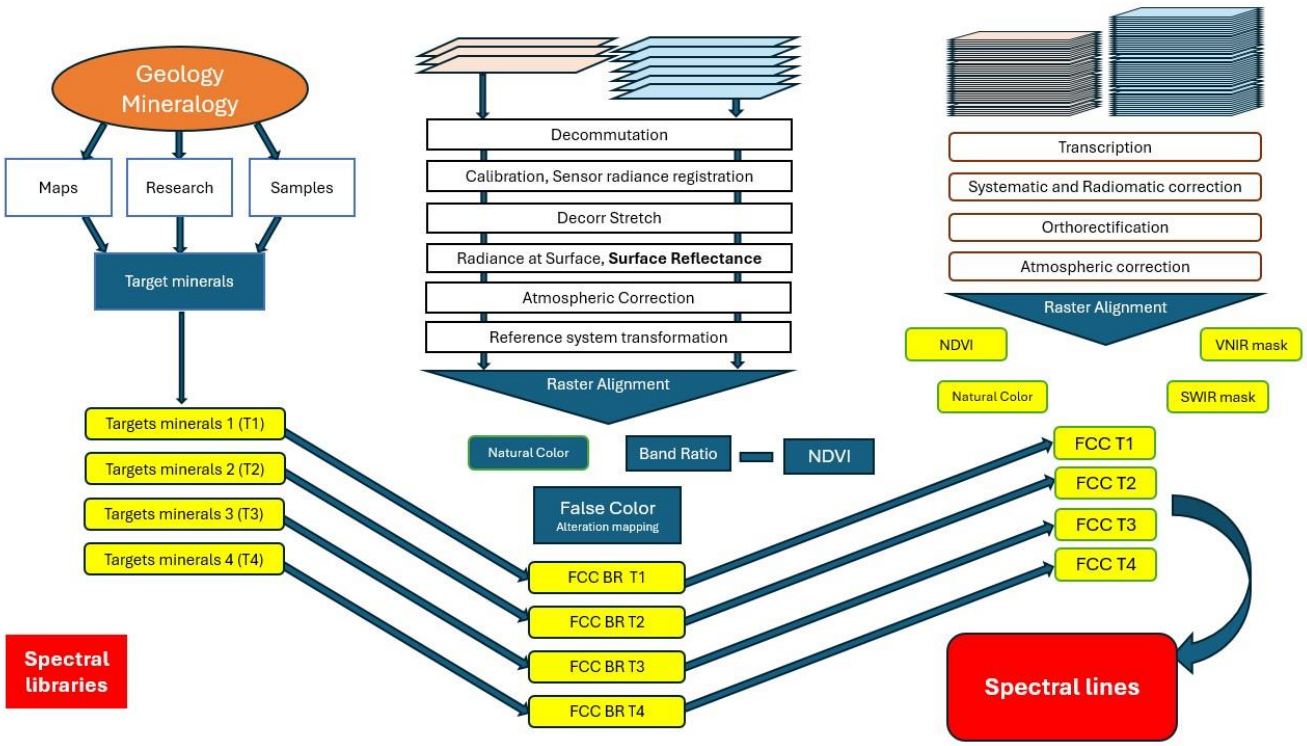

Figure 5.3. Final pipeline

The selection of specific ASTER band ratios for hydrothermal alteration mapping in Eastern Kazakhstan is based on the well-documented mineralogical characteristics of gold deposits in the region, as established through extensive geological and metallogenic studies spanning over a century of exploration [2; 69]. Gold deposits in the West Kalba belt, which hosts more than 450 documented occurrences, are characterized by distinct alteration mineral assemblages that correspond to specific spectral signatures detectable in ASTER SWIR bands (Fig. 5.5). The Bakyrchik-type gold-sulfide deposits, representing the most significant gold mineralization in the region, are associated with carbonaceous-sericite, kaolinite-hydromica (Fig. 5.6), and quartz-sericite metasomatic associations [69].

The six band ratios applied in this study target the key alteration zones summarized in Table 4.3 and described in Chapter 2: phyllic alteration (sericite/muscovite/illite) via B05/B06, argillic alteration (kaolinite-group clays) via B07/B06 and B04/B06, propylitic alteration (chlorite/epidote) via B07/B09, carbonate zones via B09/B08, ferric iron oxides via B02/B01, and ferrous silicates (biotite, chlorite, amphibole) via B05/B04 (Fig. 5.7). These ratios are based on the well-documented mineralogical characteristics of gold deposits in the West Kalba belt (Chapter 2), where alteration assemblages correspond to specific spectral signatures detectable in ASTER SWIR bands [69; 81]. The ferrous silicates ratio (B05/B04) is particularly relevant because gold-bearing sulfides (pyrite, arsenopyrite, chalcopyrite) commonly form through sulfidation of ferromagnesian silicates, where hydrothermal fluids replace biotite, chlorite, and amphibole with Fe-sulfides that host gold in refractory form [77; 78].

Vegetation cover significantly interferes with mineral spectral signatures, particularly in SWIR bands where plant absorption features overlap with mineral diagnostic features, potentially masking or distorting alteration signatures in forested and vegetated areas [7]. To minimize this interference, the Normalized Difference Vegetation Index (NDVI) was calculated for all ASTER scenes using the formula NDVI = (B03N - B02) / (B03N + B02), where B03N (0.78-0.86μm) represents near-infrared reflectance and B02 (0.63–0.69μm) represents red reflectance.

Field observations from the study areas indicate that alteration zones typically exhibit sparse vegetation (NDVI < 0.25) due to elevated concentrations of elements such as arsenic, antimony, and other pathfinder elements that inhibit plant growth, while background areas with normal soil chemistry support denser vegetation with NDVI values exceeding 0.35. Therefore, pixels with NDVI values greater than 0.3 were masked out from subsequent band ratio calculations, ensuring that mineral spectral signatures are not contaminated by vegetation absorption features (Fig. 5.4). This masking procedure improved the signal-to-noise ratio of alteration indices by excluding areas where vegetation spectral features would interfere with mineral identification, allowing for more accurate mapping of hydrothermal alteration zones in the predominantly semi-arid to arid environments of East Kazakhstan.

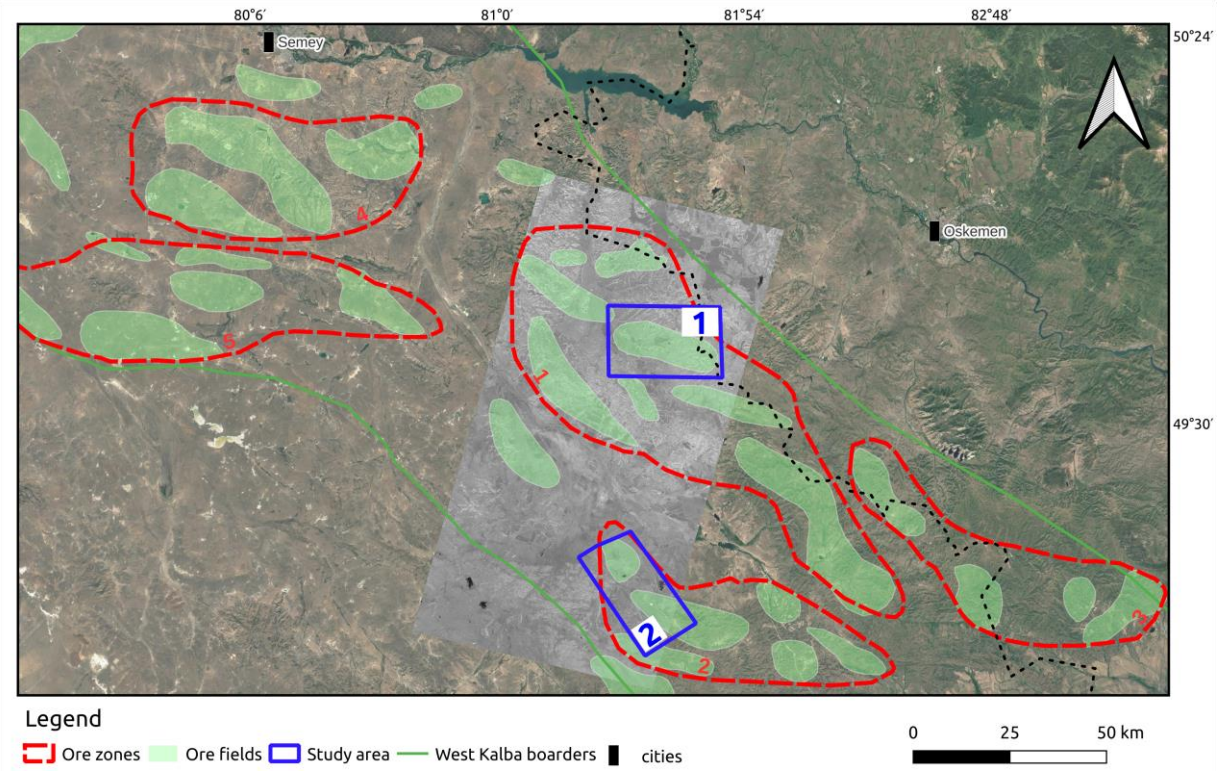

Figure 5.4. Extracted NDVI in singleband grey colors

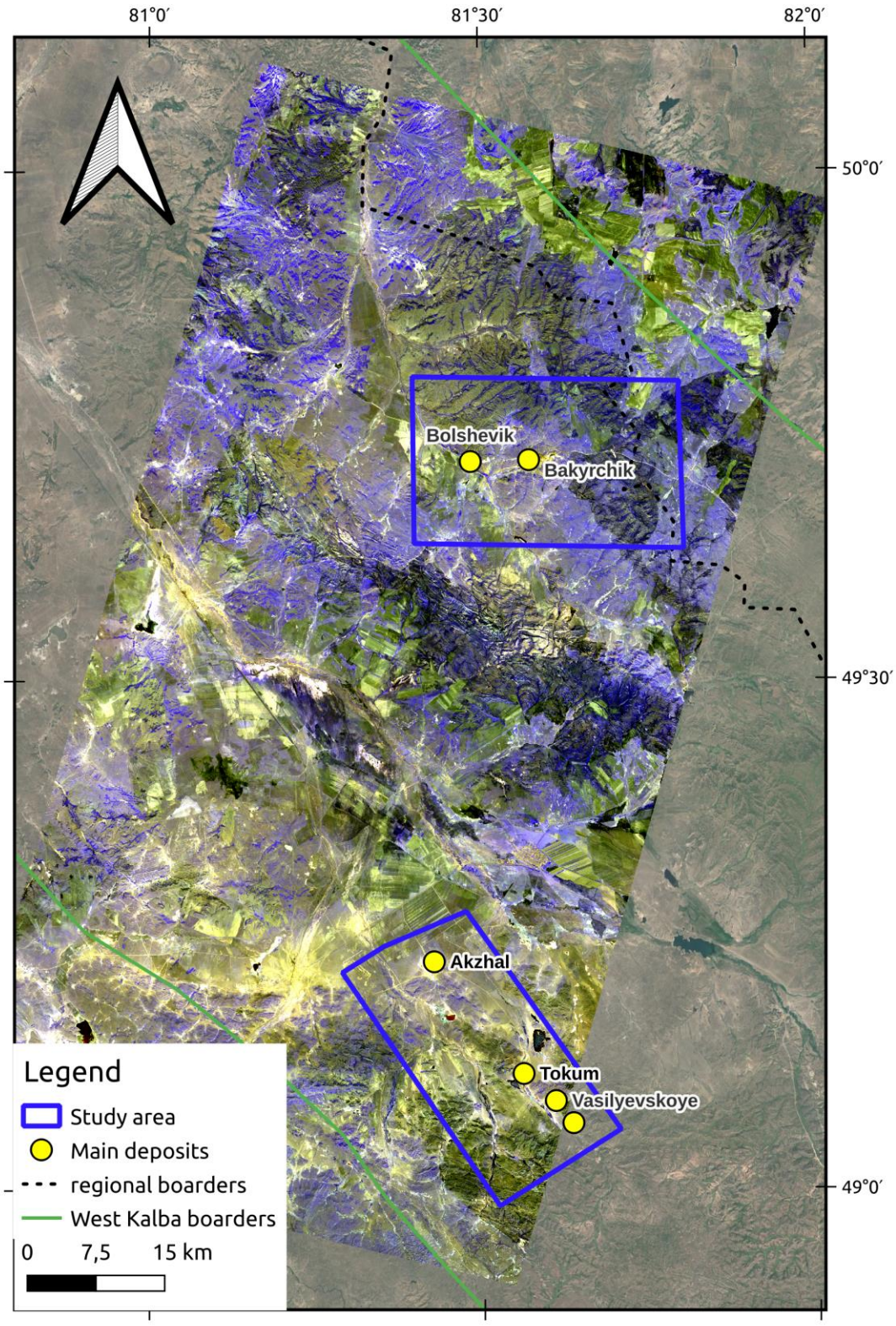

Figure 5.5. False Color Composite of all VNIR-SWIR bands, visualized with B01-B02-B03 with our study areas in blue

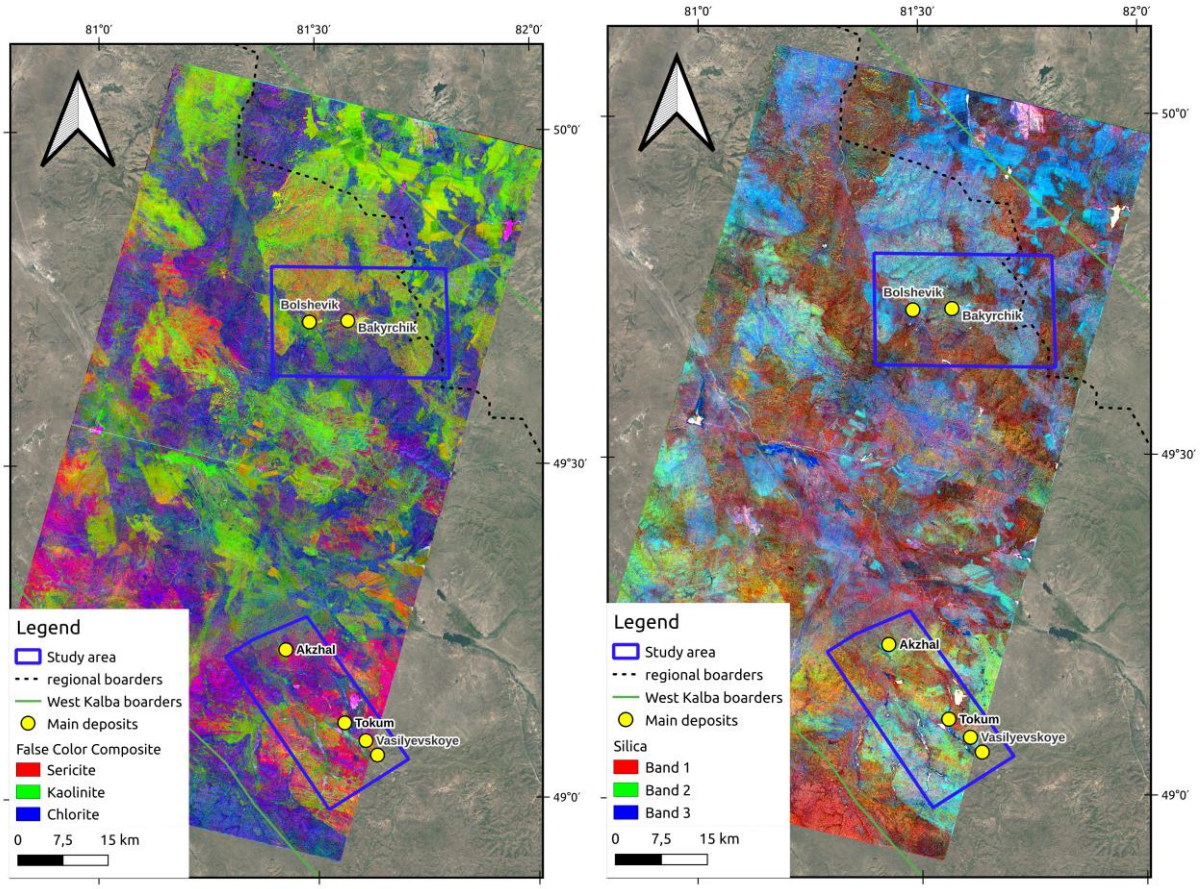

Figure 5.6. False Color Composite for clays and carbonates (left) and silica(right)

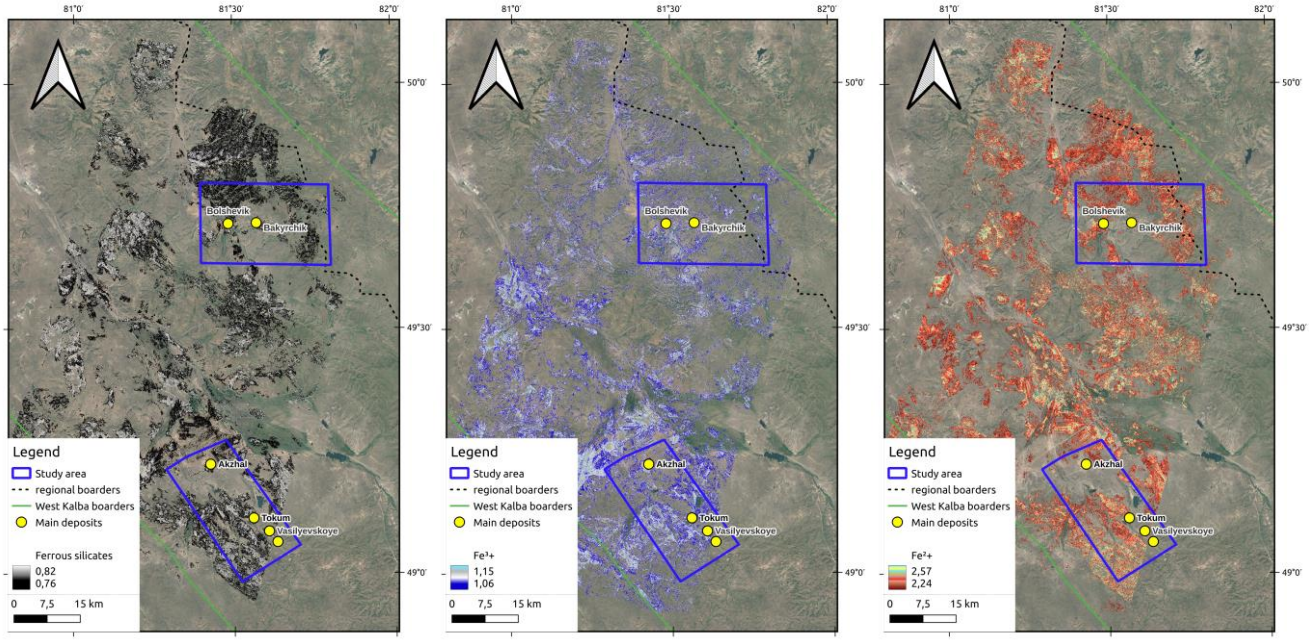

Figure 5.7. Band ratio alteration maps focused on Fe, Fe^{3+} and Fe^{2+} with 90% threshold. From left to right respectively

False Color Composites (FCCs) combine three band ratios into RGB channels to create visually interpretable maps that simultaneously highlight different alteration zones and their spatial relationships (Fig. 5.6). FCCs in this study are organized by mineral groups to emphasize specific alteration assemblages relevant to gold exploration in the West Kalba belt. The sericite–kaolinite–chlorite composite combines phyllic alteration [37] (sericite/muscovite/illite), argillic alteration (kaolinite-group clays), and propylitic halos (chlorite/epidote), highlighting the most diagnostic alteration assemblage for gold mineralization in the region. The quartz composite uses all three RGB channels to target silicification zones and quartz veining, emphasizing areas where quartz-dominant host rocks are enhanced through hydrothermal silicification. The iron oxides composite combines ferrous iron, ferric iron and ferrous silicates (biotite, chlorite, amphibole) to highlight iron-related responses, including near-surface oxidation products and sulfidation zones where ferromagnesian silicates have been replaced by Fe-sulfides. This grouping approach enables systematic examination of alteration patterns and their spatial relationships, supporting identification of prospective zones where multiple alteration indicators co-occur.

5.3 Correlation of mineral deposits and alteration mapping results

We validate the FCC composites and merged band-ratio mosaics by correlating their alteration signatures with two independent object groups: documented mineral deposits (Bakyrchik and Akzhal-Vasilyevskoye ore fields) and the broader geological exploration footprints that delineate known alteration corridors (Fig. 5.8).

For each deposit we check that the expected alteration zones from Table 4.3 correspond to the predicted FCC colors and that the merged ratio rasters spatially overlap the mapped exploration footprints. This dual comparison lets us quantify ASTER the spectral precision (which alteration zones are highlighted) and the spatial precision (which size/extent of mapped objects are recovered), providing a quantitative basis for claiming that the remote sensing workflow reliably captures the mineralogical and spatial expression of the targeted hydrothermal systems.

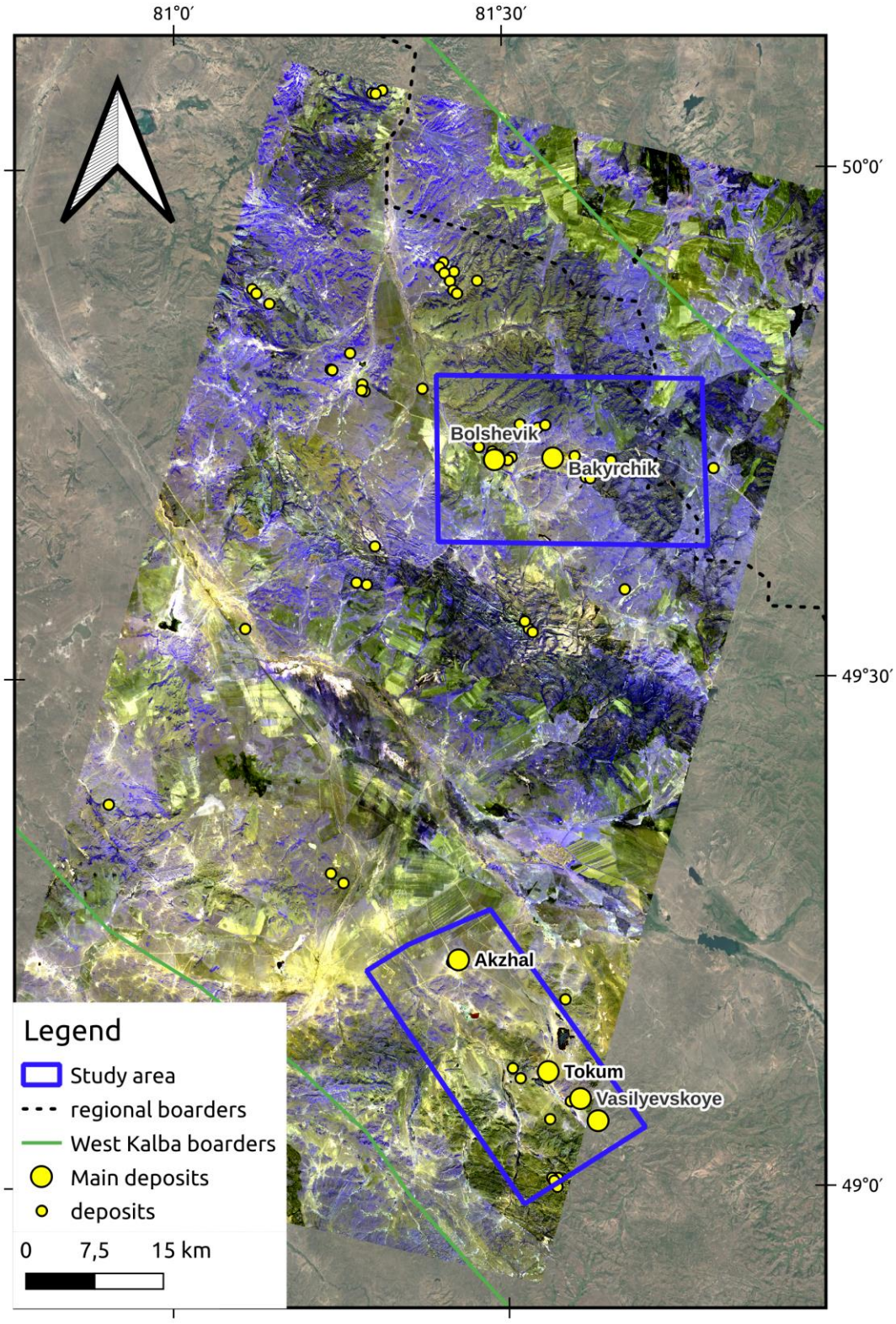

Figure 5.8. Total deposits and geological excavations on a full VNIR - SWIR FCC

Fig. 5.8 summarizes the correlation results: across the Bakyrchik and Akzhal-Vasilyevskoye focus districts, we identify 80+ mineral deposit and geological traces that spatially coincide with ASTER-derived alteration anomalies and show mineralogical consistency with the expected zonation. In the Bakyrchik ore field (including the Bolshevik deposit), matched locations are most commonly characterized by phyllic/beresite and carbonate responses (Al-OH and CO-bearing assemblages), consistent with the sericite-carbonate alteration halos typical of black-shale-hosted Au-sulfide systems mainly by quartz [77; 78]. In the Akzhal-Vasilyevskoye district, matched locations preferentially align with structurally focused phyllic and carbonate anomalies, with iron-oxide responses marking oxidation features where exposed [69].

5.4 Bakyrchik ore field: alteration expression and deposit correlation

The Bakyrchik ore field provides the clearest endmember for testing ASTER-based alteration mapping in the West Kalba belt (Fig. 5.9), because its mineralization is hosted by carbonaceous terrigenous strata and is accompanied by laterally extensive metasomatic halos [78]. In geological terms, the dominant alteration pattern is a sericite–carbonate (beresite/listvenite-type) overprint developed along ore-controlling shear zones and fractured corridors, with outer transitions to chlorite–epidote assemblages [77]. The ore mineralization is dominated by ferrous sulfides, primarily pyrite and arsenopyrite, which host gold in refractory form as micro- to submicroscopic particles within the sulfide lattice. Gold is predominantly hosted by pyrite and arsenopyrite (95–97%), with the remaining fraction occurring in other phases [77]. These sulfides occur within quartz–carbonate assemblages, aligning with the multistage mineralization sequence described in Chapter 2 where gold–pyrite–arsenopyrite associations are followed by gold–quartz–polymetallic assemblages [77; 78]. Modal analysis reveals quartz-dominant host rocks with substantial sericitic material (23.03%) and minor carbonates (3.45%) [77], providing a mineralogical framework that is well suited for multispectral detection. This mineralogical architecture is well suited for multispectral detection because the alteration halos combine strong Al–OH absorbers (sericite/illite) and CO_2 absorbers (carbonate minerals) [80], even though the main ore sulfides themselves are spectrally featureless at ASTER wavelengths [69].

At the district scale, False Color Composites (FCCs) combining phyllic and propylitic alteration zones reveal the spatial distribution of sericite, kaolinite, and chlorite alteration across the Bakyrchik ore field (Fig. 5.6 left). These composites highlight the sericite–carbonate (beresite/listvenite-type) alteration pattern that characterizes the ore-controlling structures, with sericitic material and carbonates forming the dominant alteration assemblage [77]. Chlorite responses mark distal propylitic halos, providing context for the broader alteration system.

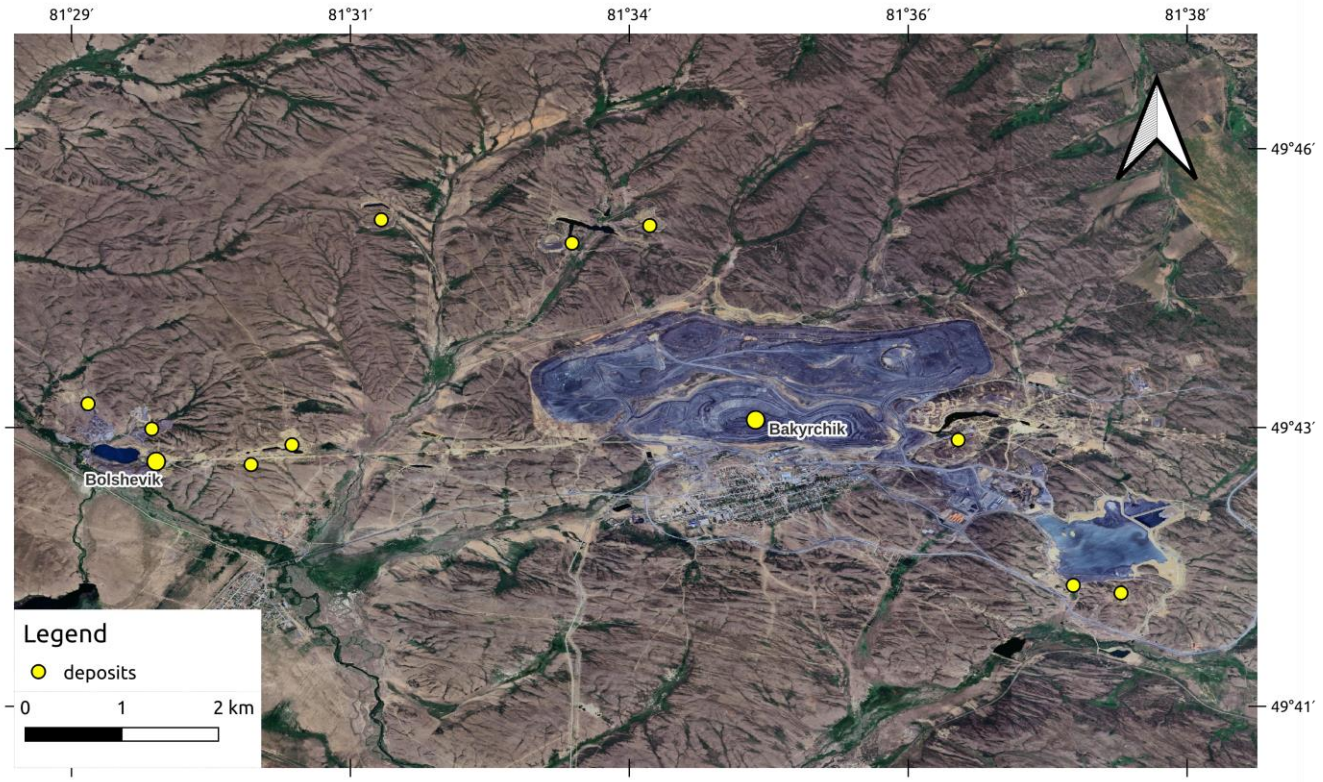

Figure 5.9. Mineral deposits at Bakyrchik ore zone.

Silicification zones and quartz veining are visualized through FCCs that emphasize areas of hydrothermal silicification (Fig. 5.10, top). The full-scale composite shows the overall distribution of silicification zones, while the 85% threshold enhancement isolates the strongest anomalies (Fig. 5.10, bottom), revealing localized patches and linear zones that mark areas of intense silicification and quartz veining associated with ore-controlling structures [77]. These silicification zones highlight areas where quartz-dominant host rocks at 52.65% modal abundance) are enhanced through hydrothermal silicification, consistent with the quartz–carbonate assemblages that host ferrous sulfides and gold mineralization [77]. The spatial correlation between strong silicification zones and ore zones supports the interpretation that silicification and quartz veining are key components of the alteration system, providing structural permeability and gangue material for gold–pyrite–arsenopyrite mineralization [78].

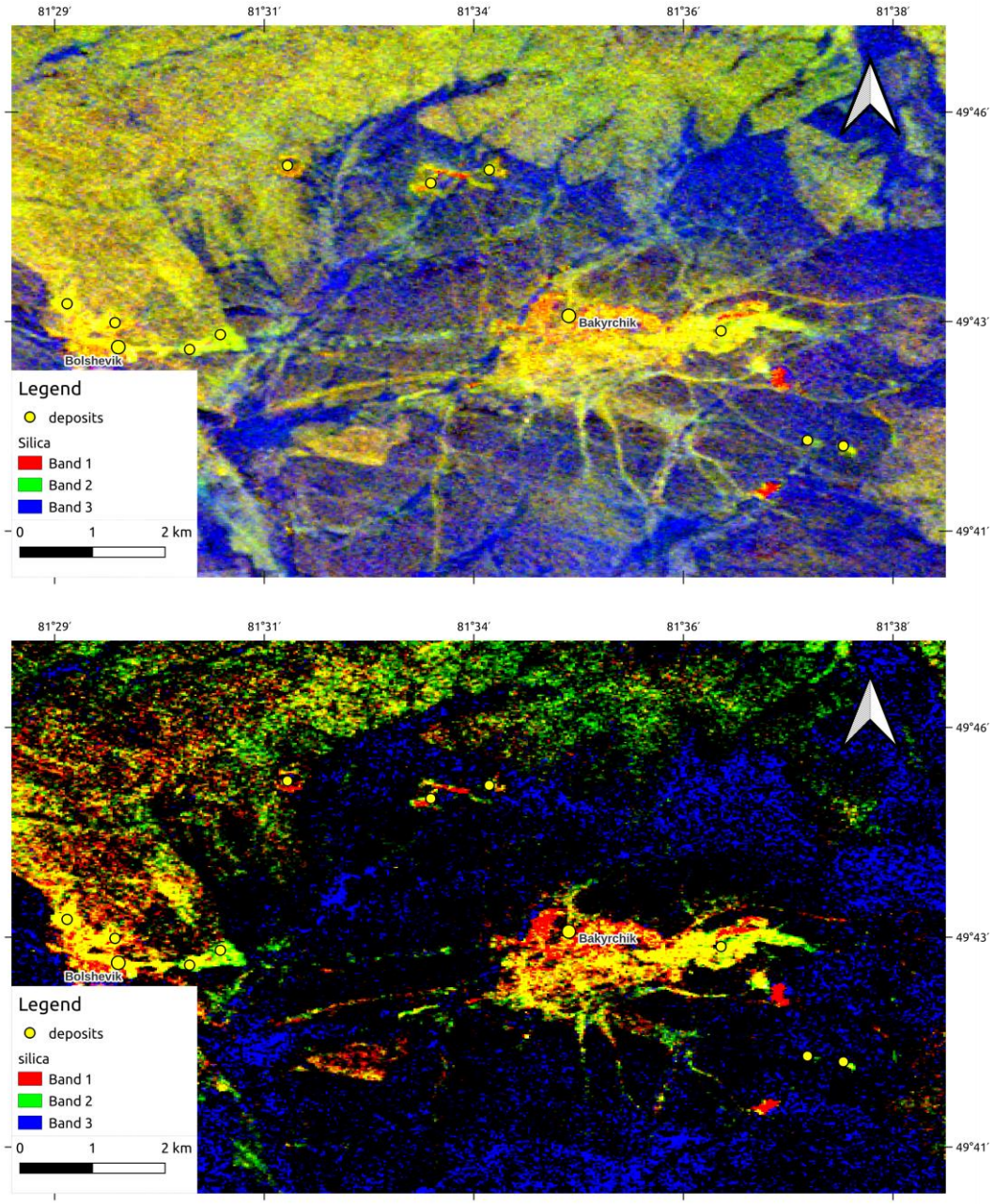

Figure 5.10. False Color Composite for Bakyrchik ore field showing silicification zones and quartz veining: top - full scale; bottom - 90% threshold enhancement

Fig. 5.10 not only shows strong correlation of quartz-rich zones and biggest mineral deposits on Bakyrch in ore field, but Band 2 follows the structural model of the area and supporting the fact of mineralization location along the structural features as in this case of faults.

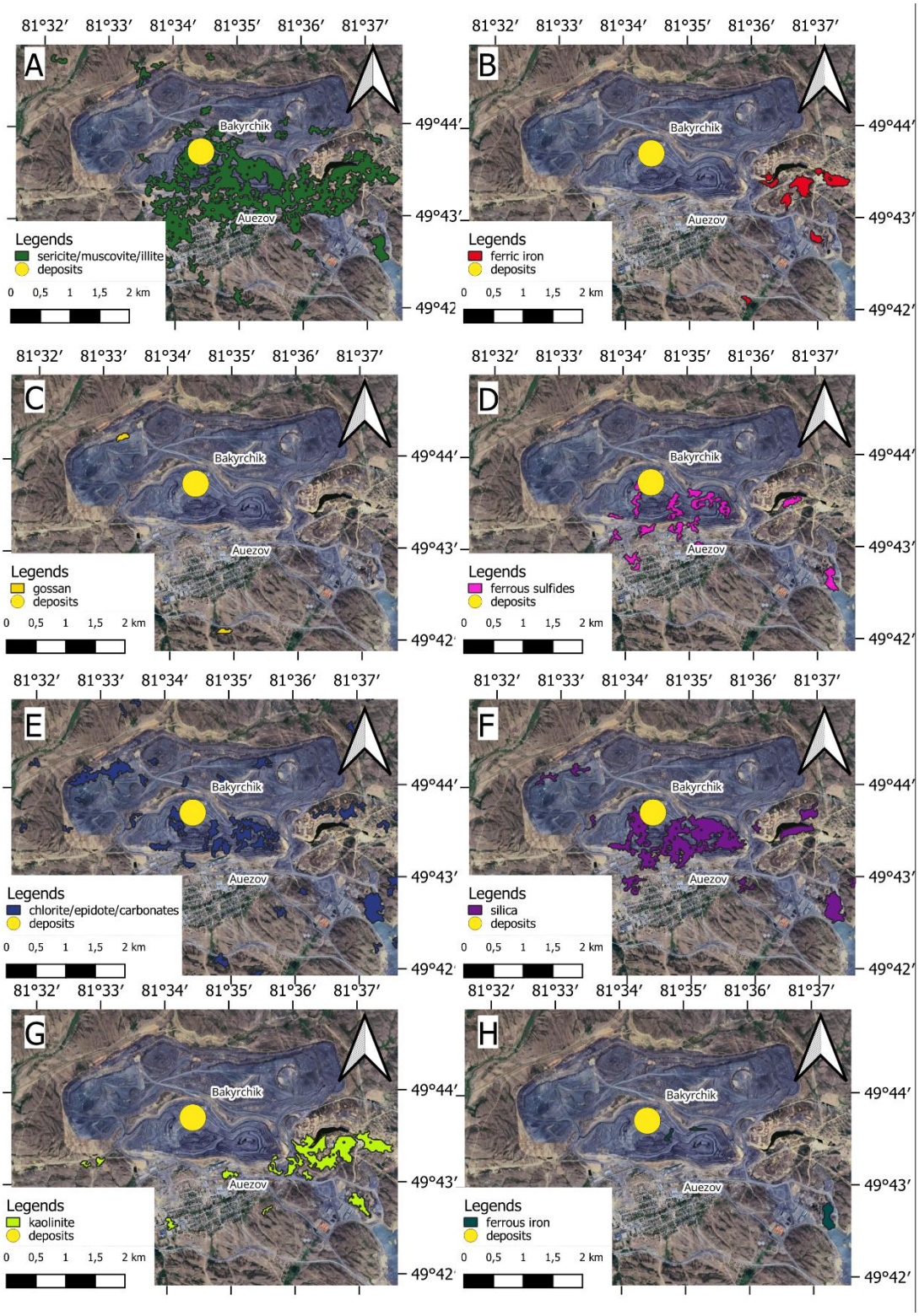

Figure 5.11. Individual band ratio maps for Bakyrchik deposit: A - phyllic alteration (sericite/muscovite/illite, Al–OH), B - oxidation zones (ferric iron), C – gossan deposits, D – sulfide-bearing zones (ferrous sulfides), E – propylitic alteration (chlorite/epidote/carbonates, Mg–OH), silicification zones (silica), G – kaolinite deposits, and H – ferrous iron

Individual band ratio maps isolate specific alteration zones to examine their spatial patterns independently (Fig. 5.11). The sericite map (Al–OH phyllosilicates) shows strong responses along ore-controlling shear zones and fractured corridors, reflecting the dominant phyllic alteration pattern. Chlorite responses (Mg–OH silicates) outline broader, lower-contrast distal halos. Silica responses highlight zones of silicification and quartz veining, consistent with the quartz-dominant host rock composition.

Ferrous sulfide zones, while spectrally featureless themselves, are inferred from spatial associations with silica and sericite responses, supporting the laboratory-confirmed occurrence of pyrite and arsenopyrite within quartz–carbonate assemblages. Ferric iron responses occur as localized patches, interpreted as near-surface oxidation products.

The spatial correlation overlay map Fig. 5.12 combines multiple band ratios to demonstrate mineral associations and structural relationships. The top panel shows a three-element overlay (sericite, silica, ferrous sulfides) that highlights the most informative pattern: the coupled occurrence of silica and Al–OH phyllosilicates adjacent to ferrous-sulfide responses, aligning with the ore mineralogy and gangue described in Chapter 2 [77].

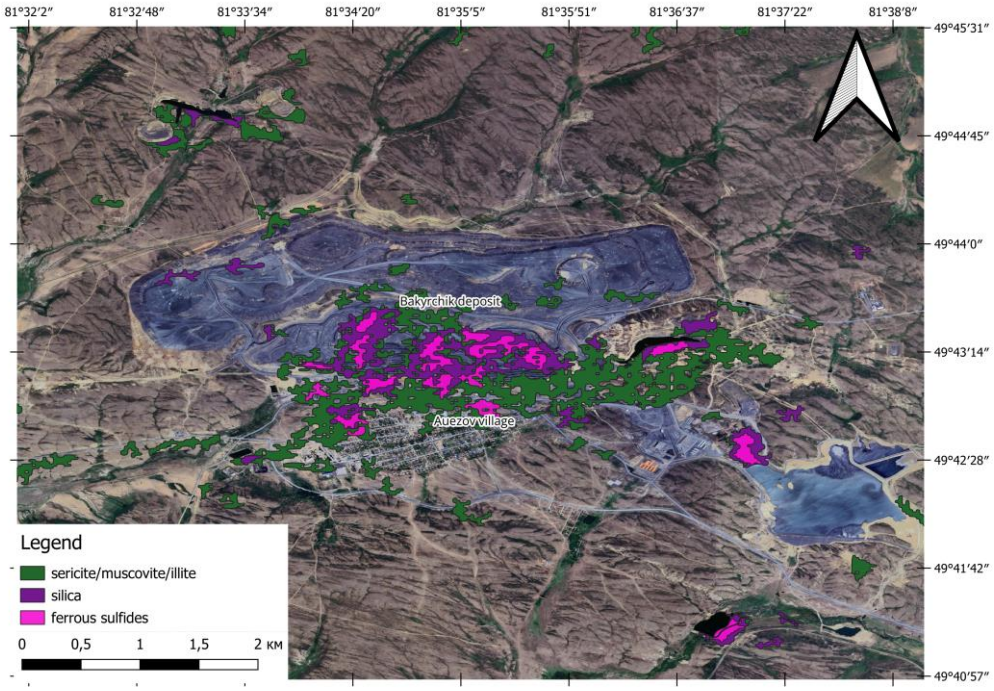

Figure 5.12. Spatial correlation overlay map for Bakyrchik ore field: three-element overlay of sericite, silica, ferrous sulfides

The Figure 5.13 shows expanding view including chlorite/epidote and ferrous iron occurances. A key observation from this expanded overlay is that ferrous iron responses are consistently correlated with sericite–muscovite–illite zones and are spatially decoupled from quartz-rich areas. This pattern is geologically significant because quartz

rarely hosts ferrous iron group minerals (hematite, goethite, etc.), and instead, ferrous iron in this system appears to be associated with phyllic alteration assemblages rather than silicification zones [78].

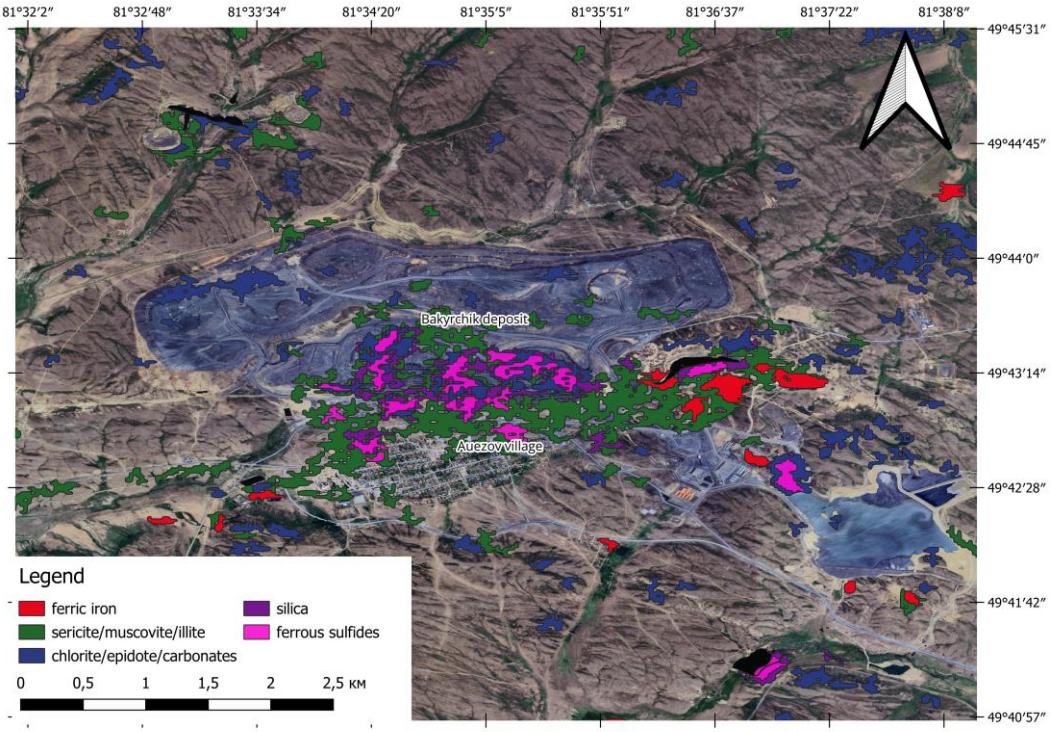

Figure 5.13. Spatial correlation overlay map for Bakyrchik ore field: five-element overlay showing sericite, chlorite/epidote, silica, ferrous sulfides, and ferrous iron to demonstrate mineral associations and structural relationships

The strongest anomalies are spatially tied to the Kyzylkovskaya fault corridor and the main disturbed/mine zone, forming coherent, belt-parallel footprints that outline the most altered structural corridors [64]. In the northwestern part of the map center, two excavation-related halos are visible: the altered host signature (sericite/muscovite/illite) forms a tight envelope around the disturbed surfaces, consistent with removal of upper material during mining and preservation of altered wall-rocks along pit margins. Ferric iron and gossan zones occur as more localized patches and streaks, interpreted as near-surface oxidation and exposure effects rather than a continuous ore footprint. Unlike ferrous sulfides, which trap gold in refractory form, ferric and ferrous iron minerals do not host gold and are therefore of non importance for exploration targeting (Table 4.3).

The Bolshevik deposit, located in the western segment of the Kyzylov ore zone, represents another great example of Bakyrchik-type black-shale-hosted Au-sulfide mineralization within the same structural corridor [77; 78]. Like Bakyrchik, Bolshevik is confined to the Kyzylov shear zone and exhibits similar sericite–carbonate (beresite/listvenite-type) alteration patterns, with gold predominantly hosted by pyrite and arsenopyrite in refractory form [77]. The deposit has been in production since 1960, with

reported production totaling 4477.2 kg Au at an average grade of 5.9 g/t, and remaining balance reserves of C_1 13,585 kg at 7.02 g/t and C_2 18,260 kg at 6.08 g/t [78; 77].

Individual band ratio maps for Bolshevik (Fig. 5.14) reveal strong sericite (Al–OH phyllosilicates) responses along the ore-controlling structure, consistent with the dominant phyllic alteration pattern. Chlorite responses outline broader distal propylitic halos, while silica responses highlight zones of silicification and quartz veining. Gossan responses are particularly prominent at Bolshevik, reflecting the presence of oxidized ores developed to shallow depths and the near-surface expression of iron-oxide/hydroxide minerals (goethite, hematite, limonite) formed through oxidation of ferrous sulfides (Fig. 5.15) [77].

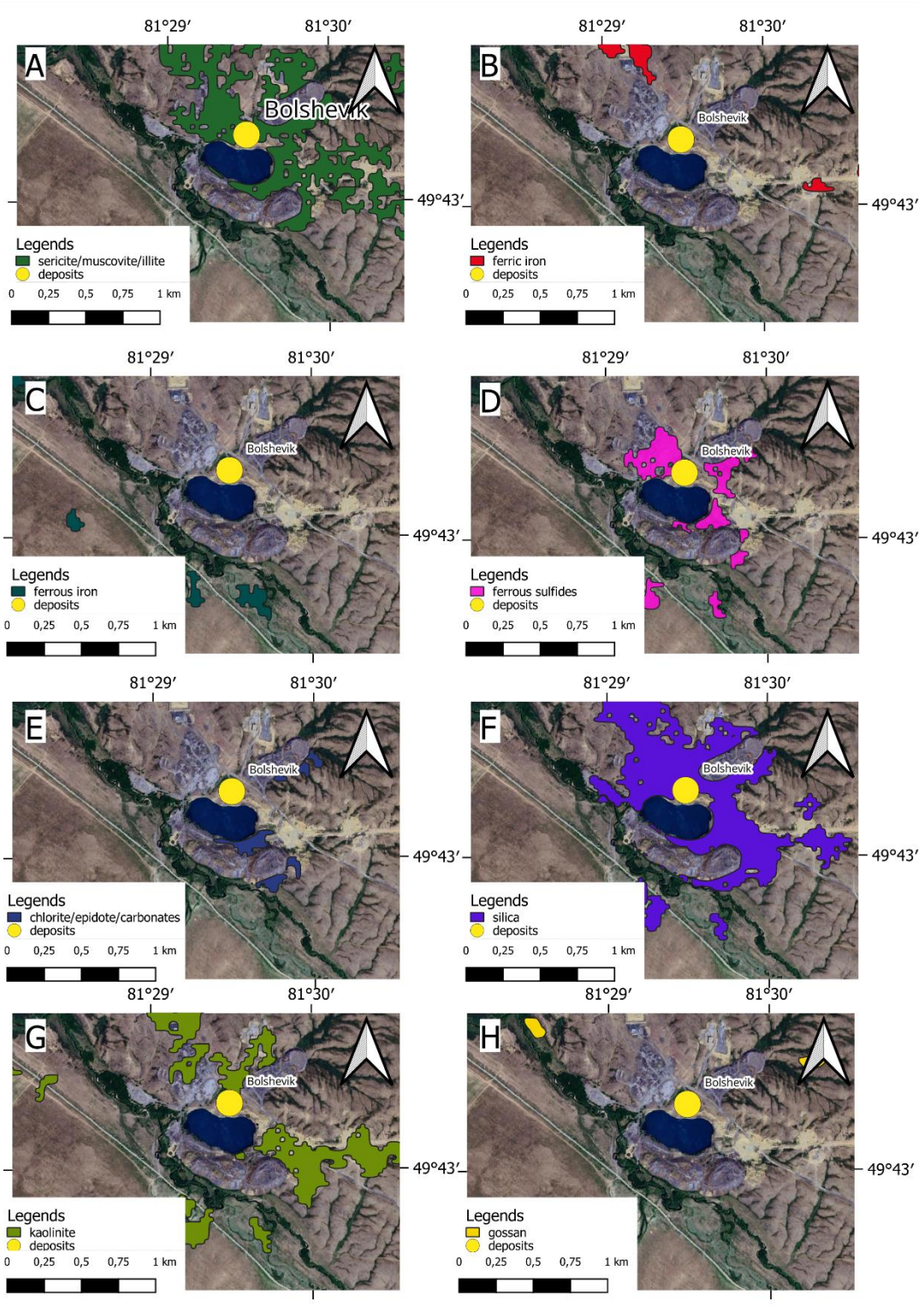

Figure 5.14. Individual band ratio maps for Bolshevik deposit: A - phyllic alteration (sericite/muscovite/illite, Al–OH), B - oxidation zones (ferric iron), C – gossan deposits, D – sulfide-bearing zones (ferrous sulfides), E – propylitic alteration (chlorite/epidote/carbonates, Mg–OH), silicification zones (silica), G – kaolinite deposits, and H – ferrous iron

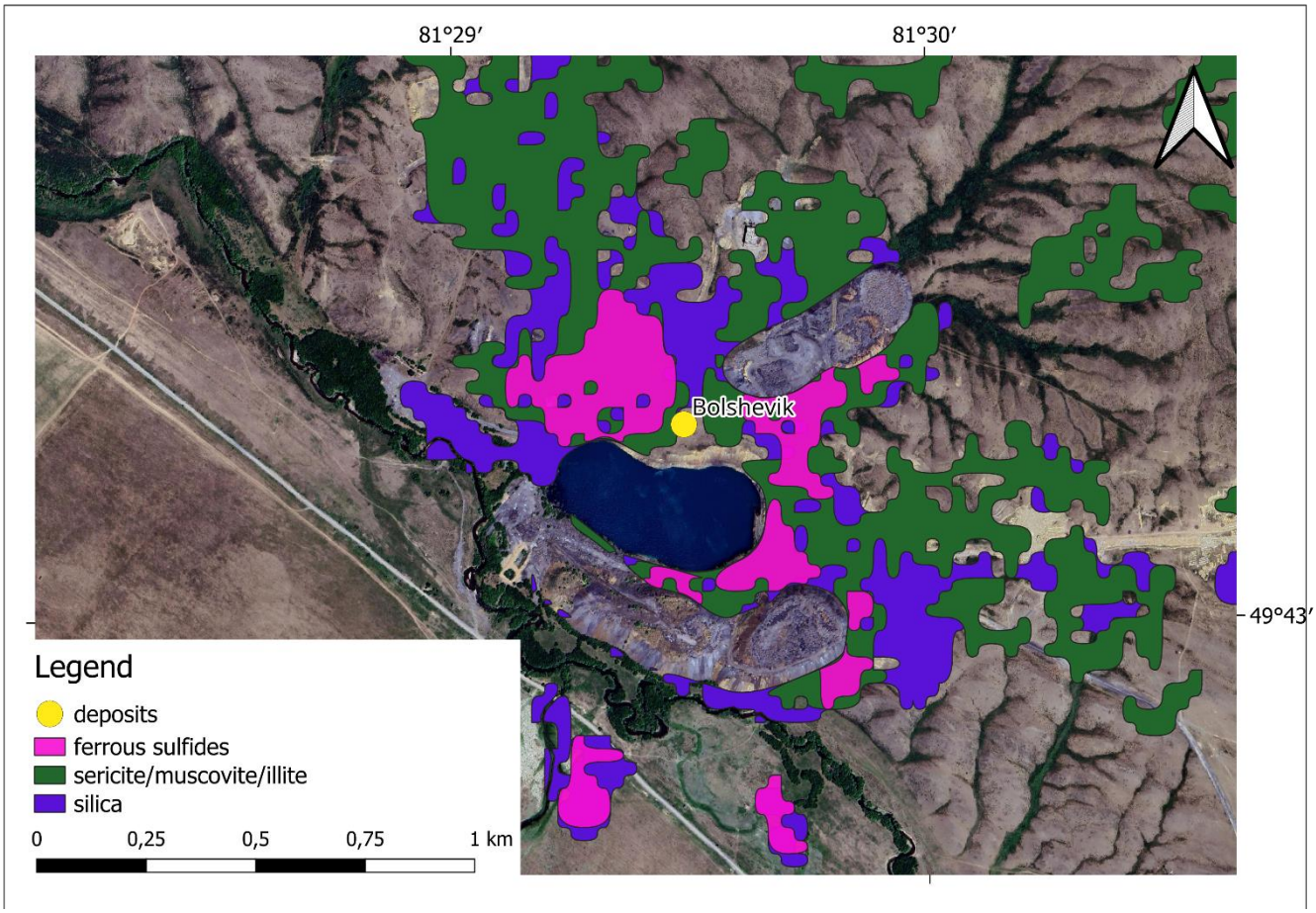

Figure 5.15. Spatial correlation overlay map for Bolshevik ore field on five-element overlay showing sericite, chlorite/epidote, silica, ferrous sulfides, and ferrous iron to demonstrate mineral associations and structural relationships

Deposit locations are indicated. Spatial correlation overlay map for Bolshevik ore field: top - three-element overlay (sericite, silica, ferrous sulfides); bottom - five-element overlay showing sericite, chlorite/epidote, silica, ferrous sulfides, and ferrous iron to demonstrate mineral associations and structural relationships. Deposit locations are indicated.

Ferrous sulfide zones, inferred from spatial associations with silica and sericite responses, mark the primary ore zones where pyrite and arsenopyrite host gold in refractory form. Ferric iron responses occur as localized patches, interpreted as near-surface oxidation products and gossan development above sulfide-bearing zones [78]. The spatial correlation between sericite, silica, and ferrous sulfides at Bolshevik reinforces the pattern observed at Bakyrchik, supporting the interpretation that coupled “quartz–sericite/illite + ferrous sulfides” responses provide reliable indicators for Bakyrchik-type gold systems.

Overall, the Bakyrchik area demonstrates that the selected band ratios and FCC composites recover the expected alteration zonation at district scale: a strong phyllic–

carbonate core associated with mineralized structures, surrounded by weaker propylitic halos and locally enhanced iron-oxide signals in oxidized near-surface domains [77; 69]. This supports the use of ASTER products for rapid screening of Bakyrchik-type black-shale-hosted Au–sulfide systems, where alteration minerals provide a more reliable remote-sensing target than the ore minerals themselves.

5.5 Akzhal–Vasilyevskoye district: alteration expression and deposit correlation

The Akzhal–Vasilyevskoye district represents a structurally controlled vein/beresite endmember within the West Kalba belt, where ore localization is strongly tied to major fault systems and their subsidiary splays [69; 81].

In contrast to Bakyrchik-type black-shale systems with broad, laterally persistent halos, the expected surface alteration footprint in Akzhal–Vasilyevskoye is typically more linear and corridor-like, reflecting narrow zones of fracturing, silicification, beresitization, and associated carbonatization along fault-controlled fluid pathways [81].

From an alteration-mineral perspective, the most diagnostic expectations for Akzhal–Vasilyevskoye are prominent phyllic/beresite responses (sericite/illite/muscovite) along ore-controlling structures and in wall-rock halos around veins and crush zones (Fig. 5.16) [69], carbonate responses where carbonatization/listvenitization accompanies the beresite overprint [81]; and localized Fe^{3+} anomalies where oxidation caps, gossans, or weathered profiles are developed above sulfide-bearing zones [69]. Propylitic signatures (chlorite/epidote) are expected to be present mainly as distal halos or as background responses in volcanic-terrigenous host rocks, and therefore tend to be lower contrast and less specific when interpreted alone [81].

In Akzhal–Vasilyevskoye, the district-scale footprint is dominated by alteration of sericite/muscovite/illite (Red) and silicification zones, whereas iron-related responses are more discontinuous and commonly coincide with exposed surfaces and disturbed ground [69].

Ferrous-sulfide patches are most consistently observed where silicification zones and Al–OH phyllosilicates overlap, supporting the ore-targeting interpretation that the coupled quartz–sericite/illite + ferrous sulfides pattern is a stronger indicator than isolated iron anomalies [69; 81]. Where ferric iron (Fe) or ferrous iron (Fe) responses dominate locally, they are treated as near-surface appearance features associated with oxidation fronts, gossans, and exposure conditions, consistent with Chapter 2’s description of supergene products above sulfide-bearing zones [77; 78].

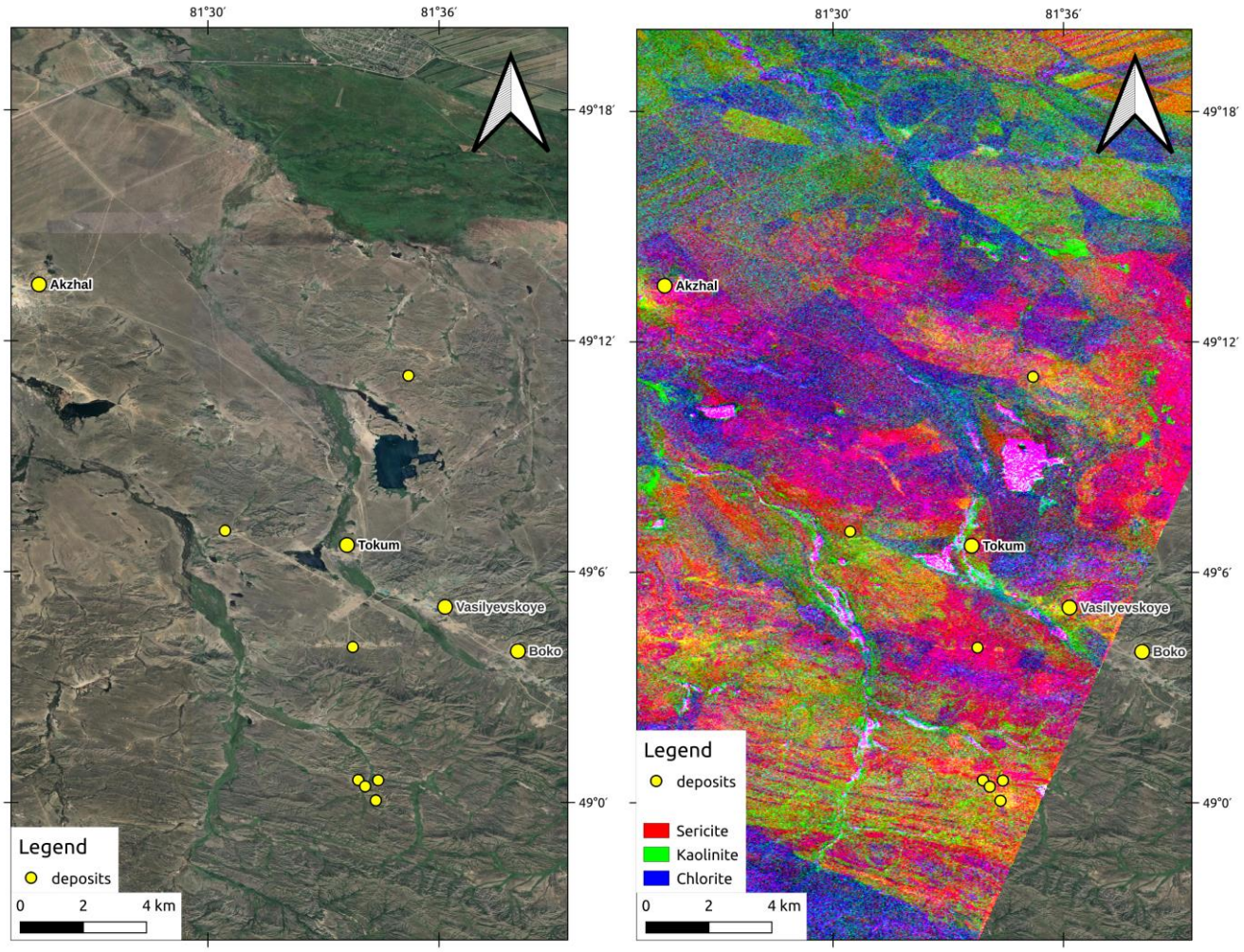

Figure 5.16. Akzhal-Vasilyevskoye complex mineral deposits: left - clean map; right - alteration mapping with phyllic, agrillic and propylitic minerals. Akzhal-Vasilyevskoye complex mineral deposits: left - clean map; right - alteration FCC map with sericite, kaolinite and chlorite

To evaluate these associations at deposit scale, we compare the spatial co-occurrence of alteration zones for Akzhal and Vasilyevskoye, focusing on whether ferrous sulfides coincide with silicification zones and sericite/muscovite/illite, and whether iron-related zones occur as localized surface expressions (Fig.5.17, 5.18).

The correlation results in the Akzhal–Vasilyevskoye area indicate that ASTER-derived products recover these expected patterns with good spatial fidelity at district scale: deposits and exploration targets align preferentially with phyllic and carbonate anomalies that form continuous or semi-continuous structural corridors, and iron-oxide responses highlight near-surface oxidation where exposure conditions permit [69; 81].

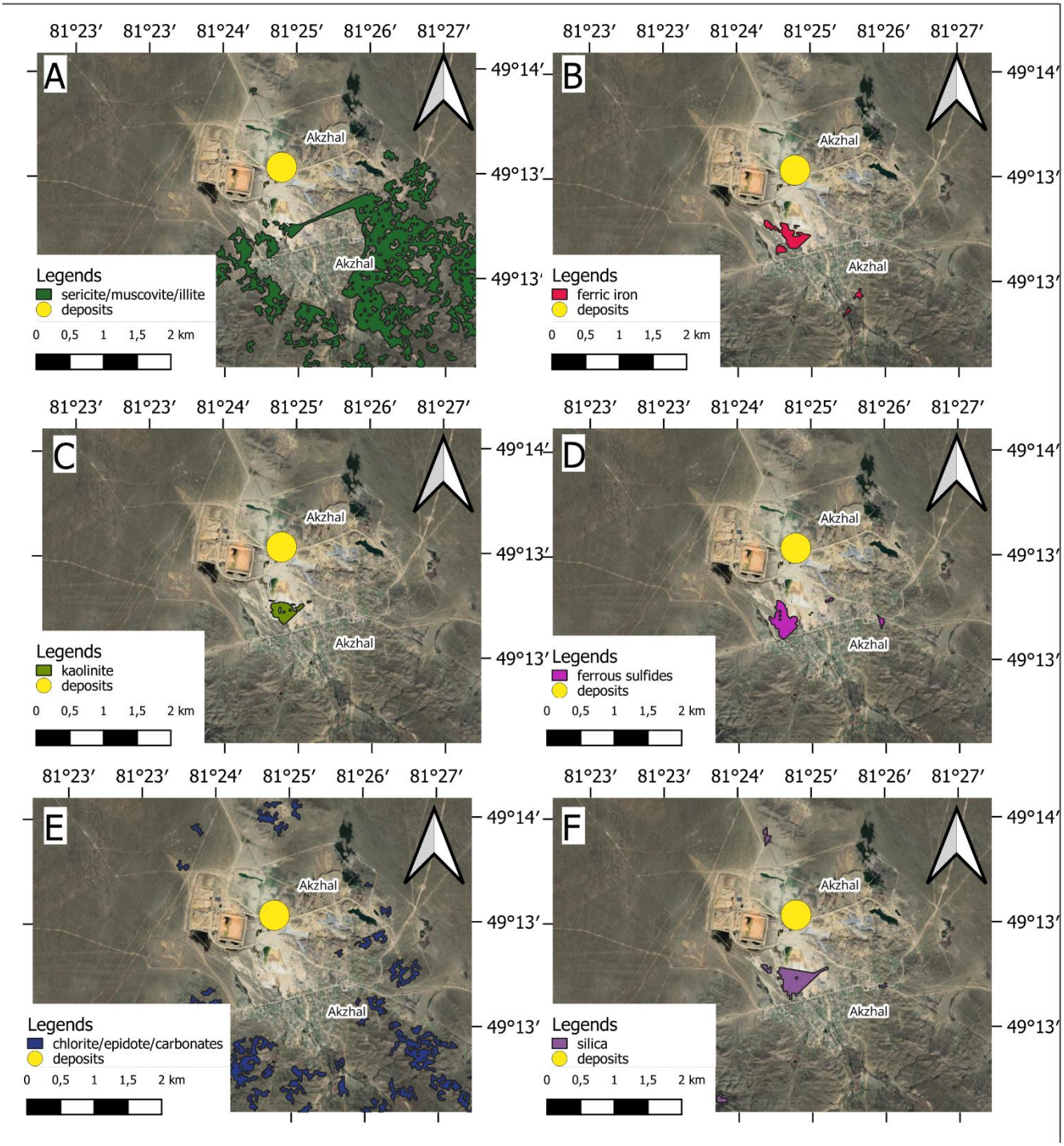

Figure 5.17. Individual band ratio maps for Akzhal deposit: A - phyllic alteration (sericite/muscovite/illite, Al–OH), B - oxidation zones (ferric iron), C – kaolinite deposits, D – sulfide-bearing zones (ferrous sulfides), E – propylitic alteration (chlorite/epidote/carbonates, Mg–OH), silicification zones (silica)

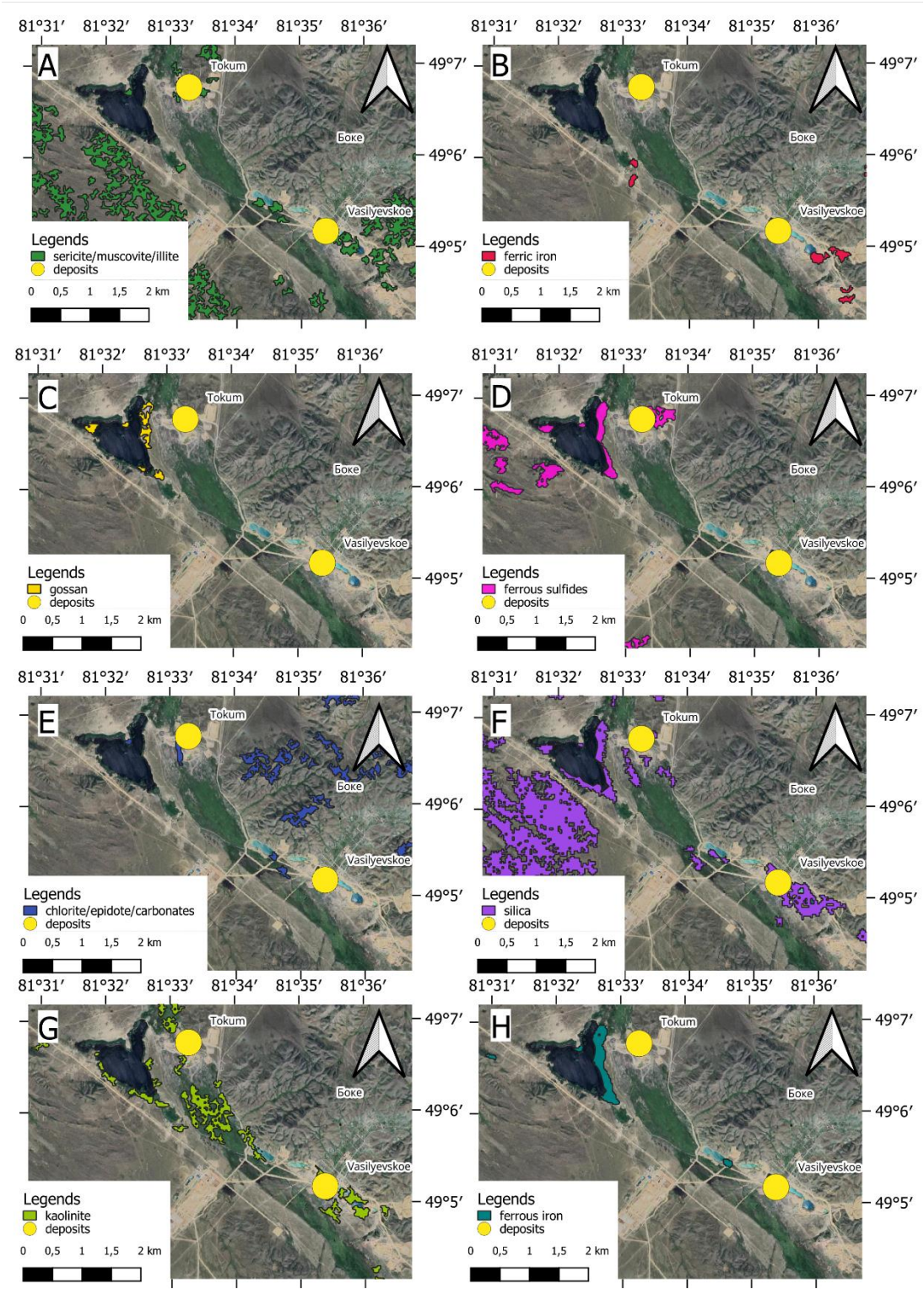

Figure 5.18. Individual band ratio maps for Vasilyevskoye deposit: A - phyllic alteration (sericite/muscovite/illite, Al–OH), B - oxidation zones (ferric iron), C – gossan deposits, D – sulfide-bearing zones (ferrous sulfides), E – propylitic alteration (chlorite/epidote/carbonates, Mg–OH), silicification zones (silica), G – kaolinite deposits, and H – ferrous iron

In practice, FCC composites integrate these alteration zones more effectively than any single ratio map; the combined color patterns improve interpretability of narrow alteration traces and reduce ambiguity caused by lithologic background variability. This makes the Akzhal–Vasilyevskoye district a strong case where ASTER mapping is not only detecting alteration minerals, but also reproducing the expected structural style of the hydrothermal footprint (fault-focused, corridor geometry) that governs ore localization in the district [69; 81].

Geological exploration traces (trenches, pits, small workings, and minor altered exposures) are often sub-pixel or only weakly expressed in any single ASTER band-ratio map, because each ratio isolates one mineral group and is sensitive to local background lithology and illumination. In practice, the FCC composites provide a clearer and more reliable way to recognize these small targets: by combining complementary alteration zones (Fig. 5.19) (e.g., Fe^{3+} for oxidation zones, Al–OH for phyllic/beresite alteration, and Mg/Fe–OH for propylitic halos) into a single color space, FCCs amplify subtle spectral contrasts and make linear or clustered alteration traces visually coherent even when their footprints are smaller than the 30 m SWIR pixel size. Therefore, for rapid screening and interpretation of geological traces, FCC-based inspection is more efficient and interpretable than relying on individual band-ratio layers alone.

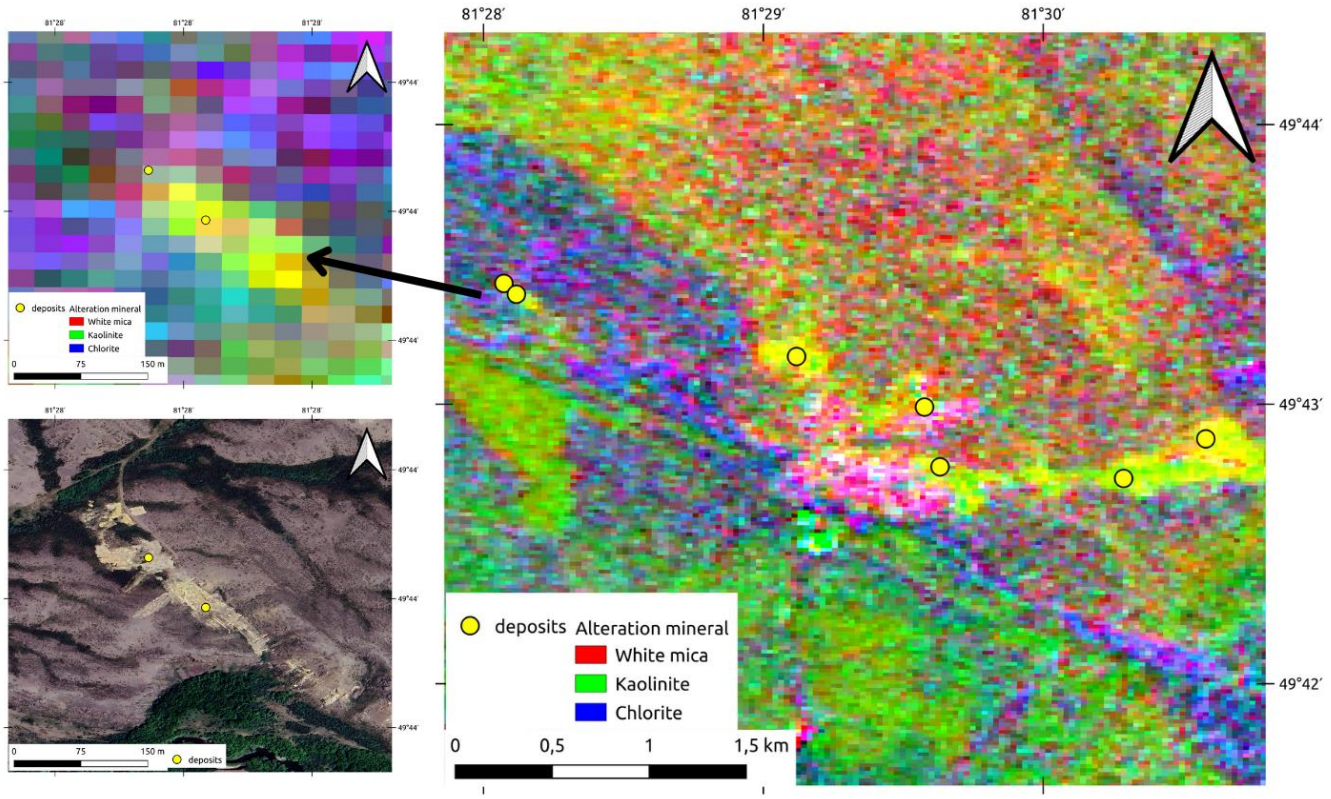

Figure 5.19. Geological exploration trace being detected by ASTER spectroscopy

5.6 Validation of Mineral Absorption Features Using EnMAP Hyperspectral Remote Sensing

While ASTER multispectral data provide the primary dataset for district-scale hydrothermal alteration mapping in this study, hyperspectral remote sensing offers enhanced spectral resolution that enables direct identification of specific mineral absorption features. As mentioned in Section 5.1, the EnMAP hyperspectral dataset does not provide complete spatial coverage of the Bakyrchik and Akzhal-Vasilyevskoye focus districts analyzed in this chapter; however, pixel-based spectral signatures can be extracted from available EnMAP tiles to validate the mineralogical interpretation of ASTER-derived alteration zones and to demonstrate the diagnostic absorption features that characterize gold-related alteration assemblages in the West Kalba belt.

Field validation represents the most direct method for verifying the effectiveness of remote sensing-based mineral identification, providing ground-truth confirmation of mapped alteration zones through direct observation and sampling. In this research, we complement traditional field validation with spectral signature analysis across the full VNIR and SWIR range (0.42–2.45μm) covered by EnMAP hyperspectral data. As demonstrated in Chapter 4, Fig. 4.1. showcases the reflectance characteristics of various surface materials encountered in the West Kalba belt, while Fig. 4.1 presents laboratory-measured reflectance spectra of key alteration minerals selected from mineral profiles of the Bakyrchik and Akzhal-Vasilyevskoye ore fields, as summarized in Table 4.1 and Table 4.2. These reference spectra establish the diagnostic absorption features that enable mineral identification: Al–OH absorption at 2.20μm (sericite, muscovite, illite), Mg–OH absorption at 2.32μm (chlorite, epidote), CO_3 absorption at 2.32–2.35μm (carbonate minerals), and Fe^{3+} charge transfer bands in the VNIR range (hematite, goethite, limonite).

Pixel-based spectral validation extracts reflectance signatures directly from EnMAP hyperspectral imagery at specific locations corresponding to known alteration zones or mineralized areas, enabling direct comparison between satellite-measured spectra and laboratory reference spectra.

Within the scope of this thesis, EnMAP hyperspectral data were not used for band ratio and false color composite generation at the district scale, as the available tiles do not provide complete coverage of the primary study areas. However, we identified a subset of EnMAP coverage that intersects with the West Kalba metallogenic zone, enabling pixel-based spectral analysis at selected locations. The validation analysis focuses on the Baybura deposit (Fig. 5.20), located within the broader West Kalba gold belt, where EnMAP hyperspectral coverage overlaps with areas of documented gold mineralization and hydrothermal alteration. This deposit provides an ideal test case for spectral validation because it exhibits well-characterized alteration assemblages typical of West Kalba gold systems, including sericite–carbonate (beresite/listvenite-type) alteration zones and associated sulfide mineralization [81].

The validation analysis at the Baybura deposit integrates spatial mapping of alteration zones with ASTER-derived false color composites and pixel-based spectral signatures from EnMAP hyperspectral imagery (Fig. 5.21). This demonstrate the spectral expression of hydrothermal alteration assemblages at 30 m spatial resolution, enabling direct comparison with laboratory reference spectra and validating the mineralogical basis for ASTER-derived alteration mapping.

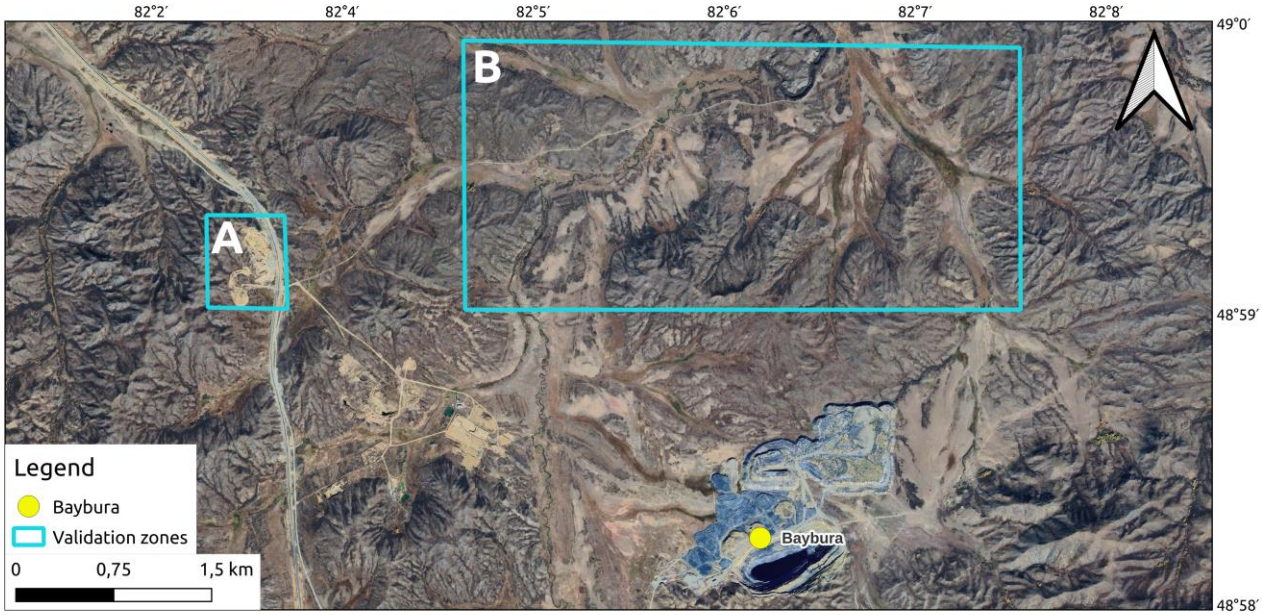

Figure 5.20. Location of the area for EnMAP-based spectral signature testing

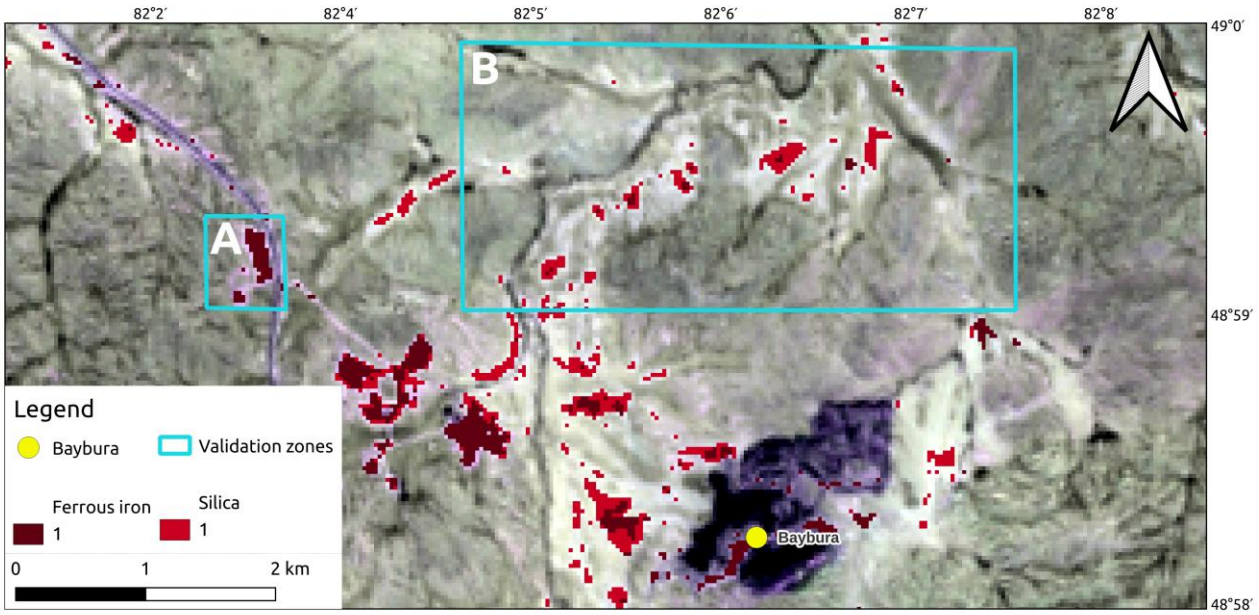

Figure 5.21. Ferrous iron and silica on the top of phyllic alteration-based FCC: A - geological traces, B - perspective zone. Ferrous iron ans silica were vectorized by a raster transformation and set min/max indexes as 75/95 respectively

The pixel-based spectral signatures extracted from EnMAP hyperspectral imagery at the Baybura deposit (Fig. 5.22) demonstrate clear diagnostic absorption features corresponding to key alteration mineral assemblages in West Kalba gold systems. The Baybura deposit is characterized by gold mineralization concentrated in the oxidized cap, where supergene weathering of sulfide-bearing alteration zones has produced Fe^{3+}-bearing minerals (hematite, goethite, limonite) that form gossan zones.

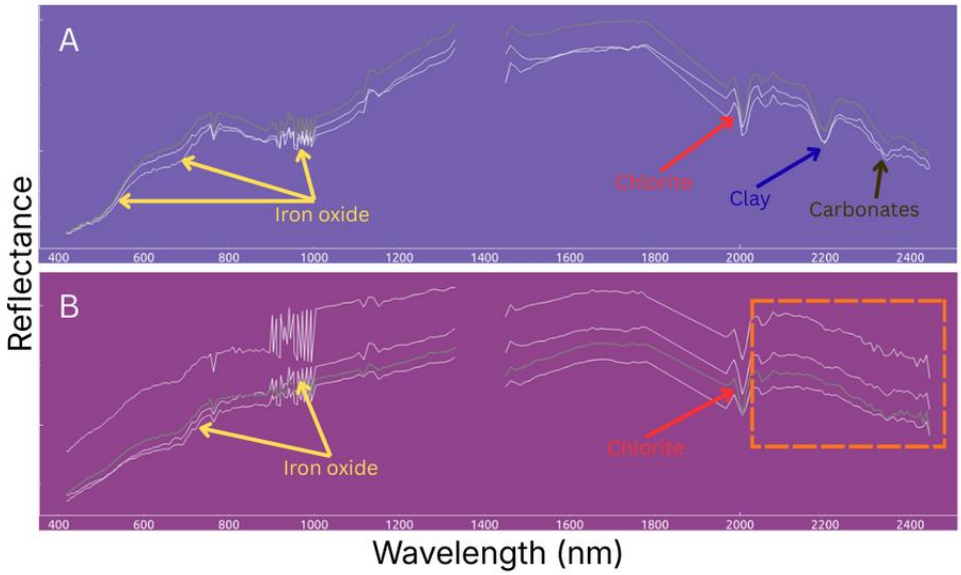

Figure 5.22. Pixel-based spectral signatures from EnMAP hyperspectral imagery at selected locations within the Baybura deposit, highlighting diagnostic absorption features in the VNIR–SWIR range: A - mineral deposits and traces, B - perspective zone. Red dashed box refers to metal-containing absorption features

In the VNIR region (400–1100 nm), broad Fe3+ absorption features (highlighted by yellow arrows in Fig. 5.22) result from charge transfer transitions in iron oxides formed as oxidation products of ferrous sulfides. In the SWIR region, three distinct absorption features are identified: chlorite at 2000 nm (Mg–OH, red arrows), clay minerals at 2200 nm (Al–OH, blue arrows), and carbonates at 2350 nm (CO3, brown arrows). These features, observed in both mineral deposits and geological traces, as well as prospective zone.

The spectral validation confirms that absorption features responsible for ASTER band-ratio responses are present in hyperspectral data and can be attributed to specific mineral phases. However, the Baybura deposit itself contains relatively low gold grades in primary ores, and economic viability may require quantification of resources and potential combination with several deposits to justify investment. The remote sensing methodology demonstrated here successfully identifies prospective locations for gold

mineralization through alteration mapping, showcasing the potential for systematic screening of similar deposits across the West Kalba belt.

This chapter conclusions summarize the application of remote sensing methodology for hydrothermal alteration mapping and validation in the West Kalba gold belt, demonstrating the effectiveness of multispectral and hyperspectral approaches for identifying prospective gold mineralization zones. The integrated analysis of ASTER multispectral data and EnMAP hyperspectral validation provides quantitative evidence that remote sensing techniques can successfully map alteration assemblages associated with gold deposits in Eastern Kazakhstan, supporting their use for systematic mineral exploration screening.

The ASTER-based alteration mapping successfully identified and characterized hydrothermal alteration zones across two representative ore districts of Bakyrchik and Akzhal–Vasilyevskoye, covering approximately 30,750 km^2 of the West Kalba metallogenic zone. Six diagnostic band ratios targeting key alteration minerals (phyllic, argillic, propylitic, carbonate, ferric iron, and ferrous silicates) were applied systematically, enabling identification of alteration assemblages that serve as indirect indicators of gold mineralization. The spatial correlation analysis revealed strong agreement between ASTER-derived alteration anomalies and documented mineral deposits, with 80+ deposit and exploration locations showing spatial coincidence with mapped alteration zones. This high correlation rate demonstrates that the selected band ratios accurately capture the mineralogical expression of hydrothermal systems at district scale [8], validating the methodological approach established in Chapter 3.

The Bakyrchik ore field analysis demonstrated that ASTER-derived products successfully recover the expected alteration zonation pattern for black-shale-hosted Au–sulfide systems: a strong phyllic–carbonate core (sericite–carbonate beresite/listvenite-type alteration) associated with mineralized structures, surrounded by weaker propylitic halos and locally enhanced iron-oxide signals in oxidized near-surface domains. The spatial correlation between alteration zones and ore bodies confirmed that coupled "quartz–sericite/illite + ferrous sulfides" responses provide reliable indicators for Bakyrchik-type gold systems, where alteration minerals provide a more reliable remote-sensing target than the spectrally featureless ore sulfides themselves. Individual band ratio maps and false color composites revealed coherent, belt-parallel footprints that outline the most altered structural corridors, with strongest anomalies spatially tied to the Kyzylkovskaya fault corridor and main disturbed zones.

The Akzhal–Vasilyevskoye district analysis demonstrated that ASTER mapping successfully captures the structurally controlled vein/beresite endmember style, where alteration footprints are more linear and corridor-like compared to Bakyrchik-type systems. The district-scale footprint is dominated by phyllic alteration (sericite/muscovite/illite) and silicification zones, with iron-related responses marking near-surface oxidation where exposure conditions permit. The correlation results showed that deposits and exploration targets align preferentially with phyllic and carbonate anomalies forming continuous or semi-continuous structural corridors, reproducing the

expected fault-focused, corridor geometry that governs ore localization in the district. This demonstrates that ASTER mapping not only detects alteration minerals but also captures the structural style of hydrothermal footprints, enabling identification of prospective zones based on both mineralogical and structural criteria.

The EnMAP hyperspectral validation at the Baybura deposit confirmed that the absorption features responsible for ASTER band-ratio responses are indeed present in hyperspectral data and can be attributed to specific mineral phases. Pixel-based spectral signatures extracted from EnMAP imagery demonstrated clear diagnostic absorption features: Fe^{3+} absorption in the VNIR region (400–1100 nm) from iron oxides formed as oxidation products of ferrous sulfides, and three distinct SWIR absorption features of chlorite at 2000 nm (Mg–OH), clay minerals at 2200 nm (Al–OH), and carbonates at 2350 nm (CO_3). These spectral features validate the ASTER band ratios used for alteration mapping and correspond to the zonal alteration distribution typical of West Kalba gold systems, providing quantitative confirmation that multispectral alteration mapping accurately captures the mineralogical expression of hydrothermal systems.

The integration of spatial mapping (ASTER false color composites) with pixel-based spectral validation (EnMAP hyperspectral signatures) demonstrates a comprehensive approach to remote sensing-based mineral exploration. The methodology successfully identifies prospective locations for gold mineralization through alteration mapping, showcasing the potential for systematic screening of similar deposits across the West Kalba belt. While individual deposits such as Baybura may contain relatively low gold grades requiring resource quantification and potential combination with several deposits to justify investment, the remote sensing approach provides an efficient and cost-effective method for rapid identification of prospective zones, reducing exploration risk and guiding targeted field investigation.

The results presented in this chapter establish that ASTER multispectral remote sensing provides a reliable and practical tool for hydrothermal alteration mapping in gold exploration contexts, with strong spatial correlation between mapped anomalies and known deposits validating the methodological framework. The successful application across two contrasting deposit styles (Bakyrchik-type black-shale-hosted Au–sulfide systems and Akzhal–Vasilyevskoye-type structurally controlled vein/beresite systems) demonstrates the broad applicability of the approach within the West Kalba metallogenic zone. The hyperspectral validation confirms the mineralogical basis for multispectral mapping, providing confidence that the identified alteration zones represent genuine mineralogical responses rather than artifacts. Together, these results support the use of multispectral remote sensing for rapid screening and mineral targeting in similar geological settings, contributing to more efficient and cost-effective gold exploration strategies in Eastern Kazakhstan and analogous terrains worldwide.

6 PERSPECTIVE ZONES FOR GOLD EXPLORATION

As demonstrated in the previous chapter, remote sensing methodology effectively maps hydrothermal alteration assemblages associated with gold mineralization in the West Kalba belt. The multispectral and hyperspectral approaches successfully detect not only known deposits but also individual alteration types, mineral assemblages, and their spatial distribution patterns. While ASTER's 30 m spatial resolution represents a fundamental limitation for detailed deposit-scale mapping, this constraint does not significantly impede the effectiveness of the methodology for district-scale exploration targeting. The strong spatial correlation observed between a substantial number of known deposits and geological traces with hydrothermal alteration zones identified through remote sensing validates that the 30 m pixel size is sufficient to capture alteration footprints that extend beyond individual deposit boundaries, particularly in areas with well-developed alteration halos and zoned hydrothermal systems.

Following verification of the methodology through spatial correlation with numerous deposits and geological traces, the validated approach can be systematically applied to identify prospective areas that exhibit promising alteration signatures within the same ore districts analyzed in this study (Fig. 6.1).

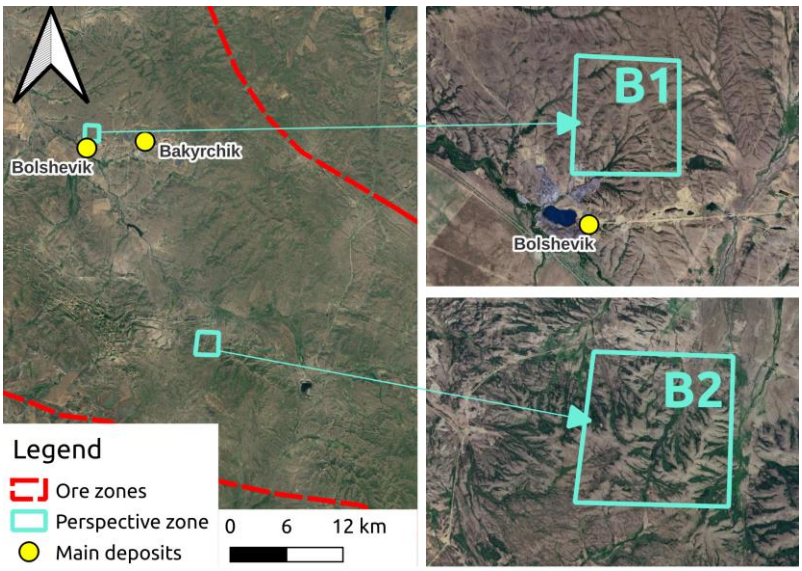

Figure 6.1. Perspective zones, located in Bakyrchik ore zone: B1 - B2

The Bakyrchik and Akzhal–Vasilyevskoye ore zones, which host the majority of known gold deposits in the West Kalba belt, provide ideal test cases for applying the remote sensing methodology to identify new exploration targets. The following sections present three perspective zones identified through systematic screening of alteration maps, where multiple alteration indicators converge to suggest potential gold mineralization targets worthy of follow-up field investigation.

6.1 Perspective Zone B1

Perspective Zone B1 is located approximately 1 km from the Bolshevik gold deposit within the Bakyrchik ore field. While geological maps mark this area as a geological trace, satellite imagery reveals no visible surface expression of the trace, suggesting potential subsurface or concealed mineralization. Unlike most deposits in the Bakyrchik district, Zone B1 does not lie directly on the Kyzylovskaya fault but is positioned less than 1 km offset from this major ore-controlling structure, indicating potential secondary fault control or structural complexity in the area.

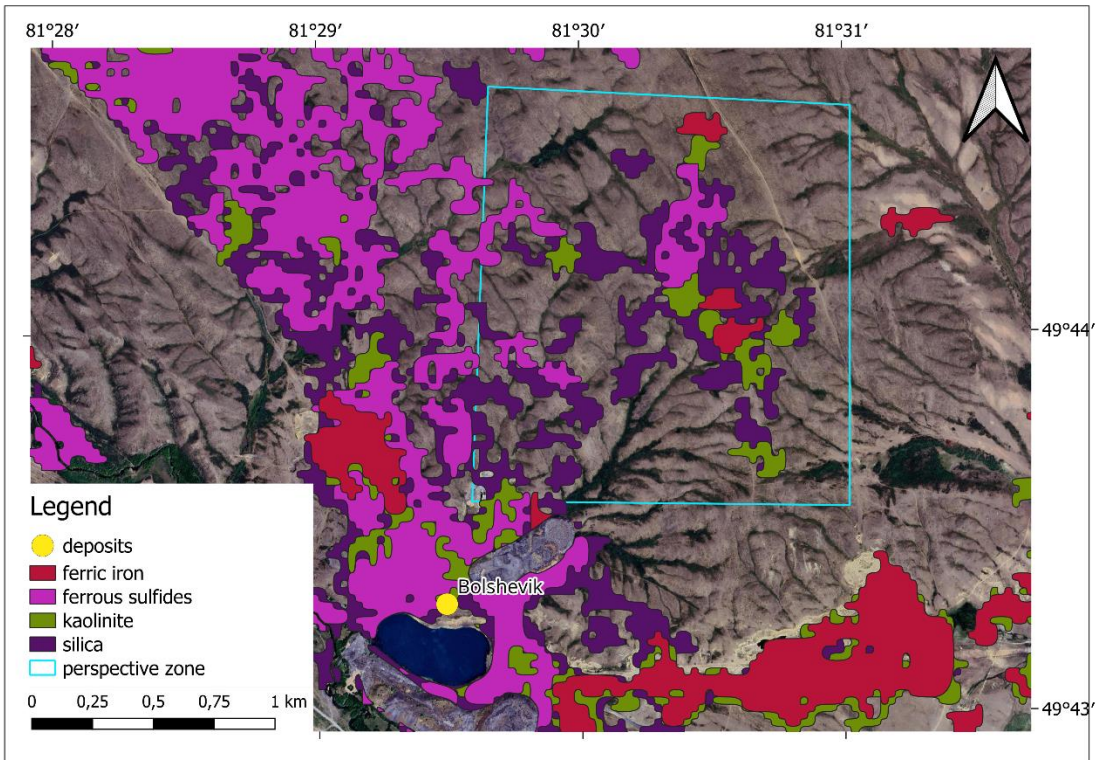

Figure 6.2. Perspective Zone B1 with overlapped alteration maps

Analysis of hydrothermal alteration maps reveals that Zone B1 exhibits deposit-level reflectance responses for all mineral species characteristic of the alteration profile typical of the Bakyrchik ore field (Fig. 6.2 and 6.3). The zone is particularly rich in sericitization and silicification (quartzitization), which are typically associated with gold-bearing sulfide mineralization in West Kalba gold systems. Meanwhile, oxidized minerals (Fe^{3+} phases) are concentrated directly along the fault trace, suggesting that the primary alteration zone may extend from the fault into the offset area where Zone B1 is located. The convergence of multiple alteration indicators, combined with the structural position relative to the Kyzylovskaya fault and proximity to the Bolshevik deposit, suggests that Zone B1 deserves detailed field investigation and may represent a significant concealed or blind deposit target.

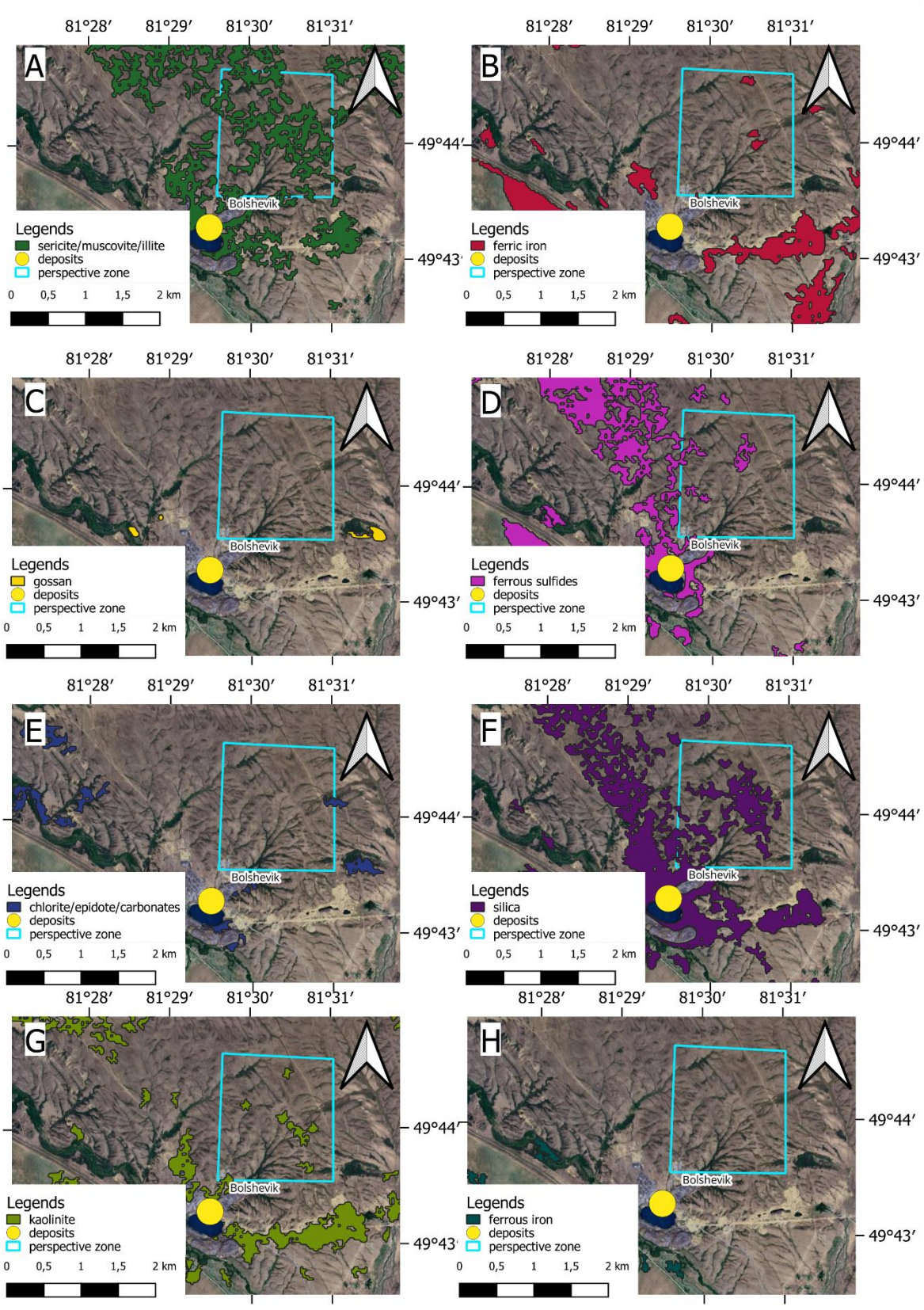
A
81°28′
81°29′
81°30′
81°31′
49°44′
49°43′
Bolshevik
Legends
sericite/muscovite/illite
deposits
perspective zone
0 0,5 1 1,5 2 km
B
Legends
ferric iron
deposits
perspective zone
C
Legends
gossan
deposits
perspective zone
D
Legends
ferrous sulfides
deposits
perspective zone
E
Legends
chlorite/epidote/carbonates
deposits
perspective zone
F
Legends
silica
deposits
perspective zone
G
Legends
kaolinite
deposits
perspective zone
H
Legends
ferrous iron
deposits
perspective zone

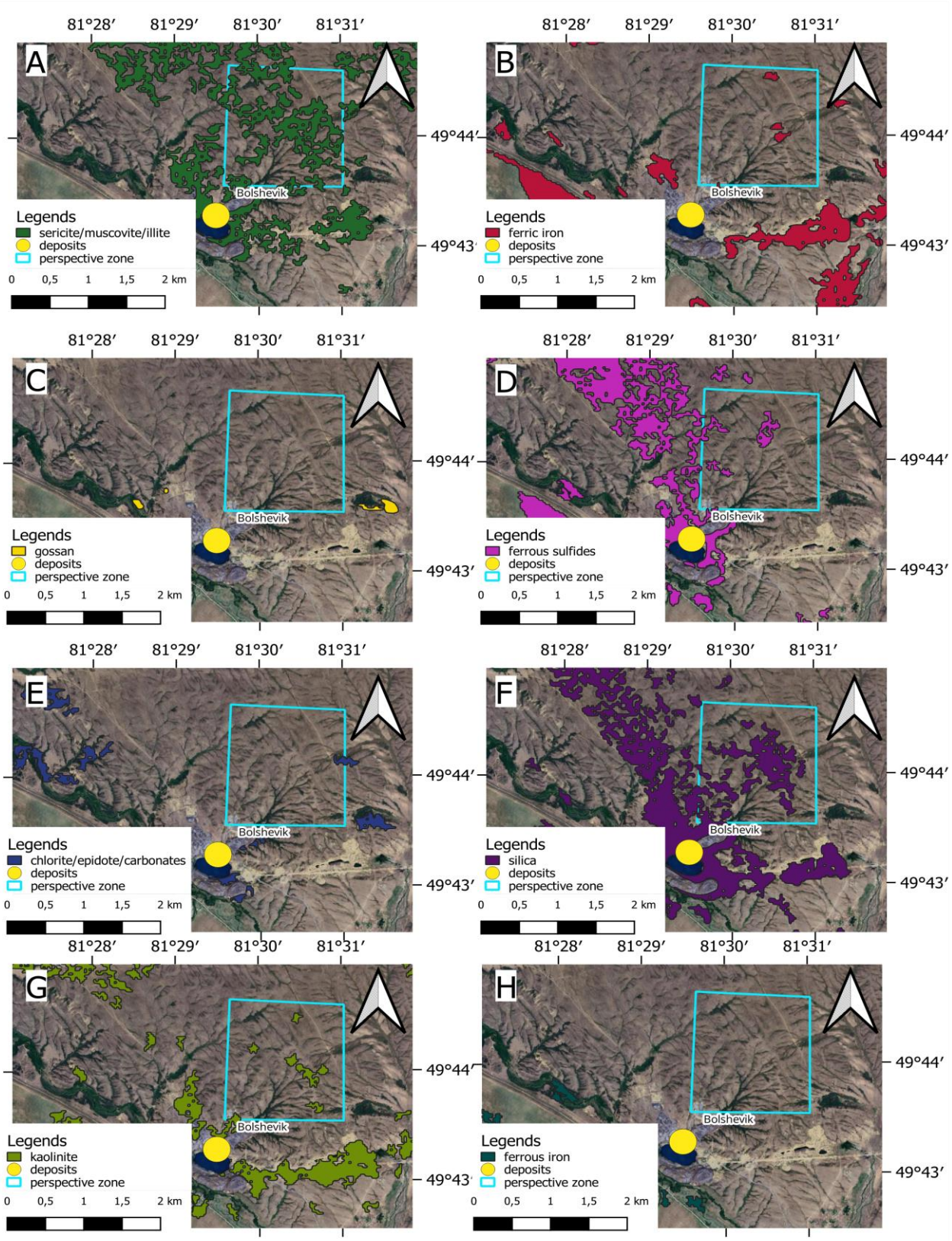

Figure 6.3. Mineral-based enhanced band combination results: Perspective zone B1

6.2 Perspective zone B2

Perspective Zone B2 presents a surprising case, as geological maps and traditional exploration expectations would not predict significant mineralization in its surroundings. The area lacks documented deposits, and geological mapping indicates that Zone B2 is located in an area characterized by Taubinskaya Formation (C_2tb) deposits, which consist of fine- to medium-grained sandstones with siltstone clasts, interbedded siltstones and sandstones, and are interpreted as olistostrome facies containing remnants of tectonic nappes. The zone is further overlain by Quaternary surficial deposits ($Q_{II–IV}$), including deluvial-proluvial and alluvial-proluvial loams, sands, and gravels, which would typically mask underlying alteration signatures. Despite these geological constraints and the absence of known deposits in the immediate vicinity, remote sensing analysis reveals a distinct alteration signature in Zone B2 (Fig. 6.4, 6.5), suggesting that subsurface hydrothermal processes may have occurred beneath the surficial cover, or that alteration zones extend beyond the areas traditionally mapped through surface geological investigation. This finding highlights the value of remote sensing for identifying prospective zones in areas where traditional surface-based exploration methods may have overlooked potential mineralization due to limited outcrop exposure or cover by younger sedimentary deposits.

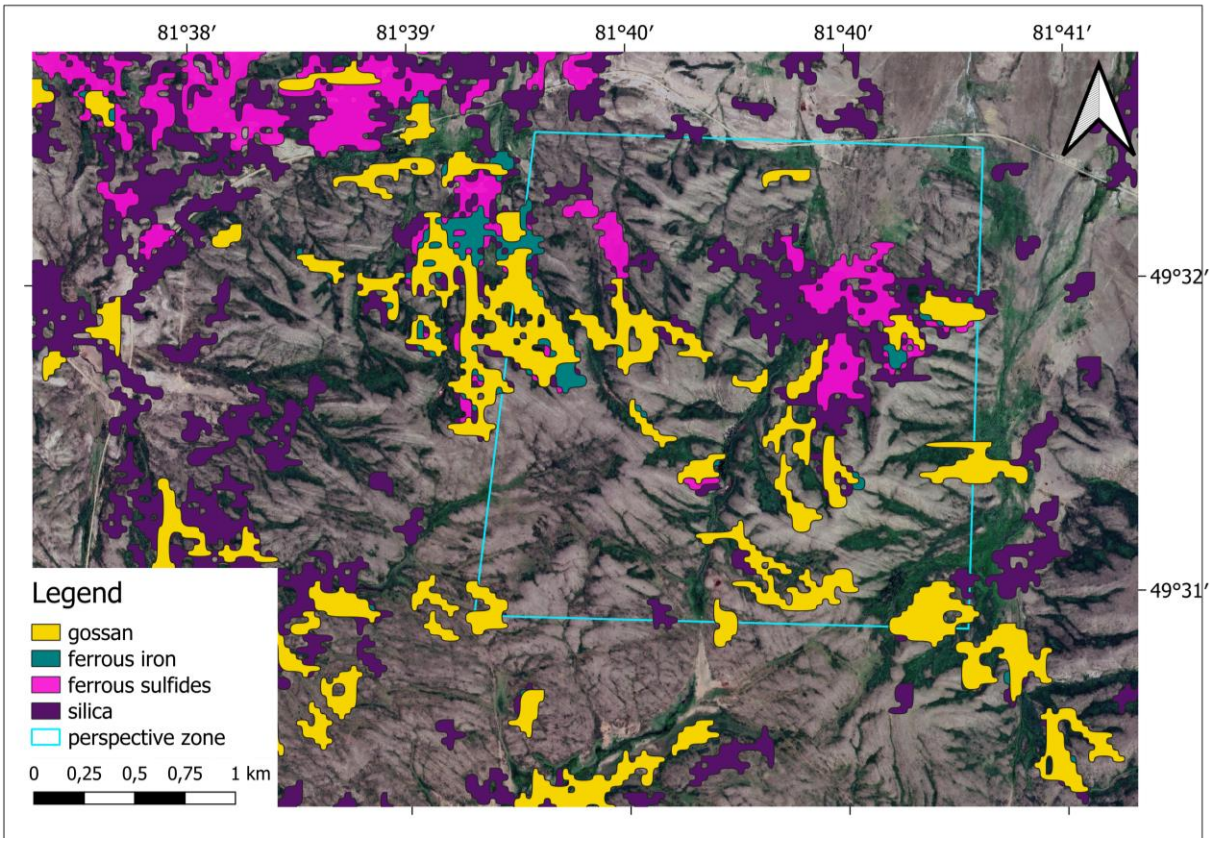

Figure 6.4. Perspective Zone B2 with overlapped alteration maps

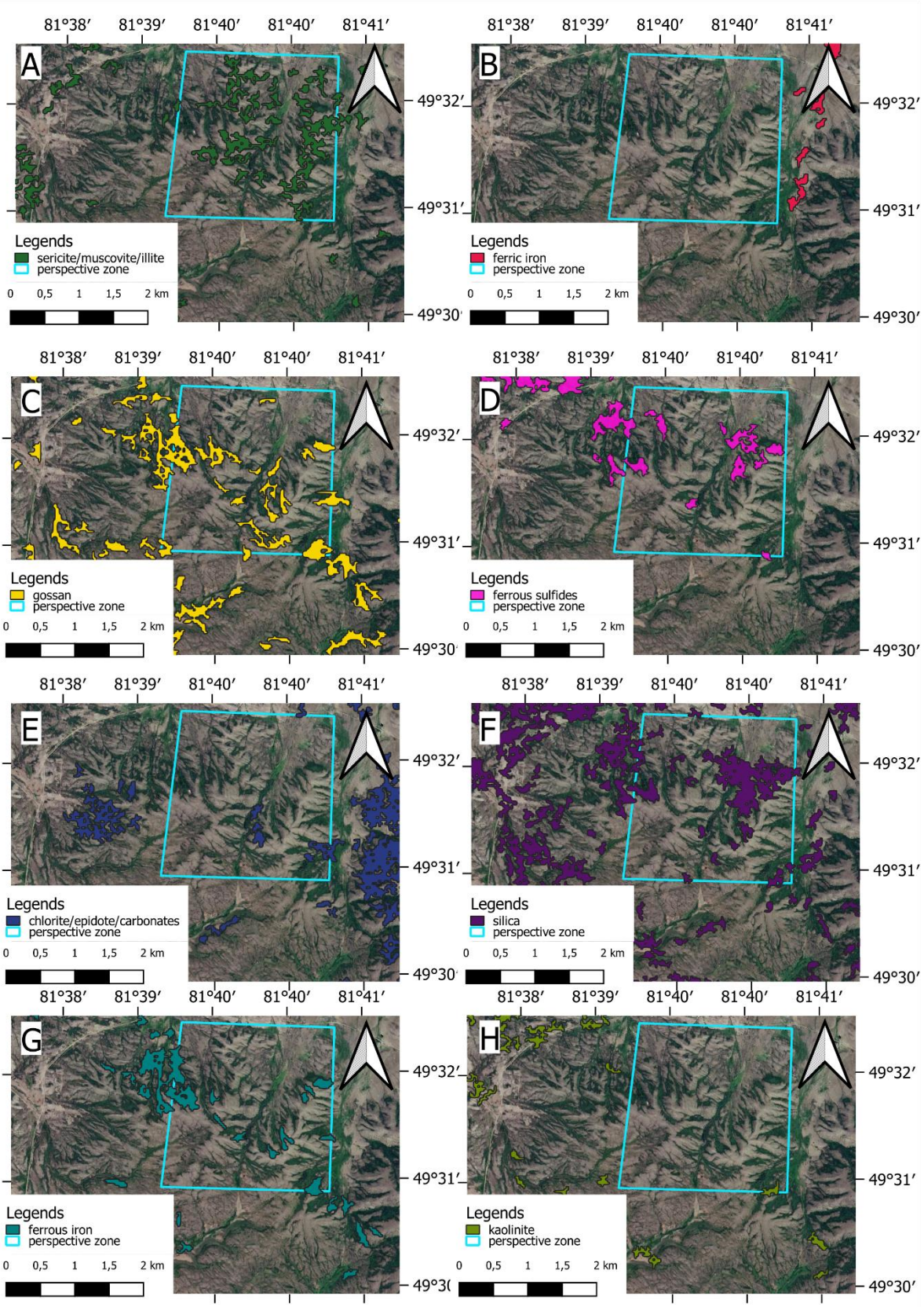

Figure 6.5. Mineral-based enhanced band combination results: Perspective zone B2

6.3 Perspective zone A1

Perspective Zone A1 is located within the Akzhal–Vasilyevskoye ore zone but, unlike most deposits in the district, does not lie directly on the main northwest–southeast trending fault system. Geological mapping indicates that Zone A1 is associated with Permian system rocks and contains predominantly porphyritic mineralization, following the main metallogenic trend of the Akzhal–Vasilyevskoye ore zone (Fig. 6.6). The zone exhibits a distinctive hydrothermal alteration signature characterized by a natural concentration of iron-related minerals, forming a “hot spot” within the regional alteration system.

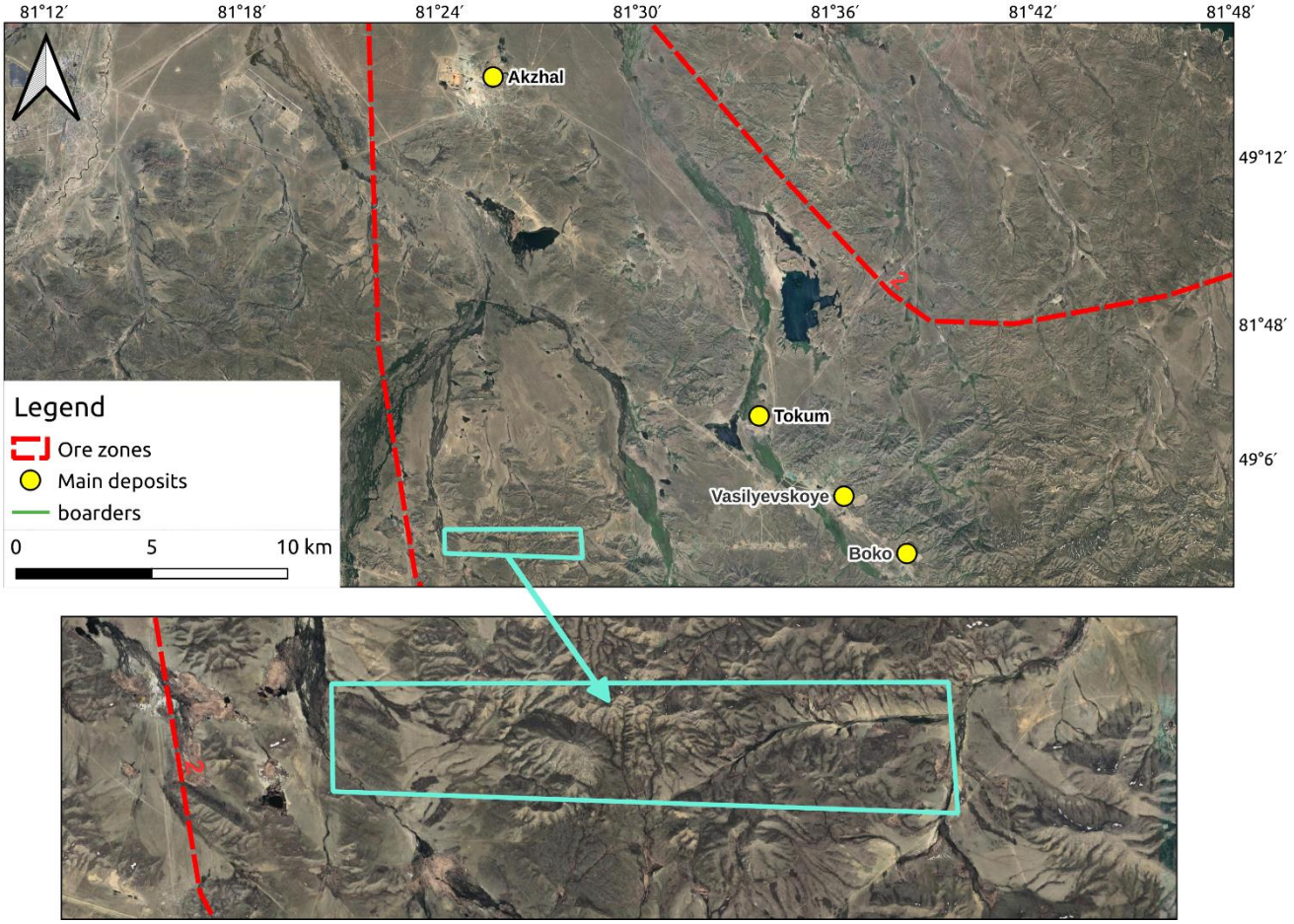

Figure 6.6. Location of perspective zone A1 with respect to Akzhal-Vasilyevskoye system

The alteration mineralogy of Zone A1 is consistent with the typical alteration patterns of the West Kalba belt, with minerals experiencing sericitization and silicification (quartzitization), whose spatial distribution and abundance agree with the regional alteration framework. Analysis of the alteration maps (Fig. 6.7) reveals four to five distinct spots where the highest concentrations of both oxides (ferrous iron and gossan) and sulfides (ferrous sulfides) are detected. These areas are spatially co-located but differ in

their spatial coverage, which is interpreted as a reflection of the relative abundance of the respective mineral phases. The spatial variation in coverage suggests that while the mineral groups occur in the same general locations, their individual distributions reflect different intensities of alteration and mineralization processes (Fig. 6.8).

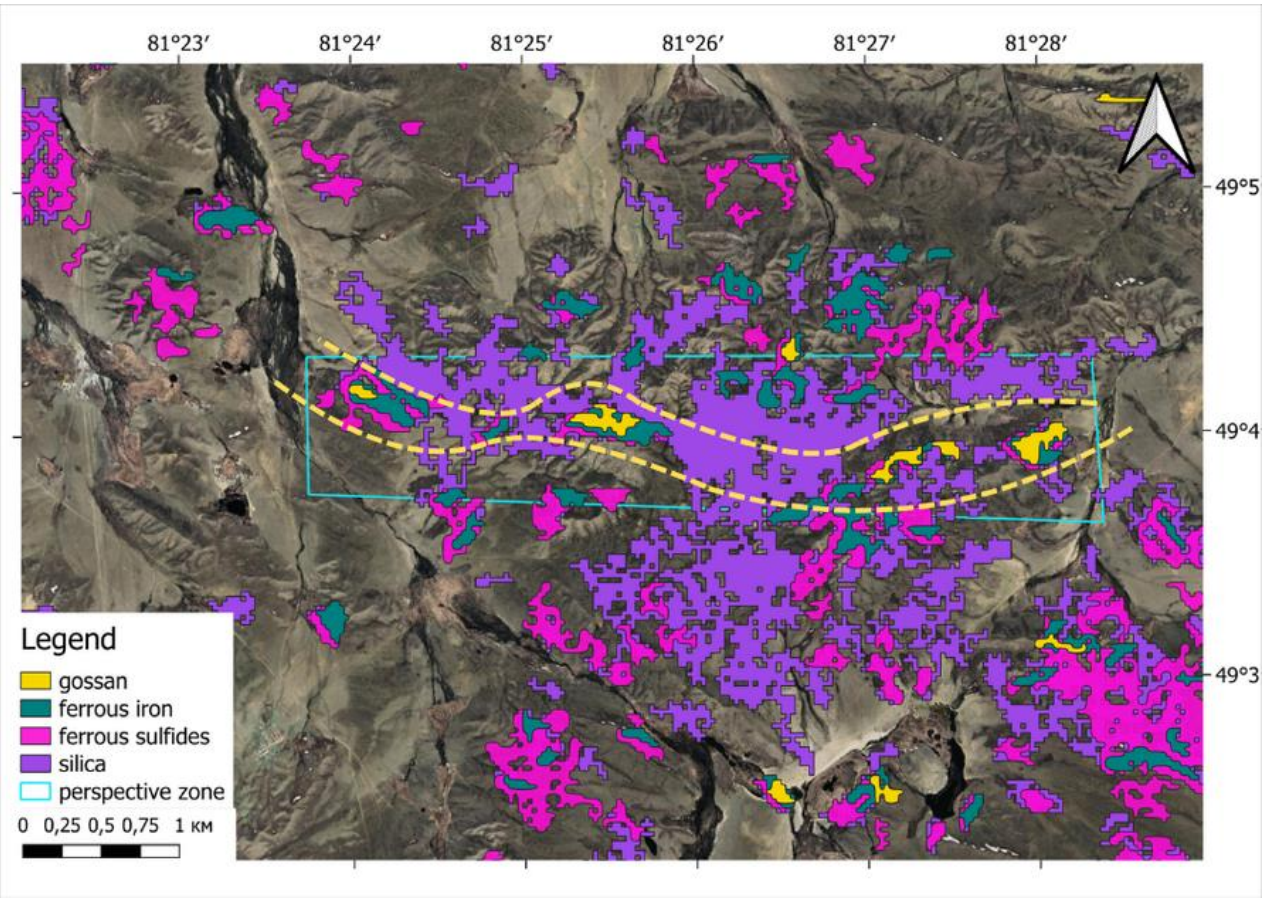

Figure 6.7. Perspective Zone A1 with overlapped alteration maps: Yellow dashed line was added to highlight the potential structural potential of A1 perspective zone

Structurally, the four to five high-concentration areas form a coherent bended line pattern, aligned with a curved dashed yellow line visible in the alteration maps, that suggests the presence of a small fault structure. This inferred fault, which is not reported in the most recent geological maps, may represent a secondary or subsidiary structure that controls the localization of alteration and mineralization in Zone A1. The bended line geometry of the alteration pattern, combined with the concentration of iron-related minerals and sulfides, suggests that this structure may serve as a fluid pathway and mineralization conduit, similar to the role played by major faults in controlling gold mineralization elsewhere in the West Kalba belt. The identification of this potential fault structure through remote sensing analysis highlights the value of systematic alteration mapping for revealing structural controls that may not be immediately apparent in

traditional geological mapping, particularly in areas with limited surface exposure or complex structural relationships.

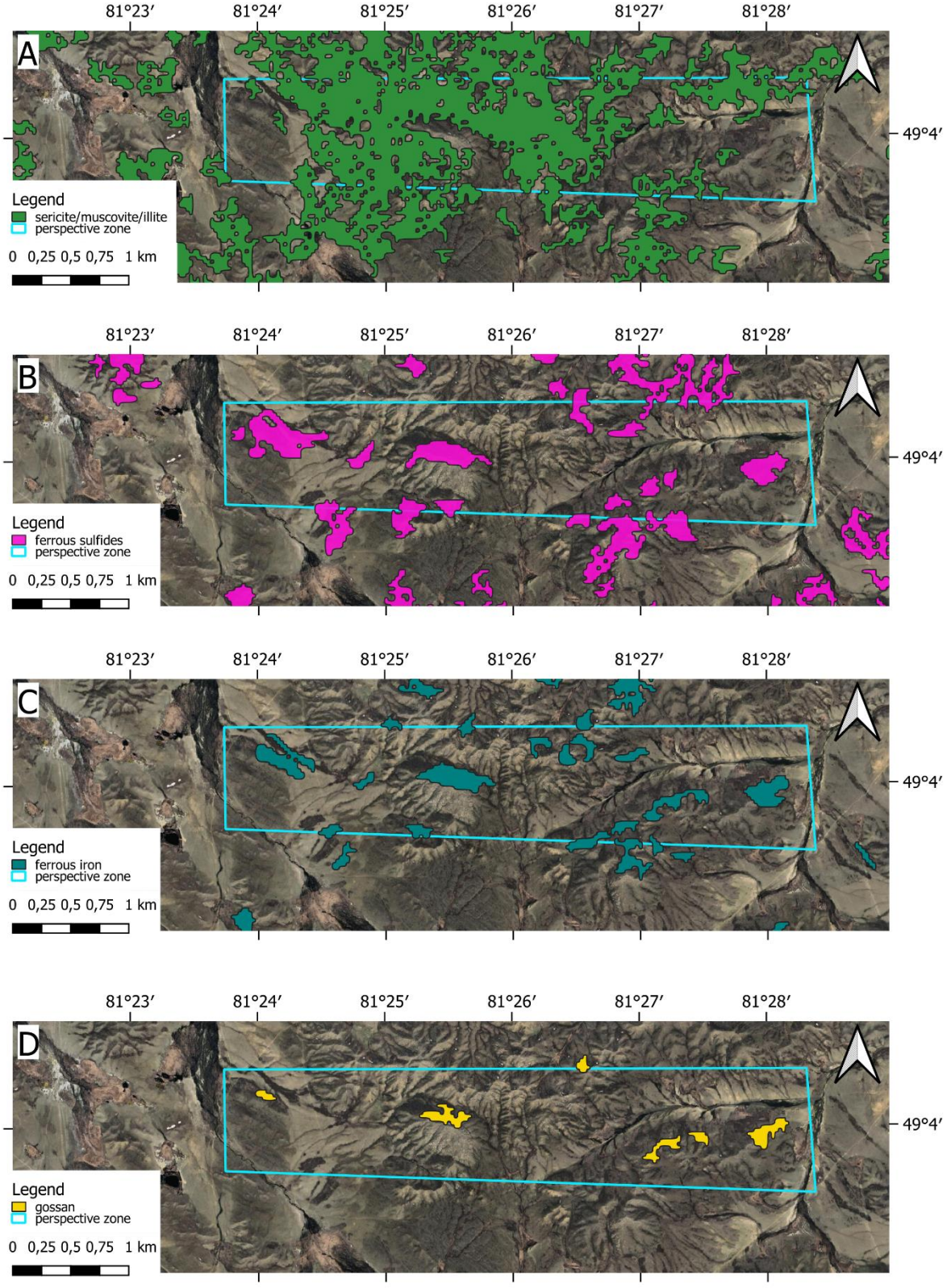

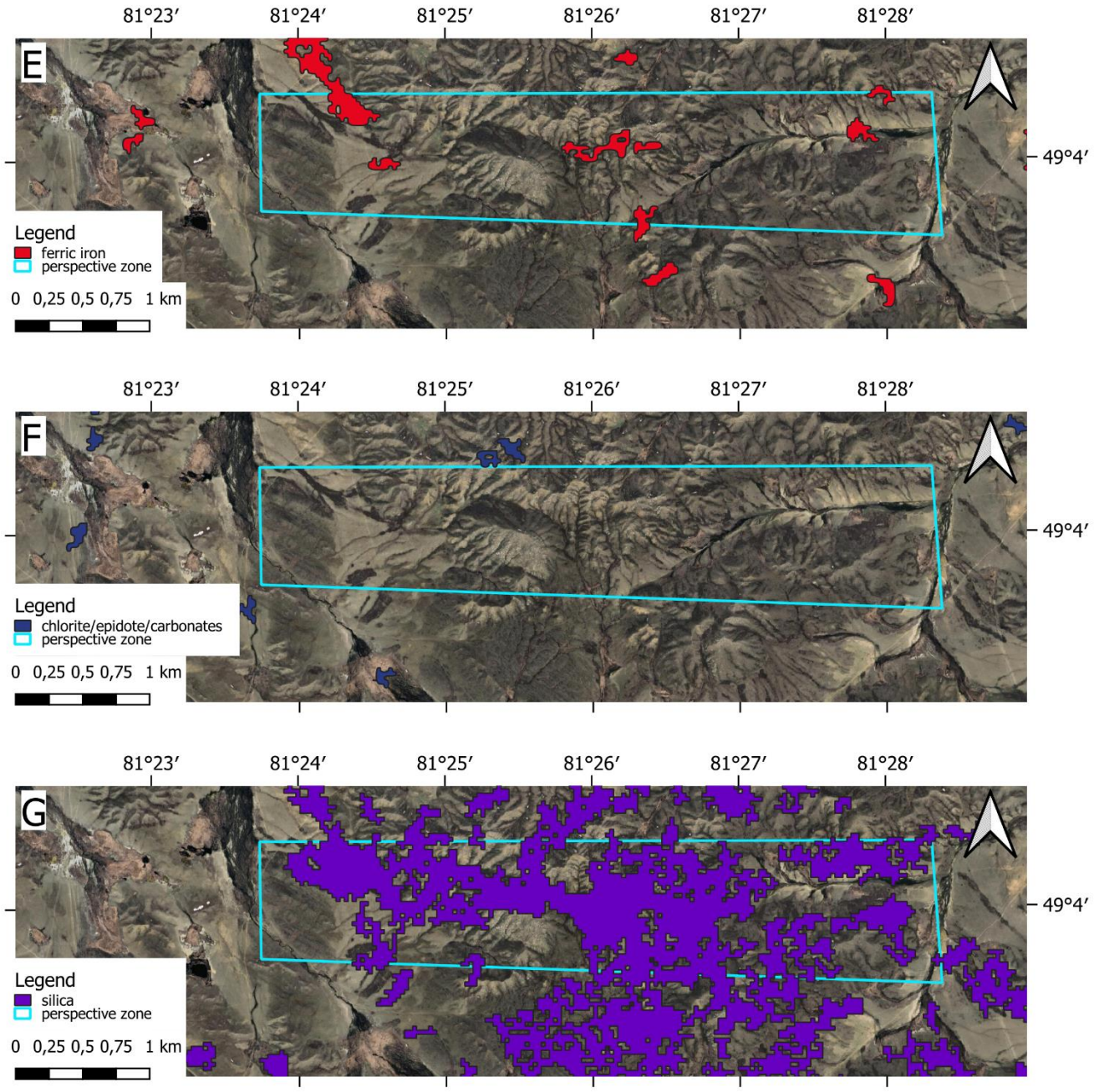

Figure 6.8. Mineral-based enhanced band combination results: Perspective zone A1

This chapter conclusions demonstrate the practical application of validated remote sensing methodology for identifying prospective gold exploration targets in the West Kalba belt. Systematic screening of alteration maps across the Bakyrchik and Akzhal–Vasilyevskoye ore zones identified three perspective zones (B1, B2, A1) where multiple alteration indicators converge to suggest potential gold mineralization targets worthy of follow-up field investigation. Zone B1, located approximately 1 km from the Bolshevik deposit, exhibits deposit-level reflectance responses for all mineral species characteristic of the Bakyrchik ore field alteration profile, with particular richness in sericitization and silicification - alteration types typically associated with gold-bearing sulfide

mineralization. The zone's structural position relative to the Kyzylovskaya fault and proximity to known deposits suggests it may represent a significant concealed or blind deposit target.

Zone A1, located within the Akzhal–Vasilyevskoye ore zone and associated with Permian system porphyritic mineralization, characterized by several distinct areas with highest concentrations of oxides (ferrous iron, gossan) and sulfides (ferrous sulfides). The spatial co-location of these mineral groups, combined with their arc-like geometric pattern, suggests the presence of an unreported secondary fault structure that may control alteration and mineralization. This finding highlights the value of systematic alteration mapping for revealing structural controls not immediately apparent in traditional geological mapping. The identification of these perspective zones demonstrates that the remote sensing methodology successfully extends beyond validation with known deposits to identify new exploration targets, providing a practical tool for prioritizing areas for detailed field investigation and reducing exploration risk in the West Kalba gold belt.

CONCLUSIONS

This thesis has successfully developed and demonstrated a comprehensive remote sensing methodology for gold exploration in the West Kalba gold belt of Eastern Kazakhstan, addressing a critical research gap in the application of satellite remote sensing to mineral exploration in Kazakhstan. The work integrates geological understanding, spectral theory, and practical remote sensing techniques to create a reproducible workflow for hydrothermal alteration mapping that supports systematic mineral exploration targeting at regional scale.

The research was motivated by the declining potential for discovering new large and medium gold deposits using traditional exploration methods in Eastern Kazakhstan, where major deposits face depletion by 2025–2040. Kazakhstan ranks 13th globally in gold production, with Eastern Kazakhstan accounting for 32.6% of the country's gold reserves, yet the mineral resource base requires scalable and reproducible screening methods to identify new targets. The West Kalba gold belt, hosting more than 450 documented gold deposits and occurrences, provides an ideal test case for remote sensing applications, combining extensive geological documentation with favorable conditions for spectral analysis in semi-arid to arid environments.

Chapter 1 established the economic and regional context, demonstrating that while Kazakhstan's gold mining industry shows steady growth, the potential for discovering new large deposits using traditional methods is increasingly limited. The mineral resource base of East Kazakhstan, while substantial, faces depletion of major deposits, creating a clear need for advanced exploration methods. The West Kalba belt has been extensively studied through over a century of geological investigations, providing a well-documented foundation for remote sensing validation, yet systematic application of satellite remote sensing methods had not been implemented prior to this research.

Chapter 2 established the geological framework essential for interpreting remote sensing results, describing the geotectonic position of the Great Altai within the Central Asian Orogenic Belt and providing detailed characterization of the Bakyrchik and Akzhal–Vasilyevskoye ore fields. The chapter linked deposit-scale alteration mineralogy and zoning patterns to spectral signatures detectable by remote sensing, forming the basis for the mineral targeting framework. The West Kalba zone occupies an axial position within the Ob-Zaisan fold system, formed during Late Paleozoic collision, with gold mineralization characterized by association with hydrothermal alteration processes (sericitization, chloritization, silicification, carbonatization, albitization) and control by regional and local fault systems. The detailed geological characterization of contrasting deposit styles - Bakyrchik-type black-shale-hosted Au–sulfide systems and Akzhal-Vasilyevskoye-type structurally controlled vein/beresite systems - provided the foundation for testing remote sensing approaches across different mineralization styles.

Chapter 3 presented the theoretical and methodological foundations, covering electromagnetic radiation fundamentals, spectral properties of geological materials, ASTER remote sensing systems, preprocessing techniques, and spectral transformation

methods. The chapter established that ASTER's spectral band configuration, specifically optimized for geological applications, enables systematic mapping of hydrothermal alteration zones through band ratios targeting Al–OH (2.20μm), Mg/Fe–OH (2.32μm, CO_3 (2.32–2.35μm), and Fe^{3+} (VNIR) absorption features. The preprocessing methods, including atmospheric correction and radiometric calibration, ensure that spectral signatures accurately represent surface mineralogical composition, while spectral transformation methods (band ratios, indices, FCCs) provide practical tools for mapping alteration zones and identifying prospective areas for mineralization.

Chapter 4 established the mineralogical and spectral framework specific to West Kalba gold systems, demonstrating that six primary alteration types - silicification, sericitization/argillization, chloritization/propylitization, carbonatization, sulfidation/oxidation, and beresitization/listvenitization - form diagnostic spectral signatures that serve as indirect indicators of gold mineralization. While primary ore minerals as pyrite, arsenopyrite, native gold are spectrally featureless in the VNIR–SWIR range, their detection is enabled through associated alteration halos dominated by OH-bearing phyllosilicates, carbonates, and Fe-oxide oxidation products. The zonal distribution of alteration types, from peripheral propylitic halos through inner beresite/listvenite zones to core sulfide-bearing domains, provides a predictive framework for remote sensing-based mineral targeting.

Chapter 5 applied the integrated methodology to ASTER multispectral data covering the Bakyrchik and Akzhal-Vasilyevskoye focus districts, implementing band ratio calculations, false color composite generation, and spatial correlation analysis with documented mineral deposits and exploration footprints. The results demonstrated that ASTER-derived alteration mapping successfully recovers expected alteration zonation patterns at district scale, with strong spatial correlation between mapped anomalies and known deposits. Across the two focus districts covering approximately 30,750 km^2, 80+ deposit and exploration locations showed spatial coincidence with ASTER-derived alteration anomalies, demonstrating that the selected band ratios accurately capture the mineralogical expression of hydrothermal systems. The Bakyrchik ore field analysis confirmed that coupled "quartz–sericite/illite + ferrous sulfides" responses provide reliable indicators for Bakyrchik-type gold systems, while the Akzhal–Vasilyevskoye district analysis demonstrated that ASTER mapping successfully captures the structurally controlled vein/beresite endmember style, reproducing the expected fault-focused, corridor geometry that governs ore localization. EnMAP hyperspectral validation at the Baybura deposit confirmed that absorption features responsible for ASTER band-ratio responses are present in hyperspectral data and can be attributed to specific mineral phases, providing quantitative confirmation that multispectral alteration mapping accurately captures the mineralogical expression of hydrothermal systems.

Chapter 6 demonstrated the practical application of the validated methodology by identifying three perspective zones (B1, B2, B3) that exhibit promising alteration signatures within the Bakyrchik and Akzhal–Vasilyevskoye ore zones. These zones, identified through systematic screening of alteration maps, show convergence of multiple

alteration indicators suggesting potential gold mineralization targets worthy of follow-up field investigation. Perspective Zone B1, located approximately 1 km from the Bolshevik deposit, exhibits deposit-level reflectance responses for all mineral species characteristic of the Bakyrchik ore field alteration profile, with particular richness in sericitization and silicification - typically associated with gold-bearing sulfide mineralization. The zone's structural position relative to the Kyzylovskaya fault and proximity to known deposits suggests it may represent a significant concealed or blind deposit target.

The research successfully addressed all five stated objectives. The geological and metallogenic context was comprehensively summarized, establishing the framework for alteration and gold mineralization in the West Kalba belt. A mineral targeting framework was constructed using regional geological sources and reference laboratory spectra, prioritizing minerals and diagnostic absorbers detectable with ASTER. A reproducible processing pipeline was developed for ASTER multispectral data, including co-registration, NDVI masking, band ratio calculations, FCC generation, and multi-scene mosaicking. Alteration mapping results were validated through object-based spatial correspondence analysis and hyperspectral EnMAP spectral confirmation, demonstrating both spectral plausibility and spatial precision. Regional alteration composites were produced and prospective zones identified for follow-up work.

The scientific novelty of this work lies in integrating a geology-driven mineral targeting framework for the West Kalba belt with a reproducible multi-scene ASTER processing pipeline and a two-level validation strategy combining object-based spatial correspondence with hyperspectral spectral confirmation. This contribution addresses a national research gap, as hyperspectral remote sensing for mineral exploration in Kazakhstan has been rarely reported in the published literature. The practical significance is the creation of a reproducible workflow and map products that enable rapid regional screening of hydrothermal alteration footprints, support prioritization of exploration targets, and provide a defensible basis for selecting prospective zones for follow-up mapping and sampling campaigns.

The methodology demonstrated here provides a reliable and practical tool for hydrothermal alteration mapping in gold exploration contexts, with strong spatial correlation between mapped anomalies and known deposits validating the methodological framework. The successful application across two contrasting deposit styles demonstrates the broad applicability of the approach within the West Kalba metallogenic zone. While the 30m spatial resolution of ASTER represents a fundamental limitation for detailed deposit-scale mapping, this constraint does not significantly impede effectiveness for district-scale exploration targeting, as validated by the strong correlation observed between a substantial number of known deposits and alteration zones identified through remote sensing.

Future work should prioritize development of regional spectral libraries tailored to Kazakh lithologies and alteration styles, standardized preprocessing workflows ensuring consistency across projects, and integration with national geological and geophysical databases to enable multi-criteria prospectivity analysis at regional scales. The systematic

application of remote sensing methods demonstrated here can be extended to other metallogenic provinces in Kazakhstan and analogous terrains worldwide, contributing to more efficient and cost-effective gold exploration strategies. As demonstrated through the identification of perspective zones, the remote sensing approach provides an efficient method for rapid identification of prospective locations, reducing exploration risk and guiding targeted field investigation, ultimately supporting the sustainable development of Kazakhstan's mineral resource base.

BIBLIOGRAPHY

1. Ananyev Yu.S., Korobeynikov A.F. Metasomatoz i blagorodnometall'noe orudenenie v chernoslantsevykh tolshchakh Zapadnoi Kalby. TPU Tomsk, 1999. –206 p.

2. Shcherba G.N., D'yachkov B.A. Great Altai (Geology and Metallogeny). Book. 1. Geology.Gylym, Almaty, 1998. –304 p.

3. Ermolov P.V., Vladimirov A.G., Izokh A.E., Polyansky N.V., Kuzybny V.S., Revyakin P.S., Bortsov V.D. Orogennyi magmatizm ofiolitovykh poyasov (na primere Vostochnogo Kazakhstana). Novosibirsk: Nauka, 1983. –211 p.

4. Polyansky N.V., Dobretsov N.L., Ermolov P.V., Kuzybny V.S. Struktura i istoriya razvitiya Charskogo ofiolitovogo poyasa. Geologiya i geofizika 5, 1979. – P. 66-78.

5. Abrams M. The Advanced Spaceborne Thermal Emission and Reflection Radiometer (ASTER): Data products for the high spatial resolution imager on NASA's Terra platform. International Journal of Remote Sensing 21 (5), 2000. – P. 847-859.

6. Abrams M., Tsu H., Hulley G., Iwao K., Pieri D., Cudahy T., Kargel J. The Advanced Spaceborne Thermal Emission and Reflection Radiometer (ASTER) after fifteen years: Review of global products. International Journal of Applied Earth Observation and Geoinformation 38, 2015. – P. 292-301.

7. Pinet P., Kaufmann C., Hill J. Imaging spectroscopy of changing Earth’s surface: a major step toward the quantitative monitoring of land degradation and desertification. Geoscience 338 (2006). – P. 1042-1048.

8. Amer R., Kusky T., Ghulam A. Lithological mapping in the Central Eastern Desert of Egypt using ASTER data. Journal of African Earth Sciences 56, 2010. – P. 75-82.

9. Boltzmann L. Ableitung des Stefan'schen Gesetzes, betreffend die Abhängigkeit der Wärmestrahlung von der Temperatur aus der electromagnetischen Lichttheorie. Annalen der Physik 22, 1884. – P. 291-294.

10. Chavez P.S. Image-based atmospheric corrections--revisited and improved. Photogrammetric Engineering and Remote Sensing 62 (9), 1996. – P. 1025-1036.

11. Clark R.N. Spectroscopy of Rocks and Minerals, and Principles of Spectroscopy. In: Rencz A.N. (ed), Remote Sensing for the Earth Sciences: Manual of Remote Sensing, Volume 3. John Wiley & Sons: New York, USA, 1999. – P. 3-58.

12. Colby J.D. Topographic normalization in rugged terrain. Photogrammetric Engineering and Remote Sensing 57 (5), 1991. – P. 531-537.

13. Drusch M., Del Bello U., Carlier S., Colin O., Fernandez V., Gascon F., Hoersch B., Isola C., Laberinti P., Martinort P., Meygret A., Spoto F., Sy O., Marchese F., Bargellini P. Sentinel-2: ESA's Optical High-Resolution Mission for GMES Operational Services. Remote Sensing of Environment 120, 2012. – P. 25-36.

14. Einstein A. Über einen die Erzeugung und Verwandlung des Lichtes betreffenden heuristischen Gesichtspunkt. Annalen der Physik 17, 1905. – P. 132-148.

15. Fujisada H., Bailey G.B., Kelly G.G., Hara S., Abrams M.J. ASTER DEM performance. IEEE Transactions on Geoscience and Remote Sensing 43 (12), 2005. – P. 2707-2714.

16. Gao B.C., Montes M.J., Davis C.O., Goetz A.F.H. Atmospheric correction algorithms for hyperspectral remote sensing data of land and ocean. Remote Sensing of Environment 113 (S1), 2009. – P. S17-S24.

17. Gillespie A.R., Rokugawa S., Matsunaga T., Cothern J.S., Hook S.J., Kahle A.B. A temperature and emissivity separation algorithm for Advanced Spaceborne Thermal Emission and Reflection Radiometer (ASTER) images. IEEE Transactions on Geoscience and Remote Sensing 36 (4), 1998. – P. 1113-1126.

18. Goetz A.F.H., Vane G., Solomon J.E., Rock B.N. Imaging Spectrometry for Earth Remote Sensing. Science 228, 1985. – P. 1147-1153.

19. Guanter L., Kaufmann H., Segl K., Foerster S., Rogass C., Chabrillat S., Kuester T., Hollstein A., Rossner G., Chlebek C., Straif C., Fischer S., Schrader S., Storch T., Heiden U., Mueller A., Bachmann M., Mühle H., Müller R., Habermeyer M., Ohndorf A., Hill J., Buddenbaum H., Hostert P., van der Linden S., Leitão P.J., Rabe A., Doerffer R., Krasemann H., Xi H., Mauser W., Hank T., Locherer M., Rast M., Staenz K., Sang B. The EnMAP Spaceborne Imaging Spectroscopy Mission for Earth Observation. Remote Sensing 7 (7), 2015. – P. 8830-8857.

20. Chabrillat S., Guanter L., Kaufmann H., Foerster S., Beamish A., Brosinsky A., Wul, H., Asadzadeh S., Bochow M., Bohn N., Boesche N., Bracher A., Brell M., Buddenbaum Cerra D., H., Fischer S., Hank T., Heiden U., Heim B., Heldens W., Hill J., Hollstein A., Hostert P., Krasemann H., LaPorta L., Leitão P.J., van der Linden S., Mauser W., Milewski R., Mottus M., Okujeni A., Oppelt N., Pinnel N., Roessner S., Röttgers R., Schneiderhan T., Schickling A., Soppa M., Staenz K., Segl K. (2022) EnMAP Science Plan. EnMAP Technical Report, GFZ German Research Centre for Geosciences, Potsdam, Germany, 2022. – 88. p. DOI: http://doi.org/10.48440/enmap.2022.001

21. Hapke B. Theory of Reflectance and Emittance Spectroscopy. Cambridge University Press: Cambridge, UK, 2012. –512 p.

22. Horler D.N.H., Dockray M., Barber J. The red edge of plant leaf reflectance. International Journal of Remote Sensing 4 (2), 1983. – P. 273-288.

23. Hunt G.R. Spectral signatures of particulate minerals in the visible and near infrared. Geophysics 42 (3), 1977. – P. 501-513.

24. Iwasaki A., Fujisada H., Akao H., Shindou O., Akagi S. Enhancement of spectral separation performance for ASTER/SWIR. IEEE Transactions on Geoscience and Remote Sensing 43 (12), 2005. – P. 2741-2746.

25. Jordan T.R., Tischler M.B., Kirkland L., Clancy K., Ibrahim K., Grant G. Advanced Land Imager (ALI) for NASA's Earth Observing-1 (EO-1) mission. Optical Engineering 42 (9), 2005. – P. 2656-2667.

26. Kaufman Y.J., Tanré D., Remer L.A., Vermote E.F., Chu A., Holben B.N. Operational remote sensing of tropospheric aerosol over land from EOS moderate

resolution imaging spectroradiometer. J. Geophys. Res. 102 (D14), 1997. – P. 17051-17067.

27. Kruse F.A., Lefkoff A.B., Boardman J.W., Heidebrecht K.B., Shapiro A.T., Barloon P.J., Goetz A.F.H. The Spectral Image Processing System (SIPS)-Interactive Visualization and Analysis of Imaging Spectrometer Data. Remote Sensing of Environment 44 (2-3), 1993. – P. 145-163.

28. Lopinto E., Ananasso C., Dini L., Galeazzi C., Longo F., Santoro M., Schiavon G. PRISMA Mission Status and Perspective. In: IGARSS 2019 - 2019 IEEE International Geoscience and Remote Sensing Symposium, 2019. – P. 4503-4506.

29. Maxwell J.C. A Dynamical Theory of the Electromagnetic Field. Philosophical Transactions of the Royal Society 155, 1865. – P. 459-512.

30. Mie G. Beiträge zur Optik trüber Medien, speziell kolloidaler Metallösungen. Annalen der Physik 25, 1908. – P. 377-445.

31. Minnaert M. The reciprocity principle in lunar photometry. Astrophysical Journal 93, 1941. – P. 403-410.

32. Nicodemus F.E., Richmond J.C., Hsia J.J., Ginsberg I.W., Limperis T. Geometrical Considerations and Nomenclature for Reflectance. U.S. National Bureau of Standards Monograph 160, 1977. –52 p.

33. Ninomiya Y., Fu B., Cudahy T.J. Detecting lithology with Advanced Spaceborne Thermal Emission and Reflection Radiometer (ASTER) multispectral thermal infrared "radiance-at-sensor" data. Remote Sensing of Environment 99 (1-2), 2005. – P. 127-139.

34. Pearlman J.S., Barry P.S., Segal C.C., Shepanski J., Beiso D., Carman S.L. Hyperion, a space-based imaging spectrometer. IEEE Transactions on Geoscience and Remote Sensing 41 (6), 2003. – P. 1160-1173.

35. Planck M. Ueber das Gesetz der Energieverteilung im Normalspectrum. Annalen der Physik 4, 1901. – P. 553-563.

36. Rayleigh J.W.S. On the light from the sky, its polarization and colour. Philosophical Magazine 41, 1871. – P. 107-120.

37. Rowan L.C., Hook S.J., Abrams M.J., Mars J.C. Mapping hydrothermally altered rocks at Cuprite, Nevada, using the Advanced Spaceborne Thermal Emission and Reflection Radiometer (ASTER), a new satellite-imaging system. Economic Geology 98 (5), 2003. – P. 1019-1027.

38. Nikolaeva A. N. Telluro-bismuth Mineralization in the Abyz and Maleevskoe Sulfide Deposits (Republic of Kazakhstan): PhD Dissertation in Geological and Mineralogical Sciences: 1.6.10. - Tomsk, 2024. - 182 p.

39. Report on scientific and research work AP 05131489 “Technology for advances estimation of gold deposits using modern methods of mineralogical mapping” 2020. // EKTU: research manager: Mizernaya M.A. - Ust-Kamenogorsk, 2020. - 83 p.

40. Miroshnikova A.P., Mizernyy A.I., Orazbekova G.B., Mizernaya M.A., D’yachkov B.A., Aytbaeva S.S. Zoloto-sul’fidno-kvartsevo-zhil’nye mestorozhdeniya

Severo-Vostoka Kazakhstana – perspektivnoe napravlenie rasshireniya mineral'no-syr'evoy bazy zolota. Trudy Universiteta. 2 (71), 2018. – P. 124–127.

41. Roy D.P., Wulder M.A., Loveland T.R., Woodcock C.E., Allen R.G., Anderson M.C., Helder D., Irons J.R., Johnson D.M., Kennedy R., Scambos T.A., Schaaf C.B., Schott J.R., Sheng Y., Vermote E.F., Belward A.S., Bindschadler R., Cohen W.B., Gao F., Hipple J.D., Hostert P., Huntington J., Justice C.O., Kilic A., Kovalskyy V., Lee Z.P., Lymburner L., Masek J.G., McCorkel J., Shuai Y., Trezza R., Vogelmann J., Wynne R.H., Zhu Z. Landsat-8: Science and product vision for terrestrial global change research. Remote Sensing of Environment 145, 2014. – P. 154-172.

42. Sabins F.F. Remote Sensing: Principles and Interpretation. W.H. Freeman: New York, USA, 1999. –494 p.

43. Salisbury J.W., Walter L.S., Vergo N., D'Aria D.M. Infrared (2.1-25 μm) Spectra of Minerals. Johns Hopkins University Press: Baltimore, USA, 1991. –267 p.

44. Sillitoe R.H. Porphyry Copper Systems. Economic Geology 105 (1), 2010. – P. 3-41.

45. Stefan J. Über die Beziehung zwischen der Wärmestrahlung und der Temperatur. Sitzungsberichte der mathematisch-naturwissenschaftlichen Classe der kaiserlichen Akademie der Wissenschaften 79, 1879. – P. 391-428.

46. Teillet P.M., Guindon B., Goodenough D.G. On the slope-aspect correction of multispectral scanner data. Canadian Journal of Remote Sensing 8 (2), 1982. – P. 84-106.

47. Ulaby F.T., Moore R.K., Fung A.K. Microwave Remote Sensing: Active and Passive. Volume II: Radar Remote Sensing and Surface Scattering and Emission Theory. Artech House: Norwood, USA, 1986. – P. 962-966.

48. Vermote E.F., Tanré D., Deuzé J.L., Herman M., Morcette J.J. Second Simulation of the Satellite Signal in the Solar Spectrum, 6S: An overview. IEEE Transactions on Geoscience and Remote Sensing 35 (3), 1997. – P. 675-686.

49. Wien W. Ueber die Energievertheilung im Emissionsspectrum eines schwarzen Körpers. Annalen der Physik 58, 1896. – P. 662-669.

50. Malenovsky Z., Rott H., Cihlar J., Schaepman M., Garcia-Sntos G., Fernandes R., Berger M. Sentinels for science: Potential of Sentinel-1, -2, and -3 missions for scientific observations of ocean, cryosphere, and land, Williams D.L., Goward S., Arvidson T. Landsat: Yesterday, today, and tomorrow. Remote Sensing of Environment, 2012. - P. 91-101.

51. Belogub E.V., Novoselov K.A., Yakovleva V.A., Spiro B.F. Supergene sulphates from the supergene zone of sulphide deposits (exemplified by the Urals deposits). Geology of Ore Deposits 59 (7), 2017. – P. 582-602.

52. Blanchard R. Interpretation of leached outcrops. Nevada Bureau of Mines Bulletin 66, 1968. –196 p.

53. Cook N.J., Ciobanu C.L., Spry P.G., Voudouris P. Understanding gold-(silver)-telluride-(selenide) mineral deposits. In: Robb, L.J. (ed), Introduction to Ore-Forming Processes. John Wiley & Sons: Chichester, UK, 2013. – P. 263-295.

54. Cooke D.R., Hollings P., Wilkinson J.J., Tosdal R.M. Geochemistry of porphyry deposits. Treatise on Geochemistry, 2nd ed. Elsevier: Amsterdam, Netherlands, 2014. – P. 357-381.

55. Crosta A.P., Souza Filho C.R., Azevedo F., Brodie C. Targeting key alteration minerals in epithermal deposits in Patagonia, Argentina, using ASTER imagery and principal component analysis. International Journal of Remote Sensing 24 (21), 2003. – P. 4233-4240.

56. Gahlan H.A., Arai S., Ahmed A.H., Ishida Y., Abdel-Aziz Y.M., Rahimi A. The origin of the ultramafic rocks of the Fawakhir ophiolite in the Central Eastern Desert of Egypt: Implications for the tectonic evolution of the Central Eastern Desert. Gondwana Research 77, 2020. – P. 308-324.

57. Groves D.I., Goldfarb R.J., Gebre-Mariam M., Hagemann S.G., Robert F. Orogenic gold deposits: a proposed classification in the context of their crustal distribution and relationship to other gold deposit types. Ore Geology Reviews 13, 1998. – P. 7-27.

58. Groves D.I., Goldfarb R.J., Robert F., Hart C.J.R. Gold deposits in metamorphic belts: overview of current understanding, outstanding problems, future research, and exploration significance. Economic Geology 98, 2003. – P. 1-29.

59. Large R.R., Bull S.W., Maslennikov V.V. A carbonaceous sedimentary source-rock model for Carlin-type and orogenic gold deposits. Economic Geology 102 (2), 2007. – P. 291-304.

60. Lobato L.M., Ribeiro-Rodrigues L.C., Vieira F.W.R. Brazil's premier gold province. Part II: geology and genesis of gold deposits in the Archean Rio das Velhas greenstone belt, Quadrilátero Ferrífero. Mineralium Deposita 36, 2001. – P. 249-277.

61. Pirajno F. Hydrothermal Processes and Mineral Systems. Springer: Dordrecht, Netherlands, 2009. –1250 p.

62. Ridley J.R., Mikucki E.J., Groves D.I. Archean lode-gold deposits: fluid flow and chemical evolution in vertically extensive hydrothermal systems. Ore Geology Reviews 18 (1-2), 2000. – P. 1-28.

63. Robert F., Poulsen K.H., Cassidy K.F., Hodgson C.J. Gold metallogeny of the Superior and Yilgarn cratons. In: Eckstrand, O.R., Sinclair, W.D., Thorpe, R.I. (eds), Geology of Canadian Mineral Deposit Types. Geological Survey of Canada, Geology of Canada 8, 1995. – P. 343-371.

64. Mizernaya M.A., D'yachkov B.A. Technology of advanced estimation of gold deposits using modern methods of mineralogical mapping: on scientific and research work (final). Non-profit stock company «D. Serikbayev east Kazakhstan technical university». Ust-Kamenogorsk, 2020. –100 p.

65. Marghany M. Remote Sensing and Image Processing in Mineralogy. CRC: Boca Raton (Taylor & Francis Group), 2020. – 300 p.

66. Khain V.E. Tektonika kontinentov i okeanov (god 2000). M.: Nauchnyi mir, 2001. –604 p.

67. Polyansky N.V., Khomyakov V.D. Ofiolity Charskogo poyasa. In: Ofiolity. Alma-Ata: Nauka, 1981. – P. 103-178.

68. Clark R.N., Swayze G.A., Wise R., Livo E., Hoefer T., Kokaly R., Sutley S.J. USGS Digital Spectral Library splib06a. U.S. Geological Survey Digital Data Series 231, 2007. https://www.usgs.gov/

69. Pan, P.P., Chen, G.Y., Saruta, K. and Terata, Y. (2015) Snow Cover Detection Based on Visible Redand Blue Channel from MODIS Imagery Data. International Journal of Geosciences, 6, P. 51-66

70. Pan Z., Huang J., Wang F., Han L., van Genderen J. International Journal of Applied Earth Observation and Geoinformation, Volume 14, P. 112–128

71. Phillips G.N., Powell R. Formation of gold deposits: a metamorphic devolatilization model. Journal of Metamorphic Geology, 28 (6), 2010. - P. 689-718

72. Rowan L.C., Schmidt R.G., Mars J.C. Distribution of hydrothermally altered rocks in the Reko Diq, Pakistan mineralized area based on spectral analysis of ASTER data. Remote Sensing of Environment 104 (1), 2006. – P. 74-87. DOI: 10.1016/j.rse.2006.05.014.

73. Vaulin O.V. Vostochno-Kazakhstanskaya oblast. Zoloto. Spravochnik, Ust-Kamenogorsk – Bishkek: ROKIZOL, 2016. - 331 p.

74. Rafailovich M.S., D'yachkov B.A. Stratourovni zolotogo orudeniya v chernoslantsevykh tolshchakh kazakhstana. IV. Ranne-srednekamennougol'nyi period. Geologiya i okhrana nedr 3 (44), 2012. – P. 15-30.

75. Ermolov P.V. Current Problems of Isotopic Geology and Metallogeny of Kazakhstan. Karaganda: Publishing and Printing Center of Kazakhstan-Russian University, 2013. –206 p.

76. Elachi C., van Zyl J. Introduction to the Physics and Techniques of Remote Sensing. John Wiley & Sons: Hoboken, USA, 2006. –576 p.

77. Maslennikov V.V. Geologiya i genezis zoloto-sul'fidnykh mestorozhdenii Zapadno-Kazakhstanskoi zony (na primere mestorozhdenii Bakyrchik i Bol'shevik). Geologiya rudnykh mestorozhdenii 39 (5), 1997. – P. 392-410.

78. Yurchenkov A.V. Geologo-strukturnye osobennosti zoloto-sul'fidnykh mestorozhdenii Bakyrchikskogo rudnogo polya. Geologiya i geofizika 27 (9), 1986. – P. 48-56.

79. Lowell J.D., Guilbert J.M. Lateral and vertical alteration-mineralization zoning in porphyry ore deposits. Economic Geology 65 (4), 1970. – P. 373-408.

80. Rockwell B.W. Spectral variations in rocks and soils containing ferric iron hydroxide and (or) sulfate minerals as seen by AVIRIS and laboratory spectroscopy. U.S. Geological Survey Open-File Report 2004-1431, 2004. DOI: 10.3133/ofr20041431. https://www.usgs.gov/

81. D'yachkov B.A., Mizernaya M.A., Khromykh S.V., Bissatova A.Y., Oitseva T.A., Miroshnikova A.P., Frolova O.V., Kuzmina O.N., Zimanovskaya N.A., Pyatkova A.P., Zikirova K., Ageyeva O.V., Yeskaliyev Y.T. Geological History of the Great Altai: Implications for Mineral Exploration. Minerals. 12 (6), 2022. 744. https://doi.org/10.3390/min12060744

82. Mizernaya M., Miroshnikova A., Yeskaliyev Y., Oitseva T.A., Kuzmina O.N. Structural position, magmatism and mineralization of Bakyrchik Ore field (Kazakhstan). International Multidisciplinary Scientific GeoConference Surveying Geology and Mining Ecology Management, SGEM 22 (1.1), 2022. – P. 499-506. https://doi.org/10.5593/sgem2022/1.1/s04.058

83. Yeskaliyev Y., Zikirova K. Methodology of scientific forecasting based on GIS of precious metal deposits in Eastern Kazakhstan // «Geoinformatics» European Association of Geoscientists & Engineers, 11- 14 May, 2021. Kiev, Ukraine. Volume 2021, 21093, P. 1-6. https://doi.org/10.3997/2214-4609.20215521093

84. Mizernaya M.A., Zikirova K.T., Yeskaliyev Y.T., Aitkazyyev T., Joyashish T. The Scientific Basis of the Investment Attractiveness of Geological Structures on the Example of Rudny Altai. Universitet Enbekteri – University Proceedings. 1 (90). - 2023. – P. 144-150. DOI 10.52209/1609-1825_2023_1_144

85. Mizernaya M.A., Dyachkov B., Miroshnikova A., Zikirova K.T., Yeskaliyev Y.T. Features of Geological Structure, Magmatism and Ore Formation of Bakyrchik ore Field Deposits. Universitet Enbekteri – University Proceedings. №3 (84). - 2021. - P. 94 – 99. DOI:10.52209/1609-1825_2021_3_94

86. World Gold Council. Gold.org. https://www.gold.org/

87. Kalinowski A., Oliver S. ASTER Mineral Index Processing Manual. Remote Sensing Applications, Geoscience Australia, 2004. –36 p.

88. Johns Hopkins University. Spectral Library. https://www.jhu.edu/

89. DLR/GFZ. Spectral Library. https://www.gfz-potsdam.de/

90. ASD/HySpex. Spectral Library. https://www.malvernpanalytical.com/

91. ECOSTRESS/JPL. Spectral Library. https://ecostress.jpl.nasa.gov/

92. Wilson C., Tunningley A. Understanding Low Sulfidation (LS) Epithermal. Deposits. Association of Mining Analysts, 2013. https://cdn.ceo.ca.s3-us-west-2.amazonaws.com/1d88pu0-LS-Epithermal_2013_07_AMA.pdf

93. Kerr A., Rafuse H., Sparkes G., Hinchey J., Sandeman H. Visible/infrared spectroscopy (VIRS) as a research tool in economic geology: Background and pilot studies from Newfoundland and Labrador. Geol. Surv. Rep. 11, 2011. - P. 145–166.

94. Gupta R.P. Remote Sensing Geology, Springer 2017, 423 p.

APPENDIX A

Act of Implementation of Research Results in Educational process

AGREED
Member of the Board Vice-Rector
for Science and Innovation
NJSC «D. Serikbayev EKTU»
_____ Zh.T. Konurbayeva
« 31 » 12 2025

APPROVED
Member of the Board - Vice-Rector
for Academic Affairs
NJSC «D. Serikbayev EKTU»
_____ A. Mashekenova
« 31 » 12 2025

IMPLEMENTATION ACT

on the incorporation into the university's educational process of research results on the title «Methodology for prospecting gold-bearing deposits using modern satellite technologies, case study West Kalba gold belt»

We, the undersigned,	
Director of the Department for Academic Affairs	Nurekenova E.S.
Director of the Department for SRA	Uazyrkhanova G.K.
Dean of School of Earth Sciences	Rakhymberdina M.Ye.
Head of the Educational Program	Rakhymberdina M.Ye.

We, the undersigned, have drawn up this report stating that the research results of Yertay Talgatovich Yeskaliyev - a doctoral student of the NJSC "D. Serikbayev East Kazakhstan Technical University" - were implemented in the educational process of the educational program 7M07302 «Geodesy», School of Earth Sciences in 2025 year.

The research results (2020 - 2025) on the title "Methodology for prospecting of gold-bearing deposits using modern satellite technologies, case study of the West Kalba gold belt" are used in lectures and practical classes for master's students of the «Geodesy» educational program in the course "Automated systems for collecting and processing remote sensing results." Implementation effect: collection and analysis of ASTER satellite data, working with spectral data, visualization of spectral indices.

In practical classes for the course "Automated systems for collecting and processing remote sensing results," basic spectral indices (reflectance of water, buildings, soil, and minerals) are studied. Soil modeling and mineral mapping have been developed and are used in the educational process.

These materials are reflected in the Work Modular Curriculum (syllabus) for the course "Automated systems for collecting and processing remote sensing results" in the topics of lecture classes (Topic 12. «Modern remote sensing methods for mapping gold-ore deposits») and practical classes (Topic 6. «Processing and analysis of remote sensing data to identify hydrothermal alteration»).

Director of the Department for Academic Affairs	Nurekenova E.S.
Director of the Department for SRA	Uazyrkhanova G.K.
Dean of School of Earth Sciences	Rakhymberdina M.Ye.
Head of the Educational Program	Rakhymberdina M.Ye.

APPENDIX B

Act of Implementation of Research Results in Production

APPROVED
Member of the Board Vice-Rector
for Science and Innovation
NJSC «D. Serikbayev EKTU»
_____ Zh.T. Konurbayeva
"08" 01 2026

APPROVED
Director of «GEOSAT» LLP
_____ E.V. Grokhotov
"08" 01 2026

IMPLEMENTATION REPORT
results of research work in higher educational institutions

By order: «GEOSAT» Limited Liability Partnership.

This act confirms that the results of the dissertation "Methodology for prospecting gold-bearing deposits using modern satellite technologies, case study West Kalba gold belt", performed at the NJSC "D. Serikbayev East Kazakhstan Technical University":

- cost: no cost
- implemented: in "GEOSAT" Limited Liability Partnership.

1. Type of implemented results: methodology for prospecting gold-bearing deposits using modern satellite technologies.
2. Characteristics of the implementation scale: single.
3. Implementation form: technical documentation, algorithm.
4. Novelty of research results: an effective Band Ratios method is presented, a spectral catalog is compiled that serves as verification methods based on the USGS spectral library, and a modern Cross Validation verification technique is proposed, which increases the number and quality of results.
5. Implemented:
- in project works: for use in satellite data collection and processing plans.
6. Social and scientific and technological impact: strengthening and expanding the use of satellite technology methods for various applications.

From the University
Head of the EP
_____ N.A. Zimanovskaya

PhD student _____ Y.T. Yeskaliyev

From the Company
Director of «GEOSAT» LLP
_____ E.V. Grokhotov